TÉCNICO LISBOA

UNIVERSIDADE DE LISBOA
INSTITUTO SUPERIOR TÉCNICO

Improving Streamflow Calculation by Combining Physical Models and Neural Networks

Ana Isabel Baião Ramos de Oliveira

Supervisor: Doctor Ramiro Joaquim de Jesus Neves
Co-supervisor: Doctor Tiago Cunha Brito Ramos

Thesis approved in public session to obtain the PhD Degree in Environmental Engineering

Jury final classification: Pass with Distinction

2023

UNIVERSIDADE DE LISBOA
INSTITUTO SUPERIOR TÉCNICO

Improving Streamflow Calculation by Combining Physical Models and Neural Networks

Ana Isabel Baião Ramos de Oliveira

Supervisor: Doctor Ramiro Joaquim de Jesus Neves
Co-supervisor: Doctor Tiago Cunha Brito Ramos

Thesis approved in public session to obtain the PhD Degree in Environmental Engineering

Jury final classification: Pass with Distinction

Jury

Chairperson: Doctor José Manuel de Saldanha Gonçalves Matos, Instituto Superior Técnico, Universidade de Lisboa

Members of the Committee:

Doctor Ramiro Joaquim de Jesus Neves, Instituto Superior Técnico, Universidade de Lisboa

Doctor Agustín Millares Valenzuela, Andalusian Institute for Earth System Research (IISTA), University of Granada, Spain

Doctor Rodrigo de Almada Cardoso Proença de Oliveira, Instituto Superior Técnico, Universidade de Lisboa

Doctor Rui José Raposo Rodrigues, Laboratório Nacional de Engenharia Civil, I.P.

2023

Resumo

A modelação hidrológica é crítica para a avaliação do estado presente, tendências passadas e perspetivas futuras das disponibilidades de água. Mais especificamente, o conhecimento sobre os regimes e valores de caudais nos rios é essencial em diversas atividades e situações. O presente trabalho foca-se, assim, na estimativa do caudal considerando quatro domínios onde diferentes problemas relacionados com a água foram identificados. Os quatro domínios correspondem à zona Oeste da Península Ibérica (OPI) e às bacias hidrográficas do Guadiana, Maranhão e rio Ulla. A previsão do caudal foi realizada usando três abordagens diferentes, nomeadamente, um modelo físico, MOHID-Land, um modelo baseado em dados e uma solução híbrida na qual os dois tipos de modelos são acoplados.

O domínio OPI inclui diferentes bacias hidrográfica independentes entre si. Este domínio foi modelado com o MOHID-Land para a estimativa do caudal em regime natural. Os resultados mostraram que a consideração de um domínio tão grande e diversificado não é a abordagem mais adequada na modelação de bacias hidrográficas. A bacia hidrográfica do Guadiana também foi simulada com o MOHID-Land considerando não só o caudal em regime natural mas, também, o impacto da operação das barragens no caudal. Nesta abordagem, à escala da bacia hidrográfica, foi possível demonstrar a capacidade do modelo em reproduzir o caudal em condições de regime natural. Contudo, aquando da consideração da operação das barragens, os resultados demonstraram uma diminuição na capacidade do modelo em reproduzir o regime de caudal. As limitações identificadas em ambos os estudos foram o ponto de partida para o restante trabalho.

O MOHID-Land foi, assim, alvo de uma análise de sensibilidade por forma a identificar os principais parâmetros que influenciam a simulação do caudal. Esta análise foi realizada utilizando como caso de estudo a bacia hidrográfica do rio Ulla e os resultados permitiram que a simulação do caudal em regime natural nesta bacia atingisse um nível bastante bom. Os resultados deste estudo contribuíram, também, para o sucesso da modelação da bacia hidrográfica do Maranhão. Contudo, neste último caso o MOHID-Land foi calibrado e validado para uma sub-bacia, cujos parâmetros calibrados foram posteriormente expandidos ao domínio completo. A validação desses resultados foi, então, realizada considerando um balanço de massa ao nível da albufeira, a qual estava situada no ponto mais a jusante da bacia. Posteriormente, um modelo baseado em dados do tipo rede neuronal foi testado para a estimativa do caudal seguindo o mesmo procedimento. Assim, um modelo do tipo *convolutional neural network* (CNN) foi desenvolvido e treinado para a sub-bacia referida anteriormente e os resultados

foram posteriormente expandidos ao domínio completo através da substituição das variáveis de entrada.

Por fim, e por forma a ultrapassar a dificuldade na representação da operação das barragens em modelos hidrológicos, foi estudada uma solução híbrida aplicada à bacia hidrográfica do rio Ulla. Assim, o caudal de saída de uma barragem situada naquela bacia e com alta capacidade de armazenamento foi estimado com um modelo do tipo *convolutional long short-term memory* (CLSTM). Este modelo foi alimentado pelos valores de caudal de entrada e nível estimados pelo MOHID-Land, enquanto os caudais de saída previstos pelo modelo CLSTM foram impostos nesse mesmo modelo hidrológico. Os resultados obtidos indicaram uma melhoria substancial quando o modelo acoplado é considerado, relevando a importância de considerar este tipo de infraestruturas durante a modelação.

A presente tese discute a fiabilidade de diferentes métodos para a estimação do caudal em regime natural e em sistemas complexos marcados por alterações antrópicas. A discussão centra-se nas principais limitações e nos principais parâmetros que interferem na precisão da representação dos sistemas. Os resultados levaram ao desenvolvimento de uma nova abordagem que conecta o modelo MOHID-Land e uma rede neuronal, permitindo ultrapassar as limitações identificadas inicialmente.

Palavras-chave: modelação hidrológica; caudal; modelo físico; MOHID-Land; redes neuronais.

Abstract

Hydrological modeling is critical for evaluating the status, past trends, and future perspectives of water availability. More specifically, knowledge about streamflow regimes and values is essential for different activities and situations. This work focuses on the estimation of streamflow considering four different domains in which different water related problems were identified: the Western Iberian Peninsula (WIP), and the Guadiana, Maranhão and Ulla River watersheds. Streamflow was estimated using three different approaches, namely, with a physically based model, MOHID-Land, a data-driven model, and a hybrid solution coupling both types of models.

The WIP, which contained several independent watersheds, was modelled with MOHID-Land for natural streamflow estimation. Results demonstrated the inadequacy in considering such a large and diversified domain. The Guadiana watershed was also modelled with MOHID-Land, considering the natural regime flow and the influence of reservoirs operation. This study at the watershed scale demonstrated the relative adequacy of the model in simulating the natural regime flow at the watershed scale, but identified several shortcomings when considering reservoirs' operation, which the work that followed aimed to overcome.

The MOHID-Land was first subjected to a sensitivity analysis to identify the key parameters impacting streamflow simulation. The Ulla River watershed was the selected case study, with the MOHID-Land showing high accuracy for simulations of the natural regime flow. The results of that study also contributed to the successful implementation of MOHID-Land model in the Maranhão watershed. In this case study, the MOHID-Land model was calibrated and validated for a sub-basin, and the calibrated parameters were extended to the entire watershed. The results' validation was performed considering a mass balance of the reservoir located in the watershed's outlet. Afterward, a data-driven model was tested following the same procedure in the same study area. A convolutional neural network model was developed and trained for the sub-basin and then extended to the entire watershed. Both approaches were compared, and the advantages and shortcomings of both solutions were discussed.

Finally, a hybrid solution was applied to the Ulla River watershed. To overcome the difficulty in representing reservoirs' operation in hydrological models, the outflow of a high-capacity reservoir placed in the watershed was estimated with a convolutional long short-term memory (CLSTM) model, with this model being fed by the inflow and level values estimated by MOHID-Land. Then, the outflow values obtained with the CLSTM model were imposed in MOHID-Land model. Results demonstrated a drastic improvement when the coupled system

was considered, highlighting the importance of considering this type of infrastructure during the modelling task.

Hence, this thesis discusses the reliability of different methods for streamflow estimation considering natural regime flow and complex systems with anthropogenic modifications, centering the discussion on the main limitations and key parameters influencing the accurate representation of systems. The findings allowed the development of a new approach that connects MOHID-Land with a neural network model, and which allowed to surpass many of the initial shortcomings.

Keywords: hydrological modelling; streamflow; physically based model; MOHID-Land; neural networks.

Agradecimentos

Agradeço ao Prof. Ramiro Neves pelo apoio, pela oportunidade e pela tranquilidade que me proporcionou para desenvolver e finalizar este trabalho e esta etapa da minha vida. Sei que as condições que encontrei no MARETEC não são o padrão, mas foram essenciais neste percurso. Agradeço-lhe, também, a liberdade de pensamento e de trabalho, a confiança, e todas a oportunidades a que tive acesso. Agradeço-lhe as reuniões de projetos, as conferências, e os congressos onde pude ir, não só, divulgar o nosso trabalho, mas também conhecer e aprender com outras realidades. Agradeço-lhe, principalmente, a confiança que depositou em mim para orientar, e ao dar-me a responsabilidade de lecionar os cursos de MOHID-Land e algumas das suas aulas. Foi uma experiência extremamente gratificante.

Agradeço, igualmente, ao Tiago Ramos por toda a disponibilidade e ajuda desde o meu primeiro dia no MARETEC. Agradeço-lhe a paciência, as discussões produtivas e as não produtivas, a atenção, os momentos de descontração, as horas gastas a ler e reler artigos, e, acima de tudo, o tanto que me ensinou sobre o que é a vida de investigador. Tem sido, sem dúvida, uma companhia essencial no meu percurso neste mundo da investigação científica.

Ao Lucian, ao Jorge e à Débora agradeço-lhes a sua generosidade na partilha de conhecimento, o seu apoio constante, o seu companheirismo e os momentos partilhados dentro e fora das paredes do MARETEC. O que me ensinaram em todos os aspetos da minha vida é, sem dúvida, imensurável.

À Sara C. e à Marta L., as minhas espanholas, obrigada pela amizade, pelos bons momentos, pelo companheirismo e, claro, pelas *tortillas de patatas*!

Agradeço, também, aos restantes colegas do MARETEC que cruzaram o meu caminho durante mais ou menos tempo, mas que de alguma forma contribuíram para o meu percurso. À Lígia, à Cristina, à Sara F., à Ya G., à Michelle, à Hilda, ao João, ao Guilherme e ao Marcos, o meu muito obrigada.

Ao meu amigo Kiko agradeço o apoio, a partilha de ideias e a nossa amizade.

Ao Tomás agradeço por, mesmo sem saber, ter alegrado tantas das minhas tardes e por ter trazido a leveza de se ser criança para os últimos passos deste percurso.

À minha tia Idália, ao meu tio Carlos e ao meu primo António, agradeço o apoio incondicional.

À minha Mãe, ao meu Pai e às minhas irmãs, Inês e Mariana, não há como agradecer o caminho que têm feito comigo. Por sempre me terem proporcionado as condições e o apoio de que precisei, por me guiarem, pela honestidade, pela partilha, pelas conversas, pelos momentos

de diversão e alegria, o meu mais sincero e gigante obrigada. Este momento não teria o mesmo significado sem vocês ao meu lado.

Index

Index of figures

Index of tables

1 Introduction

In 2015 the United Nations defined 17 Sustainable Development Goals (SDG) in the attempt to promote planet protection, end poverty, hunger and disease spreading, and to create a more egalitarian world (SDG-UNDP, n.d.). Part of these SDGs are directly or indirectly related to water. For instance, SDG6 intends to promote access to clean water and sanitation, and SDG 14 and 15 are related with life below water and on land, respectively. Also, SDG 1, no poverty, and SDG 2, zero hunger, are both water dependent, since poverty and hunger eradication rely on food production, which in turn relies on the availability of water for irrigation. SDG 3, good health and well-being, SDG 7, affordable and clean energy, SDG 12, responsible consumption and production, and SDG 13, climate action, can also be intimately related to water as, to successfully deal with these issues, water availability and good water management practices need to be put into practice. Thus, water represents one of the pillars for a more sustainable and fairer world.

In parallel, the last Intergovernmental Panel on Climate Change (IPCC) report (Pörtner et al., 2022) refers that nowadays half of the world's population is already experiencing sever water scarcity for at least 1 month per year due to climatic and other factors, a condition that is exacerbated by inadequate water governance. Those situations are aggravating the societal impacts of droughts and floods, are impacting agriculture and energy production, are contributing to land degradation, and are increasing the incidence of water-borne diseases, especially in low-income countries. That same report makes an analysis of the water related projected risks. It points out that 800 million to 4 thousand million people will face different levels of water scarcity dependent of the projected warming temperature. It also evidences that 10% of the global land area can face increasing high extreme streamflow and decreasing low extreme streamflow simultaneously. Changes in the water cycle will also affect the ecosystem services, with predictions pointing to 42% to 79% of the world's watersheds environmental critical streamflow being affected. It also predicts an increase of wildfires combined with soil erosion due to deforestation causing a degradation of water supplies. The increase of evapotranspiration, the alteration of spatial patterns and amount of precipitation, the consequent changes in groundwater recharge, runoff and streamflow will then affect terrestrial, freshwater, estuarine and coastal ecosystems, and the transport of materials through the biogeochemical cycles. These changes, in turn, have an impact on humans and societal well-being, with agriculture, energy production and urban water uses being affected. Population growth will also increase water needs in terms of food production, which is irrigation

dependent. Also drinking water needs and industrial water supplies are predicted to increase with population growth. The projected risks of extreme hydrological events are also a focus of the IPCC report, which states that South and Southeast Asia may face significative problems related to food availability and prices. The Mediterranean and parts of Europe will suffer potential reductions of hydropower of up to 40%, and up to 410 million people living in urban areas will be exposed to water scarcity because of severe droughts. Flood local events and associated societal damages are also predicted to increase as a consequence of more intense precipitation events, with coastal areas being at higher risk because of the projected sea level rise. All this problematic can then explain the increase in freshwater demands, with local, national, and regional hydrological systems being put under a high level of pressure.

With water being such an important and essential resource for life on Earth, the understanding of water resources systems, the study of water processes and its complexity, the capacity to forecast near and long-term future hydrological events and integrate all this knowledge to improve water resources management is of extreme importance.

In this regard, Droogers and Bouma (2014) state that simulation models are appropriate and indispensable tools to supply relevant information, based on reliable data, to assess past, present, and future conditions of water resources. More specifically, from a water governance perspective, the authors defend that hydrological models applied at the operational level allow water resources managers to shift their behavior from a reactive to a proactive approach, including in the decision-making process information about different possible scenarios. This will lead to more substantiated and assertive decisions.

Streamflow knowledge and estimation are assumed by several authors as essential in a wide range of applications and studies (Bourdin et al., 2012; Ni et al., 2020). The list includes flood warning systems, hydroelectric reservoir operation, hydraulic structure design, fish production and survival, nutrient transport and water quality assessment, evaluation of long-term climate or land use change impacts, and the definition of water management policies, besides the proper management and allocation of water resources, especially in areas with highly variable climate conditions and where there is not enough available data to adequately support decision-making (Humphrey et al., 2016).

1.1 Hypothesis and research objectives

Models driven by physical laws are usually considered powerful tools to understand and predict the conditions of a modelled system. They can represent different processes and the corresponding interactions very accurately. However, their physical basis together with the

detail with which their implementations are characterized makes the incorporation of random and unpredictive human behavior difficult. Thus, the hypothesis of this work is:

- When natural regime flow is altered by human impacts, it is possible to accurately predict streamflow values if different modelling techniques are combined.

The hypothesis was tested focusing the assessment of streamflow values in different watersheds, where different water related problems were already identified. The hydrological modelling was mainly performed considering two types of models, namely, a physically based model and a data-driven model. These types of models are opposite in terms of complexity, data needs, and the capacity of explicitly consider the hydrological processes. As a consequence, the implementation of both approaches is obviously distinct, implying a level of understanding and knowledge about the modelled system that is totally different. If on one hand, more complex models can give a wider view of the system and allow the investigation of different processes taking place in the modelled domain, their complexity and the amount of data needed can make its implementation difficult. On the other hand, less complex models are easier to implement. They need long time series data for the variables included in the analysis, but, besides that, no further characterization of the studied domain needs to be made, reducing the data necessities when compared with more complex models. However, since they are blind to physical processes, the interpretation of their results and errors can be a hard task and they do not allow an integrated view of different processes occurring in the modelled domain. Thus, to verify the hypothesis presented before, the main objectives of this research were defined as:

1. Present and discuss the strengths and the weaknesses of different modelling approaches at different scales.
2. Evaluate the capacity and robustness of different types of models to estimate streamflow and evaluate if the modelling performance is improved when they are combined.
3. Demonstrate the contribution of hydrological modelling to improve water resources management.

1.2 Thesis structure

The present thesis is composed of 9 chapters, starting with the current Introduction, and ending with the Conclusions chapter, where the main conclusions of the work carried out and the proposed ideas for future work are presented. The 2nd chapter contextualizes the research developed, focusing on the importance of hydrological modelling nowadays, followed by a

contextualization of the MOHID-Land model and the neural network models, which are the two main modelling tools used here. The chapter finishes with a brief presentation of the studied domains.

The other 6 chapters describe the work developed on this thesis, with each chapter corresponding to a manuscript (published or submitted). The title of the chapters/manuscripts, authors, journal, and candidate's role of each publication are listed below:

- **Chapter 3:** Modeling streamflow at the Iberian Peninsula scale using MOHID-Land: challenges from a coarse scale approach.

  Details: Ana R. Oliveira, Tiago B. Ramos, Lucian Simionesei, Maria C. Gonçalves, Ramiro Neves. Water 2022, 14, 1013, https://doi.org/10.3390/w14071013.

  Candidate's role: the candidate was responsible for the implementation of the modelling approach and the analysis of the results, as well as the writing of the manuscript. The conceptualization and the definition of the methodology were shared between all the authors.

- **Chapter 4:** Influence of reservoir management on Guadiana streamflow regime.

  Details: Nelson Canuto, Tiago B. Ramos, Ana R. Oliveira, Lucian Simionesei, Marta Basso, Ramiro Neves. Journal of Hydrology: Regional Studies 2019, 25, 100628, https://doi.org/10.1016/j.ejrh.2019.100628.

  Candidate's role: the candidate was responsible for the guidance given for model implementation and results analysis. The conceptualization and the methodology followed that presented in the previous chapter.

- **Chapter 5:** Sensitivity analysis of the MOHID-Land hydrological model: a case study of the Ulla River basin.

  Details: Ana R. Oliveira, Tiago B. Ramos, Lucian Simionesei, Lígia Pinto, Ramiro Neves. Water 2020, 12, 3258, https://doi.org/10.3390/w12113258.

  Candidate's role: the candidate was responsible for the conceptualization and methodology definition together with other authors. The programming task, the modelling process, results analysis, and manuscript writing were performed by the candidate.

- **Chapter 6:** Streamflow estimation in a Mediterranean watershed using neural network models: a detailed description of the implementation and optimization.

  Details: Ana R. Oliveira, Tiago B. Ramos, Ramiro Neves. Water 2023, 15, 947, https://doi.org/10.3390/w15050947.

Candidate's role: the candidate was responsible for the conceptualization, definition of the methodology, the programming and modelling processes, the analysis of the results, and the manuscript writing.

- **Chapter 7:** Assessing the reliability of a physical based model and a convolutional neural network in an ungauged watershed for daily streamflow prediction.

  Details: Ana R. Oliveira, Tiago B. Ramos, Lucian Simionesei, Ramiro Neves. Submitted to

  Candidate's role: the candidate was responsible for the conceptualization, development of part of the software, formal analysis, modelling task, and writing of the original draft. The methodology was elaborated by all the authors.

- **Chapter 8:** Direct integration of reservoirs' operations in a hydrological model for streamflow estimation: coupling a CLSTM model with MOHID-Land.

  Details: Ana R. Oliveira, Tiago B. Ramos, Lígia Pinto, Ramiro Neves. Submitted to Hydrology and Earth System Sciences.

  Candidate's role: the conceptualization was defined by all the authors, while the candidate defined the methodology, performed the programming job, executed the modelling task, analyzed the results, and wrote the first draft of the paper.

The organization of this thesis intends to demonstrate the steps that were taken to reach good performances in streamflow estimation with the applied models. Because the research process is not only based on successful cases, chapters 3 and 4 present two situations where the selected modelling approach was not adequate, being the basis for the work developed in the following chapters. Chapter 5 presents a sensitivity analysis of the physically based model in order to master its behavior and obtain better performances. Then, in the attempt to investigate the adequacy and introduce the more recent solutions available in the literature, an application of neural network models to a small watershed is presented in chapter 6. The study made in chapter 6 is complemented by chapter 7, where the same small watershed was modelled by the physically based model and the ability of both approaches to represent the streamflow generation in a larger watershed that contains the first was compared. The study detailed in chapter 8 intends to demonstrate the improvement that streamflow estimation can have if those models are used to complement each other the gaps. Therefore, this last chapter presents the use of a neural network model to estimate the outflow of a reservoir and the results are introduced in the physically based model implemented to simulate the hydrological processes in the watershed where the reservoir is placed.

It is also important to denote other works that were developed during the period that contemplates the PhD degree reported here, and the two years before. Without being exclusively dedicated to streamflow estimation, those projects were essential for the development of a deeper understanding about hydrological modelling and, especially, about the physically based model used in this research. Some of those works are already published and what they represented to the development of this study justifies their reference in the following list:

- Horta, A.; **Oliveira, A. R.**; Azevedo, L.; Ramos, T. B. *Using digital soil hydraulic properties maps to simulate soil-water balance – implications for water management plans* (submitted to Geoderma Regional).
- Campuzano, F.; Santos, F.; Simionesei, L.; **Oliveira, A. R.**; Olmedo, E.; Turiel, A.; Fernandes, R.; Brito, D.; Alba, M.; Novellino, A.; Neves, R. *Framework for improving land boundary conditions in ocean regional products*. Journal of Marine Science and Engineering 2022 10, 852.
- Rosa, A.; Cardoso, C.; Vieira, R. R.; Faria, R.; **Oliveira, A. R.**; Navarro, G.; Caldeira, R. *Impact of flash flood events on the coastal waters around Madeira Island: the 'Land Mass Effect'*. Frontiers Marine Science 2022, 8:749638.
- Ramos, T. B.; Simionesei, L.; **Oliveira, A. R.**; Neves, R.; Darouich, H. *Exploring the use of vegetation indices for validating crop transpiration fluxes computed with the MOHID-Land model*. Application to vineyard. Agronomy 2021, 11, 1228.
- Simionesei, L.; Ramos, T. B.; Palma, J.; **Oliveira, A. R.**; Neves, R. *IrrigaSys: A web-based irrigation decision support system based on open source data and technology*. Computers and Electronics in Agriculture 2020, 178, 105822.
- Ramos, T. B.; Simionesei, L.; **Oliveira, A. R.**; Darouich, H.; Neves, R. *Assessing the impact of LAI data assimilation on simulations of the soil water balance and maize development using MOHID-Land*. Water 2018, 10, 1367.

1.3 References

Bourdin, D. R.; Fleming, S. W.; Stull, R. B. *Streamflow Modelling: A Primer on Applications, Approaches and Challenges*. Atmos. Ocean 2012, 50:4, 507-536. https://doi.org/10.1080/07055900.2012.734276

Droogers, P.; Bouma, J. *Simulation modelling for water governance in basins*. Int. J. Water Resour. Dev. 2014, 30, 3, 475-494. http://dx.doi.org/10.1080/07900627.2014.903771

Humphrey, G.B.; Gibbs, M.S.; Dandy, G.C.; Maier, H.R. *A hybrid approach to monthly streamflow forecasting: Integrating hydrological model outputs into a bayesian artificial neural network*. J. Hydrol. 2016, 540, 623–640. https://doi.org/10.1016/j.jhydrol.2016.06.026

Pörtner, H.-O.; Roberts, D.C.; Adams, H.; Adelekan, I.; Adler, C.; Adrian, R.; Aldunce, P.; Ali, E.; Ara Begum, R.; BednarFriedl, B.; et al. Technical Summary. In: Climate Change 2022: Impacts, Adaptation and Vulnerability. Contribution of Working Group II to the Sixth Assessment Report of the Intergovernmental Panel on Climate Change. Cambridge University Press 2022, Cambridge, UK and New York, NY, USA, pp. 37–118, doi:10.1017/9781009325844.002.

Ni, L.; Wang, D.; Singh, V.P.; Wu, J.; Wang, Y.; Tao, Y.; Zhang, J. *Streamflow and rainfall forecasting by two long short-term memory-based models*. J. Hydrol. 2020, 583, 124296. https://doi.org/10.1016/j.jhydrol.2019.124296

SDG-UNDP (Sustainable Development Goals | United Nations Development Programme). (n.d.). Available online: https://www.undp.org/sustainable-development-goals (accessed on 29 March 2023)

2 Context

2.1 Hydrological modelling

Hydrological models can be important tools to predict unexpected changes regarding water supplies that create uncertainties for water managers. Linsley (1976) was one of the first hydrologists that worked in the development of hydrological modeling (Droogers and Bouma, 2014). He stated that the main objectives of model applications are: (i) to express hydrological processes and their interaction using quantitative mathematical expression, providing clarity and understanding, and (ii) to promote analysis of future scenarios that cannot be measured.

As with any other model, hydrological models are a simplified representation of the "real-world" system (Wheater et al., 2007, Droogers and Bouma, 2014). Even with this limitation, hydrological models, together with the continuous improvement of computational capacity, continue to be one of the best available tools to provide relevant information in the search of better managed water resources systems. Hydrological modelling is thus an efficient way to analyze spatial and temporal data taking into account the interactions and impacts of different river basin components (Loucks et al., 2005). As is well known, all the components of the hydrological cycle are intimately related (Figure 2.1), and the management of a single component can affect the performance of other components in a river basin system. This linking between components results in a necessity for multi-component models that can represent the different processes of the system.

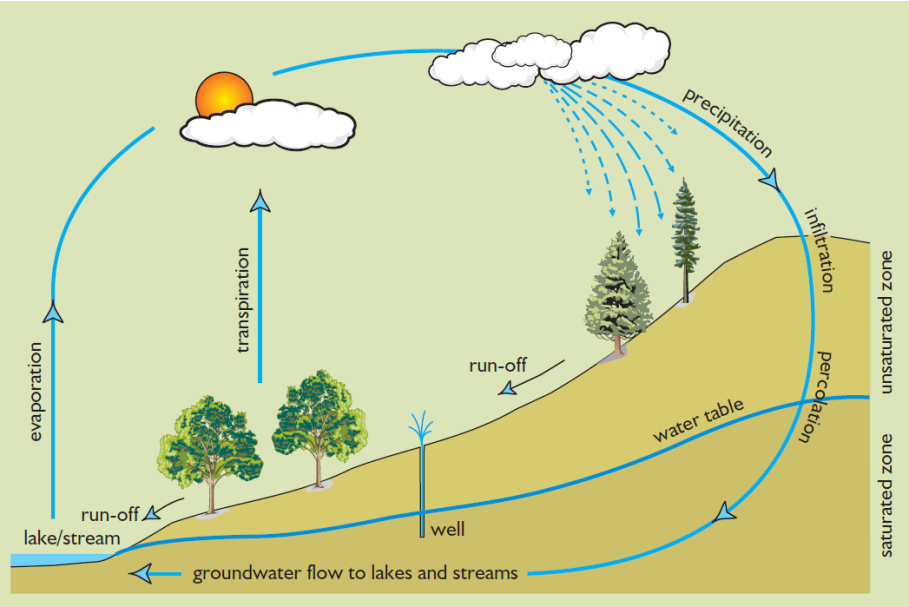

Figure 2.1 A schematic diagram of the hydrological cycle applied to a watershed (source: Loucks et al., 2005).

The classification of hydrological models can be made considering different aspects. It can consider the basis of the model, the randomness of the variables, the time coverage, and the way a model accounts for the spatial characterization of the watershed (Loucks et al., 2005).

Considering the rationale, a model can be classified as theoretical or empirical. Empirical models, also known as statistical models, are totally blind to physical principles and are considered representations of the observed data. In opposition, there are theoretical, also known as physically based, models, which are governed by physical principles described by mathematical functions. However, it is common to simplify the calculations of physically based models using empirical components, such as the Manning's equation.

According to the type of variables used, models can be divided into deterministic or stochastic. If model's variables are totally free from random variation, the model is classified as deterministic, while if the values of one or more variables of the model can change unpredictably over time it is considered a stochastic model. Hydrological models are usually classified as deterministic models.

If a hydrological model simulates a single event, usually with a time coverage of about an hour to several days, the model is classified as event based. However, if the model considers the simulation of a sequence of time periods and for each period it determines the state of the watershed keeping a continuous account of the watershed surface and groundwater conditions, it is classified as a continuous-time model. In the former case, results accuracy is dependent on the reliability of the system's initial conditions, which are often assumed or determined by other means. In the latter case, the effect of initial conditions usually decreases rapidly as simulation time advances.

Finally, hydrological models can be classified as lumped, distributed or quasi- or semi-distributed, the latter resulting from a mix of the first two. This classification is related to the spatial discretization of the modelled domain. Lumped models simulate hydrological processes assuming homogeneous or average conditions for the entire or portions of a watershed, while distributed models consider the locations of different watershed characteristics such as land cover, soil type, and topography. Semi-distributed models are then made up of multiple connected lumped models representing parts of watersheds.

2.2 MOHID-Land, a physically based model

MOHID, which stands for Hydrodynamic Model (MOdelo HIDrodinâmico, in Portuguese), is the name of the water modelling system that includes the MOHID-Water and MOHID-Land models. With MOHID-Water dedicated to surface water bodies simulation,

MOHID-Land is directed to the simulation of the hydrological processes inland. Both are open-source models (github.com/Mohid-Water-Modelling-System/Mohid) written in ANSI Fortran 95 and based on a modular structure. They are characterized by an objected oriented programming philosophy and based on a finite volume approach. Because MOHID-Water and MOHID-Land belong to the same modelling system, they share basic functions and input and output formats. This simplifies the interface between both models, facilitating the integration of their results in each other's simulations.

The development of MOHID-Land started in 2000 with the inclusion of the numerical simulation of water fluxes and storages in the MOHID system (Neves et al., 2000). After that, Trancoso et al. (2009) presented the MOHID River Network, which was a one dimensional (1D) hydrodynamic model to simulate river networks. From then to present, MOHID-Land has known significative developments and improvements. These changes were made to provide the model with different methods of computation for some of the processes, aiming to improve the ability of the model to answer different problems. Also, the increasing number of case studies has given rise to different realities to be modelled. This led to the emergence of new processes and situations needing to be simulated, which were not contemplated at first. Thus, the changes made in the model over the last decades were driven by a need to overcome the limitations caused by the lack of conditions to properly simulate the new domains. Nowadays, MOHID-Land is able to consider the simulation of different processes with respect to the hydrological cycle.

MOHID-Land (Trancoso et al. 2009, Canuto et al, 2019, Oliveira et al. 2020) is a fully distributed and physically based model that considers the mass and momentum conservation equations combined with a finite volume approach to simulate the water movement. To avoid instability problems and save computational time, the model time step is variable, being higher during dry seasons and lower in wet periods when water fluxes increase.

The control volumes result from the discretization of the modelled domain by a combination of two grids: one in the surface plane and one in the vertical direction, the latter corresponding to the discretization of the porous media. The surface grid is a regular grid constructed based on the coordinate system chosen by the user, while the vertical grid follows a cartesian coordinate system. According to the elevation values assigned to each cell in the surface grid, the river network is constructed linking the surface cell centers (nodes). Thus, the river network is represented by a one-dimensional (1D) domain, the surface land is represented by a two-dimensional (2D) domain, and the porous media is represented by a three-dimensional

(3D) domain, with the water movement being simulated according to this discretization (Figure 2.2).

MOHID-Land works based on 4 main compartments, namely, the atmosphere, the porous media, the surface land, and the river (Figure 2.2). The atmosphere compartment is essentially simulated considering the MOHID's atmosphere module, which is shared by MOHID-Land and MOHID-Water. It is the only compartment that is not explicitly simulated, being responsible for dealing with the information related to meteorological boundary conditions (precipitation, air temperature, solar radiation, etc.). Meteorological boundary conditions can be time and space variant. The remaining three compartments are simulated based on 9 modules that constitute the core of the MOHID-Land model.

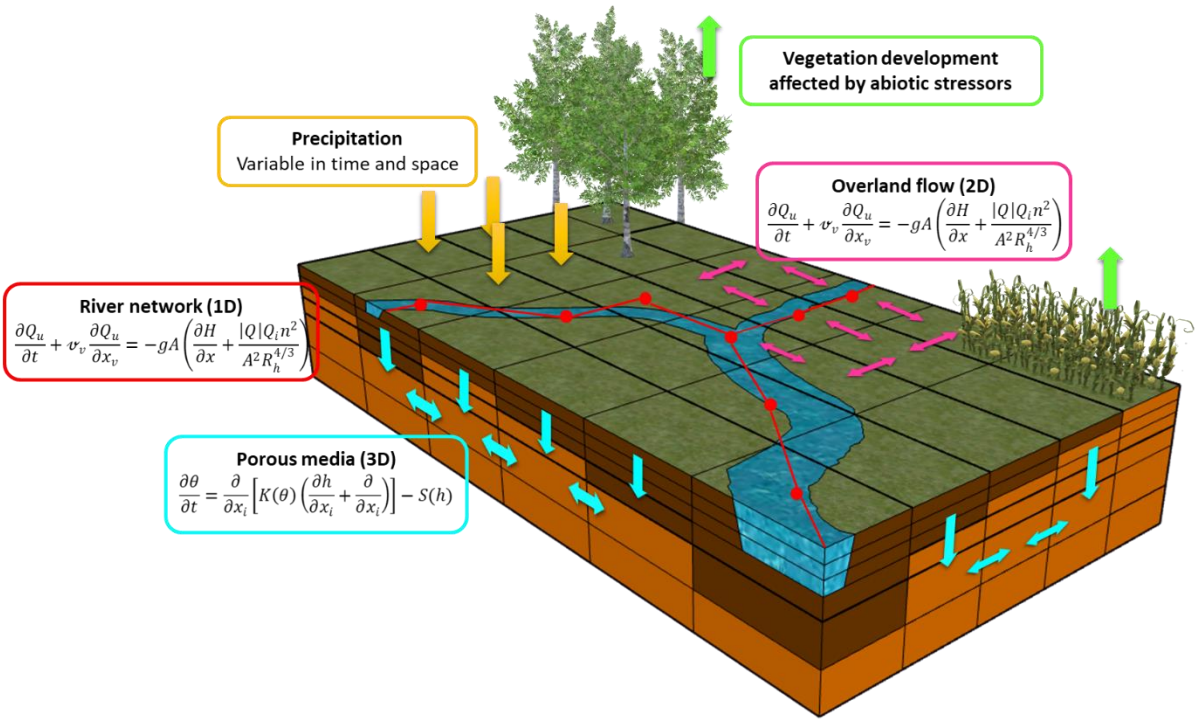

Figure 2.2 Scheme of discretization of a domain modelled with MOHID-Land.

The 9 modules that constitute MOHID-Land are: basin, irrigation, porous media and porous media properties, reservoirs, runoff and runoff properties, snow, and vegetation. Besides those modules, there are several other modules of MOHID Water Modelling system that are shared inside the system. Most of the functions to deal with the input data, boundary conditions and the initialization of the models are placed in shared libraries. Among those shared modules are included the already referred atmosphere module, the discharge module, the drainage network, and the basin geometry modules. Figure 2.3 presents a simplified scheme of the interactions of the modules belonging to MOHID-Land's core.

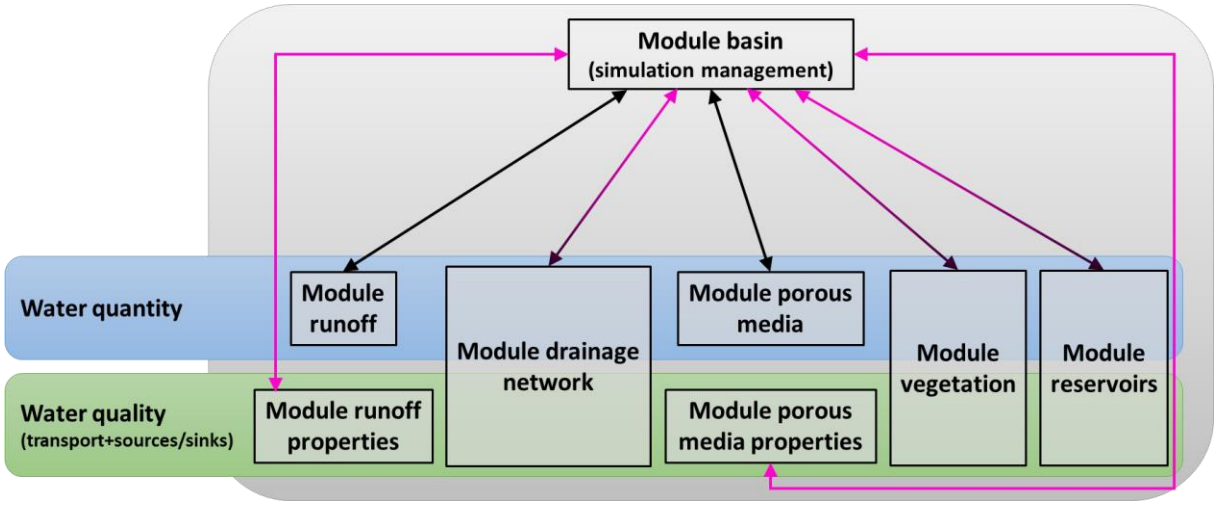

Figure 2.3 Scheme of MOHID-Land modules and corresponding information fluxes for water balance (black arrows) and property balance (pink arrows).

The basin module is responsible for the management of the simulation and calls the modules responsible for meteorological boundary conditions, overland flow and drainage network processes, and the porous media and vegetation processes. It is also here that potential evapotranspiration and the basin water balance are estimated. When a simplified scheme (Green and Ampt or SCS CN method) describing the infiltration process is active, this module is responsible for estimating the infiltration rate.

Potential evapotranspiration rates are obtained by multiplying reference evapotranspiration by a crop coefficient specific to each type of vegetation. While crop coefficient values are tabulated for most of the crops, reference evapotranspiration is here calculated based on the weather conditions and according to the FAO Penman-Monteith method (Allen et al., 1998). Potential evapotranspiration is then divided into potential transpiration and potential evaporation as a function of the plant stage, with these processes being detailed further below.

In MOHID-Land the precipitated water at a certain time step is first divided into the amount of water that is intercepted by leaves and the amount of water that effectively reaches the surface. After that, the estimated infiltration rate drives the subsequent processes, estimating the amount of water that can enter the porous media and the remaining being transformed into surface and river runoff.

2.2.1 Infiltration and porous media

In MOHID-Land, the infiltration rate can be estimated according to three different methods: Darcy's law (Eq. 2.1), Green and Ampt method (Green and Ampt, 1911), and SCS Curve Number (SCS CN) method (Soil Conservation Service, 1972).

$$i = -K_{sat}\left(\frac{\partial h}{\partial z} + 1\right) \quad \text{(Eq. 2.1)}$$

with i being the infiltration rate (LT^{-1}), K_{sat} the saturated hydraulic conductivity (LT^{-1}), h the soil pressure head (L), and z the vertical space coordinate (L).

The Green and Ampt and SCS CN are both classified as empirical methods and can be used without considering the fluxes in the porous media, while Darcy's law is driven by physical conditions. In the case of the SCS CN model, it first estimates the amount of water transformed into surface runoff, with the remaining becoming available for infiltration.

Infiltration rates represent the velocity of the water entering the soil, which are then converted to vertical fluxes. If porous media is not being simulated (only possible for Green and Ampt and SCS CN methods), the infiltrated water is lost from the system. However, if porous media's fluxes are considered in the simulation, the water contents in each cell of the 3D domain are estimated taking into account the vertical and horizontal fluxes imposed by the infiltration process. Then, the water content values are analyzed by comparison with the saturated water content of the corresponding cell. If a saturation threshold is exceeded, the excess of water can be infiltrated to the next layer of soil, can arise to the above layer by capillarity, or can be exfiltrated, contributing to the surface water column, if the process is occurring in the surface soil layer.

The movement of the water that infiltrates in the soil is computed according to Richards' equation:

$$\frac{\partial \theta}{\partial t} = \frac{\partial}{\partial x_i}\left[K(\theta)\left(\frac{\partial h}{\partial x_i} + \frac{\partial}{\partial x_i}\right)\right] - S(h) \quad \text{(Eq. 2.2)}$$

where θ is the volumetric water content (L^3L^{-3}), x_i represents the xyz directions (-), K is the hydraulic conductivity (LT^{-1}), and S is the sink term representing root water uptake ($L^3L^{-3}T^{-1}$). The soil hydraulic properties are described using the van Genuchten Mualem functional relationships (Mualem, 1976; van Genuchten, 1980) with the definition of 6 different parameters for each type of soil: residual and saturated water contents, saturated hydraulic conductivity, pore connectivity/tortuosity parameter, and two other values that are empirical shape parameters. That saturated hydraulic conductivity is defined by the user and corresponds to the vertical direction. The horizontal saturated hydraulic conductivity ($K_{sat,hor}$) is then obtained from the vertical saturated hydraulic conductivity ($K_{sat,ver}$) considering a factor (f_h) defined by the user. This factor represents the ratio between horizontal and vertical saturated hydraulic conductivities ($f_h = K_{sat,hor}/K_{sat,ver}$).

Porous media processes also contemplate the evaporation of the surface soil layer. This process can be activated or deactivated by the user, who can also define a limit for the evaporation velocity and for the evaporation head.

The biogeochemical cycles that take place in soil can also be added to the simulation, however those processes are not analyzed here because the subject of the present work is water quantity.

2.2.1.1 Vegetation

The sink term of Richards' equation represents the soil water loss caused by root water uptake, which occurs when vegetation is present. The root water uptake is estimated considering the potential transpiration and corrected considering the soil water availability.

Based on the reference evapotranspiration (ET_0, LT^{-1}), potential crop evapotranspiration (ET_c, LT^{-1}) is calculated by multiplying the first by a crop coefficient (K_c) defined for each type of vegetation. Then, potential crop evapotranspiration is partitioned into potential crop transpiration (T_p, LT^{-1}) and soil evaporation (E_p, LT^{-1}). Potential crop transpiration is calculated as a function of the leaf area index (LAI, L^2L^{-2}), which in its turn is simulated considering a modified version of the EPIC model (Neitsch et al., 2011; Williams et al., 1989) and the heat units' approach for the plant to reach maturity:

$$T_p = ET_c\left(1 - e^{-\lambda LAI}\right) \quad \text{(Eq. 2.3)}$$

where λ is the extinction coefficient of radiation attenuation within the canopy (-). The potential soil evaporation is then obtained by the difference between the potential crop evapotranspiration and the potential crop transpiration.

The actual crop transpiration is then calculated considering root water uptake reductions due to depth-varying stressors, such as water and salinity stresses (Šimůnek and Hopmans, 2009; Skaggs et al., 2006). The root water uptake reductions are computed according to the macroscopic approach proposed by Feddes et al. (1978), where the real crop transpiration is calculated as a function of the soil pressure head. The actual soil evaporation is also reduced imposing a head threshold value (ASCE, 1996).

With the transpiration water loss completely dependent on the plant stage, the vegetation module is responsible for the simulation of plants' evolution and the estimation of their properties in each instant. Based on the heat units' approach, each type of vegetation needs the definition of the minimum and optimal temperatures for its development and the total heat units to reach maturity. Then, according to the ratio of heat units accumulated by plant and the respective maturity heat units, the plant stage is updated. The updated plant's properties include

the root depth, the root biomass, the total plant biomass, the leaf area index, and the canopy height.

In previous versions of MOHID-Land, it was not possible to directly simulate the evolution of the crop coefficient when different types of vegetation are present in the modelled domain. Thus, most of the implementations at the watershed scale assumed a constant single crop coefficient throughout the entire simulated period. However, crop evapotranspiration varies during the crop season as a function of LAI development. The evapotranspiration evolution can be directly integrated in the simulation by imposing a variation of crop coefficient as a function of the plant growth stage (Figure 2.4).

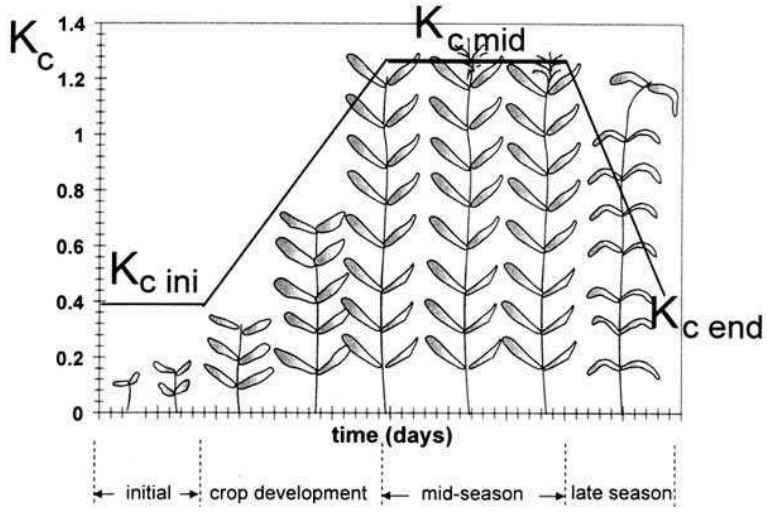

Figure 2.4 Evolution of single crop coefficient in time (source: Allen et al.,1998).

Considering the simulation already being performed for other properties, a similar approach was implemented for the crop coefficient. Thus, the simulation of the evolution of crop coefficient was based on Allen et al. (1998), with the definition of three single crop coefficients for the initial ($K_{c,ini}$), the mid-season ($K_{c,mid}$), and the end.season ($K_{c,end}$) stages of plant development. In each instant, the crop coefficient was estimated following Eq. 2.4.

$$K_c = \begin{cases} K_{c,ini}, & GFr < GFr1 \\ K_{c,ini} + \dfrac{GFr - GFr1}{GFr2 - GFr1}\left(K_{c,mid} - K_{c,ini}\right), & GFr1 < GFr < GFr2 \\ K_{c,mid}, & GFr2 < PS < GFrLAI_{Sen} \\ K_{c,mid} + \dfrac{GFr - GFr2}{1.0 - GFr2}\left(K_{c,end} - K_{c,mid}\right), & GFr2 < GFr < 1.0 \\ K_{c,end}, & GFr > 1.0 \end{cases} \quad \text{(Eq. 2.4)}$$

where GFr, GFr1, GFr2 and $GFrLAI_{Sen}$ are the plant growth fractions in the current instant, in the initial and mid-season stages, and when the LAI senescence starts, respectively. Those growth stages are represented as percentage of maturity heat units, and the values for GFr1,

GFr2 and $GFrLAI_{Sen}$ are defined in the plant growth database of MOHID-Land. Also, the three crop coefficients introduced here should be defined in the plant growth database. With all those parameters being set independently for each type of vegetation, this method allows the estimation of the crop coefficient in each simulated instant and for each type of vegetation present in the domain.

Finally, the plant development is triggered when the planting date, defined by the user, is reached. Planting date can be set as Julian day or in heat units, as a percentage of the total temperature degrees that an entire year can comprehend. This annual accumulation of temperature degrees is not directly calculated by MOHID-Land, with the user defining this value before the simulation starts. This value is defined considering the average temperature of one day in the modelled domain multiplied by the number of days within a common year.

User can also activate the simulation of other activities present in the simulated domain, namely, the grazing activity, the harvest and/or the kill activities, the dormancy, and the application of fertilizers and pesticides. With the dormancy cycle being dependent on the length of the day light, its beginning and ending dates are estimated by the model. However, for the remaining activities, the user must define the dates when they occur. As for the planting date, those dates can be set as Julian day or using the heat units' approach, but in this case the percentage of heat units respects the plant's maturity heat units.

Supplementary information about the simulation of plant development in MOHID-Land can be found in Simionesei et al. (2016) and Ramos et al. (2017), where the update of different plant properties within the growth period is explained in detail.

The application of fertilizers and pesticides implies the activation of the simulation of biogeochemical cycles in porous media. However, since the study of water quality properties is not the target of the present work, that capability is not analyzed here.

2.2.1.2 Irrigation

Although irrigation is not considered in this work, it is an important part of the water balance in a watershed, especially in areas where summer is characterized by high temperatures and low precipitation values.

In MOHID-Land, the irrigation can be imposed or estimated. Irrigation can be imposed by the user when the applied irrigation depths and times are known. However, when those values are unknown irrigation needs can be estimated by the model and directly applied during the simulation. In both cases the irrigation fluxes are added to the precipitation fluxes and the resulting water volume is applied to the domain.

As described by Ramos et al. (2017), when irrigation depths are estimated by MOHID-Land, the first task performed by the model is to check the water stored in each cell of the simulated domain. For that, the user must define a minimum threshold pressure head (h_{min}) and a target pressure head (h_{tar}). Then, considering each layer of the rootzone domain of each cell defined in the surface plane, the model checks if the water content is lower than h_{min}. If it is, the volume of water needed to reach h_{tar} is the deficit of water that 3D cell. The water deficit estimated in 3D cell is then accumulated in the soil column and the total represents the irrigation needs. However, to prevent the occurrence of too many irrigation events or the application of meaningless irrigation amounts, a minimum irrigation pulse, a maximum irrigation pulse, a minimum area to irrigate and a minimum irrigation interval must be defined. The model will only apply the estimated irrigation needs when they are higher than the minimum irrigation pulse, the area to be irrigated is higher than the minimum area to irrigate, and if the minimum irrigation interval since the previous irrigation event is overcame. The amount of irrigation applied is never higher than the maximum irrigation pulse, but if the water needs are higher than that maximum, the irrigation events will be scheduled in a way that all the constraints imposed by the system are fulfilled.

In MOHID-Land, the development of the irrigation module was more focused on the plot scale. In that sense, the source of the water for irrigation purposes is not relevant and impossible to consider. Thus, MOHID-Land does not allow the definition of the water sources for irrigation purposes, which can have a relevant effect when the simulation of this activity is considered at the watershed level.

Also, the fact that the simulations at plot scale (1D simulation, considering only vertical fluxes) are much simpler than those at watershed scale (3D domains), affects the usage of the irrigation module in the latter case. With more water being introduced in the porous media when irrigation is applied, computational time increases significantly, with much more impact on 3D domains. This increase may be such that it makes it impossible to consider the irrigation processes as they are being simulated in large 3D domains.

2.2.2 Surface flow

MOHID-Land solves the Saint-Venant equation (Eq. 2.5) to compute the surface flow, which occurs considering two dimensions in the surface plane and considering one dimension in the river network. The equation is solved in its conservative form, accounting for advection, pressure, and friction forces.

$$\frac{\partial Q_u}{\partial t} + \mathcal{v}_v \frac{\partial Q_u}{\partial x_v} = -gA\left(\frac{\partial H}{\partial x} + \frac{|Q|Q_i n^2}{A^2 R_h^{4/3}}\right) \quad \text{(Eq. 2.5)}$$

where Q is the flow in the river (LT^{-1}), A is the cross-sectional flow area (L^2), g is the gravitational acceleration (LT^{-2}), $\mathcal{v}$ is the flow velocity (LT^{-1}), $\partial H/\partial x$ is the hydraulic gradient (-), n is the Manning coefficient ($TL^{-1/3}$), R_h is the hydraulic radius (L), x e the length that separate, and subscripts u and v denote flow direction.

The cross-sectional flow area in the surface plane considers the water column and the dimension of the cell in the flow direction, while in the river network the geometry and dimensions of node's cross sections are defined by the user.

The available water to generate surface flow results mainly from the amount of water that did not infiltrate. However, as was focused on the porous media section (see section 2.2.1) some water can be exfiltrated from the soil, contributing to the surface flow on the horizontal plane.

Water exchanges also occur between the river network and the porous media, with the fluxes being driven according to the head pressure gradient. Thus, when head pressure is higher in soil than in the river, the water flows from the soil contributing to the river flow, while in the opposite situation the water in the river infiltrates into the soil.

Biogeochemical cycles can also be simulated in the runoff medium, as well as the erosion and deposition processes.

2.2.2.1 Reservoirs

In MOHID-Land, reservoirs work as a box where a mass balance is performed (Figure 2.5). It is essential to know the water stored volume (V_{stored}), and the volume of the inflow (I), outflow (O), and other discharges that go in (D_{In}) and/or out (D_{Out}) of the reservoir (Eq. 2.6).

$$V_{stored}^{i} = V_{stored}^{i-1} + (I + D_{In}) - (O + D_{Out}) \quad \text{(Eq. 2.6)}$$

with i representing the instant being simulated.

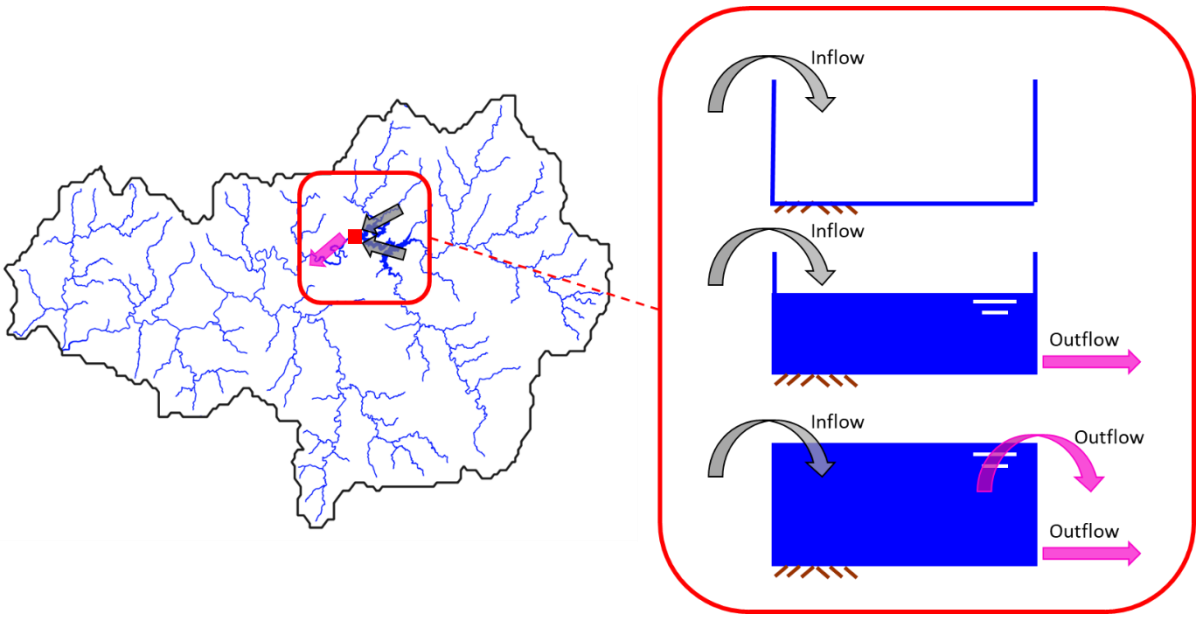

Figure 2.5 Scheme of reservoir operation in MOHID-Land.

Reservoirs are placed in the nodes of the river network with the inflow considered for the mass balance being that in the nodes immediately upstream. More than one reservoir can be simulated at the same time in MOHID-Land, with the reservoirs operationality being dependent on the definition of several of its characteristics. The minimum requirements are the minimum and maximum volumes, the minimum outflow, and the curve defining the relation between the level and the stored volume must be defined. That curve allows the inference of the level of the reservoir for each estimated stored volume. The maximum outflow can also be defined.

The outflow of each reservoir can be imposed or estimated. When imposed, the user must define a discharge and the corresponding volume of water removed from the reservoir is allocated to the river network in the node immediately downstream the reservoir. In case that the outflow is estimated by the model, it is necessary to define its type of operation. The type of operation allows the estimation of reservoir's outflow as a function of the inflow, the stored volume and/or the level. The outflow can then be defined as an absolute value according to the level of the reservoir in each instant. Also, as a function of the level, the outflow can be defined as a percentage of the inflow. Considering the stored volume, the outflow can be defined as an absolute value, as a percentage of the inflow or as a percentage of the maximum outflow. In all the cases a curve with at least two points must be specified.

Mainly to consider water supplies with their source in the reservoir, reservoirs' module is prepared to take into account the imposition of water withdrawals. The volume of water removed by this method is considered to leave the system. Discharges entering the reservoir

can also be considered, with the origin of the water discharged into the reservoir being also undefined.

The processes of infiltration and evaporation significantly affect the volume of water stored in a reservoir. Although they are not yet considered in the reservoirs' processes simulated in MOHID-Land, they are of extreme importance in the mass balance performed at reservoir scale.

2.3 Neural networks, empirical models

The machine learning term has its origins in 1959, in the context of game-learning computers and arises from the fundament that software can learn how to play strategic games with a better performance than that obtained by a human programmer (Lange and Sippel, 2020). In the beginning, machine learning was closely connected with artificial intelligence (AI). However, over the years, that connection has been diminished, mostly because machine learning has a strong connection with statistics and probability theory, using tools mainly for regression and/or classification problems, while AI is based on expert systems and knowledge-based software. It is then easy to conclude that machine learning techniques are totally dependent on data availability, including the capacity of automatically collect, store, and distribute data.

Neural networks are a type of supervised machine learning method, as well as decision trees, random forest, support vector machines, and others. Neural networks are data-oriented, or data-driven, approaches, in which the main goal is to detect and describe patterns in univariate or multivariate datasets. Those patterns are then generalized and used to make predictions on the system state.

The history of neural networks started in 1958, when a psychologist, Rosenblatt, developed an investigation about an electronic device, a perceptron (Rosenblatt, 1958), which had the ability to learn, and which construction was based on biological principles (Macukow, 2016). Then, in 1960, Widrow and Hoff (1960) developed a different method for leaning based on the Least-Mean-Squares learning rule.

After those first attempts, there was a period when neural networks were discredited. Minsky and Papert (1969) published a book discussing a number of fundamental problems of the perceptron approach. However, that discussion was based on a perceptron two-layer machine that was only able to deal with linearly separable problems, instead of the powerful multiple layer perceptron machine defined by Rosenblatt. Although minimal resources were dedicated to this field of research during this negative period, some researchers made valuable

improvements. Klopf (1972) presented a basis for learning considering the biological principle, Werbos (1974) developed a back-propagation learning method, Fukushima (1975) studied a stepwise trained multilayered neural network to interpret handwritten characters, and Grossberg (1976) introduced the adaptative resonance as a theory of human cognitive information processing.

In the decade of 1980, a renewed interest in neural networks emerged. Several works where new advances were presented were published (Kohonen, 1982; Hopfield, 1982; Rumelhart et al., 1986; Carpenter and Grossberg, 1987), older studies were revisited with a different perspective (Werbos ,1974), annual meetings and conferences were launched (Neural Networks for Computing meeting; IEEE International Conference on Neural Networks), several journals were founded (Neural Networks; Neural Computation; IEEE Transactions on Neural Networks), and the International Neural Network Society was created.

In more recent years, the recurrent neural networks and deep feedforward neural networks were introduced, and a processor (TrueNorth) with the size of a postage stamp capable of simulate the work of millions of neurons and 256 million of synapses in real time was developed.

The research in this field has experienced a huge advance, with neural networks being used in a variety of applications. Hydrology is not an exception, and Lange and Sippel (2020) presented a review of key machine learning algorithms already used in that field including artificial neural networks (ANNs), convolutional neural networks (CNNs), support vector machines (SVMs), decision trees learning, random forest, and gradient boosting machine.

Sit et al. (2020) also presented a review of deep learning applications in hydrology and water resources. Limiting the review to papers that must include some form of deep ANN technique in their methodology, and considering a period that starts in 2018 and ends in March 2019, the authors analyzed 129 publications. From this set, they refer that the most used neural network architectures are convolutional neural networks (CNNs), Generative adversarial networks (GANs), recurrent neural networks (RNNs), long short-term memory (LSTM) networks, gated recurrent unit (GRU) networks, nonlinear autoregressive (NAR) models, Elman network (ENN), autoencoders (AEs), restricted Boltzmann machines (RBM), deep belief networks (DBNs), extreme learning machines (ELMs), and deep Q networks (DQNs).

Although the impressive development that has been seen in the field of deep learning in the last few years and the significative number of studies proving the ability of these techniques to model and predict hydrological processes, climate change and earth systems, there are still skeptics concerning the application of this type of approach. However, as pointed out by Lange

and Sippel (2020), machine learning techniques are just one more tool available in the modelling process, with its main strengths being the achievement of higher accuracy, robustness, efficiency, computation cost, and overall model performance (Ardabili et al. 2020). Also, these techniques are not formulated to replace process-based modelling approaches, since they are only suitable for situations where machines are good at learning and when enough and appropriate data are available to teach the model (Lange and Sippel, 2020). In that sense, the modelling process can take a significative advantage from the combination of data-driven and process-based approaches, with the improvement of predictions using this hybrid modelling approach already demonstrated by several authors (Humphrey et al., 2016; Okkan et al., 2021; Dong et al. 2023).

2.4 Case studies

There were 4 different areas modelled in this study, namely, the western part of Iberian Peninsula, and the Guadiana, Ulla River and Maranhão watersheds (Figure 2.6). The definition of those domains is in accordance with the work developed on the behalf of several projects that were carried out during the period in which this thesis was developed. In the following sections a brief description of the modelled domains is presented.

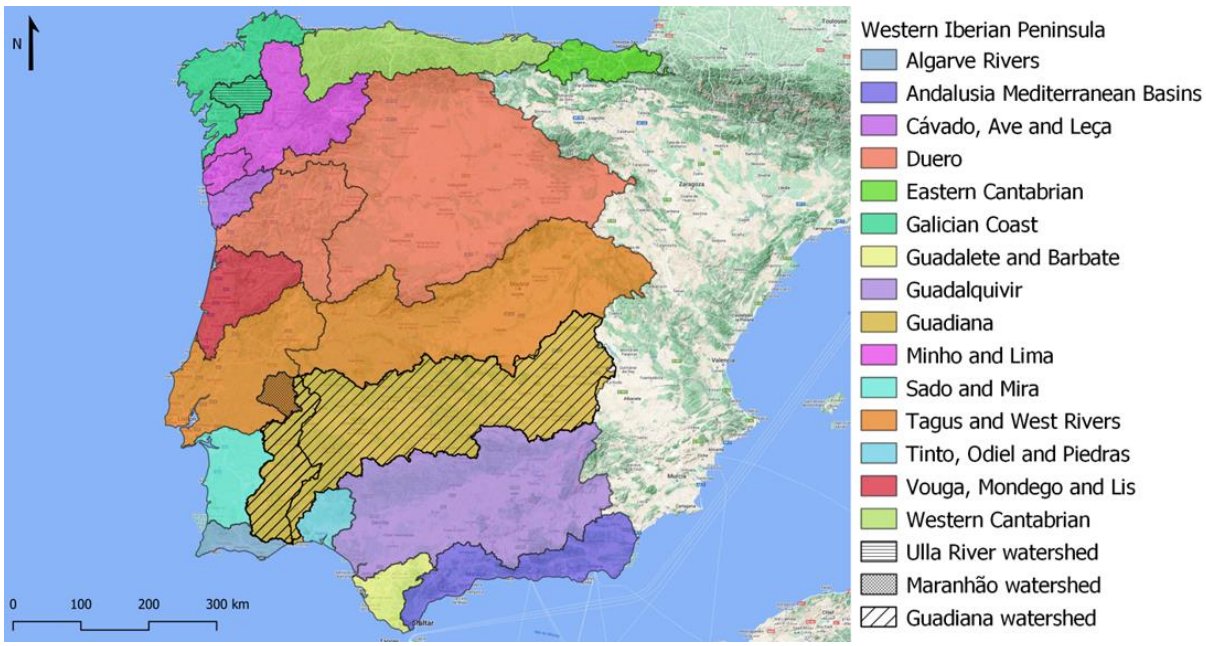

Figure 2.6 Studied domains.

2.4.1 Western Iberian Peninsula

The Western Iberian Peninsula domain was modelled on the behalf of INTERREG SUDOE AGUAMOD project. It was a research project in which the main goal was to promote the cooperation between managers and land users involved with water resources management

in Southwest Europe (Portugal, Spain, Andorra, and part of France) with the development, sharing and implementation of innovative methodologies. Because drought events are getting more and more common in Southwest Europe, AGUAMOD's focus relied on low flow periods. However, a global analysis of the water needs and stocks using numerical models was performed in the entire domain considering wet and dry periods.

Reflecting the ability of MOHID-Land to consider domains that do not need to be coincident with the delineation of watersheds, the modelling approach adopted to answer AGUAMOD's purposes considered the division of the entire project's area into 3 sub-domains, with each of them including several watersheds. Thus, considering Portugal's geographical position, a special attention was given to the sub-domain where the country is contained. Defined as the Western Iberian Peninsula, the referred sub-domain included 19 river basin districts that were modelled in a single MOHID-Land implementation (Figure 2.6).

The Western Iberian Peninsula sub-domain covers an area of 438 178 km^2 (75% of the Iberian Peninsula) that comprises different climatic patterns. In the North, the climate is characterized by warm summers, dry in the West and without a dry season in the East. The South and Southwest have dry and hot summers, while the central and East parts are mainly characterized by an arid, steppe and cold climate. These differences in climatic patterns have a strong impact in the differences in flow regimes within the domain, with the South part presenting a higher risk of hydrological droughts.

To prevent water scarcity problems in drier areas, namely, in the South of the Iberian Peninsula, water storage through the construction of reservoirs was promoted. Thus, in the studied domain a total of 1113 reservoirs were identified, with 65% of them being placed in the South. Those 65% of the reservoirs in the South also correspond to about 64% of the total storage capacity in the entire domain. However, the adoption of these types of strategies alters the natural river flow regimes, with the modelling approach of these areas being hampered because of the anthropogenic modifications caused by those infrastructures.

Besides that, the simulation of such a large and diversified area also implies the generalization of several properties and characteristics of the domain to simplify the modelling approach. However, that generalization can make it difficult to correctly represent the modelled domain, interfering in the accurate representation of the processes that take place in different areas of the domain.

The Western Iberian Peninsula was here modelled considering the natural regime flow (no reservoirs were included) and using the MOHID-Land model. The discretization of the modelled domain in the surface plane comprehended a grid with a resolution of 0.045° in both

directions (Figure 2.7). The vertical discretization included a grid composed of six layers, with a maximum depth of 30 m.

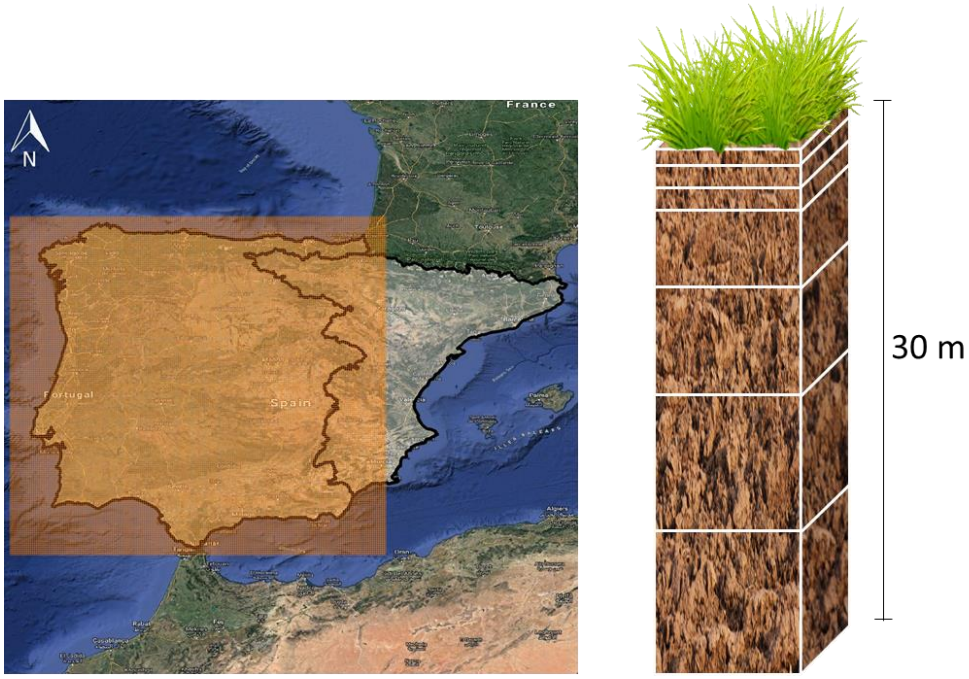

Figure 2.7 Discretization of Western Iberian Peninsula domain.

2.4.2 Guadiana

The modelling of Guadiana watershed (Figure 2.6) was also performed within the scope of the AGUAMOD project. If the modelling of Western Iberian Peninsula was performed for natural regime flow and including different and independent watersheds in the same application, the modelling work carried out in Guadiana watershed was focused on this single watershed and considered one scenario with reservoirs and other scenario without the presence of reservoirs.

The Guadiana watershed is one of the four watersheds divided between Portugal and Spain, with Spain holding 83% of the area and Portugal the remaining 17%. According to the Portuguese and Spanish Management River Basin Plans, Guadiana watershed has a regularization index of 266 in Portugal and 248 in Spain, being both the highest values found within the watersheds located in the western of the Iberian Peninsula. Combining the areas that lie on both countries, Guadiana watershed presents the highest storage capacity (14 213 hm^3, 25%) in the Western Iberian Peninsula. However, with its East part included in an area classified as arid, steppe and cold climate, and the West part characterized by dry and hot summers, its annual surface flow is the sixth lower value among the watersheds comprehended in the west Iberian Peninsula.

Guadiana watershed was modelled with the MOHID-Land model. This implementation followed the one made for the Western Iberian Peninsula domain. Thus, Guadiana watershed was modelled considering a grid in the surface plane with a resolution of 0.045° in West-East and North-South directions and a vertical grid with 7 layers and a maximum soil depth of 30 m.

To consider the modification of the flow regime caused by reservoirs' operations, 39 reservoirs with a storage capacity larger than 10 hm^3 were considered. Of those, 11 reservoirs were present since the beginning of the simulation, while the remaining 28 were added during the simulation according to their construction year. Also, only 31 of the 39 reservoirs had outflow data available. For those 31 reservoirs the observed outflow values were imposed on the simulation while for the remaining the outflow was estimated according to one of the operation curves available in MOHID-Land model.

2.4.3 Maranhão

The OMeGA (optimization of reservoirs' management, Otimização da Gestão de Albufeiras in Portuguese) project was developed under a scenario of an increasing use of water resources for different purposes. Considering that agricultural activity is the major actor in water consumption worldwide, including Portugal, and with the Portuguese rainfall regime demonstrating a higher uncertainty in its intra and interannual variability, the need to improve the efficiency of water resources management is obvious. The OMeGA project's main goal was to develop a tool that supports the management of the water stored in hydro-agricultural reservoirs in real-time and considering the quantity and the quality of that resource. This tool integrated observed data, such as information collected from meteorological stations and from satellite images, and several types of models to provide the system with the capacity of predicting near-future conditions.

The Sorraia River watershed, where Maranhão and Montargil reservoirs are included, was adopted as the case study. In this area a meteorological high-resolution model was implemented to predict future meteorological conditions and a hydrodynamic model (MOHID-Water) was applied to Montargil and Maranhão reservoirs to simulate the hydrodynamics and the biogeochemical processes in the reservoirs. The reservoirs' inflows were predicted using the MOHID-Land model, which was implemented to Maranhão and Montargil watersheds.

The Maranhão watershed is part of the Tagus watershed, being placed on its left margin and with part of its delineation corresponding to the border of Tagus and Guadiana watersheds (Figure 2.6). It is a small watershed with about 2300 km^2 and is characterized by a

Mediterranean hot-summer climate. The watershed presents a significative problem of lack of data. The data publicly available for Maranhão reservoir includes only total water consumptions and discharges with a monthly timestep. The reservoir's level and stored volume data have a daily timestep. Only four hydrometric stations are located in the watershed. From those, two drain small areas (9%) of the watershed, which makes them unrepresentative. The other two drain areas between 30% and 40% of the Maranhão watershed, but one of them only has data between 1985 and 1990. Therefore, only one hydrometric station (Ponte Vila Formosa) remains adequate to deduce the streamflow in Maranhão watershed. For that, the sub-basin drained by that station was the target of the modelling task and the results obtained there were generalized to the Maranhão watershed.

Thus, for the purpose of this work, the Maranhão watershed and the sub-basin that drains to the hydrometric station were modelled using MOHID-Land model and neural networks. In the former case, both watersheds were simulated using the same implementation. This implementation considered a surface plane grid with a resolution of 0.006°C (~600 m) in both longitudinal and latitudinal directions and the vertical direction, i.e., the porous media, was discretized using a grid with 6 layers, with a maximum soil depth of 5 m (Figure 2.8).

Figure 2.8 Discretization of Maranhão watershed.

Considering the neural network approach, Ponte Vila Formosa sub-basin and Maranhão watershed streamflow were estimated based on the same neural network. While this neural network was developed and trained with data of Ponte Vila Formosa hydrometric station and the respective drained watershed, its adequacy to represent the flow regime of Maranhão watershed by just replacing the input variables was investigated.

A convolutional neural network (CNN) was used in this case study, with its structure being composed by three 1D convolutional layers with each being followed by a MaxPooling1D layer and ending with a dense layer (Figure 2.9). As input variable only precipitation was considered, but it was accumulated in 1, 2, 3, 4, 5, and 10 days and delayed by 1, 2, 3, 4, 5, 6, and 7 days.

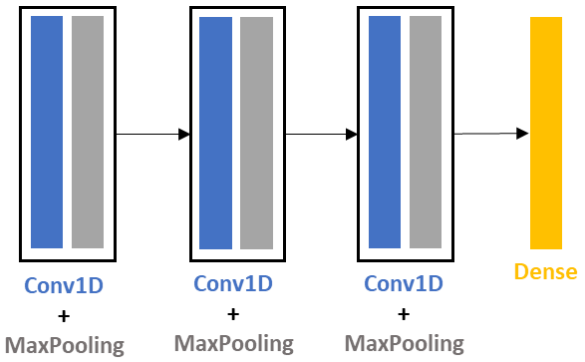

Figure 2.9 CNN structure for Maranhão watershed.

2.4.4 Ulla River watershed

The Ulla River watershed was modelled as one of the four case studies adopted in this work on behalf of HazRunoff project.

The HazRunoff project was developed to integrate sensing and modelling technologies to improve early warning and detection systems, follow-up, and early response to different or combined types of flooding and hazmat pollution in inland and transitional waters. The project aimed to provide a comprehensive framework to reach the proposed goal. That framework combined different technologies, namely, in-situ sensing technologies, airborne and satellite remote sensing, and high-resolution modelling. It also included operational tools for situational awareness and crisis management and improved contingency planning and adapted protocols for response and communication. The approach designed in this project is focused on the preparation and response to civil health impacts and on the evaluation of environmental damage.

The Ulla River is located in the Galicia Region, Northwest Spain (Figure 2.6). Its watershed drains an area of 2803 km^2 and the river's mouth is located in Ria de Arosa. The region is classified with a Mediterranean warm summer climate, which is characterized by warm and dry summers with the average monthly temperature of the warmest month not going above 22°C.

There are three reservoirs in Ulla River watershed, namely, Portodemouros, Bandariz and Touro. Portodemouros is the most upstream reservoir, followed by Bandariz and with the system ending with Touro, the most downstream reservoir. Portodemouros is a high storage

capacity reservoir while Bandariz and Touro are dams of run-of-the-river type, characterized by low storage capacities. The three reservoirs work together for energy production purposes, while Portodemouros is also used for flood control.

The Ulla River watershed was modelled with MOHID-Land model. This implementation considered a surface plane grid with a resolution of 0.005° (~500 m) in longitudinal and latitudinal directions (Figure 2.10). The vertical grid, corresponding to the discretization of the porous media, comprehended 6 layers with a maximum soil depth of 5.0 m (Figure 2.10).

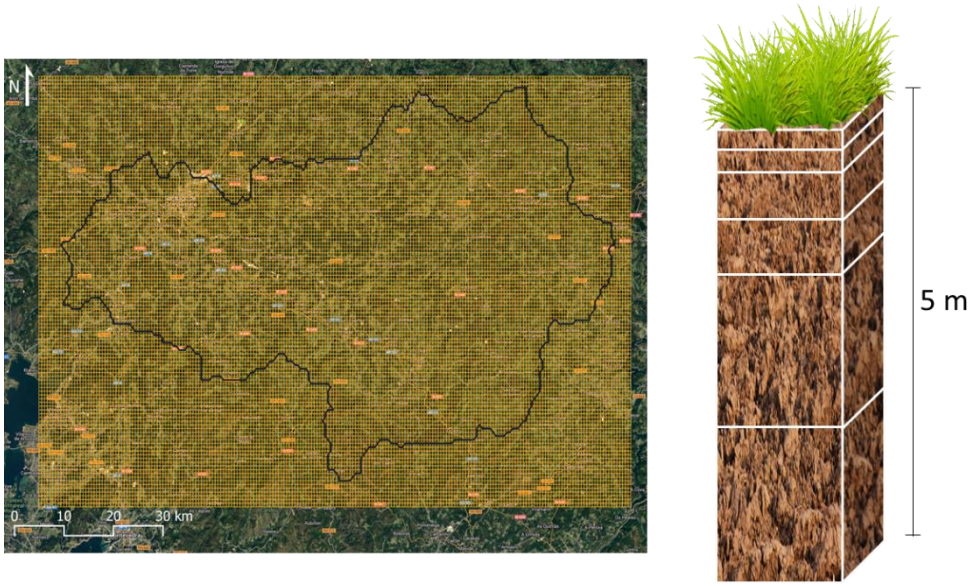

Figure 2.10 Discretization of Ulla River watershed.

MOHID-Land model was first calibrated and validated for the natural regime flow considering hydrometric stations not influenced by the presence of the reservoirs. Then, the hydrological model was complemented by a neural network developed with the goal of estimating Portodemouros outflow. In this hybrid approach the neural network elected to predict Portodemouros outflow was of convolutional long short-term memory (CLSTM) type, and its structure comprises three sets of convolutional 1D plus MaxPooling layers, followed by a long short-term memory (LSTM) layer and a dense layer as output (Figure 2.11). The performance of the resulting coupled system was then evaluated in those stations downstream of the reservoirs.

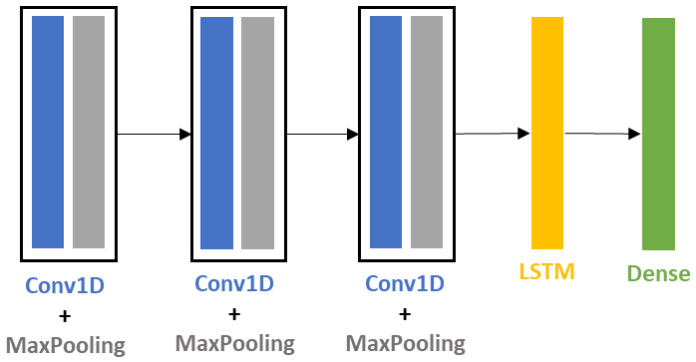

Figure 2.11 CLSTM structure for Portodemouros reservoir.

2.5 References

Allen, R. G.; Pereira, L. S.; Raes, D.; Smith, M. *Crop Evapotranspiration—Guidelines for Computing Crop Water Requirements*; Irrigation & Drainage Paper 56; Food and Agriculture Organization (FAO): Rome, Italy, 1998.

Ardabili, S.; Mosavi, A.; Dehghani, M.; Várkonyi-Kóczy, A.R. *Deep Learning and Machine Learning in Hydrological Processes Climate Change and Earth Systems a Systematic Review*. In: Várkonyi-Kóczy, A. (eds) Engineering for Sustainable Future. INTER-ACADEMIA 2019. Lecture Notes in Networks and Systems 2020, vol 101. Springer, Cham. https://doi.org/10.1007/978-3-030-36841-8_5

ASCE, Task Committee on Hydrology Handbook of Management Group D of ASCE. *Hydrology Handbook (Second Edition)*. American Society of Civil Engineers 1996. https://doi.org/10.1061/9780784401385

Canuto, N.; Ramos, T. B.; Oliveira, A. R.; Simionesei, L.; Basso, M.; Neves, R. *Influence of reservoir management on Guadiana streamflow regime*. J. Hydrol. Reg. Stud. 2019, 25, 100628. https://doi.org/10.1016/j.ejrh.2019.100628

Carpenter, G. A.; Grossberg, S. *A massively parallel architecture for a self-organizing neural pattern recognition machine*. Comp. Vis. Graph. Image Proc. 1987, 37, 54–115. https://doi.org/10.1016/S0734-189X(87)80014-2

Dong, N.; Guan, W.; Cao, J.; Zou, Y.; Yang, M.; Wei, J.; Chen, L.; Wang, H. *A hybrid hydrologic modelling framework with data-driven and conceptual reservoir operation schemes for reservoir impact assessment and predictions*. J. Hydrol. 2023, 619, 129246. https://doi.org/10.1016/j.jhydrol.2023.129246

Droogers, P.; Bouma, J. *Simulation modelling for water governance in basins*. Int. J. Water Resour. Dev. 2014, 30, 3, 475-494. http://dx.doi.org/10.1080/07900627.2014.903771

Feddes, R. A.; Kowalik, P. J.; Zaradny, H. *Simulation of Field Water Use and Crop Yield*; Wiley: Hoboken, NJ, USA, 1978.

Fukushima, K. *Cognitron: a self-organizing multilayered neural network*. Biol. Cyber. 1975, 20, 121–136. https://doi.org/10.1007/BF00342633

Green,W. H.; Ampt, G. A. *Studies on Soil Physics, Part 1, the Flow of Air and Water through Soils*. J. Agric. Sci. 1911, 4, 11–24.

Grossberg, S. *Adaptive pattern classification and universal recoding*. Biol. Cyber. 1976, 23(3), 121–134. https://doi.org/10.1007/BF00340335

Hopfield, J. J. *Neural networks and physical systems with emergent collective computational abilities*. Proc. Natl. Acad. Sci. 1982, 79, 2554–2558. https://doi.org/10.1073/pnas.79.8.2554

Humphrey, G.B.; Gibbs, M.S.; Dandy, G.C.; Maier, H.R. *A hybrid approach to monthly streamflow forecasting: Integrating hydrological model outputs into a bayesian artificial neural network*. J. Hydrol. 2016, 540, 623–640. https://doi.org/10.1016/j.jhydrol.2016.06.026

Klopf, A. H. *Brain function and adaptive systems – a heterostatic theory*. Air Force Research Laboratories Technical Report, AFCRL-72-0164, 1972.

Kohonen, T. *Self-organized formation of topologically correct feature maps*. Biol. Cyber. 1982, 43, 59–69. https://doi.org/10.1007/BF00337288

Lange, H.; Sippel, S. *Machine Learning Applications in Hydrology*. In D. F. Levia, D. E. Carlyle-Moses, S. Iida, B. Michalzik, K. Nanko, & A. Tischer (Eds.), Forest-Water Interactions 2020, 240, 233–257. Springer International Publishing. https://doi.org/10.1007/978-3-030-26086-6_10

Linsley, R.K. *Why simulation?* Hydrocomp simulation network newsletter 1976, Vol/ 8-5. Available on: http://www.hydrocomp.com/whysim.html

Loucks, D. P.; van Beek, E.; Stedinger, J. R.; Dijkman, J. P.M.; Villars, M. T. *Water Resources Systems Planning and Management-An Introduction to Methods, Models and Applications*. UNESCO 2005. Available on: http://ecommons.cornell.edu/handle/1813/2804

Macukow, B. *Neural Networks – State of Art, Brief History, Basic Models and Architecture*. In K. Saeed & W. Homenda (Eds.), Computer Information Systems and Industrial Management 2016, 9842, 3–14. Springer International Publishing. https://doi.org/10.1007/978-3-319-45378-1_1

Minsky, M.; Papert, S. A. *Perceptrons: An Introduction to Computational Geometry*. The MIT Press 1969. https://doi.org/10.7551/mitpress/11301.001.0001

Mualem, Y. *A new model for predicting the hydraulic conductivity of unsaturated porous media*. Water Resour. Res. 1976, 12, 513–522. https://doi.org/10.1029/WR012i003p00513

Neitsch, S. L.; Arnold, J. G.; Kiniry, J. R.; Williams, J. R. *Soil and Water Assessment Tool, Theoretical Documentation*, Version 2009; Texas Water Resources Institute. Technical Report No. 406; Texas A&M University System: College Station, TX, USA, 2011.

Neves, R.; Chambel-Leitão, P.; Leitão, P. C. *Modelação Numérica da Circulação da Água no Solo. O Modelo MOHID.* Pedologia 2000, 28, 46–55.

Okkan, U.; Ersoy, Z. B.; Ali Kumanlioglu, A.; Fistikoglu, O. *Embedding machine learning techniques into a conceptual model to improve monthly runoff simulation: A nested hybrid rainfall-runoff modeling*. J. Hydrol. 2021, 598, 126433. https://doi.org/10.1016/j.jhydrol.2021.126433

Oliveira, A. R.; Ramos, T. B.; Simionesei, L.; Pinto, L.; Neves, R. *Sensitivity Analysis of the MOHID-Land Hydrological Model: A Case Study of the Ulla River Basin*. Water 2020, 12(11), 3258. https://doi.org/10.3390/w12113258

Ramos, T. B.; Simionesei, L.; Jauch, E.; Almeida, C.; Neves, R. *Modelling soil water and maize growth dynamics influenced by shallow groundwater conditions in the Sorraia Valley region, Portugal*. Agric. Water Manage. 2017, 185, 27–42. https://doi.org/10.1016/j.agwat.2017.02.007

Rosenblatt, F. *The perceptron: A probabilistic model for information storage and organization in the brain*. Psychol. Rev. 1958, 65(6), 386–408. https://doi.org/10.1037/h0042519

Rumelhart, D. E.; Hinton, G. E.; Williams, R. J. *Learning internal representations by error propagation*. In: Parallel Distributed Processing: Explorations in the Microstructure of Cognition 1986, 1, 318–362. MIT Press, Cambridge. ISBN:9780262291408.

Šimůnek, J.; Hopmans, J. W. *Modeling compensated root water and nutrient uptake*. Ecol. Model. 2009, 220(4), 505–521. https://doi.org/10.1016/j.ecolmodel.2008.11.004

Simionesei, L.; Ramos, T. B.; Brito, D.; Jauch, E.; Leitão, P. C.; Almeida, C.; Neves, R. *Numerical simulation of soil water dynamics under stationary sprinkler irrigation with MOHID-Land*. Irrig. Drain. 2016, 65, 98–111. https://doi.org/10.1002/ird.1944

Sit, M.; Demiray, B. Z.; Xiang, Z.; Ewing, G. J.; Sermet, Y.; Demir, I. *A comprehensive review of deep learning applications in hydrology and water resources*. Water Sci. Technol. 2020, 82(12), 2635–2670. https://doi.org/10.2166/wst.2020.369

Skaggs, T. H.; van Genuchten, M. Th.; Shouse, P. J.; Poss, J. A. *Macroscopic approaches to root water uptake as a function of water and salinity stress*. Agric. Water Manag. 2006, 86(1–2), 140–149. https://doi.org/10.1016/j.agwat.2006.06.005

Soil Conservation Service. *Design hydrographs. In National Engineering Handbook*; United States Department of Agriculture: Washington, DC, USA, 1972.

Trancoso, A. R.; Braunschweig, F.; Chambel Leitão, P.; Obermann, M.; Neves, R. *An advanced modelling tool for simulating complex river systems*. Sci. Total Environ. 2009, 407(8), 3004–3016. https://doi.org/10.1016/j.scitotenv.2009.01.015

van Genuchten, M.T. *A closed-form equation for predicting the hydraulic conductivity of unsaturated soils*. Soil Sci. Soc. Am. J. 1980, 44, 892–898. https://doi.org/10.2136/sssaj1980.03615995004400050002x

Werbos, P. *Beyond Regression: New Tools for Prediction and Analysis in the Behavioral Sciences*, Ph.D. Thesis, Harvard University, Cambridge, 1974.

Wheater, H.; Sorooshian, S.; Sharma, K. *Hydrological Modelling in Arid and Semi-Arid Areas (International Hydrology Series)*. Cambridge: Cambridge University Press 2007. https://doi.org/10.1017/CBO9780511535734

Widrow, B.; Hoff, M. *Adaptive Switching Circuits*. IRE WESCON Convention Record, Part 4, 96-104. New York, IRE, 1960

Williams, J. R.; Jones, C. A.; Kiniry, J. R.; Spanel, D. A. *The EPIC crop growth model*. Trans. Am. Soc. Agric. Biol. Eng. 1989, 32, 497–511. https://doi.org/10.13031/2013.31032

3 Modeling Streamflow at the Iberian Peninsula Scale Using MOHID-Land: Challenges from a Coarse Scale Approach

Authors: Ana R. Oliveira[1], Tiago B. Ramos[1], Lucian Simionesei[1], Maria C. Gonçalves[2] and Ramiro Neves[1]

[1] Centro de Ciência e Tecnologia do Ambiente e do Mar (MARETEC-LARSyS), Instituto Superior Técnico, Universidade de Lisboa, Av. Rovisco Pais, 1, 1049-001 Lisboa, Portugal

[2] Instituto Nacional de Investigação Agrária e Veterinária (INIAV), Av. República, 2780-157 Oeiras, Portugal

Published in: Water, 2022, 14 (7): 1013 (https://doi.org/10.3390/w14071013), **Impact Factor:** 3.53

Abstract

Hydrological modeling is nowadays critical for evaluating the status, past trends, and future perspectives of water availability at the global, regional, and local scales. The Iberian Peninsula is registering more frequent and severe droughts and water scarcity caused not only by extreme meteorological events, but also by increased demand for water for urban, industrial, and agricultural supplies. Better simulation models are thus needed for accurately quantifying the availability of local water resources. In this study, the natural flow regime in different watersheds of the Iberian Peninsula was simulated using the process-based, fully distributed, MOHID-Land model from 1979 to 2013. Streamflow results were compared with measurements at 73 hydrometric stations not influenced by reservoirs, and with the data available in the management plans of each hydrographic region. The results showed a high dispersion of the goodness-of-fit indicators, with the coefficient of determination (R^2) ranging between 0 and 0.91, and the modeling efficiency (NSE) being higher than 0.35 at only 22 (calibration) and 28 (validation) hydrometric stations. Considering the scale of application, results were acceptable but evidenced the difficulties in simulating streamflow in watersheds using a coarse resolution. As such, this paper further deals with the difficulties and challenges of the adopted modeling approach. Nevertheless, this study constitutes a further step towards the more accurate assessment of water resources availability at the Iberian Peninsula scale using process-based modeling.

Keywords: Iberian Peninsula; MOHID-Land; natural flow; regional modeling; transnational watersheds

3.1 Introduction

According to the Intergovernmental Panel on Climate Change (IPCC) report (Barros et al., 2014), climate change is predicted to continue impacting the hydrology of river basins in Europe, particularly hydroclimatic extreme events. There is no generalized consensus about the areas that will be affected by the increase in the 100-year return period of discharge. Some studies project an increase in Continental Europe while others expect a decrease in parts of Northern and Southern Europe by 2100 (Dankers and Feyen, 2008; Rojas et al., 2012). Studies more focused on individual catchments indicate an increase in extreme discharge in regions such as Finland (Veijalainen et al, 2010), France (Quintana-Seguí et al., 2011; Chauveau et al., 2013), and the Rhine basin (Görgen et al, 2010; Te Linde et al., 2010). On the other hand, meteorological droughts are to occur with greater intensity and for longer periods in Southern Europe. It is also highlighted that even in regions where an increase in summer precipitation is predicted, soil moisture may become more limited and hydrological droughts more severe because of the increasing evapotranspiration (Wong et al., 2011). More recently, the updated IPCC report (Shukla et al., 2019) projected an increase in air temperature over the Mediterranean from 1.5°C to 2°C compared to the present (Masson-Delmotte et al., 2018). This temperature rise is intimately related to the increase in the drought risk in that area and the intensification of the hydrological cycle, facilitating more vapor in the atmosphere, which affects regional extreme precipitation events and leads to amplification or weakening of future precipitation extremes (O'Gorman, 2015; Pfahl et al., 2017).

Climate change projections, together with the evident rise in water needs for agricultural, industrial, urban, and rural population consumptions, are submitting surface and groundwater bodies to great pressures and causing water shortages throughout the world (Hoekstra et al., 2012). Simulation models are thus key tools to improve water management at various scales, and to provide clarity and understanding on hydrological processes and their interaction in the studied domains, being also useful for scenario analysis and for exploring possible future trends (Linsley, 1976).

A more detailed look at the Iberian Peninsula shows that the impact of climate change is already being noticed in this region, with a noticeable increase in air temperatures combined with a decrease in precipitation (García-Ruiz et al., 2011). Included in the Mediterranean basin, this area has long been identified as a regional climate change hotspot (Diffenbaugh and Giorgi, 2012). Lorenzo-Lacruz et al. (2012) found a generalized and significant annual and seasonal trend for streamflow, which would decrease in most parts of the Iberian Peninsula during winter

and spring and increase in summer and autumn seasons. Further, climate change, reforestation, and increased water demand were pointed out as responsible for this trend. The increase in streamflow was then related to water management strategies that were developed to avoid water scarcity during dry seasons, but which were contributing to the decrease in streamflow during the wet seasons. This study evidences the need for better management of Iberian water resources, shared by Portugal and Spain, considering the increasing scarcity that is being observed in already highly human-modified basins.

For coordinated management and a fair access to water resources in the transnational basins of the Iberian Peninsula (Minho, Lima, Douro, Tejo, and Guadiana), Portugal and Spain signed the Albufeira Convention in 1998, which was later revised in 2008. This agreement, approved in the Portuguese (Resolução da Assembleia da República n. 66/99, 1999) and Spanish legislation (Convenio Sobre Cooperación Para la Protección y el Aprovechamiento Sostenible de las Aguas de las Cuencas Hidrográficas Hispanoportuguesas, 2000), primarily established the scope of application of the convention, the type of information that should be shared between the two countries, the mechanisms for sharing it, and the communication, alert, and emergency systems to be used. Furthermore, the Albufeira Convention defined the guidelines regarding the behavior of the two countries in exceptional situations, namely, in case of accidental pollution events, floods, droughts, and scarcity of resources. The convention further promoted the protection and the sustainable use of water resources, with a focus on the prevention and control of pollution, water quality, water use, and streamflow values that must be assured in strategic points located along the borders of the two countries.

Following Brito et al. (2015) and Campuzano et al. (2016) this study aims to simulate the flow regime in different watersheds of the Iberian Peninsula using the MOHID-Land model (Trancoso et al., 2009; Canuto et al., 2019) for better quantification of regional water resources. This fully distributed, physically based, three-dimensional model considers the interactions between multiple media (atmosphere–surface–soil), with fundamental processes being formulated at the grid cell level, i.e., at the model's most basic component. The fluxes in each of these basic components (each cell) are after considered by its neighbors' cells, contributing to the dynamics of the entire modeled domain. Thus, fully distributed models such as MOHID-Land, with a high capacity to describe in detail the spatial variation of characteristics in the modeled domain, are considered to provide improved estimations of streamflow when compared with lumped and semi-distributed models. The former is not able to consider the spatial variation inside a watershed, while the latter can only assume such variation by dividing the studied domain into sub-basins.

Brito et al. (2015) and Campuzano et al. (2016) aimed to quantify streamflow in transnational Iberian catchments using coarse-scale implementations of the MOHID-Land model but were never able to quantify the prediction errors associated with the modeling performance through a comprehensive calibration/validation process of the modeling tool. As shown in Canuto et al. (2019) whose study focused only on the Guadiana catchment, this task can be quite laborious as the Iberian watersheds are highly changed by anthropogenic activities. As such, by extending the work in Canuto et al. (2019) to other transnational Iberian catchments, this study aims now to simulate the natural flow regime of the rivers in different watersheds of the Iberian Peninsula from 1979 to 2014. The estimation of the natural flow regime allows a better understanding and assessment of the impacts caused by changes made in the watersheds. On the other hand, the non-consideration of some processes, such as reservoirs management and water treatment plants discharge, helps reduce the sources of uncertainty related to the processes themselves and the input variables. Thus, in this application, reservoirs were not considered. Streamflow predictions were calibrated/validated through the comparison with measurements taken in hydrometric stations not influenced by this type of structure. Additionally, data available in the management plans of each hydrographic region was also used for model calibration/validation purposes. Hence, this paper aims: (i) to simulate streamflow in the Iberian transnational catchments using the MOHID-Land model; (ii) to quantify the prediction errors associated with the coarse-scale approach adopted in previous studies (Brito et al., 2015; Campuzano et al., 2016; Canuto et al., 2019); (iii) to discuss the limitations of the modeling approach and the challenges that still need to be faced for improving the hydrological model when implemented at such a coarse scale.

3.2 Materials and Methods

3.2.1 Description of the Studied Area

The Iberian Peninsula, in southwest Europe, covers a total area of 583 832 km^2, mainly occupied by Portugal (89 060 km^2) and Spain (492 175 km^2) (Ferreira, 2000; Instituto Nacional de Estadística, 2006). The Peninsula is divided into 24 river basin districts, with these being defined as “the area of land and sea, made up of one or more neighboring river basins together with their associated groundwaters and coastal waters” and constituting the main units for management of river basins according to the EU directive Establishing a framework for Community action in the field of water policy (European Commission, 2000).

In this application, the study area covered a total area of 438 178 km^2 (75% of the Iberian Peninsula), comprehending 19 river basin districts located in the west and north part of the

Iberian Peninsula (Figure 3.1a). The main river basins were Douro (98 107 km^2), Tagus (86 283 km^2), Guadiana (78 234 km^2), and Guadalquivir (57 228 km^2), with the first three being transnational basins divided between Portugal and Spain (Table 3.1). According to the Koppen climate characterization, the selected region is mainly characterized by four climate units (Figure 3.1b). In the north, the climate is temperate, with warm and dry summers in the northwest (Csb), and warm but not dry summers in the northeast (Cfb). The south and southwest regions have a temperate climate characterized by dry and hot summers (Csa), while the eastern part is characterized by an arid, steppe, and cold climate (BSk). The elevation of the study area ranges between 5 m and 3332 m (Figure 3.1a), with the highest value located in Sierra Nevada, Spain. In Portugal, the highest point is at an altitude of about 1990 m in Serra da Estrela. The more representative soil reference groups are Cambisols (43%), Regosols (22%), Leptosols (11%), Luvisols (10%), and Fluvisols (5%) (Nachtergaele et al., 2009). The land use is mainly characterized by non-irrigated arable land (18.7%), broad-leaved forest (11.1%), agroforestry areas (7.4%), sclerophyllous vegetation (6.9%), and transitional woodland-shrub (6.9%) (CLC, n.d.).

Table 3.1 Characteristics of the studied river basin districts (Area; number of reservoirs and respective total capacity, C_{total}; total storage capacity, $C_{storage}$; natural surface flow; regularization index, RI).

River Basin District	Country	Area (km^2)	Number of reservoirs with C_{total}			$C_{storage}$ (hm^3)	Surface flow (hm^3/year)	RI (%)	Source
			≤10 hm^3	[10 hm^3; 1000 hm^3]	>1000 hm^3				
Western Cantabrian	Spain	17 433	29	7	0	518	13 243	4	CEDEX, 2020
Eastern Cantabrian	Spain	5806	30	3	0	79	5056	2	CEDEX, 2020
Cávado, Ave and Leça	Portugal	3585	4	6	0	1194	3607	33	APA-RH2, 2016
Andalusia Mediterranean Basins	Spain	17 952	31	14	0	1174	2813	42	CEDEX, 2020
Douro (PT)	Portugal	19 218	31	22	0	2681	8010	33	APA-RH3, 2016
Duero (ES)	Spain	78 889	53	27	2	7507	11 438	66	CEDEX, 2020
Galician Coast	Spain	12 991	14	10	0	684	11 912	6	CEDEX, 2020
Guadalete and Barbate	Spain	5948	15	7	0	1651	1097	151	CEDEX, 2020
Guadalquivir	Spain	57 228	59	58	0	8113	6921	117	CEDEX, 2020
Guadiana (PT)	Portugal	11 534	14	11	1	4715	1771	266	APA-RH7, 2016
Guadiana (ES)	Spain	66 700	138	32	2	9498	3829	248	CEDEX, 2020
Minho and Lima (PT)	Portugal	2464	1	3	0	406	3275	3	APA-RH1, 2016
Miño-Sil (ES)	Spain	17 581	30	26	0	3030	11 823	26	CEDEX, 2020
Algarve Rivers	Portugal	5511	0	4	0	268	622	43	APA-RH8, 2016
Sado and Mira	Portugal	12 149	6	9	0	1148	1159	99	APA-RH6, 2016
Tagus and West Rivers (PT)	Portugal	30 502	25	16	1	2789	6710	42	APA-RH5, 2016
Tagus (ES)	Spain	55 781	247	45	3	11 056	8368	132	CEDEX, 2020
Tinto, Odiel and Piedras	Spain	4762	48	9	0	229	787	29	CEDEX, 2020
Vouga, Mondego and Lis	Portugal	12 144	16	4	0	875	6826	13	APA-RH4, 2016

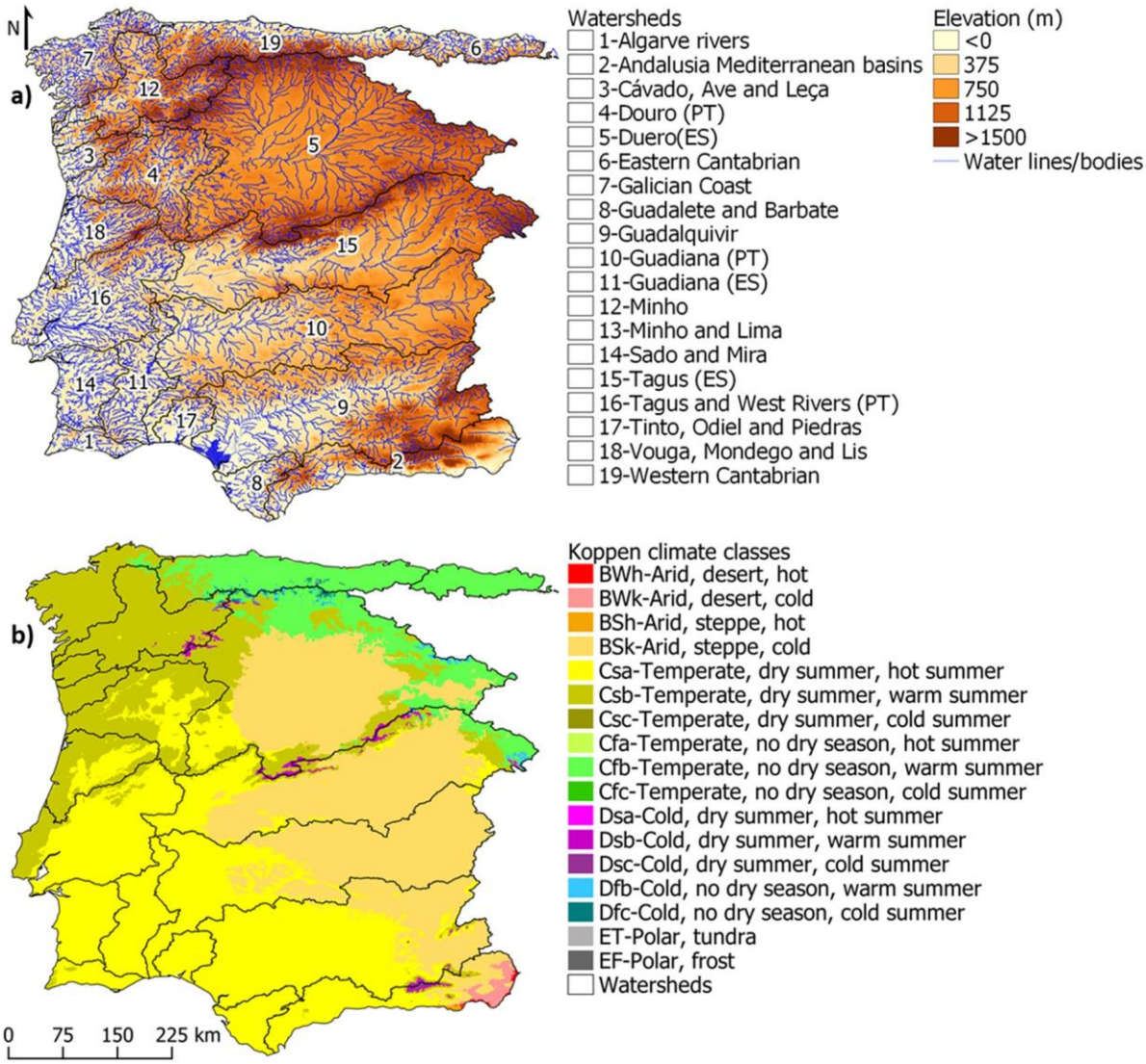

Figure 3.1 Study area: (a) Watershed's identification and digital terrain model; (b) Koppen climate characterization according to Beck et al. (2018).

The studied domain further comprises a total of 1113 reservoirs, 71% of these with a total capacity lower than 10 hm^3, 28% between 10 and 1000 hm^3, and 1% higher than 1000 hm^3 (MITERD, n.d.; SNIRH-Albufeiras, n.d.). As presented in Table 3.1, the river basin districts with more reservoirs are the Spanish Tagus (295 reservoirs, storage capacity of 11 056 hm^3), Spanish Guadiana (172 reservoirs, storage capacity of 9498 hm^3), Guadalquivir (117 reservoirs, storage capacity of 8113 hm^3), Spanish Douro (82 reservoirs, storage capacity of 7507 hm^3), and Tinto, Odiel and Piedras (57 reservoirs, storage capacity of 229 hm^3). From this set, only Tinto, Odiel, and Piedras are not included in the top five basin districts with the highest storage capacity, which is attributed to the Portuguese Guadiana (4715 hm^3) instead. On the other hand, the impact of reservoirs does not only depend on the storage capacity installed in a river basin

district, but it is intimately related with the ratio between the surface flow and the storage capacity, which is here represented by the regularization index (RI) computed as follows:

$$RI(\%) = \frac{Surface\ flow}{C_{storage}} \times 100 \quad \text{(Eq. 3.1)}$$

The surface flow values presented in Table 3.1 correspond to the natural flow regime in each basin district. These values were obtained from the Portuguese and Spanish river basin management plans. River basin management plans are the reports developed under the implementation of the Water Framework Directive of the European Union (European Commission, 2000) and aim to characterize the river basin district, diagnose the state of its water bodies in terms of water quantity and quality, and propose solutions to improve that state when necessary. In these sources, for both countries, the natural flows were estimated using the Témez model (Témez, 1977) for the Portuguese river basin districts and the SIMulación Precipitación-Aportación (SIMPA) model (Monreal et al., 1996; Monreal et al., 1999; Álvarez et al., 2004) for the Spanish territory. This latter approach was developed by CEDEX and is also based on the Témez model. Considering the regularization index, the river basin districts where the storage capacity has more impact on streamflow are the Portuguese Guadiana (266%), Spanish Guadiana (248%), Guadalete and Barbate (151%), Spanish Tagus (132%), and Guadalquivir (117%), with all having a storage capacity higher than the volume of water naturally produced in an average year. The alterations in the natural flow regime of these rivers caused by the presence of these dams were already reported in different studies (Lorenzo-Lacruz et al., 2012; Vicente-Serrano et al., 2016; Marcinkowski and Grygoruk, 2017). Aside from the modifications in the flow regimes caused by dams, the transfer of water between Tagus and Segura watersheds (not considered in the modeling approach) also affects the natural regime flow in both watersheds (Confederación Hidrográfica del Tajo, n.d.), modifying the hydrological cycle in Tagus headwaters from where water is transferred (Lorenzo-Lacruz et al., 2010).

3.2.2 Model Description

MOHID-Land (Trancoso et al., 2009; Canuto et al., 2019) is a fully distributed, physically based model, which uses mass and momentum conservation equations to simulate water movement between four main compartments (atmosphere, porous media, soil surface, and river network) using a finite volume approach. To avoid instability problems and save computational time, the model time step is variable, acquiring higher values during dry seasons, and lower values in wet periods when water fluxes increase.

The atmosphere processes are not explicitly simulated, but this compartment allows the input of atmospheric data, which can be space and time-variant, as surface boundary conditions. The simulated domain is represented by a regular grid in the surface plane, with a user-defined grid size and cell resolution. The soil discretization (three-dimensional) considers this same grid in the horizontal plane and a division by layers with variable thickness in the vertical direction following a cartesian coordinate system. The river network is defined by a one-dimensional (1D) domain, by connecting the surface cell centers (nodes) with lower altitude in the digital terrain model.

The free surface flow is computed according to the Saint–Venant equation in its conservative form and considering the advection, pressure, and friction forces:

$$\frac{\partial Q_u}{\partial t} + v_v \frac{\partial Q_u}{\partial x_v} = -gA\left(\frac{\partial H}{\partial x_i} + \frac{|Q|Q_i n^2}{A_v^2 R_h^{4/3}}\right) \quad \text{(Eq. 3.2)}$$

where Q is the water flow (L^3T^{-1}), A is the cross-sectional flow area (L^2), g is the gravitational acceleration (LT^{-2}), v is the flow velocity (LT^{-1}), H is the hydraulic head (L), n is the Manning coefficient ($TL^{-1/3}$), R_h is the hydraulic radius (L), x_i represents the xyz directions (−) and the subscripts u and v denote flow directions. This equation is solved for one direction (1D domain) in the river network and for two directions (2D domain), coinciding with the directions of the horizontal grid, in cells without drainage network (overland flow). In the boundary of the drainage network and overland flow, the water exchanges are calculated according to a kinematic approach, neglecting bottom friction.

In the porous media, the variable-saturated water flow is computed using the Richards' equation in three directions (3D domain):

$$\frac{\partial \theta}{\partial t} = \frac{\partial}{\partial x_i}\left[K(\theta)\left(\frac{\partial h}{\partial x_i} + \frac{d}{\partial x_i}\right)\right] - S(h) \quad \text{(Eq. 3.3)}$$

where θ is the volumetric water content (L^3L^{-3}), x_i represents the xyz directions (−), K is the hydraulic conductivity (LT^{-1}), and S corresponds to the sink term, representing the root water uptake ($L^3L^{-3}T^{-1}$). The soil hydraulic properties are defined following the van Genuchten Mualem functional relationships (Mualem, 1976; Van Genuchten, 1980). The water exchanges between the porous media and the river network are driven by the pressure differences in the interface of these mediums.

The crop evapotranspiration rates (ET_c) are obtained from the product of the reference evapotranspiration (ET_o) rates computed according to the FAO Penman–Monteith method and a crop coefficient (K_c) (Allen et al., 1998). ET_c rates are then divided into potential soil evaporation (E_p, LT^{-1}) and crop transpiration (T_p, LT^{-1}) based on Ritchie (1972). The T_p rates

define the maximum values of the sink term for root water uptake in the Richards equation. These may be reduced due to the presence of rootzone stressors following a macroscopic approach proposed by Feddes et al. (1978). On the other hand, the actual soil evaporation (E_a, LT^{-1}) is estimated by imposing a pressure threshold value to the potential evaporation values (ASCE, 1996). The connection between the surface runoff and the porous media is based on infiltration and exfiltration processes (Brito et al., 2017). The infiltration rate can be simulated according to three approaches, namely, Darcy's law, the Green and Ampt method (Green and Ampt, 2011), or a modified version of the SCS curve number (SCS-CN) method (Soil Conservation Service, U.S., 1972). In the SCS-CN case, the first step comprehends the estimation of the surface runoff, with the remaining amount of water infiltrating the soil; however, when the soil has saturated, a correction in the infiltration rate (and consequently in the runoff flow) is made to respect the physical limitations of the system.

More detailed information on the MOHID-Land model can be found in Canuto et al. (2019), Oliveira et al. (2020), and Ramos et al. (2017).

3.2.3 Model Setup

The MOHID-Land model was implemented in the studied area using a constant horizontally spaced grid, with a resolution of 0.045° (~5 km) in the longitudinal and latitudinal axis (180 rows × 200 columns; origin on 35.85°N and 10°W). The grid covered a domain that included all watersheds flowing to the Atlantic Ocean (West) and the Cantabrian Sea (North). Elevation data were interpolated from the Shuttle Radar Topography Mission of NASA (NASA-SRTM, n.d.), with an approximate resolution of 90 m. After burning in the main river lines and removing the depressed cells of the interpolated digital terrain model (DTM), the elevation values varied between −21 and 3093 m (Figure 3.2a).

The river network was delineated based on the interpolated DTM, considering the steepest slope in all 8 directions of each cell, by connecting the cell centers (nodes) with the lowest height. The river cross-sections were defined according to the Strahler order of each reach (Strahler, 1952; Strahler, 1957). A trapezoidal geometry was adopted for all cross-sections, with the height and top and bottom widths being set according to Canuto et al. (2019).

The soil data were interpolated from the rasterized Harmonized World Soil Database (Nachtergaele et al., 2009), with an original resolution of 30 arc-second (~1 km). The main soil units identified in the model domain were Calcic Cambisol (28%), Calcaric Regosol (17%), Humic Cambisol (12%), Lithosol (7%), Calcaric Fluvisol (5%), and Albic Luvisol (5%) (Figure 3.2d). In-depth, the soil was defined by three horizons comprehending six grid layers.

The surface horizon corresponded to a layer of 0.3 m thickness, the middle horizon was composed of a layer with 0.5 m thickness, and the bottom horizon comprehended four layers with depth increasing thicknesses of 0.42, 0.50, 10.0, and 10.0 m. For each soil horizon, the Mualem–van Genuchten model parameters (Mualem, 1976) were obtained from the soil texture classes described in the Harmonized Soil Database using the HYPRES class pedotransfer functions (Wösten et al., 1999). The soil's maximum and minimum depth were defined as 30 and 0.3 m, respectively, with the soil depth in each cell being adjusted according to its slope. The initial soil condition was set as 80% saturated (from the bottom to the surface) and in the unsaturated zone water content was set to field capacity.

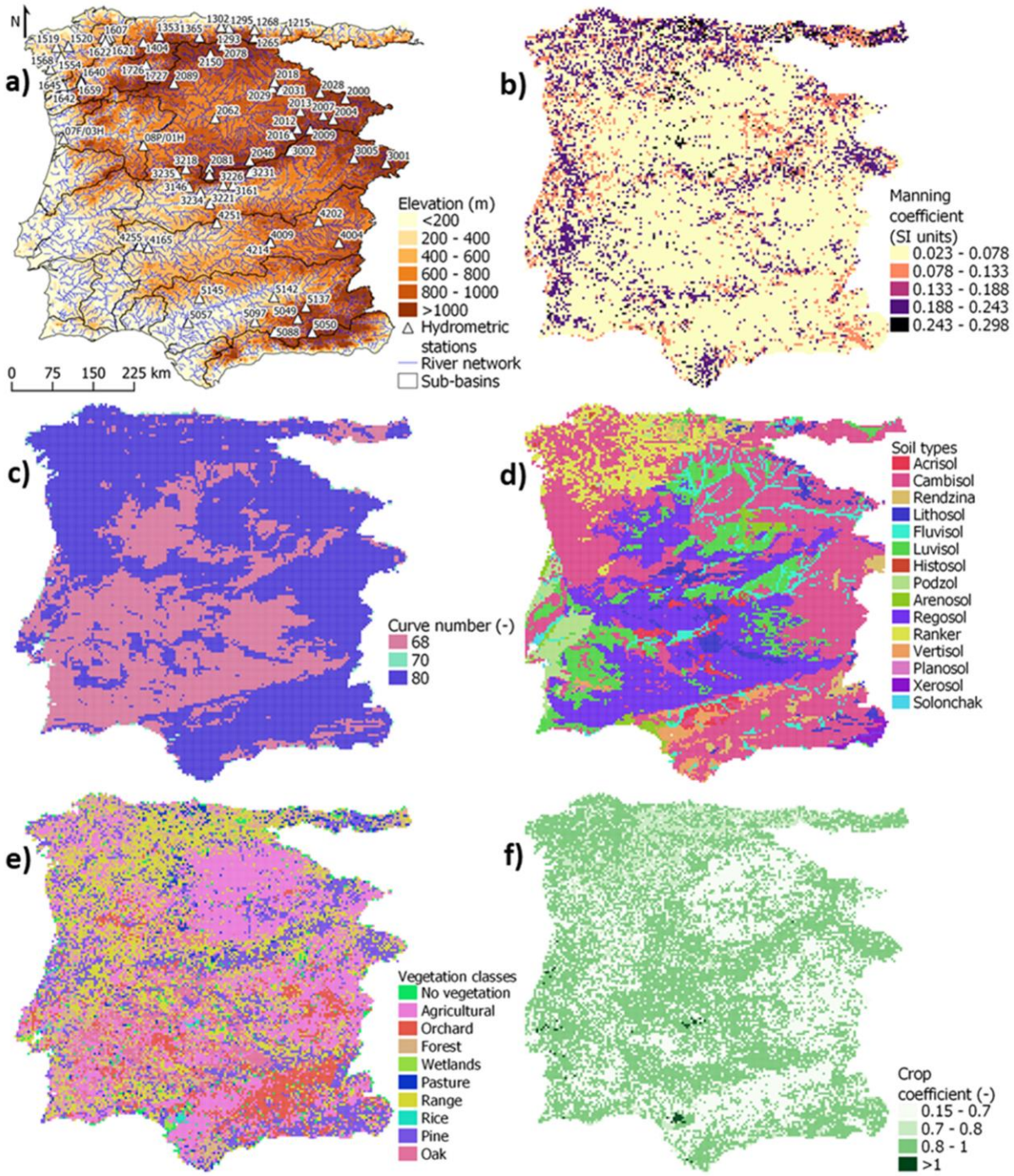

Figure 3.2 Characterization of the modeled domain: (a) digital terrain model, delineated drainage network, and localization of hydrometric stations not influenced by reservoirs with a total capacity larger than 10 hm^3; (b) surface Manning coefficient; (c) curve number values for the SCS CN method; (d) major soil units; (e) vegetation classes according to the MOHID database; (f) crop coefficients.

The land use in the studied domain was obtained from the CORINE Land Cover (CLC) 2012, with a resolution of 100 m (CLC, n.d.). The information of the CLC map was interpolated to the horizontal grid by assigning to each CLC class: (i) a Manning coefficient according to van der Sande et al., 2003; (ii) a corresponding vegetation class from the MOHID-Land database (Figure 3.2e); an annual K_c value following Canuto et al. (2019) (Figure 3.2f). The

hydrologic soil groups were defined by combining land use and soil texture data to derive the respective CN values following the Soil Conservation Service (Soil Conservation Service, U.S., 1972) tables (Figure 3.2c).

The meteorological data were obtained from the SAFRAN model, which was developed, calibrated, and validated by Quintana-Seguí et al. (2017). SAFRAN is a meteorological analysis system based on an optimal algorithm that combines observations and a first guess, such as the outputs of a global meteorological model. The resulting dataset is in gridded format, with a resolution of 5 km, and includes hourly data of precipitation, surface air temperature, wind speed, relative humidity, and solar radiation from 1979 to 2014. The information of these meteorological properties was interpolated to the MOHID-Land grid following a triangular method.

3.2.4 Model Evaluation

Model performance was evaluated by comparing simulated and measured monthly streamflow data at 73 stations not influenced by reservoirs operation (Figure 3.2a), i.e., only hydrometric stations under natural flow regime were considered. The simulation period was from 1985 to 2013 (35 years). The measured dataset was obtained from MITERD, n.d., and SNIRH (SNIRH-Monitorização, n.d.) for the stations in Spain and Portugal, respectively. Table 3A.1, in Appendix 3A, presents the number of records as well as the minimum, maximum, mean, and standard deviation values of the measured monthly streamflow in each station. The calibration period was defined from January 1985 to December 1999, while the validation period went from January 2000 to December 2013. A warm-up period was also considered from September 1979 to December 1984. The calibration procedure considered the modification of selected model parameters, one at a time, within reasonable ranges, to minimize deviations between simulated and observed streamflow in the selected hydrometric stations. Following Oliveira et al. (2020), who identified the most sensitive parameters affecting simulations of streamflow in MOHID-Land, the modified parameters were: the vertical saturated hydraulic conductivity; the multiplying factor relating the vertical and horizontal saturated hydraulic conductivities (f_h); the surface and channel Manning coefficients; the crop coefficients; the dimensions (height and top and bottom widths) of the river cross-sections. The calibrated parameters were then used for validation of streamflow predictions, with the deviation between model simulations and observed data being assessed again at the same hydrometric stations using the validation dataset.

Model performance was evaluated using four statistical parameters, namely, the coefficient of determination (R^2), the percent bias (PBIAS), the root mean square error-observation standard deviation ratio (RSR), and the Nash–Sutcliffe model efficiency (NSE), which are computed, respectively, as follows:

$$R^2 = \left[\frac{\sum_{i=1}^{p}\left(Q_i^{obs} - Q_{mean}^{obs}\right)\left(Q_i^{sim} - Q_{mean}^{sim}\right)}{\sqrt{\sum_{i=1}^{p}\left(Q_i^{obs} - Q_{mean}^{obs}\right)^2}\sqrt{\sum_{i=1}^{p}\left(Q_i^{sim} - Q_{mean}^{sim}\right)^2}} \right]^2 \quad \text{(Eq. 3.4)}$$

$$PBIAS = \frac{\sum_{i=1}^{p}(Q_i^{obs} - Q_i^{sim})}{\sum_{i=1}^{p} Q_i^{obs}} \times 100 \quad \text{(Eq. 3.5)}$$

$$RSR = \frac{RMSE}{STDEV_{obs}} = \frac{\sqrt{\sum_{i=1}^{p}(Q_i^{obs} - Q_i^{sim})^2}}{\sqrt{\sum_{i=1}^{p}(Q_i^{obs} - Q_{mean}^{sim})^2}} \quad \text{(Eq. 3.6)}$$

$$NSE = 1 - \frac{\sum_{i=1}^{p}(Q_i^{obs} - Q_i^{sim})^2}{\sum_{i=1}^{p}(Q_i^{obs} - Q_{mean}^{obs})^2} \quad \text{(Eq. 3.7)}$$

where Q_i^{obs} and Q_i^{sim} are the observed and simulated flow on day i, respectively, Q_{mean}^{obs} and Q_{mean}^{sim} are the observed and simulated mean flow for the analyzed period, respectively, and p is the total number of days in this period. When NSE > 0.5, RSR ≤ 0.7, PBIAS ± 25%, and R^2 > 0.5 the results of the modelled streamflow are considered satisfactory (Moriasi et al., 2007).

Finally, model results were also compared with the official values available in Portuguese river basin management plans and in a report produced by Centro de Estudios y Experimentación de Obras Públicas (CEDEX) in the scope of Spanish river basin management plans (Table 3.1). This type of validation allows the assessment of the general values of streamflow obtained by watershed instead of considering only the headwater areas defined by the hydrometric stations presented before; however, it is important to denote that the values presented in the river basin management plans are also results of models and, consequently, they are also subjected to uncertainty, but in the end, they constitute official information. The values available in the river basin management plans and used in this study for comparison with model results were the average annual precipitation and the average annual natural surface runoff in each river basin district. The corresponding difference, in percentage, between the MOHID-Land modeled and official results were computed as follows:

$$\Delta(\%) = \frac{V_{model} - V_{official}}{V_{model}} \times 100 \quad \text{(Eq. 3.8)}$$

where V_{model} and $V_{official}$ are the modeled and official average annual values of precipitation/surface runoff, respectively, and Δ is the difference between these values.

3.3 Results and Discussion

3.3.1 Model Parametrization

The best fit between simulated and observed streamflow values was obtained for a simulation in which the Manning coefficient ranged in the different soil units from 0.02 to 0.298 s $m^{-1/3}$ (Figure 3.2b), and the annual K_c value for the different crops varied from 0.15 to 1.02 (Figure 3.2f). The curve number was set to values between 68 and 80 (Figure 3.2d), with these values not having a significant impact on the streamflow simulation, as demonstrated by Oliveira et al. (2020). The multiplying factor f_h was set to 10. The soil hydraulic parameters were adjusted to the values presented in Table 3B.1 of Appendix 3B, with the saturated water content (θ_s), the residual water content (θ_r), the empirical shape parameters α and η, and the vertical saturated hydraulic conductivity (K_s) ranging between 0.35 and 0.766 m^3 m^{-3}, 0.01 and 0.025 m^3 m^{-3}, 0.198 and 3.83 m^{-1}, 1.086 and 1.377, and 9.26×10^{-7} and 6.94×10^{-6} m s^{-1}, respectively. The connectivity/tortuosity parameter (L, m) adopted the value 0.5 as proposed by Mualem (1976). A summary of the ranges for the calibrated parameters is presented in Table 3.2. Finally, the calibrated dimensions for the river cross-sections were defined as presented in Table 3.3. The calibrated values of the Manning coefficient, K_c, CN, f_h, and the dimensions of the river cross-sections were thus in agreement with those used in Canuto et al. (2019), and Oliveira et al. (2020), for simulating streamflow in different catchments of the Iberian Peninsula. The soil hydraulic parameters were also in the range of those proposed by Ramos et al. (2013) for the different texture classes of soils in Portugal.

Table 3.2 Summary of calibrated parameters.

Parameter	Minimum value	Maximum value
n (s $m^{-1/3}$)	0.02	0.298
K_c (−)	0.15	1.02
CN (−)	68	80
f_h (−)	10	
θ_s (m^3 m^{-3})	0.35	0.766
θ_r (m^3 m^{-3})	0.01	0.025
α (m^{-1})	0.198	3.83
η (−)	1.086	1.377
K_s (m s^{-1})	9.26×10^{-7}	6.94×10^{-6}
L (m)	0.5	

Table 3.3 River cross-sections dimensions.

Strahler order	Height (m)	Bottom width (m)	Top width (m)
1	8	20	30
2	10	30	40

Strahler order	Height (m)	Bottom width (m)	Top width (m)
3	12	70	80
4	15	95	105
5	20	145	155
6	25	175	205

3.3.2 Model Performance

Figure 3.3 presents the histograms of the distribution of the statistical parameters obtained by comparing simulated and measured streamflow data at 73 hydrometric stations selected for calibration/validation. In general, the statistical parameters showed a large dispersion. In the calibration period, the R^2, RSR, PBIAS, and NSE values ranged from 0 to 0.91, 0.36 to 9.83, −1160% to 81%, and −96 to 0.87, respectively. The R^2 histogram showed that the most populated classes were those between 0.4 and 0.6 (at 21 stations) and 0.6 and 0.8 (21 stations), thus expressing the model's capability in explaining most of the variability of the observed data at 57% of the selected hydrometric stations. For the RSR parameter, values higher than 1 were obtained at 29 stations, being the most frequent and indicating a large error of the estimate. Yet, at 31 stations the RSR values were within the 0.4 to 1.0 range, thus showing a more acceptable performance. The class with a deviation lower than −25% was the most populated (33 stations) for the PBIAS statistical parameter, revealing a small tendency of overestimation of the observed data in these stations. Lastly, the NSE values lower than 0.15 were the most frequent at 32 stations; however, the NSE values were within the acceptable range at 22 stations, being higher than 0.35 in 11 of those stations and higher than 0.55 in the remaining 11 stations. In the validation period, the R^2 values ranged between 0.01 and 0.88, the RSR between 0.4 and 19.22, the PBIAS was in the range −3500% and 90%, and the NSE varied from −368 to 0.84. In this period, the most populated classes for R^2, RSR, PBIAS, and NSE were, respectively, $]0.6,0.8]$ at 38 stations, $]1,+\infty[$ at 34 stations, $]-\infty,-25\%]$ at 42 stations, and $]-\infty,0.15]$ at 39 stations, thus showing the same tendencies observed during calibration.

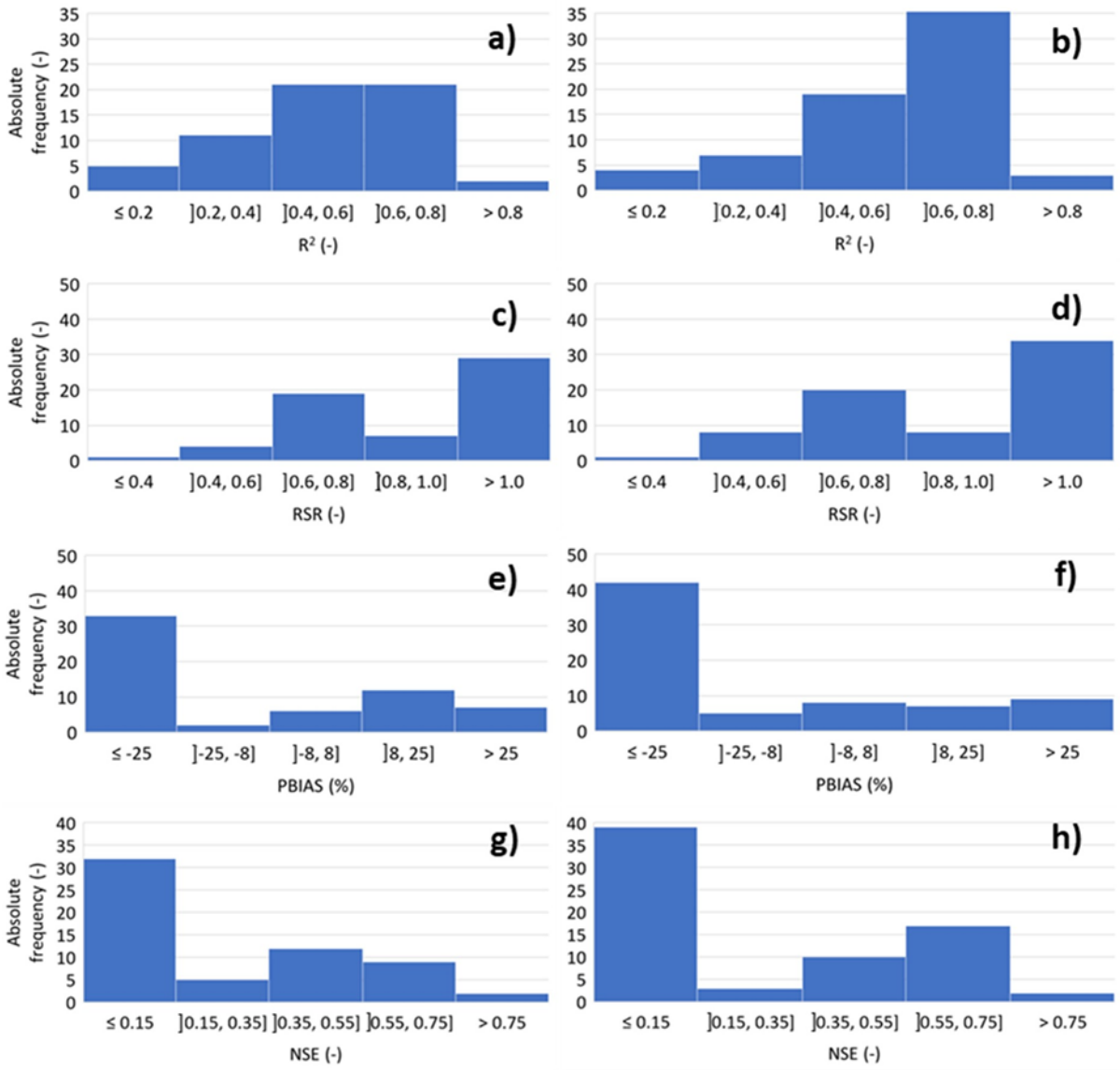

Figure 3.3 Histograms with the statistical parameters obtained at 73 hydrometric stations during model evaluation: (a,b) coefficient of determination (R^2) for calibration and validation periods, respectively; (c,d) root mean square error-observation standard deviation ratio (RSR) for calibration and validation periods, respectively; (e,f) percent bias (PBIAS) for calibration and validation periods, respectively; (g,h) model efficiency (NSE) for calibration and validation periods, respectively.

The analysis of the results in each hydrometric station (Figure 3.4) shows that three stations (1215, 1353, and 1519) in the Galician Coast and Western Cantabrian river basin districts, two stations (2028 and 2089) in the Douro basin, and three stations (3226, 3234, and 3235) in the Tagus basin presented satisfactory statistical indicators for both calibration and validation periods. Stations 2081 in the Douro basin, 3146 in the Tagus basin, and 5097 and 5145 in the Guadalquivir basin also obtained satisfactory results but only for the calibration period. The stations 1404, 1620, and 1621 in the Galician Coast and Western Cantabrian, 2016 and 2150 in the Douro basin, and 3231 in the Tagus basin had satisfactory results but this time only for the validation period. Hence, results were much in line with Canuto et al. (2019) for

the Guadiana basin, showing the difficulties in correctly portraying the spatial dynamics of evapotranspiration, soil moisture, and land-use change impacts on simulations of streamflow in coarse-scale applications of a distributed-based model such as MOHID-Land in highly anthropogenic watersheds. As such, the use of these models for conducting scenario analysis should be carried out with great care due to the great uncertainty associated with model predictions, and calibration of model parameters should definitely not be limited to one or two locations as sometimes is observed in the literature since these are hardly representative of the hydrological processes across the catchments.

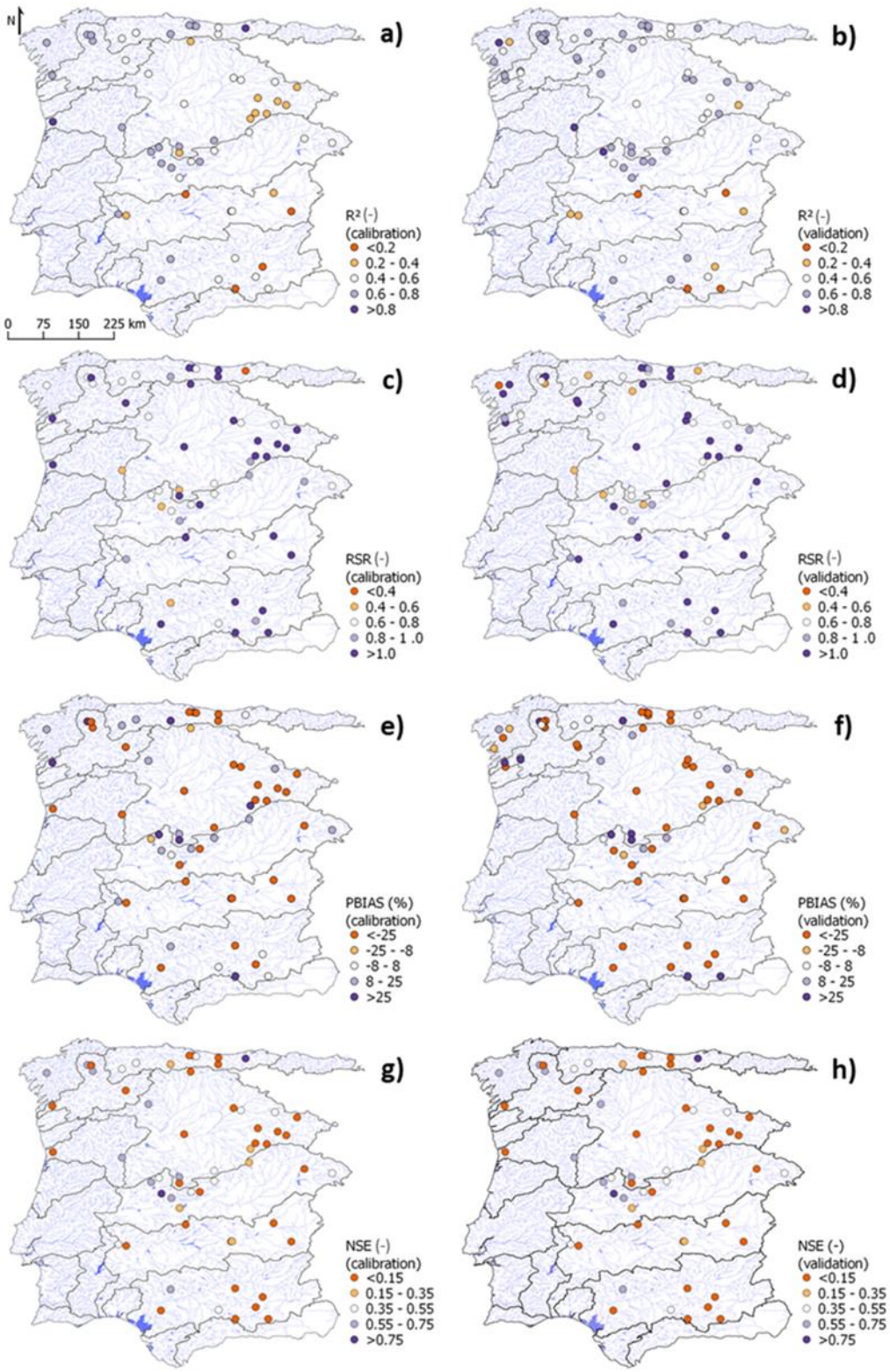

Figure 3.4 Statistical parameters by stations for calibration (left side) and validation (right side) periods: (a,b) coefficient of determination (R^2); (c,d) root mean square error-observation standard deviation ratio (RSR); (e,f) percentage bias (PBIAS); (g,h) Nash–Sutcliffe efficiency (NSE).

A more general analysis allowed the comparison of the annual average precipitation from the SAFRAN model, and the respective annual natural surface flow generated by the MOHID-Land model with the corresponding information available in the Portuguese and Spanish river

basin management plans (Table 3.4). With the natural surface flow values available in these sources already presented (Table 3.1) and explained in the description of the studied area, it is also important to denote that the average annual precipitation presented in river basin management plans was estimated based on observations from meteorological stations. The official precipitation and flow annual average values were estimated considering a period of 28 years for Portugal (1985–2013) and 38 years for Spain (1980–2018).

Table 3.4 Comparison of annual precipitation and surface flow between model and official values of river basin management plans.

River Basin District	Precipitation (mm/year)		Precip. difference (%)	Surface flow (hm^3/year)		Flow difference (%)	Source
	Model	Plan		Model	Plan		
Western Cantabrian	1 351	1 264	-7	12 334	13 243	7	CEDEX, 2020
Eastern Cantabrian	1 449	1 461	1	4 851	5 056	4	CEDEX, 2020
Cávado, Ave and Leça	1 299	1 778	27	2 624	3 607	27	APA-RH2, 2016
Andalusia Mediterranean Basins	544	528	-3	2 868	2 813	-2	CEDEX, 2020
Douro (PT)	854	999	15	10 365	8 010	-29	APA-RH3, 2016
Duero (ES)	602	576	-5	21 698	11 438	-90	CEDEX, 2020
Galician Coast	1 554	1 516	-2	10 764	11 912	10	CEDEX, 2020
Guadalate and Barbate	775	724	-7	2 436	1 097	-122	CEDEX, 2020
Guadalquivir	582	561	-4	15 322	6 921	-121	CEDEX, 2020
Guadiana (PT)	608	566	-7	3 196	1 771	-80	APA-RH7, 2016
Guadiana (ES)	512	498	-3	10 296	3 829	-169	CEDEX, 2020
Minho and Lima (PT)	1 625	1 946	17	4 009	3 275	-22	APA-RH1, 2016
Miño-Sil (ES)	1 157	1 163	1	12 772	11 823	-8	CEDEX, 2020
Algarve Rivers	575	676	15	451	622	28	APA-RH8, 2016
Sado and Mira	550	634	13	1 268	1 159	-9	APA-RH6, 2016
Tagus and West Rivers (PT)	616	728	15	6 806	6 710	-1	APA-RH5, 2016
Tagus (ES)	599	590	-2	14 603	8 368	-75	CEDEX, 2020
Tinto, Odiel and Piedras	676	669	-1	1 407	787	-79	CEDEX, 2020
Vouga, Mondego and Lis	687	1 136	39	3 310	6 826	52	APA-RH4, 2016

The comparison between precipitation values used as input to MOHID-Land and the river basin management plans showed that the main differences occurred in the Portuguese river basin districts, namely, Vouga, Mondego, and Lis (Δ = 39%); Cávado, Ave, and Leça (Δ = 27%); Minho and Lima (Δ = 17%); Douro (PT), Tagus and West Rivers (PT), and Algarve Rivers (Δ = 15%) (Figure 3.5a). Precipitation data used in the MOHID-Land model were thus higher than that considered in the river management plans; however, the pattern found for the precipitation differences was not reproduced for flow, with the more significative flow differences occurring in Spanish river basin districts, especially in Guadiana (ES) (Δ = 169%), Guadalate and Barbate (Δ = −122%), and Guadalquivir (Δ = −121%) (Figure 5b). This time, flow data in the MOHID-Land model were smaller than in the river management plans at these watersheds.

Although SAFRAN was classified as a robust dataset, differences in precipitation values could result from limitations of the SAFRAN algorithm, already highlighted by MITERD (n.d.) namely, the overestimation of the number of precipitation days, the missing of high precipitation events, and the errors often found at the border of the homogenous climatic zones; however, the high precipitation differences reported in Portugal result from the fact that SAFRAN has been extended to this country without considering any meteorological station in this area to better apply the SAFRAN methodology, which favors high station density, thus resulting in the reported difference errors.

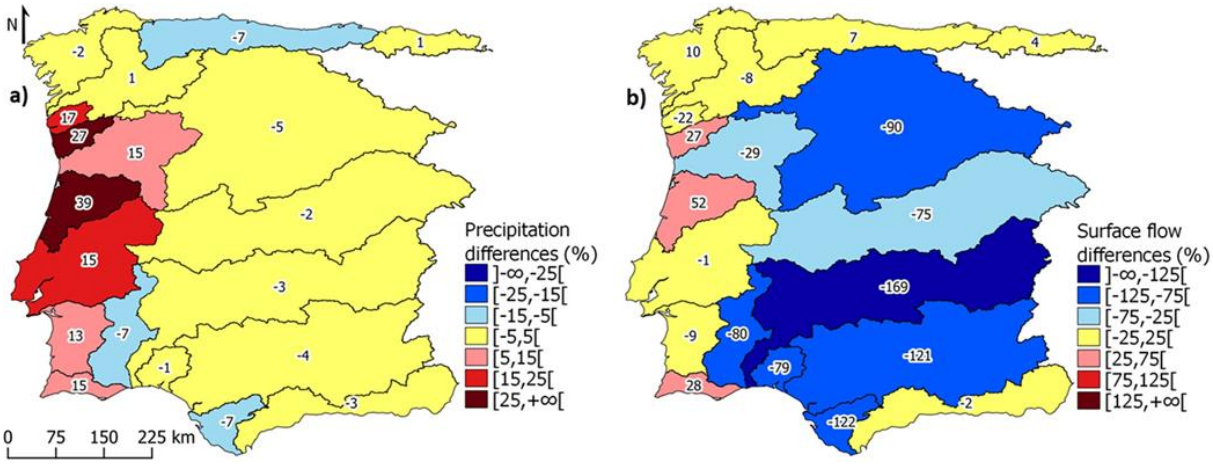

Figure 3.5 Percentage of difference between model and plan's precipitation (a) and natural surface flow (b) values.

The differences found for natural surface flow do not have the same magnitude as the precipitation differences, with the former being much higher than the latter in central and south Spanish river basin districts where the differences in precipitation are not significant. Since the

only water input in this implementation was rainfall, these results show that the hydrological model might be evaporating or retaining too much of the precipitated water in the soil or sub-surface layers instead of accounting it to surface flow. In Portugal, Minho and Lima, Douro (PT), Tagus and West Rivers (PT), Sado and Mira, and Guadiana (PT) also presented a similar behavior, but less pronounced. Finally, model results in some river basin districts, such as Eastern Cantabrian and Andalusia Mediterranean Basins, correctly reproduced the average annual natural surface flow or, at least, maintained a correspondence between surface flow and precipitation when the latter was overestimated by SAFRAN. This occurred in the river basin districts where the drainage network had more and/or shorter branches (Figure 3.1a).

3.3.3 About Model Predictions

Canuto et al. (2019) extensively discussed the challenges of modeling streamflow in highly complex, anthropogenic catchments using a coarse-scale approach and the MOHID-Land model. These referred to the calibration procedures to meet the set of parameters that best describe the simulated landscape processes, but also a set of causes related to field measurements, and to model input and model structure errors. While most of those causes are still valid for this study, a few more can be added.

The choice of a 5 km grid resolution hindered the correct delineation of the drainage network in the headwaters of the watershed where the analyzed hydrometric stations were located. That resolution grid was chosen to save computational time since this factor has a significant impact on simulation time (Oliveira et al., 2020). Errors in the delineation of the river network happened even after the main river lines were forced to flow through the correct cells of the grid domain by using the burn-in process in the MOHID-Land model. This tool allows the subtraction of a constant value to the elevation in cells identified as river path (usually, this information is available in shapefile format). Since the drainage network is delineated to make the river lines follow the lower elevation cells, this process should force those lines crossing the right cells, correcting the river path; however, after observing the details of the drainage network in the watershed's headwaters, it is possible to identify several cases where the adoption of this coarse resolution caused a connection between cells that corresponded to different river lines. As exemplified in Figure 3.6, this situation led to significant differences between the real and the simulated drained area of a hydrometric station, with an obvious impact on the amount of water flowing through that sub-basin.

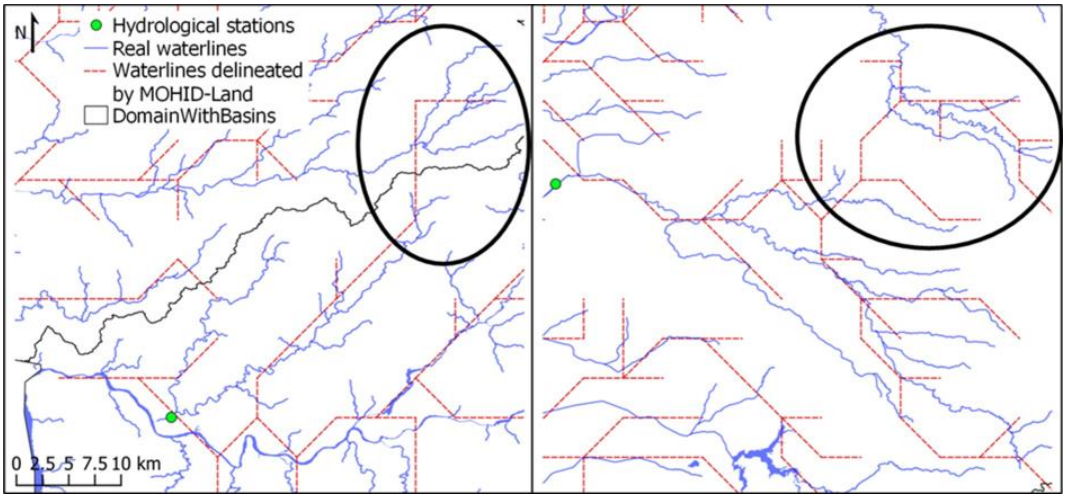

Figure 3.6 Details of the drainage network.

Oliveira et al. (2020) tested the MOHID-Land model with two different grid resolutions (0.5 and 1 km) in the Ulla basin, Northern Spain, and found that the coarser application would cause a decrease of more than 70% in streamflow values as a result of a less detailed representation of the watershed. These results suggest that, besides the errors previously mentioned in the delineation of the drainage network, the grid resolution in this type of model can lead to inferior streamflow generation by itself, especially when the adopted resolution cannot simulate the processes in the watershed with sufficient detail. The same had also been experienced in Canuto et al. (2019). These conclusions are also corroborated by Refsgaard (1997), who applied the MIKE SHE model in the Karup basin (440 km^2), Denmark, with four different resolutions, namely, 0.5, 1, 2, and 4 km, and concluded that there was a maximum grid size for a good model performance of streamflow simulations and result deteriorated for resolutions lower than this maximum. Sreedevi and Eldho (2021) applied the SHETRAN model in the humid tropical Netravathi basin (3657 km^2), Southern India, reporting that for three used resolutions (4, 2, and 1 km), there was no gain in the streamflow performance.

Furthermore, Oliveira et al. (2020) demonstrated that cross-sections geometry could significantly impact MOHID-Land simulations of streamflow. In that study, the differences in the highest and lowest values (extremes) of streamflow showed an increase of 39% and 30%, respectively, after increasing cross-sections height by 100% when compared to the baseline simulation. Canuto et al. (2019), also modified their cross sections geometry in the calibration process, reporting a ratio between the calibrated and default cross-sections area ranging from 1.5 to 10.5, thus demonstrating the sensitivity of streamflow simulation in MOHID-Land to channel geometry. Since the domain covered in the present case study is extensive, the variation of model inputs can be very large, including the channel cross-sections geometry. The database

published by Andreadis et al. (2013), who derived the river widths and depths using HydroSHEDS river topology dataset and simple geomorphic relationships between those dimensions and the drained area and the discharge, allows understanding the variation of channel geometry in the domain. Figure 7 shows the ratio between the estimated width and depth (a) and the drained area (b) using that database. The referred figure clearly shows that the ratio between width/depth does not vary linearly with the drained area and that for similar drained areas, this ratio is higher in the north than in the south; however, these differences were not able to be implemented in the model as the available preprocessing tool only allows the assignment of cross-section geometries to the entire modeled domain. Hence, it was not possible to represent with detail the existing differences in the channel river cross-sections geometry throughout the domain, preventing a detailed calibration/validation process and, consequently, deteriorating results. For this reason, applications of the MOHID-Land model at the catchment scale instead of at the regional scale are highly recommended.

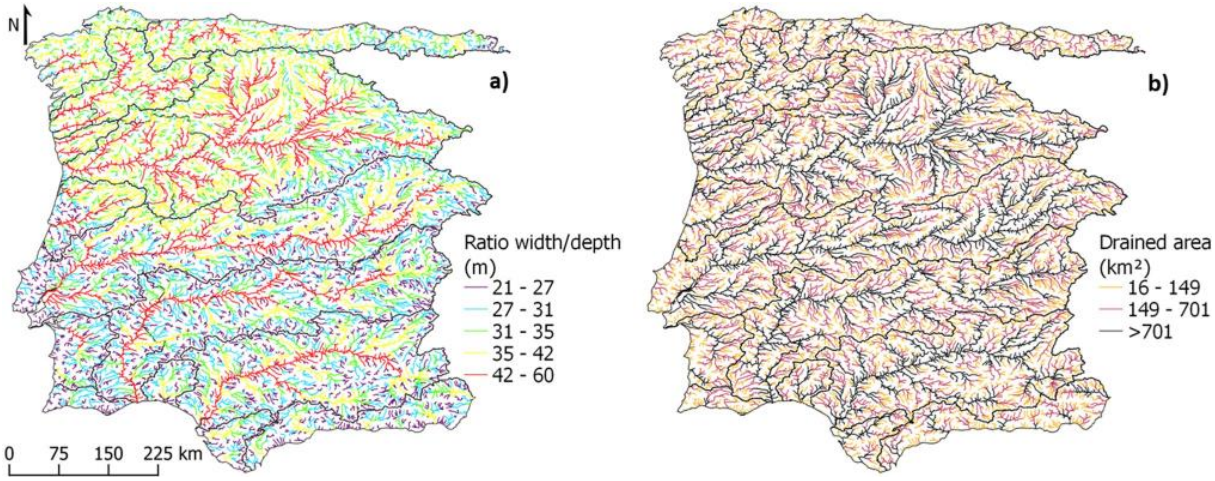

Figure 3.7 Ratio between cross-sections width and depth (a) and the drained area (b) in the studied domain, according to Sreedevi amd Eldho (2021).

Finally, it is important to denote that the solution presented here is the best from a set of tests performed during the calibration process; however, since each simulation takes about 15 days to perform, it is possible that with more efficient implementation, the calibration process would have gone further, and better results would be achieved. This also demonstrates that in fully distributed physically based models such as MOHID-Land the calibration process should not be dismissed, especially when the modeled domain is characterized by a significant lack of data (Sahoo et al., 2006). The importance of the calibration process in MOHID-Land model applications is demonstrated in Oliveira et al. (2020), Canuto et al. (2019), Epelde et al. (2016), and Brito et al. (2015), where the first three studied domains were extensively calibrated, and satisfactory results for streamflow simulation were obtained, while the latter never referred the

existence of a calibration process which along with the choice of hydrometric stations influenced by reservoirs to evaluate the model performance appears to be the reason for the model not being able to represent the observed values.

3.4 Conclusions

The MOHID-Land model was used to simulate the natural flow regime in Iberian transnational catchments using a process-based, fully distributed approach implemented in a coarse (5 km) resolution grid domain. While results were satisfactory, they also evidenced the difficulties in simulating the streamflow in highly modified basins following such a complex modeling approach. As such, the goodness-of-fit indicators computed at 73 hydrometric stations located in basins headwaters showed large variability, with the Nash–Sutcliffe modeling efficiency (NSE) reporting acceptable results for only 22 and 28 of those locations during calibration and validation, respectively. Nevertheless, the MOHID-Land application presented here shows the capacity of this model to simulate water processes at the regional scale instead of considering the division and simulation by watershed. This work also highlights the difficulties in calibrating the model in such a vast domain, as well as the importance of adopting a resolution with sufficient detail for representation of the physical processes without losing computational efficiency. Computational efficiency is essential for a successful calibration process.

The implementation of the MOHID-Land model at a regional scale can contribute to better water governance of the Iberian water resources, namely those shared by Portugal and Spain. While the modeling approach still needs to be improved, the implementation of the hydrological model at the regional scale shows that these tools can be extremely useful for improving the integrated river basin management and contribute to the study of anthropogenic and climate change impacts; however, an approach more focused on the basin level may be more suitable when studying water governance, since each basin “represents a hydrological entity with its own interval dynamics governed by the hydrological cycle”.

Author Contributions

Conceptualization, A.R.O., T.B.R. and L.S.; methodology, A.R.O.; validation, A.R.O.; resources, M.C.G.; data curation, M.C.G.; writing—original draft preparation, A.R.O.; writing—review and editing, T.B.R.; project administration, R.N.; funding acquisition, R.N. All authors have read and agreed to the published version of the manuscript.

Funding

This research was funded by FCT/MCTES (PIDDAC) through project LARSyS–FCT Pluriannual funding 2020–2023 (UIDB/50009/2020), and by INTERREG SUDOE Project AGUAMOD (Development of a water resource management platform during low water periods in the SUDOE region). T. B. Ramos was supported by contract CEECIND/01152/2017.

3.5 Appendixes

3.5.1 Appendix 3A

Table 3A.1 Number of observations (N. obs.), minimum (Min), maximum (Max), average (Ave), and standard deviation (Std. Dev.) of flow values in calibration and validation periods.

Station	Calibration					Validation				
	N. Obs.	Min ($m^3 s^{-1}$)	Max ($m^3 s^{-1}$)	Ave ($m^3 s^{-1}$)	Std. Dev. ($m^3 s^{-1}$)	N. Obs.	Min ($m^3 s^{-1}$)	Max ($m^3 s^{-1}$)	Ave ($m^3 s^{-1}$)	Std. Dev. ($m^3 s^{-1}$)
1215	180	0.1	37.9	8.1	8.4	153	0.0	49.0	8.7	9.3
1265	63	0.6	10.9	4.2	2.9	168	0.4	20.4	4.5	3.6
1268	180	1.1	68.5	12.7	10.9	168	0.3	56.7	13.1	10.6
1293	0	-	-	-	-	46	1.5	46.8	16.2	13.6
1295	180	1.3	83.7	19.7	16.7	168	1.5	59.1	18.8	14.5
1302	180	1.5	46.4	12.1	10.2	168	1.1	53.2	12.9	11.4
1303	180	1.1	40.4	9.4	8.5	168	0.9	42	9.5	8.8
1353	180	2.4	54.5	15.9	11.6	168	1.1	53.3	14.6	12.5
1365	180	0.6	36.1	9.2	7.5	165	0	43	9.8	9
1404	178	1.8	34.4	10.4	7.2	140	1.1	49.5	9.8	9.2
1519	144	3.1	176.5	38.5	33.8	21	3.1	239.2	62	72.6
1520	0	-	-	-	-	118	1.6	63.5	16.3	14.8
1554	0	-	-	-	-	63	9	187.6	51.3	44.7
1568	0	-	-	-	-	59	2.9	49.7	15.8	13.5
1605	0	-	-	-	-	72	1	38.6	11	9.9
1607	180	0.2	67.5	11.6	11.9	163	0.7	57.1	11.2	12.3
1608	180	0.3	51.7	11.5	10	158	0.5	55.2	11	12
1619	180	0.5	111.9	22.4	21.8	161	0.9	156.6	23.7	27.7
1620	0	-	-	-	-	72	0.1	15.2	3.7	4
1621	175	2	257.5	47.7	47.2	114	0.4	322.5	50.8	62.1
1622	0	-	-	-	-	63	2.7	201.5	54	53.8
1640	0	-	-	-	-	72	0.6	77.3	20.8	19.2
1642	0	-	-	-	-	62	35.2	1031.5	326.5	267.2
1645	180	0.6	111.8	16.8	18.7	168	0.6	108	14	16.5
1659	0	-	-	-	-	72	0.5	38.9	9.1	9.7
1726	0	-	-	-	-	72	0.9	30	8.4	7.8
1727	180	0.7	83.9	14.1	13.1	114	1	94.7	12.2	16.2
2000	151	0	8.9	1.8	1.7	168	0	15	2.3	2.5

Station	Calibration					Validation				
	N. Obs.	Min ($m^3 s^{-1}$)	Max ($m^3 s^{-1}$)	Ave ($m^3 s^{-1}$)	Std. Dev. ($m^3 s^{-1}$)	N. Obs.	Min ($m^3 s^{-1}$)	Max ($m^3 s^{-1}$)	Ave ($m^3 s^{-1}$)	Std. Dev. ($m^3 s^{-1}$)
2004	170	4.2	58.2	14.9	8.2	168	2.6	79.3	12.3	11.5
2007	81	4.9	92.6	16.3	12.5	0	-	-	-	-
2009	178	0	2.9	0.5	0.5	168	0	2	0.5	0.4
2012	171	0.4	7.2	1.7	1.3	168	0.8	9.4	1.9	1.3
2013	176	2.8	103.5	16.4	14.2	168	4	116.7	15.9	17.5
2016	168	0	20.7	3.4	4	168	0	12.4	1.9	2.4
2018	0	-	-	-	-	156	0	34.1	2.9	4.8
2028	180	0	18.5	2.9	3.3	168	0	30.9	3.4	4.8
2029	180	1.1	146.2	16.6	20.8	168	2.2	186.1	20.3	28.4
2031	180	0	78.2	13.9	15.6	168	0.2	154.5	16.4	22.5
2046	180	0	46.6	3.2	6.4	168	0	22.5	3	4.3
2062	180	5	643	86.2	94.9	168	6.4	879.8	107.6	135.4
2078	180	1.5	19.1	6.5	4.2	168	0.5	20.2	3.8	3.1
2081	27	0	103	24.6	25.6	168	0	172.9	24.9	29.8
2085	51	0.4	95.1	43	29.9	39	0.2	47.5	14.5	12.9
2089	178	0.4	48.9	4.4	5.5	168	0.4	28.1	4.4	5.1
2150	0	-	-	-	-	159	0.2	34.8	6.9	7.1
3001	180	0.8	24.3	4.2	4.3	168	0.6	24.2	3.9	4
3002	180	0.1	6.7	1.3	1.2	168	0.1	5	1.3	1.2
3005	180	4.1	82.9	14.3	11.1	168	3.6	70.9	12.9	11.5
3146	145	0.1	121.3	11.3	16.2	39	0	38.6	7.2	7.8
3161	179	0	84	6.8	12.7	168	0	111.7	6.5	12.6
3218	179	0	24.8	2.5	3.5	168	0	15.4	2.3	2.9
3221	180	0	33.1	2.6	4.5	168	0	28.5	2.6	3.9
3226	178	0	21.9	2.6	3.6	168	0	28.3	2.2	3.5
3231	174	0	92.7	7.6	13.1	168	0.1	52.2	7.3	8.7
3234	175	0	72	5.9	8.9	168	0	57.9	5.3	7.6
3235	168	0	31.6	2.5	3.8	167	0	18.5	2.4	3.4
4004	135	0.2	13.5	1.4	1.7	168	0.6	21.5	2.4	3.1
4009	60	0	59.8	6.6	10	117	0	33.9	3	6.4
4165	29	0.1	15.4	1.1	3	104	0	4.4	0.8	0.8
4202	177	0	9.8	0.8	1.3	105	0	13.4	0.9	2.1
4214	132	0	161	4.8	17.4	144	0	45.1	4.1	7.3
4251	72	0	2.7	0.3	0.5	90	0	3.3	0.5	0.7
4255	171	0	234.2	10.3	29.3	162	0.3	151.7	9.9	19.4

Station	Calibration					Validation				
	N. Obs.	Min ($m^3 s^{-1}$)	Max ($m^3 s^{-1}$)	Ave ($m^3 s^{-1}$)	Std. Dev. ($m^3 s^{-1}$)	N. Obs.	Min ($m^3 s^{-1}$)	Max ($m^3 s^{-1}$)	Ave ($m^3 s^{-1}$)	Std. Dev. ($m^3 s^{-1}$)
5049	51	0	1.9	0.1	0.3	128	0	4.5	0.3	0.6
5050	26	0.3	2	0.8	0.4	144	0.1	48	3.6	5.9
5057	121	0.1	67.9	6.5	12.1	124	0.2	37.5	3.3	6.4
5088	138	0.3	10.3	1.9	1.6	12	0.4	3.1	1.4	1.2
5097	158	0	24.1	1.2	2.5	102	0	5.2	0.7	0.9
5137	108	0	6.4	1.3	2	153	0	1.9	0.3	0.3
5142	150	0	31.4	0.7	3.1	151	0	18.3	0.9	2
5145	100	0	24.2	2.4	4.5	155	0	11.2	1.4	2.1
07F/03H	9	0	19.2	3.7	6	0	-	-	-	-
08P/01H	180	0	196.3	15.5	27.8	141	0	176.9	16.5	28.1

3.5.2 Appendix 3B

Table B3.1 Soil hydraulic parameters.

Soil type	Layer's depth (m)	θ_s ($m^3\ m^{-3}$)	θ_r ($m^3\ m^{-3}$)	α (m^{-1})	η (-)	K_s ($m\ s^{-1}$)
Gleyic Acrisol	0–0.3	0.403	0.025	3.830	1.377	6.94×10^{-6}
	0.3–0.7	0.481	0.010	0.198	1.086	9.84×10^{-7}
	>0.7	0.350	0.025	3.830	1.377	6.94×10^{-6}
Chromic Cambisol	0–0.3	0.403	0.025	3.830	1.377	6.94×10^{-6}
	>0.3	0.392	0.010	2.490	1.170	1.25×10^{-6}
Humic Cambisol	0–0.7	0.766	0.010	1.300	1.200	9.26×10^{-7}
	>0.7	0.392	0.010	2.490	1.170	1.25×10^{-6}
Calcic Cambisol	0–0.3	0.439	0.010	3.140	1.180	1.39×10^{-6}
	>0.3	0.392	0.010	2.490	1.170	1.25×10^{-6}
Rendzina	0–0.3	0.439	0.010	3.140	1.180	1.39×10^{-6}
	>0.3	0.392	0.010	2.490	1.170	1.25×10^{-6}
Lithosol	0–0.3	0.439	0.010	3.140	1.180	1.39×10^{-6}
	>0.3	0.350	0.010	3.140	1.180	1.25×10^{-6}
Calcaric Fluvisol	0–0.3	0.439	0.010	3.140	1.180	1.39×10^{-6}
	>0.3	0.392	0.010	2.490	1.170	1.25×10^{-6}
Albic Luvisol	0–0.3	0.403	0.025	3.830	1.377	6.94×10^{-6}
	0.3–0.7	0.392	0.010	2.490	1.170	1.25×10^{-6}
	>0.7	0.350	0.025	3.830	1.377	6.94×10^{-6}
Gleyic Luvisol	0–0.3	0.439	0.010	3.140	1.180	1.39×10^{-6}
	0.3–0.7	0.481	0.010	0.198	1.086	9.84×10^{-7}
	>0.7	0.350	0.025	3.830	1.377	6.94×10^{-6}
Calcic Luvisol	0–0.3	0.439	0.010	3.140	1.180	1.39×10^{-6}
	0.3–0.7	0.481	0.010	0.198	1.086	9.84×10^{-7}
	>0.7	0.350	0.025	3.830	1.377	6.94×10^{-6}
Dystric Histosol	>0	0.766	0.010	1.300	1.300	9.26×10^{-7}
Gleyic Podzol	0–0.3	0.403	0.025	3.830	1.377	6.94×10^{-6}
	>0.3	0.350	0.025	3.830	1.377	6.94×10^{-6}
Cambic Arenosol	0–0.3	0.403	0.025	3.830	1.377	6.94×10^{-6}
	>0.3	0.350	0.025	3.830	1.377	6.94×10^{-6}
Calcaric Regosol	0–0.3	0.403	0.025	3.830	1.377	6.94×10^{-6}
	>0.3	0.350	0.025	3.830	1.377	6.94×10^{-6}
Ranker	0–0.3	0.439	0.010	3.140	1.180	1.40×10^{-6}
	>0.3	0.392	0.010	2.490	1.170	1.25×10^{-6}
Chromic Vertisol	0–0.3	0.52	0.010	3.670	1.100	2.87×10^{-6}
	0.3–0.7	0.481	0.010	0.198	1.086	9.84×10^{-7}
	>0.7	0.392	0.010	2.490	1.170	1.25×10^{-6}
Dystric Planosol	0–0.3	0.403	0.025	3.830	1.377	6.94×10^{-6}
	0.3–0.7	0.481	0.010	0.198	1.086	9.84×10^{-7}
	>0.7	0.392	0.010	2.490	1.170	1.25×10^{-6}
Calcic Xerosol	0–0.3	0.439	0.010	3.140	1.180	1.40×10^{-6}
	>0.3	0.392	0.010	2.490	1.170	1.25×10^{-6}
Gleyic Solonchak	0–0.3	0.520	0.010	3.670	1.130	2.87×10^{-6}
	0.3–0.7	0.481	0.010	0.198	1.086	9.84×10^{-7}
	>0.7	0.392	0.010	2.490	1.170	1.25×10^{-6}

3.6 References

Agência Portuguesa do Ambiente (APA-RH1). Plano de Gestão da Região Hidrográfica do Minho e Lima (RH1) (2016/2021). Parte 2-Caracterização e Diagnóstico. 2016.

Available online: https://apambiente.pt/agua/2o-ciclo-de-planeamento-2016-2021 (accessed on 19 March 2022).

Agência Portuguesa do Ambiente (APA-RH2). Plano de Gestão da Região Hidrográfica do Cávado, Ave e Leça (RH2) (2016/2021). Parte 2-Caracterização e Diagnóstico. 2016. Available online: https://apambiente.pt/agua/2o-ciclo-de-planeamento-2016-2021 (accessed on 19 March 2022).

Agência Portuguesa do Ambiente (APA-RH3). Plano de Gestão da Região Hidrográfica do Douro (RH3) (2016/2021). Parte 2-Caracterização e Diagnóstico. 2016. Available online: https://apambiente.pt/agua/2o-ciclo-de-planeamento-2016-2021 (accessed on 19 March 2022).

Agência Portuguesa do Ambiente (APA-RH4). Plano de Gestão da Região Hidrográfica do Vouga, Mondego e Lis (RH4) (2016/2021). Parte 2-Caracterização e Diagnóstico. 2016. Available online: https://apambiente.pt/agua/2o-ciclo-de-planeamento-2016-2021 (accessed on 19 March 2022).

Agência Portuguesa do Ambiente (APA-RH5). Plano de Gestão da Região Hidrográfica do Tejo e Ribeiras do Oeste (RH5) (2016/2021). Parte 2-Caracterização e Diagnóstico. 2016. Available online: https://apambiente.pt/agua/2o-ciclo-de-planeamento-2016-2021 (accessed on 19 March 2022).

Agência Portuguesa do Ambiente (APA-RH6). Plano de Gestão da Região Hidrográfica do Sado e Mira (RH6) (2016/2021). Parte 2-Caracterização e Diagnóstico. 2016. Available online: https://apambiente.pt/agua/2o-ciclo-de-planeamento-2016-2021 (accessed on 19 March 2022).

Agência Portuguesa do Ambiente (APA-RH7). Plano de Gestão da Região Hidrográfica do Guadiana (RH7) (2016/2021). Parte 2-Caracterização e Diagnóstico. 2016. Available online: https://apambiente.pt/agua/2o-ciclo-de-planeamento-2016-2021 (accessed on 19 March 2022).

Agência Portuguesa do Ambiente (APA-RH8). Plano de Gestão da Região Hidrográfica das Ribeiras do Algarve (RH8) (2016/2021). Parte 2-Caracterização e Diagnóstico. 2016. Available online: https://apambiente.pt/agua/2o-ciclo-de-planeamento-2016-2021 (accessed on 19 March 2022).

Allen, R.G.; Pereira, L.S.; Raes, D.; Smith, M. Crop Evapotranspiration—Guidelines for Computing Crop Water Requirements; Irrigation & Drainage Paper 56; FAO: Rome, Italy, 1998.

Álvarez, J.; Sánchez, A.; Quintas, L. SIMPA, a GRASS based tool for hydrological studies. In Proceedings of the FOSS/GRASS Users Conference, Bangkok, Thailand, 12–14 September 2004.

American Society of Civil Engineers (ASCE). Hydrology Handbook Task Committee on Hydrology Handbook; II Series, GB 661.2. H93; ASCE: Reston, VA, USA, 1996; pp. 96–104.

Andreadis, K.M.; Schumann, G.J.P.; Pavelsky, T. A simple global river bankfull width and depth database. Water Resour. Res. 2013, 49, 7164–7168. https://doi.org/10.1002/wrcr.20440

Barros, V.R.; Field, C.B.; Dokken, D.J.; Mastrandrea, M.D.; Mach, K.J.; Bilir, T.E.; Chatterjee, M.; Ebi, K.L.; Estrada, Y.O.; Genova, R.C.; et al. Climate Change 2014. Impacts, adaptation, and vulnerability. Part B: Regional Aspects. Q. J. Econ. 2014, 88, 1. https://doi.org/10.2307/1881805

Beck, H.E.; Zimmermann, N.E.; McVicar, T.R.; Vergopolan, N.; Berg, A.; Wood, E.F. Present and future Köppen-Geiger climate classification maps at 1-km resolution. Sci. Data 2018, 5, 180214. https://doi.org/10.1038/sdata.2018.214

Brito, D.; Campuzano, F.J.; Sobrinho, J.; Fernandes, R.; Neves, R. Integrating operational watershed and coastal models for the Iberian Coast: Watershed model implementation—A first approach. Estuar. Coast. Shelf Sci. 2015, 167, 138–146. https://doi.org/10.1016/j.ecss.2015.10.022

Brito, D.; Neves, R.; Branco, M.A.; Gonçalves, M.C.; Ramos, T.B. Modeling flood dynamics in a temporary river draining to an eutrophic reservoir in southeast Portugal. Environ. Earth Sci. 2017, 76, 377. https://doi.org/10.1007/s12665-017-6713-7

Campuzano, F.; Brito, D.; Juliano, M.; Fernandes, R.; de Pablo, H.; Neves, R. Coupling watersheds, estuaries and regional ocean through numerical modelling for Western Iberia: A novel methodology. Ocean Dyn. 2016, 66, 1745–1756. https://doi.org/10.1007/s10236-016-1005-4

Canuto, N.; Ramos, T.B.; Oliveira, A.R.; Simionesei, L.; Basso, M.; Neves, R. Influence of reservoir management on Guadiana streamflow regime. J. Hydrol. Reg. Stu. 2019, 25, 100628. https://doi.org/10.1016/j.ejrh.2019.100628

Centro de Estudios y Experimentación de Obras Públicas (CEDEX). Evaluación de Recursos Hídricos en Régimen Natural en España (1940/41–2017/18); CENTRO DE ESTUDIOS Y EXPERIMENTACIÓN DE OBRAS PÚBLICA: Madrid, Spain, 2020.

Chauveau, M.; Chazot, S.; Perrin, C.; Bourgin, P.Y.; Sauquet, E.; Vidal, J.P.; Rouchy, N.; Martin, E.; David, J.; Norotte, T.; et al. Quels impacts des changements climatiques sur les eaux de surface en France à l'horizon 2070? La Houille Blanche 2013, 99, 5–15. https://doi.org/10.1051/lhb/2013027

Confederación Hidrográfica del Tajo. Acueducto Tajo-Segura. Available online: http://www.chtajo.es/Confederacion/Infraestructuras/Paginas/AcueductoTajoSegura.aspx (accessed on 20 June 2021).

Convenio Sobre Cooperación Para la Protección y el Aprovechamiento Sostenible de las Aguas de las Cuencas Hidrográficas Hispanoportuguesas. Boletín Of. Del Estado 2000, 2882, 6703. Available online: https://www.boe.es/ (accessed on 20 November 2021).

Copernicus Land Monitoring Service (CLC). Available online: https://land.copernicus.eu/pan-european/corine-land-cover/clc-2012 (accessed on 3 July 2018).

Dankers, R.; Feyen, L. Climate change impact on flood hazard in Europe: An assessment based on high-resolution climate simulations. J. Geophys. Res. Atmos. 2008, 113, D19105. https://doi.org/10.1029/2007JD009719

Diffenbaugh, N.S.; Giorgi, F. Climate change hotspots in the CMIP5 global climate model ensemble. Clim. Change 2012, 114, 813–822. https://doi.org/10.1007/s10584-012-0570-x

Epelde, A.M.; Antiguedad, I.; Brito, D.; Jauch, E.; Neves, R.; Garneau, C.; Sauvage, S.; Sánchez-Pérez, J.M. Different modelling approaches to evaluate nitrogen transport and turnover at the watershed scale. J. Hydrol. 2016, 539, 478–494. https://doi.org/10.1016/j.jhydrol.2016.05.066

European Commission. DIRECTIVE 2000/60/EC. Establishing a Framework for Community Action in the Field of Water Policy 2000, L327, 23 October. Available online: https://eur-lex.europa.eu/eli/dir/2000/60/oj (accessed on 23 November 2021).

Feddes, R.A.; Kowalik, P.J.; Zaradny, H. Simulation of Field Water Use and Crop Yield; Wiley: Hoboken, NJ, USA, 1978.

Ferreira, A.M.P.J. Dados Geoquímicos de Base de Sedimentos Fluviais de Amostragem de Baixa Densidade de Portugal Continental: Estudo de Factores de Variação Regional. Ph.D. Thesis, Universidade de Aveiro, Aveiro, Portugal, 2000.

García-Ruiz, J.M.; López-Moreno, I.I.; Vicente-Serrano, S.M.; Lasanta-Martínez, T.; Beguería, S. Mediterranean water resources in a global change scenario. Earth Sci. Rev. 2011, 105, 121–139. https://doi.org/10.1016/j.earscirev.2011.01.006

Görgen, K.; Beersma, J.; Brahmer, G.; Buiteveld, H.; Carambia, M.; De Keizer, O.; Krahe, P.; Nilson, E.; Lammersen, R.; Perrin, C.; et al. Assessment of Climate Change Impacts on Discharge in the Rhine River Basin: Results of the RheinBlick2050 Project. Report No. I-23; International CHR: Utrecht, The Netherlands, 2010; ISBN 978-90-70980-35-1.

Green, W.H.; Ampt, G.A. Studies on Soil Physics, Part 1, the Flow of Air and Water through Soils. J. Agric. Sci. 2011, 4, 11–24.

Hoekstra, A.Y.; Mekonnen, M.M.; Chapagain, A.K.; Mathews, R.E.; Richter, B.D. Global monthly water scarcity: Blue water footprints versus blue water availability. PLoS ONE 2012, 7, e32688. https://doi.org/10.1371/journal.pone.0032688

Instituto Nacional de Estadística. Parte 1—Entorno físico y medio ambiente. In Anuario Estadístico de España; Instituto Nacional de Estadística: Madrid, Spain, 2006.

Linsley, R.K., Jr. Why simulation? Hydrocomp Simul. Netw. Newsl. 1976, 8, 5.

Lorenzo-Lacruz, J.; Vicente-Serrano, S.M.; López-Moreno, J.I.; Beguería, S.; García-Ruiz, J.M.; Cuadrat, J.M. The impact of droughts and water management on various hydrological systems in the headwaters of the Tagus River (central Spain). J. Hydrol. 2010, 386, 13–26. https://doi.org/10.1016/j.jhydrol.2010.01.001

Lorenzo-Lacruz, J.; Vicente-Serrano, S.M.; López-Moreno, J.I.; Morán-Tejeda, E.; Zabalza, J. Recent trends in Iberian streamflows (1945–2005). J. Hydrol. 2012, 414–415, 463–475. https://doi.org/10.1016/j.jhydrol.2011.11.023

Marcinkowski, P.; Grygoruk, M. Long-term downstream effects of a dam on a lowland river flow regime: Case study of the upper narew. Water 2017, 9, 783. https://doi.org/10.3390/w9100783

Masson-Delmotte, V.; Zhai, P.; Pörtner, H.-O.; Roberts, D.; Skea, J.; Shukla, P.R.; Pirani, A.; Moufouma-Okia, W.; Péan, C.; Pidcock, R.; et al. IPCC, 2018: Global Warming of 1.5 ◦C. An IPCC Special Report on the impacts of global warming of 1.5°C above pre-industrial levels and related global greenhouse gas emission pathways, in the context of strengthening the global response to the threat of climate change, sustainable development, and efforts to eradicate poverty. IPCC 2018, in press.

Ministerio para la Transición Ecológica y el Reto Demográfico (MITERD). Inventario Nacional de Presas y Embalses (National Dams Inventory). Available online: https://sig.mapama.gob.es/snczi/ (accessed on 15 April 2021).

Ministerio para la Transición Ecológica y el Reto Demográfico (MITERD). Sistema de Información de Redes de Seguimiento. Available online: https://sig.mapama.gob.es/redes-seguimiento/ (accessed on 20 November 2018).

Monreal, T.E.; Calvo-Rubio, F.C.; Lorenzo, F.E. La evaluación de los recursos hídricos en el libro blanco del agua en España. Ing. Agua 1999, 6, 2. https://doi.org/10.4995/ia.1999.2781

Monreal, T.E.; Ripoll, L.Q. El sistema integrado de modelización Precipitación-Aportación. Rev. Digit. Cedex 1996, 104, 43. Available online: http://ingenieriacivil.cedex.es/index.php/ingenieria-civil/article/view/1153 (accessed on 19 March 2022).

Moriasi, D.N.; Arnold, J.G.; van Liew, M.W.; Bingner, R.L.; Harmel, R.D.; Veith, T.L. Model Evaluation Guidelines for Systematic Quantification of Accuracy in Watershed Simulations. Trans. Am. Soc. Agric. Biol. Eng. 2007, 50, 885–900.

Mualem, Y. A new model for predicting the hydraulic conductivity of unsaturated porous media. Water Resour. Res. 1976, 12, 513–522. https://doi.org/10.1029/WR012i003p00513

Nachtergaele, F.; Van Velthuizen, H.; Verelst, L.; Batjes, N.; Dijkshoorn, K.; Van Engelen, V.; Fischer, G.; Jones, A.; Montanarella, L.; Petri, M.; et al. Harmonized World Soil Database; FAO: Rome, Italy; IIASA: Laxenburg, Austria, 2009.

NASA Shuttle Radar Topography Mission Global 3 arc second (NASA-SRTM). NASA EOSDIS Land Processes DAAC. Available online:

https://doi.org/10.5067/MEaSUREs/SRTM/SRTMGL3.003 (accessed on 30 March 2017).

O'Gorman, P.A. Precipitation extremes under climate change. Curr. Clim. Change Rep. 2015, 1, 49–59. https://doi.org/10.1007/s40641-015-0009-3

Oliveira, A.R.; Ramos, T.B.; Simionesei, L.; Pinto, L.; Neves, R. Sensitivity analysis of the MOHID-Land hydrological model: A case study of the Ulla river basin. Water 2020, 12, 3258. https://doi.org/10.3390/w12113258

Pfahl, S.; O'Gorman, P.A.; Fischer, E.M. Understanding the regional pattern of projected future changes in extreme precipitation. Nat. Clim. Change 2017, 7, 423–427. https://doi.org/10.1038/nclimate3287

Quintana-Seguí, P.; Habets, F.; Martin, E. Comparison of past and future Mediterranean high and low extremes of precipitation and river flow projected using different statistical downscaling methods. Nat. Hazards Earth Syst. Sci. 2011, 11, 1411–1432. https://doi.org/10.5194/nhess-11-1411-2011

Quintana-Seguí, P.; Turco, M.; Herrera, S.; Miguez-Macho, G. Validation of a new SAFRAN-based gridded precipitation product for Spain and comparisons to Spain02 and ERA-Interim. Hydrol. Earth Syst. Sci. Discuss. 2017, 21, 2187–2201. https://doi.org/10.5194/hess-21-2187-2017

Ramos, T.B.; Gonçalves, M.C.; Brito, D.; Martins, J.C.; Pereira, L.S. Development of class pedotransfer functions for integrating water retention properties into Portuguese soil maps. Soil Res. 2013, 51, 262–277. https://doi.org/10.1071/SR12347

Ramos, T.B.; Simionesei, L.; Jauch, E.; Almeida, C.; Neves, R. Modelling soil water and maize growth dynamics influenced by shallow groundwater conditions in the Sorraia Valley region, Portugal. Agric. Water Manage. 2017, 185, 27–42. https://doi.org/10.1016/j.agwat.2017.02.007

Refsgaard, J.C. Parameterisation, calibration and validation of distributed hydrological models. J. Hydrol. 1997, 198, 69–97. https://doi.org/10.1016/S0022-1694(96)03329-X

Resolução da Assembleia da República n. 66/99, Diário da República: I série-A, 1999, No 191, 5410–5430. Available online: https://data.dre.pt/eli/resolassrep/66/1999/08/17/p/dre/pt/html (accessed on 20 November 2021).

Ritchie, J.T. Model for predicting evaporation from a row crop with incomplete cover. Water Resour. Res. 1972, 8, 1204–1213. https://doi.org/10.1029/WR008i005p01204

Rojas, R.; Feyen, L.; Bianchi, A.; Dosio, A. Assessment of future flood hazard in Europe using a large ensemble of bias-corrected regional climate simulations. J. Geophys. Res. Atmos. 2012, 117, D17109. https://doi.org/10.1029/2012JD017461

Sahoo, G.B.; Ray, C.; De Carlo, E.H. Calibration and validation of a physically distributed hydrological model, MIKE SHE, to predict streamflow at high frequency in a flashy mountainous Hawaii stream. J. Hydrol. 2006, 327, 94–109. https://doi.org/10.1016/j.jhydrol.2005.11.012

Shukla, P.R.; Skea, J.; Calvo Buendia, E.; Masson-Delmotte, V.; Pörtner, H.-O.; Roberts, D.C.; Zhai, P.; Slade, R.; Connors, S.; van Diemen, R.; et al. IPCC, 2019: Climate Change and Land: An IPCC special report on climate change, desertification, land degradation, sustainable land management, food security, and greenhouse gas fluxes in terrestrial ecosystems. IPCC 2019, in press.

Sistema Nacional de Informação de Recursos Hídricos (SNIRH-Alburfeiras). Dados Sintetizados, Características das Albufeiras. Available online: https://snirh.apambiente.pt/index.php?idMain=1&idItem=7 (accessed on 15 April 2021).

Sistema Nacional de Informação de Recursos Hídricos (SNIRH-Monitorização). Dados de Base, Monitorização. Available online: https://snirh.apambiente.pt/index.php?idMain=2&idItem=1 (accessed on 15 April 2021).

Soil Conservation Service, U.S. National Engineering Handbook. Section 4, Design Hydrographs; U.S. Department of Agriculture, Soil Conservation Service: Washington, DC, USA, 1972.

Sreedevi, S.; Eldho, T.I. Effects of grid-size on effective parameters and model performance of SHETRAN for estimation of streamflow and sediment yield. Int. J. River Basin Manag. 2021, 19, 535–551. https://doi.org/10.1080/15715124.2020.1767637

Strahler, A.N. Dynamic Basis of Geomorphology. GSA Bulletin 1952, 63, 923–938. https://doi.org/10.1130/0016-7606(1952)63[923:DBOG]2.0.CO;2

Strahler, A.N. Quantitative analysis of watershed geomorphology. Eos Trans. AGU 1957, 38, 913–920. https://doi.org/10.1029/TR038i006p00913

Te Linde, A.H.; Aerts, J.C.J.H.; Bakker, A.M.R.; Kwadijk, J.C.J. Simulating low-probability peak discharges for the Rhine basin using resampled climate modeling data. Water Resour. Res. 2010, 46, 1–19. https://doi.org/10.1029/2009WR007707

Témez, J.R. Modelo Matemático de Transformación "Precipitación-Aportación"; Asociación de Investigación Industrial Eléctrica, Ed.; Comisión, E. Explotación y Garantía; Grupo de Trabajo de Predicciones de Precipitación y Relación entre Precipitaciones y Caudales: Madrid, España, 1977.

Trancoso, A.R.; Braunschweig, F.; Chambel Leitão, P.; Obermann, M.; Neves, R. An advanced modelling tool for simulating complex river systems. Sci. Total Environ. 2009, 407, 3004–3016. https://doi.org/10.1016/j.scitotenv.2009.01.015

Van der Sande, C.J.; de Jong, S.M.; de Roo, A.P.J. A segmentation and classification approach of IKONOS-2 imagery for land cover mapping to assist flood risk and flood damage assessment. Int. J. Appl. Earth Obs. Geoinf. 2003, 4, 217–229. https://doi.org/10.1016/S0303-2434(03)00003-5

Van Genuchten, M.T. A Closed-form Equation for Predicting the Hydraulic Conductivity of Unsaturated Soils. Soil Sci. Soc. Am. J. 1980, 44, 892–898. https://doi.org/10.2136/sssaj1980.03615995004400050002x

Veijalainen, N.; Lotsari, E.; Alho, P.; Vehviläinen, B.; Käyhkö, J. National scale assessment of climate change impacts on flooding in Finland. J. Hydrol. 2010, 391, 333–350. https://doi.org/10.1016/j.jhydrol.2010.07.035

Vicente-Serrano, S.M.; Zabalza-Martínez, J.; Borràs, G.; López-Moreno, J.I.; Pla, E.; Pascual, D.; Savé, R.; Biel, C.; Funes, I.; Martín-Hernández, N.; et al. Effect of reservoirs on streamflow and river regimes in a heavily regulated river basin of Northeast Spain. Catena 2016, 149, 727–741. https://doi.org/10.1016/j.catena.2016.03.042

Wong, W.K.; Beldring, S.; Engen-Skaugen, T.; Haddeland, I.; Hisdal, H. Climate change effects on spatiotemporal patterns of hydroclimatological summer droughts in Norway. J. Hydrometeorol. 2011, 12, 1205–1220. https://doi.org/10.1175/2011JHM1357.1

Wösten, J.H.M.; Lilly, A.; Nemes, A.; Le Bas, C. Development and use of a database of hydraulic properties of European soils. Geoderma 1999, 90, 169–185. https://doi.org/10.1016/S0016-7061(98)00132-3

4 Influence of reservoir management on Guadiana streamflow regime

Authors: Nelson Canuto, Tiago B. Ramos, Ana R. Oliveira, Lucian Simionesei, Marta Basso, Ramiro Neves

Centro de Ciência e Tecnologia do Ambiente e do Mar (MARETEC-LARSyS), Instituto Superior Técnico, Universidade de Lisboa, Av. Rovisco Pais, 1, 1049-001 Lisboa, Portugal

Published in: Journal of Hydrology: Regional Studies, 2019, 25: 100628 (https://doi.org/10.1016/j.ejrh.2019.100628) **Impact Factor:** 5.437

Abstract

Study region: Guadiana international catchment, located in the Iberian Peninsula.

Study focus: The Guadiana River catchment has registered an intense and speed up modification of its natural regime over the last few decades to cope with water scarcity. Such modifications pose a serious challenge to the development of improved management tools as information on available water resources is often not detailed enough. This study aimed to simulate the flow regime of the Guadiana River using the MOHID-Land model during a 30 year period. Two scenarios were defined by considering (or not) inputs from reservoirs. Model performance was assessed by comparing simulated and measured monthly streamflow at 24 hydrometric stations influenced (9 stations) or not (15 stations) by reservoir management.

New hydrological insights for the region: Streamflow simulations produced quite acceptable estimates for most of the hydrometric stations not influenced by reservoirs. However, results also showed the importance of non-simulated processes (e.g., groundwater abstractions) to the accurate prediction of the Guadiana flow regime. For the stations influenced by reservoir management, model simulations generally overestimated streamflow measurements. Information related to reservoir management needs thus to be made clearer for achieving better results, which can only be accomplished when national water agencies improve their cooperation protocols. Further model limitations were also addressed as well as the necessary developments for improving streamflow estimates in future modeling applications.

Keywords: Distributed model; Iberian Peninsula; MOHID-Land; Streamflow; Water scarcity

4.1 Introduction

Water resources in regions under arid, semi-arid, and even sub-humid conditions are subjected to multiple pressures that result mostly from: population growth; major demographic shifts as people move from rural to urban environments; higher demands for food security and socio-economic well-being; increased competition between users and usages; and contamination from point and diffuse pollution sources (WWAP, 2019). Agriculture is by far the largest water consumer (accounting for 69% of the global annual water withdrawals) followed by industry (19%) and households (12%) (AQUASTAT, 2019). As global water demand is expected to increase 20 to 30% above the current level of water use by 2050, mainly due to the rising demand in the industrial and domestic sectors, so will water stress levels which already afflict about 4 billion people worldwide be enhanced (WWAP, 2019). Sustainable management practices are thus needed for optimizing the use of water resources at the regional scale and reducing potential conflicts among users.

A representative example of the need for improved management plans is the Guadiana transnational river catchment shared by Portugal and Spain. The climate in the region is mostly dry-sub humid to semi-arid, with some areas being among the driest places in Europe. The seasonality of rainfall and high evapotranspiration demand typically results in a period with high winter discharges and another with low summer discharges. The region is also cyclically affected by extended droughts that further enhance the seasonality of local water resources (Vicente-Serrano, 2006; Paulo et al., 2012; Lorenzo-Lacruz et al., 2013). Consequently, the Guadiana River has been subjected to an intense and speed up modification of its natural regime, with reservoir storage capacity increasing from almost zero in 1954 to close to 14,000 hm^3 nowadays (Brandão and Rodrigues, 2000; CEH-CEDEX, 2019; SNIRH, 2019). At the same time, large agriculture projects were developed, with water withdrawals approaching sometimes the limits of sustainability. For example, the dramatic increase of groundwater abstractions for irrigation in the upper region of the Guadiana basin has led to the decline of groundwater levels, degradation of protected wetlands, rise of groundwater salinity levels, and occasional water transfers from the Tagus basin (Conan et al., 2003; Bromley et al., 2010). In Portugal, Alqueva was built to be the largest reservoir in Europe, constituting a strategic water reserve for the southern part of the country and deeply modifying the landscape and production systems by providing water for irrigation of 150,000 ha of agricultural land distributed between the Guadiana and Sado basins, urban and industrial consumption, energy production, and regularization of flows (EDIA, 2019).

The Albufeira Convention is the international agreement signed between Portugal and Spain in 1998, and later revised in 2008, which regulates the flow regime in the five transnational basins shared by the two countries (Minho, Lima, Douro, Tejo, and Guadiana). For the case of the Guadiana catchment, the Convention defines minimum flows for different trimesters of the year or, alternatively, a minimum annual flow measured at the Badajoz weir where the Guadiana River enters Portugal. Minimum flows are dependent on the amount of rainfall and water stored in pre-defined reservoirs. The Convention further defines conditions for an exceptional regime, which is usually associated with drought periods. In this case, a minimum daily flow of 2 $m^3 s^{-1}$, perceived as a basic ecological minimum, is established as the only requirement at the Badajoz weir, but also at Pomarão, as the river flows from Portugal to become the border between the two countries just 70 km above its estuary (Agência Portuguesa do Ambiente, 2016). While the compliance with the Albufeira Convention agreement is considered a top priority for water allocation in both countries, water scarcity issues in both Portugal and Spain pose already significant challenges for water resources management (Do Ó, 2012). On the Spanish side, local authorities report an annual deficit close to 600 hm^3 without the adoption of measures limiting demand (Confederação Hidrográfica do Guadiana, 2014). On the Portuguese side, irrigation during drought seasons is much dependent on the amount of water stored in Alqueva, which is now connected to smaller reservoirs to compensate for water shortages in different parts of the Alentejo region. Meanwhile, climate change projections that foresee significant reductions in rainfall and streamflow for the near future (Kilsby et al., 2007; Guerreiro et al., 2017) only add more uncertainty to the availability of water resources in the Guadiana basin.

The vulnerability of water resources in the Guadiana catchment requires a precise quantification of the volumes available with modeling being many times selected as a preferred tool for achieving such purpose. Brandão and Rodrigues (2000) used the IRAS (Interactive River Aquifer Simulation; Loucks et al., 1995) model to simulate streamflow in the Portuguese part of the Guadiana catchment, considering six hydrological scenarios that were defined to assess the impact of the Albufeira Convention and the Spanish Hydrological Plan on water volumes stored in Portuguese reservoirs. Also, Conan et al. (2003), applied the SWAT (Soil Water Assessment Tool; Neitsch et al., 2011) model to assess the impact of groundwater withdrawals on the hydrological behavior of the upper Guadiana River catchment. Later, Kilsby et al. (2007) estimated the impact of climate change projections on runoff production, streamflow, and water resources availability in the Guadiana catchment using a distributed daily rainfall-runoff model. Finally, Guerreiro et al. (2017) pursued a similar objective,

estimating the impact of climate change projections on the Guadiana River streamflow using the SHETRAN model (Ewen et al., 2000). While the previous studies provided significant insights for the accurate quantification of local water resources, they all shared similar constraints when validating model results due to simplifications adopted when describing the complexity of the Guadiana basin and the modified flow regime of the Guadiana River.

This study provides a further attempt to simulate streamflow in the Guadiana River using the MOHID-Land model (Trancoso et al., 2009). MOHID-Land is a fully distributed process-based model that considers interactions between multiple components of the soil-water-atmosphere continuum, with fundamental processes being formulated at fine spatial (at the grid cell level) and temporal scales, contributing to the overall dynamics of the catchment at a larger scale. The MOHID-Land model structure is comparable to the SHETRAN model used in Guerreiro et al. (2017) and applications include, for example, improving irrigation practices at the plot and field scales (Ramos et al., 2017, 2018; Simionesei et al., 2018), understanding the contribution of flood events to the eutrophication of water reservoirs (Brito et al., 2017, 2018), and forecasting fresh water quantity and quality in coastal rivers (Brito et al., 2015). The objectives of this study were thus: (i) to simulate streamflow in the Guadiana catchment under two scenarios that included (or not) reservoir management; and (iii) to discuss model limitations and developments (research and data) needed for better quantifying local water resources in future applications.

4.2 Materials and methods

4.2.1 Description of the study area

The Guadiana catchment is located in the southern region of the Iberian Peninsula (Figure 4.1), being the fourth largest after Douro, Tagus, and Ebro. The drainage area covers 66 999 km^2, of which 55 465 km^2 (82.8%) are in Spain and 11 534 km^2 (17.2%) are in Portugal (Agência Portuguesa do Ambiente, 2016). The river has a bed length over 800 km, with headwaters in Lagunas de Ruidera, Castilla-La Mancha, Spain (38°58′21″N, 2°53′9″W, 868 m). The river then flows in the North East – South West direction to the border cities of Vila Real de Santo António (Portugal) and Ayamonte (Spain), where it meets the Atlantic Ocean (37°10′40″N, 7°24′18″W, 0 m).

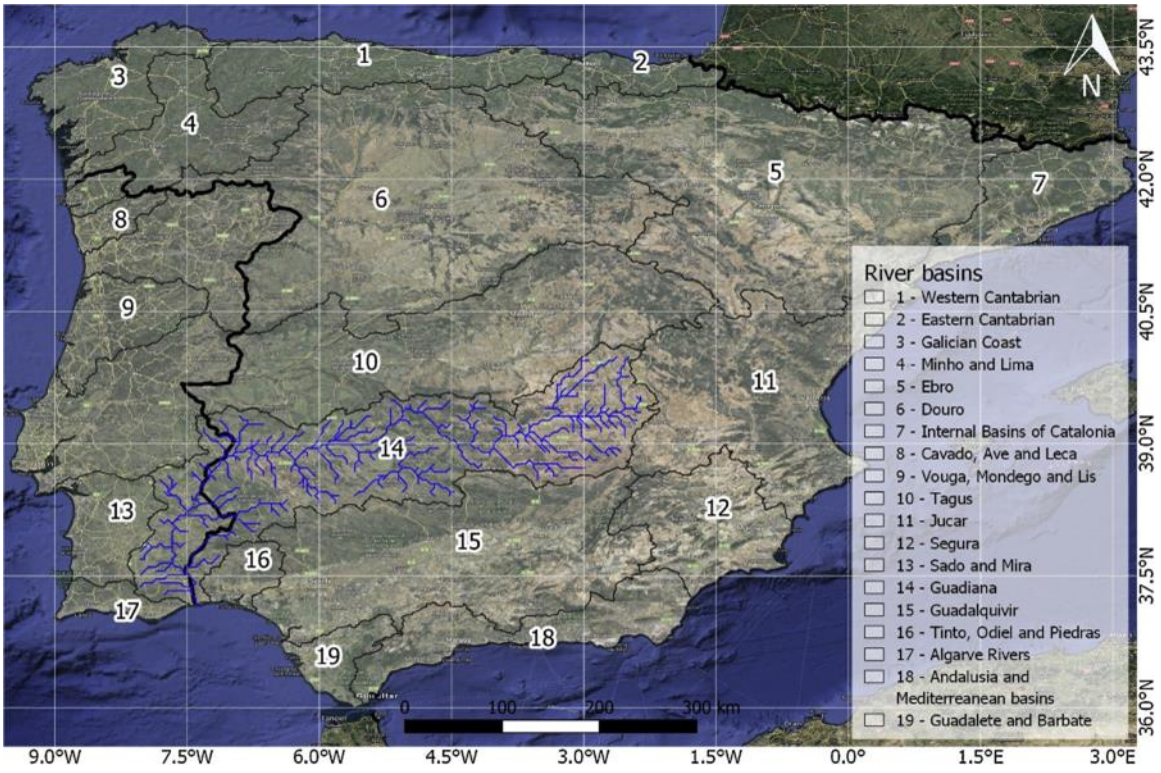

Figure 4.1 Location of the Guadiana River catchment.

The climate in the catchment ranges from hot-summer Mediterranean climate (Csa) to cold semi-arid (steppe) climate (Bsk) (IM and AEMET, 2011). The mean annual temperature is close to 16 °C, varying between 28 °C in July/August (Ciudad Real, Spain) and 8.5 °C in January (Elvas, Portugal). The mean annual rainfall is 550 mm (561 mm in Portugal and 540 mm in Spain), with minimum of 350–450 mm in the central area of the La Mancha plain (Spain) and Mértola and Moura (Portugal) and maximum of more than 1000 mm in the headwaters of the tributaries Ardila, Odeleite and Caia. The interannual distribution of precipitation is also extremely irregular, ranging from 386 mm in dry years to 766 mm in wet years. On average, more than 80% of the total annual precipitation occurs between October and April (Agência Portuguesa do Ambiente, 2016).

The dominant soils are Regosols (44% of the area), Cambisols (28%), and Luvisols (14%) (IUSS Working Group, 2014) (Figure 4.2). Soils in the upper region of the catchment are mostly derived from unconsolidated calcareous deposits, while in the middle and low regions soils originate from metamorphic rocks (schists, gneiss, migmatite). The main land uses are divided between rainfed or irrigated agriculture (65%) and Mediterranean woodland (18%) or shrubland (16%) (Figure 4.2). In Spain, 85% of the diverted water is used for irrigation; the irrigated area covers over 400 000 ha; cereals, vineyards, and industrial crops are the dominant crops, with an annual average consumption of 5300 m^3 ha^{-1} (Confederação

Hidrográfica do Guadiana, 2014). In Portugal, 88% of the diverted water is used mainly for energy production, although this is not a consumptive use; water use in agriculture totalizes only 9.1% of the diverted water (Agência Portuguesa do Ambiente, 2016); however, this number will inevitably increase in the near future as the Alqueva Project progressively adds over 150 000 ha of new irrigated land to that already existing in the region (EDIA, 2019).

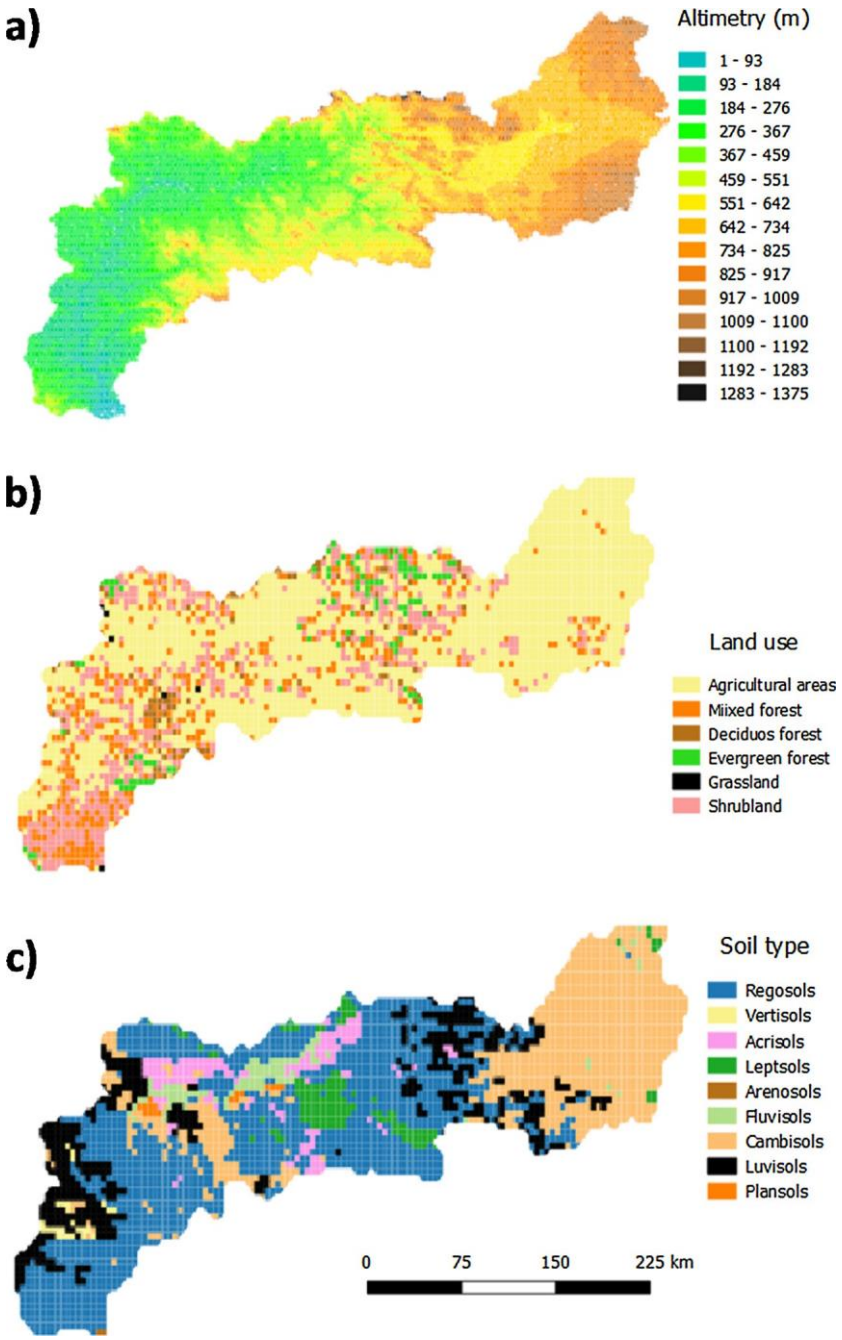

Figure 4.2 Digital terrain model (a), main land uses (b), and main soil types (c) in the Guadiana catchment.

The catchment has a population of 1.9 million inhabitants, with a density of 28 inhabitants km^{-2} in Spain and 114 inhabitants km^{-2} in Portugal (EUROSTAT, 2019). There are 39 reservoirs located along the catchment with a total storage capacity above 10 hm^3 (the

threshold limit assumed here to impact the hydrological regime of the Guadiana River). These were built between 1944 and 2010. The largest is Alqueva (38°11′48″N, 7°29′45″W, 85 m) built in 2002, with a total capacity of 4150 hm^3. The smallest is Lucefecit (38°38′09″N 7°24′22″W, 173 m) built in 1982, with a total capacity of 10.2 hm^3. Several others exist with less storage capacity (Figure 4.3).

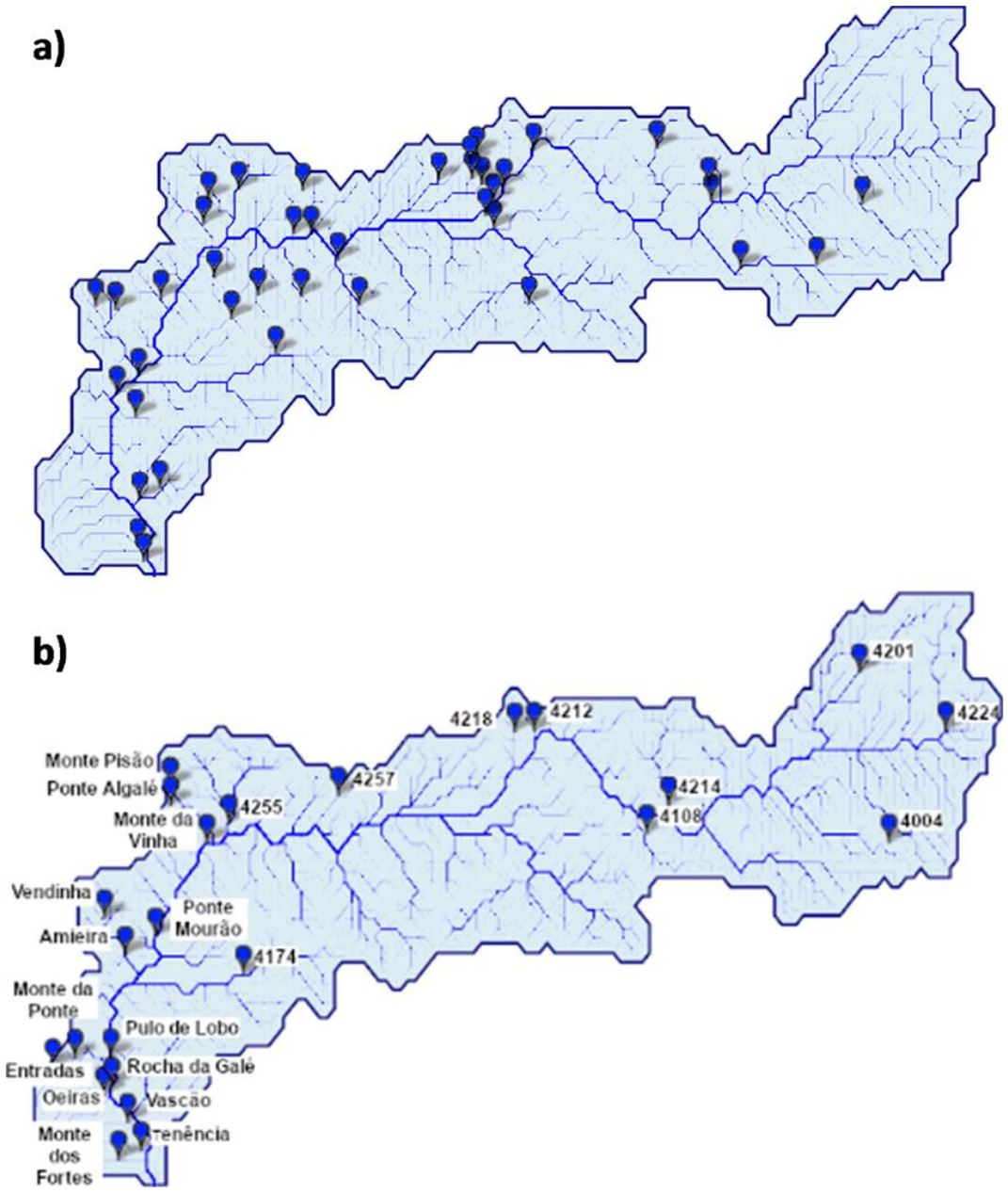

Figure 4.3 Location of the reservoirs with storage capacity above 10 hm^3 (a) and hydrometric stations used for model calibration/validation (b).

4.2.2 Model description

MOHID-Land is a physically-based, fully-distributed model designed to simulate the water cycle in hydrographic catchments (Trancoso et al., 2009). The model considers four compartments or mediums (atmosphere, porous media, soil surface, and river network). The

atmosphere is not explicitly simulated but provides data necessary for imposing surface boundary conditions that may be space and time variant. Water moves through the remaining mediums based on mass and momentum conservation equations that are computed using a finite volume approach. The simulation domain is organized into a regular structured grid, quadrangular or rectangular in the horizontal plane, and cartesian type in the vertical plane. Surface land is thus described by a 2D horizontal grid. The porous media is a 3D domain, which includes the same horizontal grid as the surface complemented with a vertical grid with variable thickness layers. The river network is a 1D domain defined from the digital terrain model (DTM), with the drainage network linking surface cell centers (nodes). The model further uses an explicit algorithm with a variable time step that is maximum during dry seasons when fluxes are reduced and minimum when fluxes increase (e.g., during rain events).

In this study, runoff and infiltration of surface water were computed using the curve number (CN) procedure (USDA Soil Conservation Service, 1972):

$$Q_{surf} = \begin{cases} 0 & \text{when } P_{day} \leq I_a \\ \dfrac{(P_{day} - I_a)^2}{(P_{day} - I_a + R)} & \text{when } P_{day} > I_a \end{cases} \quad \text{(Eq. 4.1)}$$

where Q_{surf} is the accumulated runoff or rainfall excess (L), P_{day} is the rainfall amount for the day (L), I_a is the initial abstraction which includes surface storage and infiltration prior to runoff (L), and R is a retention parameter (L):

$$R = \frac{25400}{CN} - 254 \quad \text{(Eq. 4.2)}$$

where CN is the curve number (−).

The variably saturated flow in the porous medium was computed using the Richards equation as follows:

$$\frac{\partial \theta}{\partial t} = \frac{\partial}{\partial x_i}\left[K(\theta)\left(\frac{\partial h}{\partial x_i} + \frac{\partial}{\partial x_i}\right)\right] - S(h) \quad \text{(Eq. 4.3)}$$

where θ is the volumetric water content ($L^3\ L^{-3}$), t is the time (T), x_i are the xzy directions (−), h is the soil pressure head (L), K is the hydraulic conductivity ($L\ T^{-1}$), and S is the sink term accounting for water uptake by plant roots ($L^3\ L^{-3}\ T^{-1}$). The unsaturated soil hydraulic properties were then described using the van Genuchten-Mualem functional relationships (Mualem, 1976; van Genucthen, 1980):

$$S_e(h) = \frac{\theta(h) - \theta_r}{\theta_s - \theta_r} = \frac{1}{(1 + |\alpha h|^{\eta})^m} \quad \text{(Eq. 4.4)}$$

$$K(h) = K_s S_e^{\ell}\left[1 - (1 - S_e^{1/m})^m\right]^2 \quad \text{(Eq. 4.5)}$$

where S_e is the effective saturation (L3 L^{-3}), θ_r and θ_s denote the residual and saturated water contents (L^3 L^{-3}), respectively, K_s is the saturated hydraulic conductivity (L T^{-1}), α (L^{-1}) and η (−) are empirical shape parameters, $m = 1–1/\eta$, and ℓ is a pore connectivity/tortuosity parameter (−). The MOHID-Land model uses the Richards equation in the whole subsurface domain and simulates saturated and unsaturated flow using the same grid. A cell is considered as saturated when moisture is above 98%. When a cell reaches saturation, the model uses the saturated conductivity and pressure becomes hydrostatic, corrected by friction. This procedure eases the implementation of the model and simplifies its use at annual scale. The penalty is the time step that during the wetting period must be shorter to guarantee stability. The constraint is minimized using parallel computing.

The sink term (S) in Eq. (4.3) was computed using the macroscopic approach proposed by Feddes et al. (1978). Following this approach, potential transpiration (T_p, L T^{-1}) was linearly distributed over the root zone, creating the function $T_p(z)$, which was diminished by the presence of depth-varying root zone stressors, namely water stress (Skaggs et al., 2006; Šimůnek and Hopmans, 2009) as follows:

$$T_a = \alpha(h) T_p(z) \quad \text{(Eq. 4.6)}$$

where T_a is the actual transpiration rate (L T^{-1}) and α is a prescribed dimensionless function of h ($0 \leq \alpha \leq 1$) limiting T_p over the root zone. The piecewise linear model proposed by Feddes et al. (1978) was then adopted for computing T_p reductions due to water stress ($\alpha(h)$), assuming that the water uptake was at the potential rate when the pressure head was between h_2 and h_3, dropped off linearly when $h > h_2$ or $h < h_3$, and became zero when $h < h_4$ or $h > h_1$ (subscripts 1–4 denote for different threshold pressure heads).

Plant transpiration and soil evaporation were thus the main drivers for computing soil water dynamics in the porous media. But first, crop evapotranspiration rates (ET_c, L T^{-1}) were obtained from the product of reference evapotranspiration rates (ET_o, L T^{-1}) computed with the FAO Penman-Monteith method (Allen et al., 1998) and a single crop coefficient (K_c). The K_c values were not crop stage dependent as in Allen et al. (1998), representing instead average characteristics of each vegetation type over the entire growing season as well as averaged effects of evaporation from the soil. ET_c values were then partitioned into potential soil evaporation (E_p, L T^{-1}) and T_p as a function of the leaf area index (LAI, m^2 m^{-2}), following Ritchie, 1972:

$$T_p = ET_c(1 - e^{(-\lambda LAI)}) \quad \text{(Eq. 4.7)}$$

$$E_p = ET_c - T_p \quad \text{(Eq. 4.8)}$$

where λ is the extinction coefficient of radiation attenuation within the canopy (−). The actual soil evaporation (E_a, L T^{-1}) was obtained by limiting Ep values using an imposed pressure head threshold value (American Society of Civil Engineers, 1996).

The LAI, as well as other crop growth state variables, were simulated using a modified version of the EPIC model (Williams et al., 1989; Neitsch et al., 2011). This model is based on the heat unit theory, which considers that all heat above the base temperature will accelerate crop growth and development. Crop growth was thus simulated as a function of the intercepted light, its conversion into biomass, and LAI development (Neitsch et al., 2011). LAI was calculated as a function of heat units, the crop development stages, and crop stress (Neitsch et al., 2011). Additional details can be found in Ramos et al. (2017).

Surface water movement in the soil and the river network were computed by solving a Saint-Venant equation in its conservative form, accounting for advection, pressure, and friction forces for one (in the river) or two horizontal (at the soil surface) directions of the grid:

$$\frac{\partial Q_u}{\partial t} + v_v \frac{\partial Q_u}{\partial x_v} = -gA\left(\frac{\partial H}{\partial x_i} + \frac{|Q|Q_i n^2}{A_v^2 R_h^{4/3}}\right) \quad \text{(Eq. 4.9)}$$

where Q is the water flow in the river (L^3 T^{-1}), A_v is the cross-sectional flow area (L^2), g is the gravitational acceleration (L T^{-2}), v is the flow velocity (L T^{-1}), H is the hydraulic head (L), n is the Manning coefficient (T $L^{-1/3}$), R_h is the hydraulic radius (L), x_i represents the xyz directions (−) and the subscripts u and v denote flow directions. The exchange between the river network and the subsurface flow (computed with the Richards equation) was driven by the pressure at the interface (river level) and the pressure in the porous media (phreatic level). Likewise, the eventual excess water volume reallocated to the surface of the porous media domain (exfiltration) when the soil column was saturated was driven by the phreatic level. Surface water exchange between the river and riparian zones were further computed based on the kinematic approach, neglecting bottom friction, and using an implicit algorithm to avoid instabilities.

4.2.3 Model implementation

The MOHID-Land model (Trancoso et al., 2009) was implemented in the study area using a square horizontal grid with 75 × 136 cells, each with 0.045° × 0.045° (5 km × 5 km). The digital terrain model (DTM) was obtained from the NASA Shuttle Radar Topographic Mission (SRTM) at 3 arc-second spatial resolution (approximately 70–90 m) (Rabus et al., 2003); then interpolated to the MOHID-Land grid using the average of values inside a grid cell;

and further modified to eliminate sunken or depressed cells. Topography in the modified DTM varied then from 0 to 1375 m (Figure 4.2).

The soil map was extracted from the Harmonized Soil Database (FAO/IIASA/ISRIC/ISS-CAS/JRC, 2009), with the 30 arc-second raster information being also interpolated to the MOHID-Land grid. The soil reference units represented at the scale of the study domain were Regosols (44.0%), Cambisols (28.3%), Luvisols (14.0%), Leptosols (4.6%), Acrisols (4.5%), Fluvisols (2.8%), Planosols (0.7%), Vertisols (0.7%), and Arenosols (0.4%) (Figure 4.2). First, the porous media was discretized into seven vertical layers, with varying thickness from 0.3 m at the surface to 8.9 m at the impermeable bottom. Each soil column was then divided into three horizons (by grouping layers of the vertical grid): the surface horizon was defined by the top layer of the vertical grid (0.0–0.3 m depth); the sub-surface horizon by the second layer (0.3–0.8 m depth); and the bottom horizon by the remaining five layers (0.8–30.0 m depth). Soil depth was corrected according to the surface slope provided by the DTM, assuming larger depths in valleys than in ridges. The thickness of the bottom layers was thus adjusted based on the assumed soil depths, which end up varying from 25.9 to 30.0 m. The soil hydraulic parameters of the Mualem-van Genuchten model (van Genuchten, 1980) were finally derived for each soil horizon of each soil reference group using soil texture information available in the Harmonized Soil Database and the HYPRES class pedotransfer functions (Wösten et al., 1999). The ℓ pore connectivity/tortuosity parameter was set to 0.5 following Mualem (1976). For the initial conditions, the soil was assumed as saturated for 83% of the profile (from the bottom to the surface), while the soil water content in the unsaturated zone was set to field capacity.

The CORINE Land Cover (CLC) 2012 map with 100 m resolution (Copernicus Land Monitoring Service, 2019) was likewise interpolated to the MOHID-Land grid and used for defining the vegetation type and surface rugosity. The land uses represented at the scale of the study domain were agricultural areas (65.3%), shrubland (16.5%), mixed forest (12.4%), evergreen forest (2.9%), deciduous forest (2.7%), and grassland (0.1%) (Figure 4.2). Urban areas were not included. Considering the large representation of agricultural and shrubland areas (81.9%), the definition of the CN values ended up being simplified to basically account for the soil reference group and were set following the USDA Soil Conservation Service (1972), tables. The Manning coefficient was defined for each vegetation type according to van der Sande et al., 2003. Vegetation growth parameters assumed the same default values as in Neitsch et al. (2011). The annual K_c values of each vegetation type averaged the K_c values of the different crop development stages given in Allen et al. (1998).

Hourly data from the SAFRAN model (Quintana-Seguí et al., 2017) was used for defining the atmosphere boundary conditions of the simulation domain. SAFRAN applies an interpolation algorithm that combines observations and the outputs of a meteorological model to produce a gridded dataset of precipitation, temperature, wind speed, relative humidity, and downward visible and infrared radiation for the period 1969–2014. The SAFRAN further uses climatically homogeneous zones to divide the space into the analysis areas, which are then presented in a grid format with a resolution of 5 km. This grid was here interpolated to the MOHID-Land grid using a triangulation method.

The river network was derived from the DTM using the steepest slope in 8 directions (i.e., according to the height of the surrounding cells). The river cross-sections were defined as having a trapezoidal shape, with dimensions set based on the drainage area of each node. 16 classes were considered (Table 4.1), with heights and widths at the top and bottom of the trapezoidal cross-sections being set according to Andreadis et al. (2013) and Neal et al. (2015). For the nodes with intermediate drainage areas, the dimensions of the cross-section were linear interpolated from those assumed in the upper and lower classes.

Table 4.1 Dimensions of the river cross-sections.

Drainage area (km^2)	Surface width (m)		Bottom width (m)		Height (m)		Cross-section (m^2)	
	Default	Calibrated	Default	Calibrated	Default	Calibrated	Default	Calibrated
18	3.5	6.1	2.3	4.1	0.15	0.33	0.4	1.7
25	3.8	7.4	2.5	4.9	0.16	0.45	0.5	2.8
50	4.7	10.4	3.1	6.9	0.2	0.58	0.8	5
100	6.7	21.3	4.6	14.2	0.26	0.77	1.5	13.7
200	9.8	34.2	6.5	22.8	0.34	1.03	2.8	29.4
500	15.8	53.6	10.6	35.7	0.5	1.42	6.6	63.4
750	19.5	56.2	12.9	37.5	0.6	1.48	9.7	69.3
1000	23	60.8	15.2	40.5	0.7	1.52	13.4	77
2000	30	80.6	22	53.7	0.85	1.7	22.1	114.2
5000	55	110.5	36.7	73.7	1.4	2.13	64.2	196.1
10 000	79	138.2	53	92.1	1.8	2.35	118.2	270.6
20 000	111	179.8	74	119.9	2.35	3.1	217.4	464.5
40 000	160	245.5	107	163.7	3	4.8	400.5	982
50 000	178	315	119	210	3.5	5.7	519.8	1496.3
60 000	280	350	186	233.3	4.9	6.8	1141.7	1983.3
67 000	300	358	200	238.7	5.5	7	1375	2088.3

Table 4.2 Relation between outflow/inflow and actual stored volume (operation curve) considered in the MOHID-Land model for estimating outflow in reservoirs.

Stored volume (%)	Outflow/Inflow (%)
0	0
40	5
60	10
95	30

Stored volume (%)	Outflow/Inflow (%)
96	40
97	50
98	70
99	90
100	100

For the scenario simulating the modified flow regime of the Guadiana River, model simulations further considered all reservoirs with a volume storage capacity larger than 10 hm^3. 39 reservoirs were implemented, representing a total storage capacity of 13 974 hm^3 (Figure 4.3). 11 reservoirs were present from the beginning of the simulation period while the remaining were gradually introduced depending on the respective start of operation date. The MOHID-Land model further requires the location and maximum and minimum volume capacity for simulating reservoir operation. Reservoir outflows can then be imposed (when data is available) or estimated according to an operation curve. In this study, reservoir outflows were defined for 31 reservoirs, with data being extracted from SNIRH, 2019, for Portugal and CEH-CEDEX, 2019, for Spain. The operation curve was considered for the remaining 8 reservoirs, with the outflow being estimated as a function of the inflow and the actual storage volume (in percentage values) (Table 4.2).

4.2.4 Model calibration/validation

Model simulations were conducted between October 1st, 1979, and June 30rd, 2014: the first six years (October 1st, 1979, to September 30rd, 1985) were used as model "warm-up"; the calibration period was from October 1st, 1985 to September 30rd, 1995 (10 years); and the validation period was from October 1st, 1995 to June 30rd, 2014 (19 years). During model calibration/validation, simulations of daily streamflow were compared against measured data in 24 hydrometric stations located along the catchment (Figure 4.3). Daily values were also converted to monthly data to compute the statistical indicators presented below. Only hydrometric stations having a minimum of five years of measured data were considered. Measured data were obtained from SNIRH (2019) for Portugal and from CEH-CEDEX (2019) for Spain.

A sensitive analysis was first carried out where selected parameters were modified one at a time and the model was run until the end of the calibration period to assess their impact on MOHID-Land simulations of streamflow. Model calibration/validation ended up focusing on the dimensions of the river cross-sections in the different nodes (heights and top and bottom widths), the curve number (CN), the manning coefficient (n), the annual crop coefficient (K_c),

the vertical saturated hydraulic conductivity (K_s), and the multiplying factor (f_h) for obtaining the horizontal saturated hydraulic conductivity from K_s ($K_{s,hor} = f_h K_s$). Model parameters were modified by trial-and-error during calibration until deviations between measured and simulated values were minimized. Validation was then performed by simply comparing model simulations using the calibrated parameters for the 1995–2014 period and respective measured dataset. Different goodness-of-fit tests were considered for assessing model performance, including the coefficient of determination (R^2), the ratio of the root mean square error to the standard deviation of observed data (NRMSE), the percent bias (PBIAS), and the model efficiency (NSE), respectively given by:

$$R^2 = \left[\frac{\sum_{i=1}^{n}(O_i - \bar{O})(P_i - \bar{P})}{\sqrt{\sum_{i=1}^{n}(O_i - \bar{O})^2}\sqrt{\sum_{i=1}^{n}(P_i - \bar{P})^2}} \right]^2 \quad \text{(Eq. 4.10)}$$

$$NRMSE = \frac{\sqrt{\frac{\sum_{i=1}^{n}(O_i - P_i)^2}{n-1}}}{\sqrt{\sum_{i=1}^{n}(O_i - \bar{O})^2}} \quad \text{(Eq. 4.11)}$$

$$PBIAS = 100\frac{\sum_{i=1}^{n}(O_i - P_i)}{\sum_{i=1}^{n} O_i} \quad \text{(Eq. 4.12)}$$

$$NSE = 1 - \frac{\sum_{i=1}^{n}(O_i - P_i)^2}{\sum_{i=1}^{n}(O_i - \bar{O})^2} \quad \text{(Eq. 4.13)}$$

where O_i and P_i are respectively the observed and model predicted values at time i, $\bar{O}$ and $\bar{P}$ are the respective mean values, and n is the number of observations. R^2 values close to 1 indicate that the model explains well the variance of observations. NRMSE, and PBIAS values close to zero indicate accurate model predictions (Legates and McCabe, 1999; Moriasi et al., 2007). Positive or negative PBIAS values refer to the occurrence of under- or over-estimation bias, respectively. Nash and Sutcliff, 1970, modelling efficiency NSE values close to 1 indicate that the residuals variance is much smaller than the observed data variance, hence the model predictions are good; contrarily, when NSE is very close to 0 or negative there is no gain in using the model, i.e., $\bar{O}$ is as good or better predictor than the model.

4.3 Results and discussion

4.3.1 Model parametrization

The MOHID-Land model includes a considerable number of parameters that need to be first calibrated/validated to provide reliable estimates of simulated results. The sensitive analysis carried out in this study identified the dimensions of the river cross-sections (heights

and top and bottom widths) and the CN, n, K_c, K_s, and f_h parameters as the most important in need of adjustment, suggesting the importance of horizontal flow processes (runoff and lateral flow) for reproducing the hydrological response of the Guadiana catchment. This agrees with Glaser et al. (2019), who discussed the importance of nonuniform lateral flow rather than vertical preferential flow processes observed at plot scale for simulating the hydrological regime in the Weierbach catchment, Germany, using the HydroGeoSphere model. Likewise, El-Nasr et al. (2005) simulated streamflow in the Jeker catchment, Belgium, using the MIKE-SHE model. In their application, model calibration/validation focused mostly on parameters influencing lateral flow, such as the drainage network configuration, and the vertical and horizontal hydraulic conductivity of the geological layers in the saturated zone. McMichael et al. (2006) and Im et al. (2009) further expressed the importance of horizontal flow processes in their applications using the same distributed model.

In this study, the MOHID-Land simulations required the enlargement of the river cross-sections for accommodating streamflow in the drainage network during peak events (Table 4.1). This adjustment was especially noted at the nodes discharging the smallest areas, with cross-section areas increasing size by 3 to 10 times compared to the initial default values. The CN values are listed in Table 4.3 for the main soil reference units, ranging from 66 to 79. These values were comparable to those used by Conan et al. (2003) in their SWAT model application for the Upper Guadiana basin. In this previous work, CN values were set to range from 39 for pasture in Regosols to 87 for agriculture in Luvisols. In both applications, higher CN values obviously resulted in higher runoff and lower infiltration volumes. The n values suffered only minor adjustments (Table 4.4) except for the deciduous forest class, which value increased from 0.125 to 0.230 s $m^{-1/3}$. Higher n values meant greater resistance to surface flow and reduced runoff volumes. Table 4.4 further lists the annual K_c values considered in this study, which ranged from 0.8 in the deciduous forest class to 1.0 in the evergreen forest class. Because catchment scale applications of the MOHID-Land model can only currently consider a single K_c value describing the full crop growing season, the calibrated values cannot meet the definitions given in Allen et al. (1998) and can hardly be compared to other applications. Nevertheless, higher K_c values correspond to greater potential evapotranspiration rates. The K_s values also increased when compared with Wösten et al., 1999, tabulated values (Table 4.3), which comes with no surprise since pedotransfer functions can only provide modest estimates of soil hydraulic properties. These functions are further based on measurements carried out in the laboratory in samples of limited size, with issues related to their representativeness being often raised when describing actual flow conditions, transport, and reaction processes occurring

at the field/catchment scales due to limitations in the porous medium continuum (Van Looy et al., 2017). Finally, the f_h was set to 3.0, promoting sub-surface flow.

Table 4.3 Calibrated soil parameters.

Parameters	Rg	Le	Ar	Fl	Ca	Lu	Pl	Ve	Ac
CN (−)	79	79	77	71	69	66	74	70	68
Top layer									
θ_s (−)	0.403	0.439	0.403	0.439	0.403	0.403	0.403	0.52	0.403
θ_r (−)	0.025	0.01	0.025	0.01	0.025	0.025	0.025	0.01	0.025
α (cm^{-1})	0.038	0.031	0.038	0.031	0.038	0.038	0.038	0.037	0.038
η (−)	1.38	1.18	1.38	1.18	1.38	1.38	1.38	1.1	1.38
K_s (cm d^{-1})	200	18	550	22	70	85	85	6	85
Sub-surface layer									
θ_s (−)	0.35	0.3	0.35	0.392	0.392	0.392	0.481	0.481	0.481
θ_r (−)	0.025	0.01	0.025	0.01	0.01	0.01	0.01	0.01	0.01
α (cm^{-1})	0.038	0.031	0.038	0.025	0.025	0.025	0.002	0.002	0.002
η (−)	1.38	1.18	1.38	1.17	1.17	1.17	1.09	1.09	1.09
K_s (cm d^{-1})	200	18	550	18	13	85	85	6	60
Bottom layer									
θ_s (−)	0.35	0.3	0.35	0.392	0.392	0.35	0.392	0.392	0.35
θ_r (−)	0.025	0.01	0.025	0.01	0.01	0.025	0.01	0.01	0.025
α (cm^{-1})	0.038	0.031	0.038	0.025	0.025	0.038	0.025	0.025	0.038
η (−)	1.38	1.18	1.38	1.17	1.17	1.38	1.17	1.17	1.38
K_s (cm d^{-1})	200	18	550	18	13	18	85	60	60

Rg, Regosols; Le, Leptosols; Ar, Arenosols; Fl, Fluvisols; Ca, Cambisols; Pl, Planosols; Ve, Vertisols; Ac, Acrisols. θ_r, residual water content; θ_s, saturated water content; α and η, empirical shape parameters; K_s, saturated hydraulic conductivity.

Table 4.4 Calibrated model parameters for different land uses.

Soil use	Manning coefficient, n (s $m^{-1/3}$)		Crop coefficient, K_c (−)	
	Default	Calibrated	Default	Calibrated
Agriculture	0.045	0.043	0.92	0.96
Forest – Mixed	0.227	0.225	0.95	0.95
Forest – Deciduous	0.125	0.230	0.80	0.80
Forest – Evergreen	0.125	0.127	1.07	1.00
Grassland	0.039	0.039	0.85	0.85
Shrubland	0.032	0.058	0.90	0.90

4.3.2 Model performance

4.3.2.1 Streamflow simulations not influenced by reservoirs management

Table 4.5 presents the goodness-of-fit indicators used to evaluate the level of agreement between streamflow measurements in hydrometric stations located in upstream reservoirs (Figure 4.3) and the MOHID-Land simulations. In general, the model performed reasonably well when simulating streamflow at the above-mentioned locations during the calibration (1985–1995) and validation periods (1995–2014). An example is given in Figure 4.4, which shows the flow-duration curve for the Oeiras station. The flow-duration curve is a cumulative frequency curve that shows the percent of time during which specified discharges are equaled

or exceeded in a given period (Searcy, 1959). At the Oeiras station, model simulations matched closely the measured values for streamflow values below 2.0 $m^3 s^{-1}$ but a small departure between the two data series was noticed for larger flows.

Table 4.5 Goodness-of-fit indicators obtained during calibration and validation (in brackets) of monthly streamflow simulations in hydrometric stations without the influence of reservoir management.

Hydrometric station	Records (years)	Average flow measured ($m^3 s^{-1}$)	Average flow simulated ($m^3 s^{-1}$)	R^2 (−)	NRMSE (−)	PBIAS (%)	NSE (−)
4004	7.0 (18.7)	0.72 (2.42)	0.83 (3.11)	0.03 (0.28)	0.87 (0.15)	−14.7 (−28.5)	−61.43 (−4.12)
4201	10.0 (15.7)	0.70 (1.82)	1.31 (2.70)	0.02 (0.13)	0.46 (0.20)	−87.4 (−48.5)	−23.90 (−6.42)
4224	8.7 (12.5)	0.17 (0.41)	2.90 (3.87)	0.17 (0.29)	2.31 (0.25)	−1634.0 (−446.8)	−586.06 (−9.06)
4108	9.7 (12.1)	0.46 (1.59)	1.21 (2.30)	0.83 (0.85)	0.13 (0.04)	−160.9 (−44.9)	−1.04 (0.74)
4212	5.5 (8.8)	1.75 (2.02)	2.31 (1.89)	0.80 (0.80)	0.06 (0.05)	−31.5 (6.1)	0.79 (0.78)
4218	3.6 (9.5)	2.39 (4.60)	1.80 (1.97)	0.73 (0.35)	0.10 (0.08)	24.6 (56.62)	0.51 (0.20)
4257	3.5 (12.4)	1.03 (0.75)	1.60 (1.80)	0.83 (0.44)	0.11 (0.17)	−56.2 (−142.3)	0.40 (−3.82)
Ponte Algalé	9.0 (8.5)	0.30 (0.63)	0.14 (0.09)	0.53 (0.27)	0.08 (0.12)	55.3 (87.7)	0.25 (−0.53)
Monte Pisão	9.0 (−)	0.79 (−)	0.75 (−)	0.76 (−)	0.05 (−)	5.1 (−)	0.74 (−)
Entradas	10.0 (5.6)	0.15 (0.30)	0.16 (0.28)	0.79 (0.63)	0.04 (0.08)	−4.5 (6.6)	0.78 (0.62)
Monte de Ponte	9.8 (−)	2.50 (−)	2.13 (−)	0.81 (−)	0.05 (−)	−4.0 (−)	0.75 (−)
Oeiras	9.7 (5.4)	1.81 (3.43)	2.16 (2.96)	0.88 (0.91)	0.04 (0.04)	−19.2 (13.91)	0.80 (0.89)
Vascão	9.4 (4.8)	2.25 (2.62)	2.54 (2.82)	0.87 (0.90)	0.04 (0.04)	−12.8 (−7.4)	0.80 (0.89)
Tenência	7.9 (−)	1.46 (−)	1.38 (−)	0.78 (−)	0.05 (−)	5.1 (−)	0.75 (−)
Monte dos Fontes	9.0 (5.3)	2.37 (3.23)	1.31 (1.70)	0.85 (0.76)	0.05 (0.08)	44.7 (49.1)	0.71 (0.55)

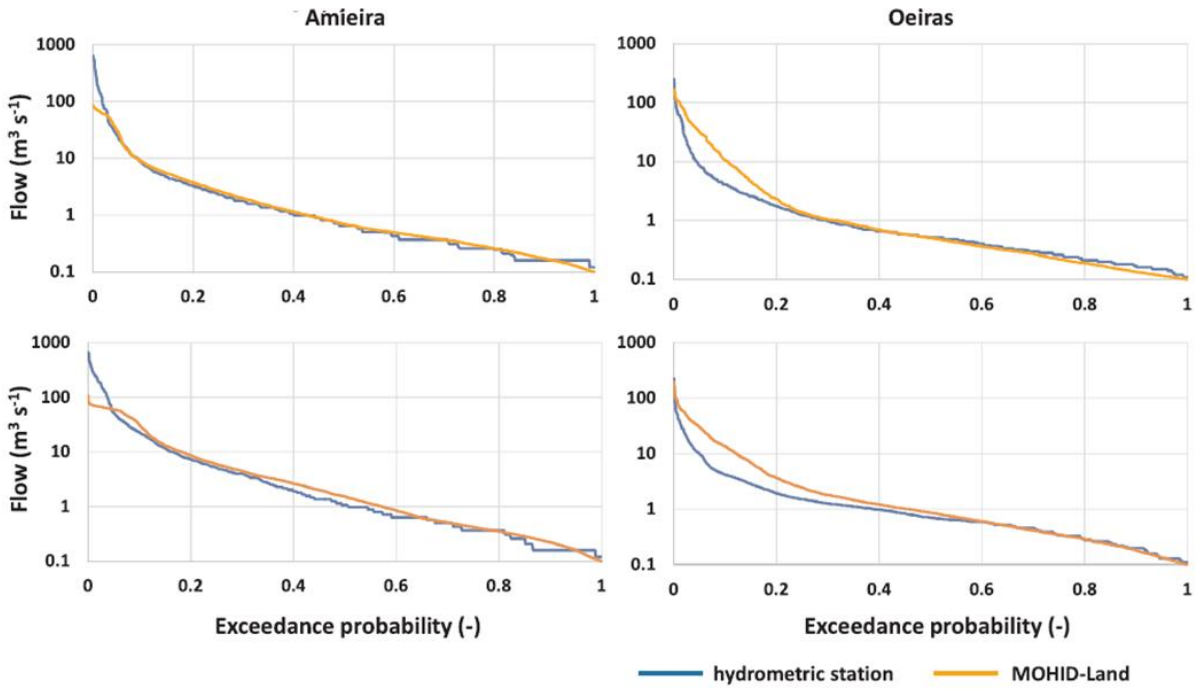

Figure 4.4 Observed and simulated flow-duration curves in the Amieira (influenced by reservoirs) and Oeiras (no reservoir influence) hydrometric stations.

Relatively high values of R^2 ($R^2 \geq 0.75$) were found for 10 of 15 hydrometric stations considered during calibration, showing that the model could explain well the variability of the observed data. Most of these stations were in the lower region of the Guadiana catchment (mostly in Portugal), while those located in the upper part (stations 4004, 4201, and 4224) failed to produce acceptable R^2 values ($R^2 \leq 0.17$) (Figure 4.5a). Model simulations performed well for 5 of the 12 hydrometric stations considered during validation. The R^2 values were generally lower than in calibration, with the upper region of the Guadiana catchment still failing to produce acceptable R^2 values ($R^2 \leq 0.29$) (Figure 4.5b).

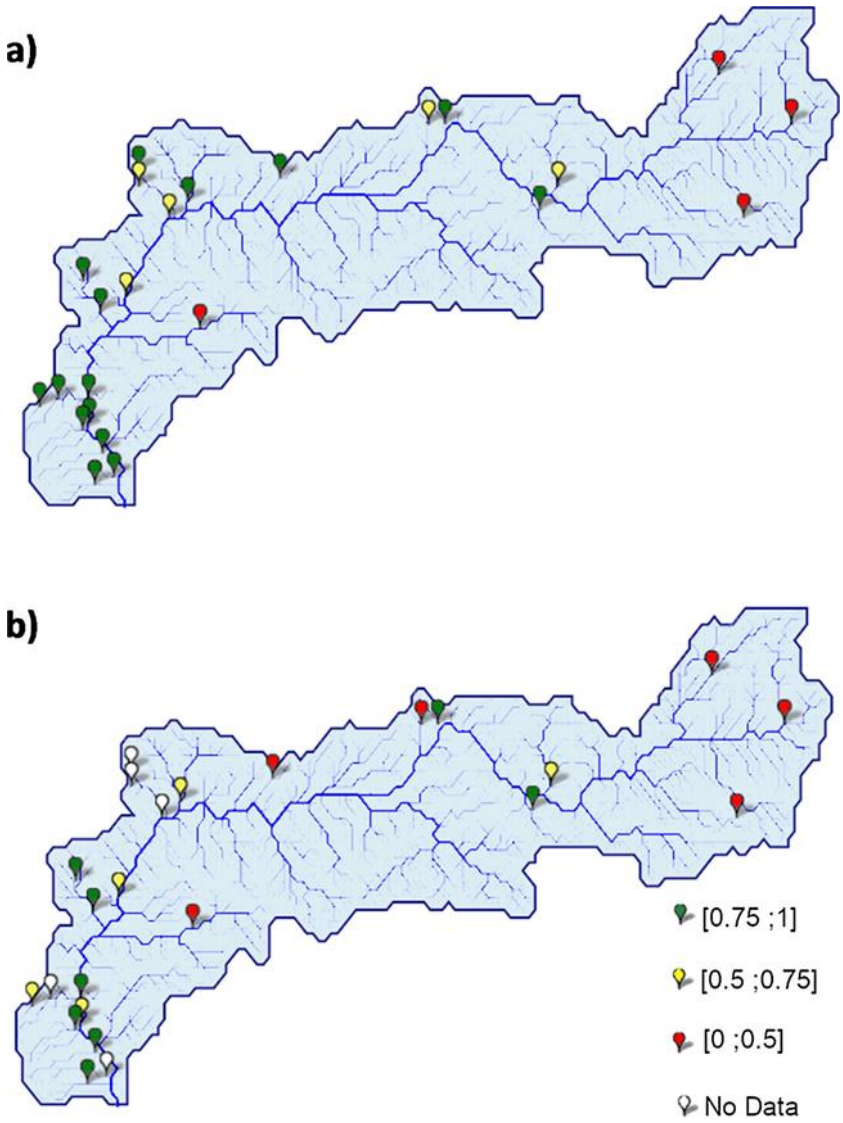

Figure 4.5 Spatial distribution of the coefficient of determination (R^2) values during calibration (a) and validation (b).

Overall, the errors of the estimates were relatively small, resulting in NRMSE values below 0.25 for 12 of 15 hydrometric stations considered in calibration (Figure 4.6a), and for all stations accounted for in validation (Figure 4.6b). On the other hand, the PBIAS values evidenced some overestimation of the measured data (negative values) in most of the Spanish hydrometric stations during both calibration and validation, which were not so relevant since average flows were relatively small at these locations (0.17 to 4.60 $m^3 s^{-1}$). For the hydrometric stations in Portugal, model simulations resulted in smaller over- or under-predictions of the measured streamflow, but no spatial trend was noticed (Figure 4.7). Exceptions were the streamflow estimates in Ponte Algalé and Monte dos Fortes where a larger bias was found.

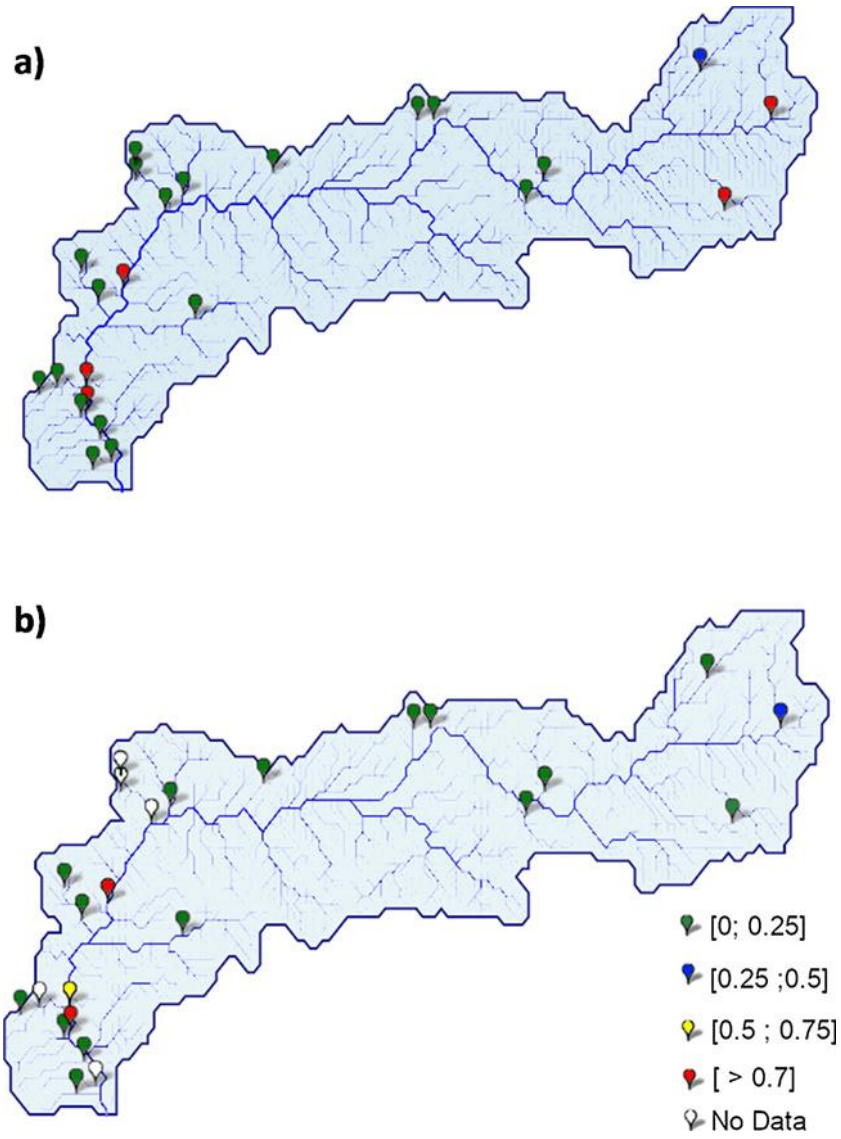

Figure 4.6 Spatial distribution of the normalized root mean square error (NRMSE) values during calibration (a) and validation (b).

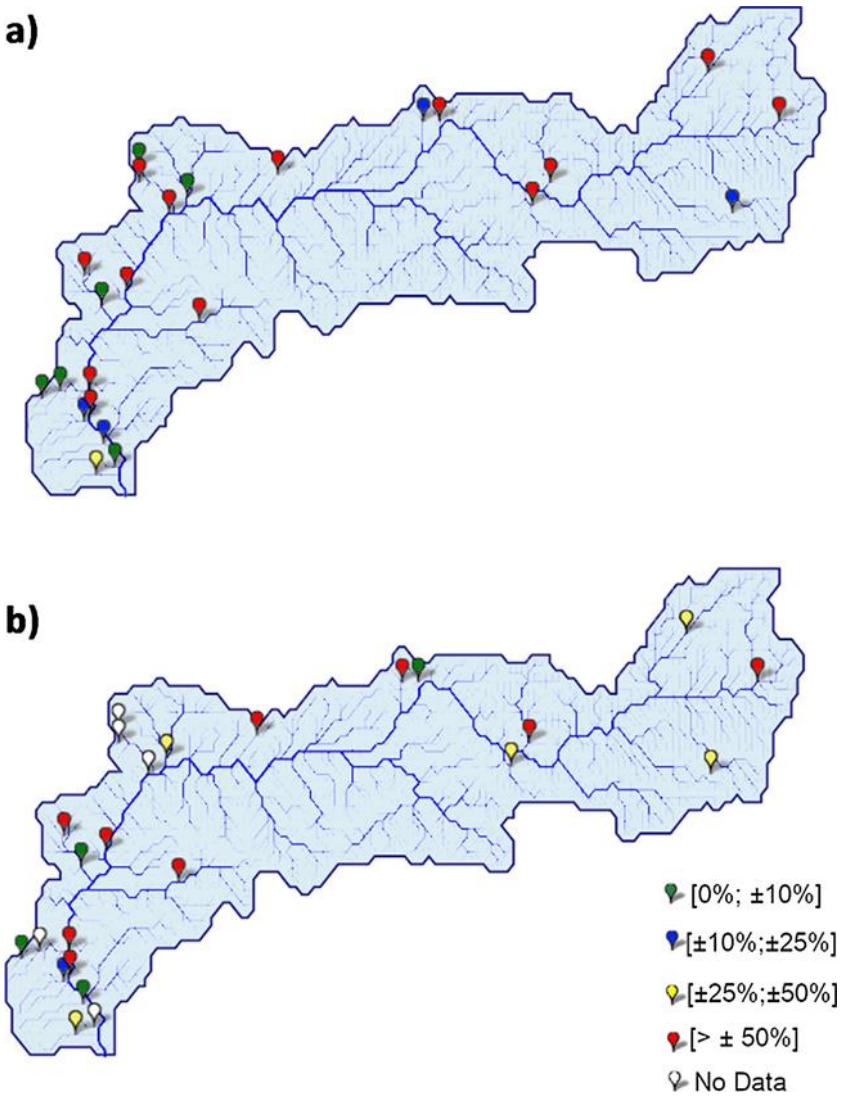

Figure 4.7 Spatial distribution of the percent bias (PBIAS) values during calibration (a) and validation (b).

Finally, the NSE modeling efficiency values were relatively high (NSE ≥ 0.75) for 7 of 15 hydrometric stations considered during calibration (Figure 4.8a), indicating that the residual variance was much smaller than the measured data variance. Most of those stations were in the lower region of the Guadiana catchment, while for the upper region results showed that the measured averages were a more reliable predictor than model simulations. Similar results were found during validation (Figure 4.8b).

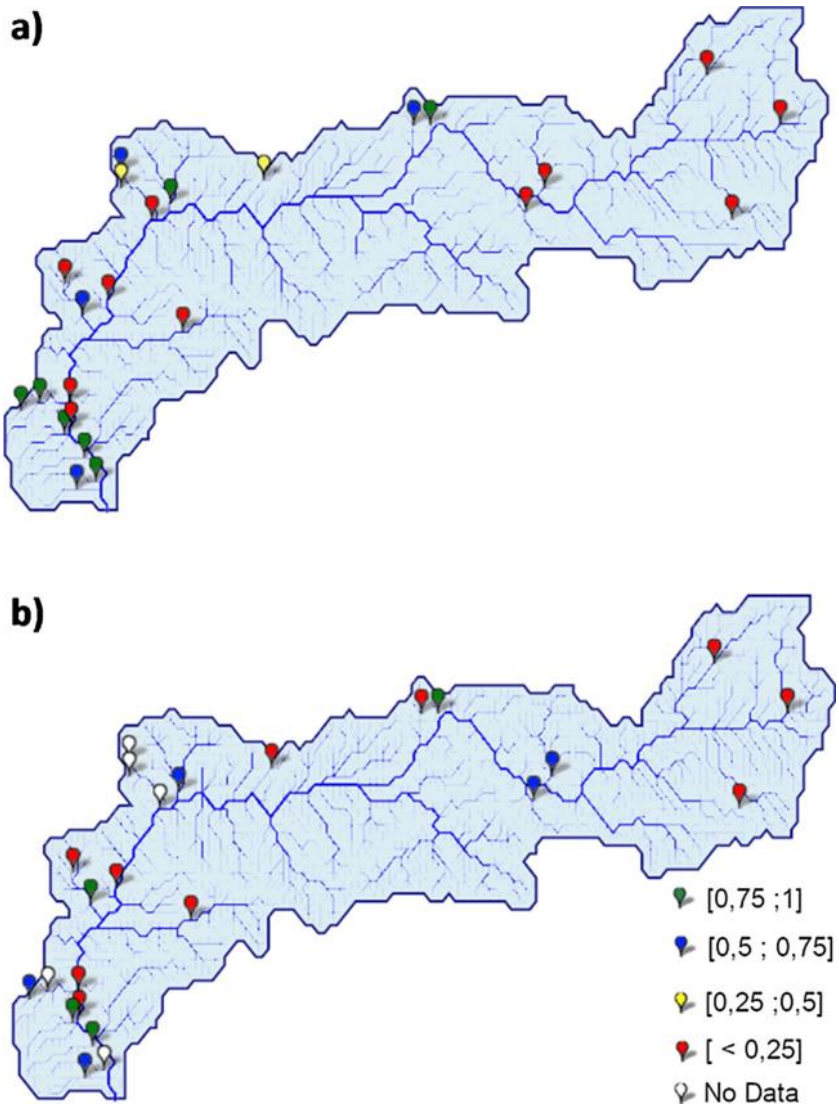

Figure 4.8 Spatial distribution of the modelling efficiency (NSE) values during calibration (a) and validation (b).

The model systematically failing in delivering accurate estimates of streamflow in the upper Guadiana was associated with the large groundwater abstractions in the region, which were not accounted for in model simulation (Conan et al., 2003; Kilsby et al., 2007). For example, Bromley et al., 2010, reported considerable annual groundwater discharge rates (from 200 to 688 $hm^3 y^{-1}$) from the West La Mancha aquifer during a period of unrestrained irrigation expansion from 1974 to 1988. Nevertheless, while the MOHID-Land model was not able to accurately simulate streamflow in all hydrometric stations located upstream the reservoirs considered in this application, results were very satisfactory for most of the locations under analysis. Note that contrarily to Guerreiro et al. (2017), who considered only a small sub-basin for calibrating/validating model predictions for the entire Guadiana basin, the MOHID-Land model performance was here assessed considering the entire extent of the catchment, thus

accounting for the different land uses, soils, slopes, and rainfall patterns found throughout the basin.

4.3.2.2 Streamflow simulations influenced by reservoir management

The goodness-of-fit indicators obtained by comparing streamflow measurements in hydrometric stations influenced by reservoir management and the MOHID-Land simulations are presented in Table 6. These monitoring stations were naturally located down-stream some reservoirs (Figure 4.3), with reservoir operation deeply modifying the flow regime. Globally, results were much worse than those presented for the scenario without reservoir management, with the MOHID-Land model failing to reproduce streamflow measurements in most stations. Exceptions were the 4255 and Amieira stations in Spain and Portugal, respectively (Figure 4.5-8). In these locations, all statistical indicators showed a relatively good agreement between model results and measured data ($R^2 \geq 0.72$; NRMSE ≤ 0.05; PBIAS $\leq 33.9\%$; and NSE ≥ 0.6). Figure 4.4 further gives an example of the flow-duration curve for the Amieira station. For the remaining hydrometric stations, the model always overestimated measured flows as seen by the large negative values of the PBIAS (Table 6). This constituted the main problem in this modeling application since measured streamflow were higher (range from 1.01 to 145.8 $m^3 s^{-1}$) than those registered in the hydrometric stations located upstream reservoir management (range from 0.17 to 4.60 $m^3 s^{-1}$). For the stations located in the main riverbed (Rocha da Galé, Pulo do Lobo, and Ponte Mourão), streamflow simulations even produced unrealistic estimates (> 1688 $m^3 s^{-1}$). Thus, the erroneous predictions found for the stations influenced by reservoir management posed here as the main obstacle to an accurate computation of the catchment water balance, in line with all previous modeling applications in the Guadiana River (Brandão and Rodrigues, 2000; Conan et al., 2003; Kilsby et al., 2007; Guerreiro et al., 2017).

Table 4.6 Goodness-of-fit indicators obtained during calibration and validation (in brackets) of monthly streamflow simulations in hydrometric stations influenced by reservoir management.

Hydrometric station	Records (years)	Average flow measured ($m^3 s^{-1}$)	Average flow simulated ($m^3 s^{-1}$)	R^2 (−)	NRMSE (−)	PBIAS (%)	NSE (−)
4174	9.8 (-11.3)	2.03 (3.84)	7.87 (11.98)	0.01 (0.01)	0.20 (0.12)	−287.3 (−212.1)	−3.72 (−1.01)
4214	6.0 (-16)	1.49 (5.37)	5.19 (8.75)	0.65 (0.72)	0.18 (0.04)	−248.3 (−62.8)	−1.35 (0.65)
4255	8.8 (-17)	5.66 (12.45)	6.17 (8.24)	0.82 (0.71)	0.04 (0.04)	−9.0 (33.9)	0.81 (0.60)
Vendinha	10.0 (-5.1)	1.01 (1.80)	2.71 (5.27)	0.85 (0.81)	0.08 (0.20)	−168.5 (−193.4)	0.21 (−1.54)
Rocha da Galé	10.0 (-5.0)	51.74 (49.74)	1799.94 (1906.28)	0.82 (0.71)	1.09 (1.39)	−3379.1 (−3732.8)	−139.76 (−112.83)
Pulo do Lobo	9.2 (-4.9)	58.68 (145.80)	1783.62 (1940.42)	0.76 (0.86)	0.99 (0.74)	−2939.6 (−1330.9)	−114.29 (−31.91)

Hydrometric station	Records (years)	Average flow measured ($m^3 s^{-1}$)	Average flow simulated ($m^3 s^{-1}$)	R^2 (−)	NRMSE (−)	PBIAS (%)	NSE (−)
Ponte Mourão	10.0 (-5.5)	38.96 (90.29)	1688.36 (1750.75)	0.52 (0.68)	1.57 (1.09)	−4233.1 (−1839.0)	−292.35 (−78.33)
Monte da Vinha	8.4 (−)	22.26 (−)	83.78 (−)	0.74 (−)	0.24 (−)	−276.5 (−)	−4.96 (−)
Amieira	8.9 (-6.1)	4.29 (9.30)	4.01 (8.65)	0.87 (0.82)	0.05 (0.05)	6.6 (7.0)	0.71 (0.79)

Figure 4.9 compares the scenarios with and without reservoirs at Amieira, 4255, and Monte da Vinha stations. Monte da Vinha was added to the figure to better explain the differences between both scenarios despite results were not validated at that location by the statistical indicators (Table 4.6). In general, the further downstream the station was located, the greater the departure between the two simulations. Streamflow at Amieira ended up being slightly influenced by reservoir management due to the size of the Monte Novo (15.3 hm^3) and Vigia (16.5 hm^3) upstream reservoirs. At 4255, the two simulations started departing after January 1996 when the Peña del Águila reservoir (130 hm^3) began operating, affecting mostly streamflow peaks. Monte da Vinha showed the greatest difference between the two simulations, but as consumptions were not considered in the modeling approach the differences between the two scenarios remained small.

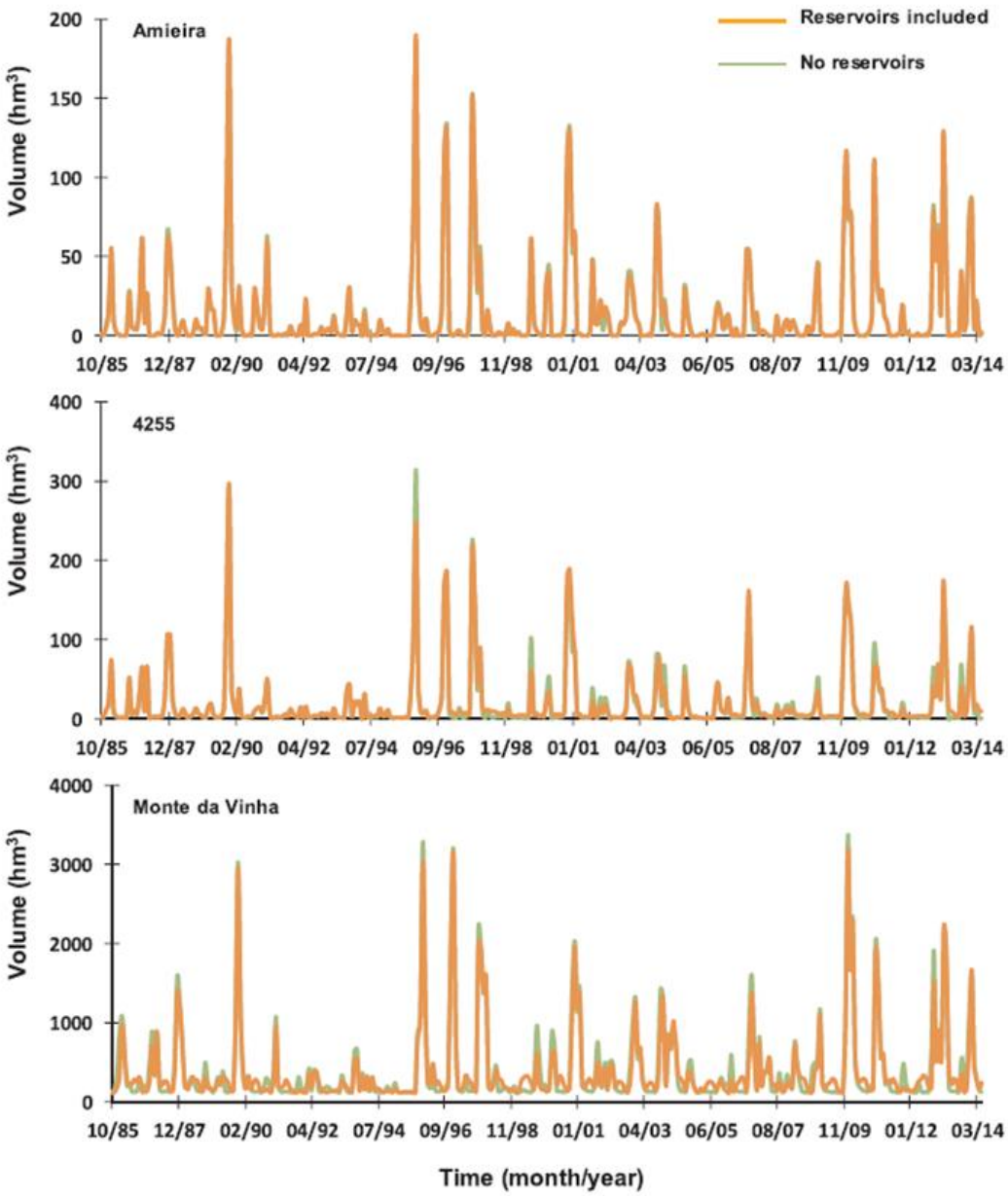

Figure 4.9 Streamflow simulations considering (or not) reservoir management at three locations (Amieira, 4255, and Monte da Vinha hydrometric stations).

4.3.3 About model predictions

Fully distributed models such as MOHID-Land are usually considered to provide improved predictions of streamflow along the river network of a catchment while also accounting for the spatial dynamics of evapotranspiration, soil moisture content, water quality, soil erosion, and land use change impacts (Yilmaz et al., 2008; Fatichi et al., 2016). Yet, their spatial complexity often limits the proper identification of model parameters, translating into significant predictive uncertainty in the simulation results (Beven and Freer, 2001). Model parameters are typically derived from soil and land use datasets or inferred from spatiotemporal data. These parameters mostly result from relationships derived from small-scale applications,

being embedded into larger-scale model grids without proper accounting for heterogeneity, emergent processes, scaling, and interactions across scales (Reed et al., 2004; Yilmaz et al., 2008; Fatichi et al., 2016).

This modeling application adopted a simple trial-and-error procedure for calibrating streamflow. A series of techniques (e.g., data mining, machine learning, and inverse optimization) exist that can be used to further optimize model parameters, but which require a considerable effort if implemented in MOHID-Land. Despite that, model uncertainty can still be associated with different causes, including errors related to field measurements, and to model input and model structure errors.

4.3.3.1 Field measurements

Streamflow measurements were obtained from public datasets used to monitor the Guadiana flow regime in both Portugal (SNIRH, 2019) and Spain (CEH-CEDEX, 2019). Those values are usually not directly measured but converted from water level (known as "stage") time series through a stage-discharge model (known as rating curve). This in turn is derived using paired stage and discharge measurements occasionally observed in the field. Horner et al. (2018) discussed the general sources of error for stage measurements, with these being site specific and associated with the channel characteristics, the information available to build the rating curve, the station management, the time interval at which streamflow data are averaged, and the streamflow range. Those authors further adverted for the fact that while stage measurement errors are generally overlooked, they may well be more substantial for hydrometric stations characterized by low flow depths such as those in the Guadiana catchment (catchments in arid/ semiarid environments). Additionally, the CADC (2017) minutes refer the need for harmonizing the measurement procedures in both Portugal and Spain as readings from some hydrometric stations are sometimes inconsistent with others available nearby.

4.3.4 Model inputs

Parameter uncertainty was associated with soil, land use, and rainfall data. Detailed soil maps are rare in most regions of the world, and soil information is even scarcer when referring to soil hydraulic properties. Pedotransfer functions are thus presented as the best possible solution for characterizing soil heterogeneity at the catchment scale since direct measurements are impractical due to the associated costs (Van Looy et al., 2017). The pedotransfer functions adopted in this study (Wösten et al., 1999) provided only a very simplified representation of soil variability by considering a set of soil hydraulic parameters for each textural class. Likewise, past applications of the MOHID-Land model (e.g., Brito et al., 2015, 2017) adopted

the same functions for characterizing soil variability. Recently, Montzka et al. (2017) and Tóth et al. (2016) developed soil hydraulic grid maps (250 m – 1 km) for different layers that may better describe soil heterogeneity, and that should provide the basis for improving soil hydraulic characterization in future catchment scale applications of the MOHID-Land model. A functional evaluation of those maps is thus required to better understand their usefulness to catchment scale modelling.

Uncertainty related to land use was mostly associated with vegetation growth stages. The corresponding set of model parameters impact directly evapotranspiration fluxes and respective partitioning into soil evaporation and crop transpiration. Ramos et al. (2018), showed the importance of an accurate description of vegetation growth, particularly the LAI curve, on estimates of the soil water balance at the plot scale. They further described the impact of assimilation of LAI data derived from Landsat 8 imagery on MOHID-Land simulations. The main conclusion was that modeling vegetation growth at the regional scale cannot depend solely on inputs from the LAI data assimilation because estimates may diverge substantially from the reality, thus confirming the need to use a proper data set for calibration. Nevertheless, the sensitivity analysis performed in this study failed to demonstrate vegetation growth as relevant for streamflow simulations, meaning that the impact of those parameters on final model results was only minor.

Finally, the SAFRAN dataset (Quintana-Seguí et al., 2017) was used for defining the atmosphere boundary conditions of the simulation domain. As the only water input considered in the modeling application, deviations between measured and simulated discharges were highly dependent on the quality of the rainfall inputs provided by that data. Limitations have been reported in Quintana-Seguí et al. (2017) and include: the existence of artificial discontinuities at the borders of the climatically homogeneous zones; the overestimation of the number of rainfall days as the model generates rainfall for a whole climatically homogeneous zone once there is a localized rainfall event in some of the stations within, thereby wrongly assigning the event to unaffected stations; and missing of high rainfall (or localized) events as the model tends to average the values of all stations in a zone. The impact of these errors on model results needs thus to be quantified, for example, by comparing streamflow simulations using different weather datasets.

4.3.4.1 Model structure errors

The MOHID-Land model was implemented using a relatively coarse grid (5 km × 5 km), which was defined considering the length of the simulation period, quality of results, and

computational speed. While that grid size was similar to Guerreiro et al., 2017, much detail was inevitably lost when converting model inputs into the grid. The impact of such losses on final model results was not assessed but streamflow simulations should expectably improve when adopting smaller grid scales as seen in other MOHID-Land applications (Oliveira et al., 2020).

While the MOHID-Land model is generically a physically based model that solves mass and momentum conservation equations for simulating landscape processes, water infiltration and surface runoff were here computed using a semi-empirical approach with the intention of simplifying the description of the simulated processes and increasing computation speed. Limitations on using the CN method for simulating such processes are well documented in Boughton (1989) and Eli and Lamont (2010), which among other critics include the systematic underestimation of runoff discharge peaks when compared with other approaches (e.g., the Green-Ampt method).

The modeling approach was also limited by not properly defining the K_c values according to the vegetation growth stages (Allen et al., 1998), systematically over or underestimating evapotranspiration in the catchment throughout the simulation period. Groundwater extractions were also not included as such information was not available with enough detail. Furthermore, irrigation was absent, but if considered would likely modify flow paths and impact the comparison of modeled and simulated streamflow. Finally, water evaporation from reservoirs was not accounted for, likely having some impact on the computation of the catchment water balance. Still, the modeling limitation that most affected model performance was not doubly related to reservoir management. On one hand, better operation rules than those given in Table 4.2 need to be defined in the MOHID-Land model for properly estimating reservoir discharge in the absence of measured data. On the other hand, the information related to reservoir discharge and consumption needs to be improved to be included in model simulations with greater detail. In this study, reservoir outflows imposed in the Portuguese reservoirs accounted for many data limitations as information was not available for the entire simulation period (SNIRH, 2019). For the Spanish reservoirs, the available information on reservoir outflows and consumptions was aggregated into one unique time series (CEH-CEDEX, 2019), obviously increasing uncertainty with the assumptions that need to be made for partitioning that data. As in this study no partitioning was considered, simulated streamflow values were inevitably higher than actual discharge values.

4.4 Conclusions

This modeling application showed the usefulness of the MOHID-Land model in simulating streamflow at hydrometric stations not influenced by reservoir management, but also the inherent limitations by not considering relevant processes such as groundwater abstractions to the accurate prediction of the Guadiana River flow regime. For the hydrometric stations located downstream reservoir management, model simulations were generally poor as the agreement with measured streamflow was dependent on reservoir discharge rather than the basic physical processes (evapotranspiration, water infiltration, soil storage, and so on) describing landscape heterogeneity. Hence, information on groundwater abstractions and reservoir management (discharges, consumptions) needs to be made available with greater detail for the better development of water management tools, including fully-distributed models like MOHID-Land. In the end, the accurate quantification of streamflow in Guadiana as well as in other transitional catchments can only benefit local water authorities and reduce potential conflicts in a context of enhanced water scarcity.

Funding

This study was performed within the Project AGUAMOD (Development of a water resource management platform during low water periods in the SUDOE region; SOE1/P5/F0026; http://www.aguamod-sudoe.eu/en/). MARETEC acknowledges the national funds from Fundação para a Ciência e Tecnologia (UID/EEA/50009/2019). T. B. Ramos was supported by contract CEECIND/01152/2017.

4.5 References

Agência Portuguesa do Ambiente (APA-RH7). Plano de Gestão da Região Hidrográfica do Guadiana (RH7) (2016/2021). Parte 2-Caracterização e Diagnóstico. 2016. Available online: https://apambiente.pt/agua/2o-ciclo-de-planeamento-2016-2021 (accessed on 20 November 2018).

Agência Portuguesa do Ambiente. Ministério do Ambiente e da Transição Energética, Lisboa, Portugal.

Allen, R.G.; Pereira, L.S.; Raes, D.; Smith, M. Crop Evapotranspiration—Guidelines for Computing Crop Water Requirements; Irrigation & Drainage Paper 56; FAO: Rome, Italy, 1998.

American Society of Civil Engineers (ASCE). Hydrology Handbook Task Committee on Hydrology Handbook; II Series, GB 661.2. H93; ASCE: Reston, VA, USA, 1996; pp. 96–104.

Andreadis, K.M.; Schumann, G.J.P.; Pavelsky, T. A simple global river bankfull width and depth database. Water Resour. Res. 2013, 49, 7164–7168. https://doi.org/10.1002/wrcr.20440

AQUASTAT, 2019. AQUASTAT website. Food and Agriculture Organization of the United Nations. Available online: http://www.fao.org/nr/water/aquastat/data/query/index.html?lang=en (accessed on 7 June 2019).

Beven, K.; Freer, J. Equifinality, data assimilation, and uncertainty estimation in mechanistic modelling of complex environmental systems. J. Hydrol. (Amst) 2001. 249, 11–29. https://doi.org/10.1016/S0022-1694(01)00421-8

Boughton, W.C. A review of the USDA SCS curve number method. Soil Res. 1989, 27, 511–523. https://doi.org/10.1071/SR9890511

Brandão, C.; Rodrigues, R. Hydrological simulation of the international catchment of Guadiana River. Phys. Chem. Earth 2000 25, 329–339. https://doi.org/10.1016/S1464-1909(00)00023-X

Brito, D.; Campuzano, F.J.; Sobrinho, J.; Fernandes, R.; Neves, R. Integrating operational watershed and coastal models for the Iberian Coast: watershed model implementation—a first approach. Estuar. Coast. Shelf Sci. 2015, 167, 138–146. https://doi.org/10.1016/j.ecss.2015.10.022

Brito, D.; Neves, R.; Branco, M.C.; Gonçalves, M.C.; Ramos, T.B. Modeling flood dynamics in a temporary river draining to an eutrophic reservoir in southeast Portugal. Environ. Earth Sci. 2017, 76, 377. https://doi.org/10.1007/s12665-017-6713-7

Brito, D.; Ramos, T.B.; Gonçalves, M.C.; Morais, M.; Neves, R. Integrated modelling for water quality management in a eutrophic reservoir in south-eastern Portugal. Environ. Earth Sci. 2018, 77, 40. https://doi.org/10.1007/s12665-017-7221-5

Bromley, J.; Cruces, J.; Acreman, M.; Martínez, L.; Llamas, M.R. Problems of sustainable groundwater management in an area of over-exploitation: the upper Guadiana

catchment, Central Spain. Int. J. Water Resour. Dev. 2010, 17 (3), 379–396. https://doi.org/10.1080/07900620120065156

CADC. Acta Da XX Reunião Plenária Da Comissão Para a Aplicação E Desenvolvimento Da Convenção. 2017. Available online: http://www.cadc-albufeira.eu/pt/documentos/ (accessed on 1 July 2019).

CEH-CEDEX. Centro de estudios y experimentación de obras públicas. Ministerio Do Fomento E Ministerio Para La Transición Ecológica, Spain. 2019. Available online: http://www.cedex.es/CEDEX/lang_castellano/ (accessed on 25 April 2019).

Confederação Hidrográfica do Guadiana. Plano Hidrológico da Região Hidrográfica Do Guadiana (ciclo 2015-2021) E Plano De Gestão Do Risco De Inundação. Esquema Para O Desenvolvimento Do Estudo Ambiental Estratégico. Anexo nº4 – Resumem Não Técnico. 2014. Região Hidrográfica Do Guadiana. Ministério de Medio Ambiente Y Medio Rural Y Marino, España.

Conan, C.; de Marsily, G.; Bouraoui, F.; Bidoglio, G. A long-term hydrological modelling of the Upper Guadiana River basin (Spain). Phys. Chem. Earth 2003, 28, 193–200. https://doi.org/10.1016/S1474-7065(03)00025-1

Copernicus Land Monitoring Service. Corine Land Cover 2012. European Environmental Agency. 2019. Available online: https://land.copernicus.eu/pan-european/corine-land-cover/clc-2012 (accessed on 24 April 2019).

Do Ó, A. Drought planning and management in transboundary river basins: the case of the Iberian Guadiana. Water Policy 2012, 14, 784–799. https://doi.org/10.2166/wp.2012.173

EDIA, 2019. Empresa De Desenvolvimento E Infraestruturas Do Alqueva. Beja, Portugal. Available online: http://www.edia.pt/en/ (accessed on 17 April 2019).

El-Nasr, A.A.; Arnold, J.G.; Feyen, J.; Berlamont, J. Modelling the hydrology of a catchment using a distributed and a semi-distributed model. Hydrol. Process. 2005, 19, 573–587. https://doi.org/10.1002/hyp.5610

Eli, R.N.; Lamont, S. Curve numbers and urban runoff modeling – application limitations. In: Low Impact Development International Conference. San Francisco, California. 2010. https://doi.org/10.1061/41099(367)36

EUROSTAT, 2019. European Commission. Available online: https://ec.europa.eu/eurostat/home (accessed on 17 April 2019).

Ewen, J.; Parkin, G.; O'Connell, P.E. SHETRAN: distributed river basin flow and transport modelling system. ASCE J. Hydrol. Eng. 2000, 5, 250–258. https://doi.org/10.1061/(ASCE)1084-0699(2000)5:3(250)

FAO/IIASA/ISRIC/ISS-CAS/JRC. Harmonized World Soil Database (version 1.1). FAO, Rome, Italy and IIASA, Laxenburg, Austria, 2009.

Fatichi, S.; Vivoni, E.R.; Ogden, F.L.; Ivanov, V.Y.; Mirus, B.; Gochis, D.; Downer, C.W.; Camporese, M.; Davidson, J.H.; Ebel, B.; et al. An overview of current applications, challenges and future trends in distributed process-based models in hydrology. J. Hydrol. (Amst) 2016, 537, 45–60. https://doi.org/10.1016/j.jhydrol.2016.03.026

Feddes, R.A.; Kowalik, P.J.; Zaradny, H. Simulation of Field Water Use and Crop Yield; Wiley: Hoboken, NJ, USA, 1978.

Glaser, B.; Jackisch, C.; Hopp, L.; Klaus, J. How meaningful are plot-scale observations and simulations of preferential flow for catchment models? Vadose Zone J. 2019, 18, 180146. https://doi.org/10.2136/vzj2018.08.0146

Guerreiro, S.B.; Birkinshaw, S.; Kilsby, C.; Fowler, H.J.; Lewis, E. Dry getting drier – the future of transnational river basins in Iberia. J. Hydrol: Reg. Studies 2017, 12, 238–252. https://doi.org/10.1016/j.ejrh.2017.05.009

Horner, I.; Renard, B.; Le Coz, J.; Branger, F.; McMillan, H.K.; Pierrefeu, G. Impact of stage measurement errors on streamflow uncertainty. Water Resour. Res. 2018, 54, 1952–1976. https://doi.org/10.1002/2017WR022039

IM, AEMET, 2011. Iberian Climate Atlas. Air Temperature and Precipitation (1971-2000). Instituto de Meteorologia de Portugal and Agência Estatal de Meteorologia de España ISBN: 978-84-7837-079-5.

Im, S.; Him, H.; Kim, C.; Jang, C. Assessing the impacts of land use changes on watershed hydrology using MIKE SHE. Environ. Geol. 2009, 57, 231–239. https://doi.org/10.1007/s00254-008-1303-3

IUSS Working Group. World Reference Base for Soil Resources 2014. International Soil Classification System for Naming Soils and Creating Legends for Soil Maps. World Soil Resources Reports No. 106, FAO, Rome, Italy, 2004.

Kilsby, C.G.; Tellier, S.S.; Fowler, H.J.; Howels, T.R. Hydrological impacts of climate change on the Tejo and Guadiana Rivers. Hydrol. Earth Syst. Sci. Discuss. 2007, 11, 1175–1189. https://doi.org/10.5194/hess-11-1175-2007

Legates, D.R.; McCabe Jr.; G.J. Evaluating the use of goodness-of-fit measures in hydrologic and hydroclimatic model validation. Water Resour. Res. 1999, 35, 233–241. https://doi.org/10.1029/1998WR900018

Loucks, D.P.; French, P.N.; Taylor, M.R. IRAS — Interactive River-Aquifer Simulation: Program Description and Operation. Resources Planning Associates, Incorporated, Ithaca, NY, USA, 1995.

Lorenzo-Lacruz, J.; Morán-Tejeda, E.; Vicente-Serrano, S.M.; López-Moreno, J.I. Streamflow droughts in the Iberian Peninsula between 1945 and 2005: spatial and temporal patterns. Hydrol. Earth Syst. Sci. Discuss. 2013, 17, 119–134. https://doi.org/10.1029/1998WR900018

McMichael, C.E.; Hope, A.S.; Loaiciga, H.A. Distributed hydrological modelling in California semi-arid shrublands: MIKE SHE model calibration and uncertainty estimation. J. Hydrol. (Amst) 2006, 317, 307–324. https://doi.org/10.1016/j.jhydrol.2005.05.023

Montzka, C.; Herbst, M.; Weihermüller, L.; Verhoef, A.; Vereecken, H. A global data set of soil hydraulic properties and sub-grid variability of soil water retention and hydraulic conductivity curves. Earth Syst. Sci. Data Discuss. 2017, 9, 529–543. https://doi.org/10.5194/essd-9-529-2017

Moriasi, D.N.; Arnold, J.G.; Van Liew, M.W.; Bingner, R.L.; Harmel, R.D.; Veith, T.L. Model evaluation guidelines for systematic quantification of accuracy in watershed simulations. Trans. ASABE 2007, 50, 885–900. https://doi.org/10.13031/2013.23153

Mualem, Y. A new model for predicting the hydraulic conductivity of unsaturated porous media. Water Resour. Res. 1976, 12, 513–522. https://doi.org/10.1029/WR012i003p00513

Nash, J.E.; Sutcliffe, J.V. River flow forecasting through conceptual models: part 1. A discussion of principles. J. Hydrol. (Amst) 1970, 10 (3), 282–290. http://dx.doi.org/10.1016/0022-1694(70)90255-6

Neal, J.C.; Odoni, N.A.; Trigg, M.A.; Freer, J.E.; Garcia-Pintado, J.; Mason, D.C.; Wood, M.; Bates, P.D. Efficient incorporation of channel cross-section geometry uncertainty into

regional and global scale flood inundation models. J. Hydrol. (Amst) 2015, 529, 169–183. https://doi.org/10.1016/j.jhydrol.2015.07.026

Neitsch, S.L.; Arnold, J.G.; Kiniry, J.R.; Williams, J.R. Soil and Water Assessment Tool. Theoretical Documentation, Version 2009. Texas Water Resources Institute. Technical Report nº 406. Texas A&M University System, College Station, Tx, 2011.

Oliveira, A. R.; Ramos, T. B.; Simionesei, L.; Pinto, L.; Neves, R. Sensitivity analysis of the MOHID-Land hydrological model: a case study of the Ulla River basin. Water, 2020, 12(11), 3258. https://doi.org/10.3390/w12113258

Paulo, A.A.; Rosa, R.D.; Pereira, L.S. Climate trends and behaviour of drought indices based on precipitation and evapotranspiration in Portugal. Nat. Hazards Earth Syst. Sci. Discuss. 2012, 12, 1481–1491. https://doi.org/10.5194/nhess-12-1481-2012

Quintana-Seguí, P.; Turco, M.; Herrera, S.; Miguez-Macho, G. Validation of a new SAFRAN-based gridded precipitation product for Spain and comparisons to Spain02 and ERA-Iterim. Hydrol. Earth Syst. Sci. Discuss. 2017, 21, 2187–2201. https://doi.org/10.5194/hess-21-2187-2017

Rabus, B.; Eineder, M.; Roth, A.; Bamler, R. The shuttle radar topography mission – a new class of digital elevation models acquired by spaceborne radar. ISPRS J. Photogramm. 2003, 57, 241–262. https://doi.org/10.1016/S0924-2716(02)00124-7

Ramos, T.B.; Simionesei, L.; Jauch, E.; Almeida, C.; Neves, R. Modelling soil water and maize growth dynamics influenced by shallow groundwater conditions in the Sorraia Valley region, Portugal. Agric. Water Manag. 2017, 185, 27–42. https://doi.org/10.1016/j.agwat.2017.02.007

Ramos, T.B.; Simionesei, L.; Oliveira, A.R.; Darouich, H.; Neves, R. Assessing the impact of LAI data assimilation on simulations of the soil water balance and maize development using MOHID-Land. Water 2018, 10, 1367. https://doi.org/10.3390/w10101367

Reed, S.; Koren, V.; Smith, M.; Zhang, Z.; Moreda, F.; Seo, D. Overall distributed model intercomparison project results. J. Hydrol. (Amst) 2004, 298 (1–4), 27–60. https://doi.org/10.1016/j.jhydrol.2004.03.031

Ritchie, J.T. Model for predicting evaporation from a row crop with incomplete cover. Water Resour. Res. 1972, 8, 1204–1213. https://doi.org/10.1029/WR008i005p01204

Searcy, J.K. Flow-duration curves. In: Pecora, W.T. (Ed.), Manual of Hydrology: Part 2, Low-Flow Techniques. U.S. Government Printing Officice. USDA, Washington, D.C., 1959.

Simionesei, L.; Ramos, T.B.; Oliveira, A.R.; Jongen, M.; Darouich, H.; Weber, K.; Proença, V.; Domingos, T.; Neves, R. Modeling soil water dynamics and pasture growth in the montado ecosystem using MOHID-Land. Water 2018, 10, 489. https://doi.org/10.3390/w10040489

Šimůnek, J.; Hopmans, J.W. Modeling compensated root water and nutrient uptake. Ecol. Modell. 2009, 220, 505–521. https://doi.org/10.1016/j.ecolmodel.2008.11.004

Skaggs, T.H.; van Genuchten, M.Th.; Shouse, P.J.; Poss, J.A. Macroscopic approaches to root water uptake as a function of water and salinity stress. Agric. Water Manag. 2006, 86, 140–149. https://doi.org/10.1016/j.agwat.2006.06.005

SNIRH, 2019. Serviço Nacional De Informação Dos Recursos. Agência Portuguesa do Ambiente, Lisboa, Portugal. Available online: https://snirh.apambiente.pt/ Hídricos (accessed on 25 April 2019)

Tóth, B.; Weynants, M.; Pásztor, L.; Hengl, T. 3D soil hydraulic database of Europe at 250 m resolution. Ecohydrology 2016, 31, 2662–2666. https://doi.org/10.1002/hyp.11203

Trancoso, A.R.; Braunschweig, F.; Chambel Leitão, P.; Obermann, M.; Neves, R. An advanced modelling tool for simulating complex river systems. Sci. Total Environ. 2009, 407, 3004–3016. https://doi.org/10.1016/j.scitotenv.2009.01.015

USDA U.S. National Engineering Handbook. Section 4, Design Hydrographs; U.S. Department of Agriculture, Soil Conservation Service: Washington, DC, USA, 1972.

van der Sande, C.J.; de Jong, S.M.; de Roo, A.P.J. A segmentation and classification approach of IKONOS-2 imagery for land cover mapping to assist flood risk and flood damage assessment. Int. J. Appl. Earth Obs. Geoinf. 2003, 4, 217–229. https://doi.org/10.1016/S0303-2434(03)00003-5

van Genuchten, M.T. A Closed-form Equation for Predicting the Hydraulic Conductivity of Unsaturated Soils. Soil Sci. Soc. Am. J. 1980, 44, 892–898. https://doi.org/10.2136/sssaj1980.03615995004400050002x

van Looy, K.; Bouma, J.; Herbst, M.; Koestel, J.; Minasny, B.; Mishra, U.; Montzka, C.; Nemes, A.; Pachepsky, Y.A.; Padarian, J.; Schaap, M.G.; Tóth, B.; Verhoef, A.; Vanderborght, J.; van der Ploeg, M.J.; Weihermüller, L.; Zacharias, S.; Zhang, Y.;

Vereecken, H. Pedotransfer functions in earth system science: challenges and perspectives. Rev. Geophys. 2017, 55, 1199–1256. https://doi.org/10.1002/2017RG000581

Vicente-Serrano, S.M. Spatial and temporal analysis of droughts in the Iberian Peninsula (1910–2000). Hydrol. Sci. J. Des Sci. Hydrol. 2006, 51, 83–97. https://doi.org/10.1623/hysj.51.1.83

Williams, J.R.; Jones, C.A.; Kiniry, J.R.; Spanel, D.A. The EPIC crop growth model. Trans. Asae 1989, 32, 497–511. https://doi.org/10.13031/2013.31032

Wösten, J.H.M.; Lilly, A.; Nemes, A.; Le Bas, C. Development and use of a database of hydraulic properties of European soils. Geoderma 1999, 90, 169–185. https://doi.org/10.1016/S0016-7061(98)00132-3

WWAP (UNESCO World Water Assessment Programme). The United Nations World Water Development Report 2019: Leaving No One Behind. UNESCO, Paris, 2019.

Yilmaz, K.K.; Gupta, H.V.; Wagener, T. A process-based diagnostic approach to model evaluation: application to the NWS distributed hydrologic model. Water Resour. Res. 2008, 44, W09417. https://doi.org/10.1029/2007WR006716

5 Sensitivity Analysis of the MOHID-Land Hydrological Model: A Case Study of the Ulla River Basin

Authors: Ana R. Oliveira, Tiago B. Ramos, Lucian Simionesei, Lígia Pinto and Ramiro Neves

Centro de Ciência e Tecnologia do Ambiente e do Mar (MARETEC-LARSyS), Instituto Superior Técnico, Universidade de Lisboa, Av. Rovisco Pais, 1, 1049-001 Lisboa, Portugal

Published in: Water, 2020, 12 (11): 3258 (https://doi.org/10.3390/w12113258), **Impact Factor:** 3.53

Abstract

Hydrological models are increasingly used for studying watershed behavior and its response to past and future events. The main objective of this study was to conduct a sensitivity analysis of the MOHID-Land model and identify the most relevant parameters/processes influencing river flow generation. MOHID-Land is a complex, physically based, three-dimensional model used for catchment-scale applications. A reference simulation was implemented in the Ulla River watershed, northwestern Spain. The sensitivity analysis focused on sixteen parameters/processes influencing water dynamics at that scale. River flow generation was influenced by the resolution of the simulation grid, soil water infiltration, and crop evapotranspiration. Baseflow was affected by soil hydraulic properties, the depth of the soil profile, and the dimensions of the river cross-sections. Peak flows were mostly constrained by Manning's coefficient in the river network, as well as the dimensions of the river cross-sections. The MOHID-Land model was then used to simulate daily streamflow during a 10-year period (2008−2017). Model simulations were compared against measured data at four hydrometric stations characterizing the natural flow regime of the Ulla River, resulting in coefficients of determination (R^2) from 0.56 to 0.85; ratios of the standard deviation of the root mean square error to observation (RSR) between 0.4 and 0.67, and Nash and Sutcliffe model efficiency (NSE) values ranging from 0.55 to 0.84. The MOHID-Land model thus has the capacity to reproduce watershed behavior at a daily scale with reliable accuracy, constituting a powerful tool to improve water governance at the watershed scale.

Keywords: MOHID-Land; physical model; sensitivity analysis; calibration; validation; river flow

5.1 Introduction

Hydrological models are, similar to any other model, a simplified representation of the "real-world" system (Wheater et al, 2007). They are usually used for two main purposes: to predict future events and to better understand different hydrological processes (Devia et al., 2015). Hydrological models can be classified considering their complexity (Sitterson et al., 2017). Empirical models are the simplest, characterized by linear and non-linear equations relating inputs and outputs without fully representing the physical processes occurring in the catchment. Conceptual models are of intermediate complexity, based on simplified equations that describe the watershed's water balance. Finally, the most complex are physical models, which are governed by laws and equations based on real hydrological responses. These models use finite difference equations as well as state variables that can be measured and are time and space dependent (Devia et al., 2015; Fatichi et al., 2016). They require a large number of parameters to describe the physical characteristics of the watershed, such as the initial water depth, topography, soil properties, and crop characteristics (Devia et al., 2015; Abbott et al., 1986a; Abbott et al., 1986b; Ranatunga et al., 2017), which add increasing complexity to their correct implementation at the watershed scale.

Pianosi et al. (2016) states that sensitivity analyses are increasingly being used in environmental modeling for multiple purposes, including uncertainty analysis, model calibration, and diagnostic evaluation. A sensitivity analysis of a hydrological model allows evaluating the influence that certain hydrological parameters have on model outputs (Silva et al., 2015; Shi et al., 2017; Song et al., 2015; Sreedevi and Eldho, 2019; Christiaens and Feyen, 2002). Since results of hydrological models are space and time dependent when applied at the watershed scale, this methodology allows us to identify the dominant characteristics and processes occurring at that particular scale, presenting itself as an essential tool for modelers and decision makers (Ranatunga et al., 2017). Sensitivity analysis is usually carried out at the beginning of model applications to identify the parameters that most strongly influence the hydrological behavior of the watershed (Hamby, 1994; Doherty and Hunt, 2009). The information obtained is very useful to understand the strengths and weaknesses of an application of a given model to a specific case study (Doherty and Hunt, 2009).

This study presents a sensitivity analysis performed with the MOHID-Land model (Trancoso et al., 2009), and its application to a case study considering calibration and validation processes based on the knowledge acquired during the former analysis. MOHID-Land is a physically based model that simulates the interactions between different mediums of the soil–

water–atmosphere continuum. The fundamental processes that affect the hydrological behavior of a watershed are formulated at detailed time and spatial scales, with the study area being discretized by a grid of which the resolution is selected by the modeler. Processes are then calculated for each cell of that grid. Because of its versatility, the MOHID-Land model has been applied in different case studies, characterized by a diversity of spatial scales. At the plot and field scale, MOHID-Land was used to study soil water dynamics and to improve irrigation practices (Simionesei et al., 2016; Ramos et al., 2017; Simionesei et al., 2017; Ramos et al., 2018; Simionesei et al., 2018). At the watershed scale, this model was used to understand the contribution of flood events to the eutrophication of water reservoirs (Brito et al., 2017; Brito et al., 2018), to develop a forecast system of fresh water quantity and quality in coastal rivers (Brito et al., 2015), to evaluate nitrogen transport and turnover (Epelde et al., 2016), to model and analyze the exchanges between groundwater and surface water in floodplains (Bernard-Jannin et al., 2016), and to study the influence of reservoir management on the streamflow regime of a semi-arid watershed (Canuto et al., 2019). Despite its increasing use, MOHID-Land was never subjected to a sensitivity analysis to better depict the main processes and parameters involved in the simulation of water dynamics at the watershed scale.

Thus, the main objective of this study is to conduct a sensitivity analysis of the MOHID-Land model following the guidelines proposed by Pianosi et al. (2016) and to identify the parameters/processes that most strongly influence river flow generation, baseflow, and peak flows in the Ulla River watershed, northwestern Spain, selected here as a case study. This watershed is frequently affected by flood events, particularly in the downstream areas. Water quality issues related to a deactivated metal mine located in an affluent area of the Ulla River have often been raised. It is thus imperative to have a reliable tool to predict the river flow regime and mitigate those events. Additionally, this study aims to identify which parameters/processes can improve the model's computational speed. Results of this study can further be very useful for future applications of the model, directing users to the most impactful parameters for river flow generation and saving time. Thus, this study constitutes an added value for those users as well as for the hydrological modeling community in general.

5.2 Materials and Methods

5.2.1 Description of the Study Area

The study area was the watershed of the Ulla River, Galicia, northwestern Spain (Figure 5.1). The Ulla River watershed has an area of 2803 km^2 (Augas de Galicia, 2015). Its origin is in Fonte de Ulla, Monterosso municipality, at a level of about 600 m, and the main watercourse

has a bed length of 142 km, crossing 19 counties. The maximum and minimum elevations are 1160 m and −0.75 m, respectively. According to the Köppen-Geiger classification, the climate in the region is a Mediterranean warm summer climate (Csb). The average annual temperature is 12°C, ranging from 7°C in February to 18°C in August. The annual precipitation is 1100 mm, occurring mainly from October to May. The dominant soil units are Umbric Leptosols and Umbric Regosols, occupying 69% and 31% of the area, respectively (FAO, 2009). The main land uses are forest and semi natural areas and agricultural areas, covering 57.2% and 40.3% of the watershed, respectively (Copernicus Land Monitoring Service, n.d.).

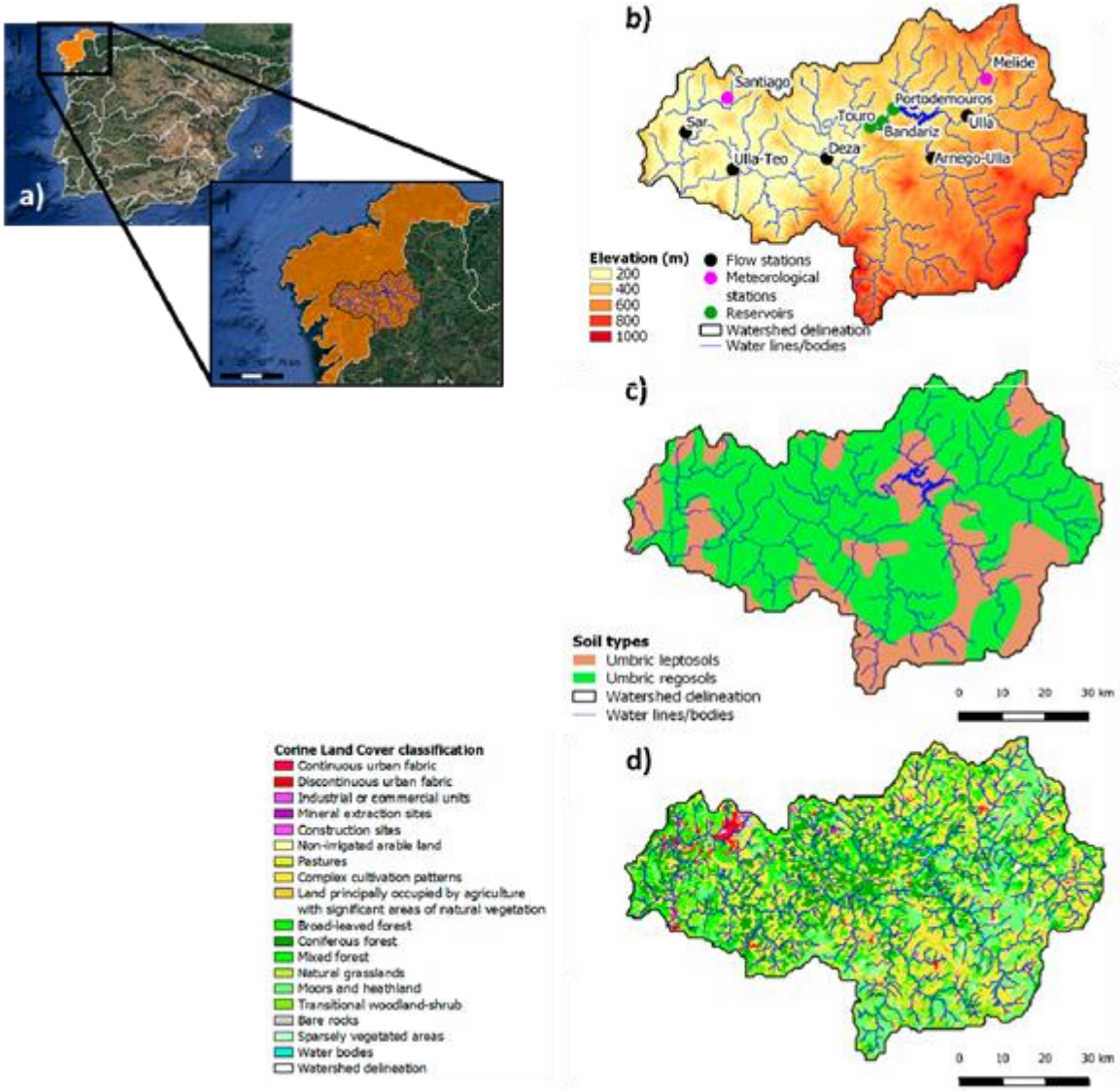

Figure 5.1 (a) Location of the study area; (b) Digital terrain model and location of reservoirs and hydrometric stations; (c) main soil units; (d) main land uses (Copernicus Land Monitoring Service, n.d.).

The watershed has a population of about 150 000 inhabitants, mainly located in the cities of Santiago de Compostela, Estrada, Lalín, and Padrón. The Ulla River further includes three reservoirs, namely, Portodemouros, Touro, and Bandariz (Figure 5.1). Portodemouros has a

total capacity of 297 hm^3, while Bandariz and Touro are smaller, storing 2.74 hm^3 and 3.78 hm^3, respectively. The reservoirs are mainly used for energy production and flood control. The three reservoirs function together, with Bandariz and Touro being used to uniformize turbinated flows in Portodemouros during peak times, reducing its impact in downstream areas.

5.2.2 Model Description

The MOHID-Land model (Trancoso et al., 2009; Canuto et al., 2019) is an open-source hydrological model; the code can be accessed from an online repository (github.com/Mohid-Water-Modelling-System/Mohid). MOHID-Land simulates the water cycle considering four compartments or mediums: atmosphere, porous media, soil surface, and river network. The atmosphere is not explicitly simulated but provides data necessary for imposing surface boundary conditions that may be space and time variant. The water moves between the remaining mediums based on mass and momentum conservation equations that are computed using a finite volume approach. MOHID-Land is thus a physically based, fully distributed model using an explicit algorithm with a variable time step. The time step is maximum during dry seasons and minimum when fluxes increase.

The simulated domain can be discretized by a regular grid, quadrangular or rectangular, in the surface plane, and by a cartesian coordinate system in the vertical direction. Thus, the surface land is described using a 2D horizontal grid while the porous media is a 3D domain, which includes the same horizontal grid on the surface complemented with a vertical grid with variable thickness layers. The river network is a 1D domain defined from a digital terrain model (DTM). The water lines of the drainage network are then delineated by linking surface cell centers (nodes) together.

5.2.2.1 Infiltration

The MOHID-Land model includes three options to compute soil water infiltration. The infiltration rate (i, LT^{-1}) can be first estimated according to Darcy's law, as follows:

$$i = -K_{sat}\left(\frac{\partial h}{\partial z} + 1\right) \quad \text{(Eq. 5.1)}$$

where K_{sat} is the saturated soil hydraulic conductivity (LT^{-1}), h is the soil pressure head (L), and z is the vertical space coordinate (L).

The infiltration rate can also be calculated according to the Green and Ampt method (Green and Ampt, 1911):

$$i = \Delta\theta\left(\frac{D_0}{2t}\right)^{1/2} \quad \text{(Eq. 5.2)}$$

where t is the time (T), D_0 is the soil water diffusivity (L^2T^{-1}), and $\Delta\theta$ is the difference between the volumetric water content in the wetted region (θ_0) and soil initial conditions (θ_i) ($\Delta\theta = \theta_0 - \theta_i$, L^3L^{-3}). Soil water diffusivity can then be calculated as:

$$D_0 = \frac{K_0 \Delta h}{\Delta\theta} \quad \text{(Eq. 5.3)}$$

where K_0 is the hydraulic conductivity of the wetted region (LT^{-1}), and Δh is the difference between the matric head in the wetted region (h_0) and at the moving front (h_F) ($\Delta h = h_0 - h_F$).

Finally, the SCS runoff curve number (CN) method (SCS, 1972) can be further used to estimate the infiltration rate. In this method, infiltration water is the amount of water not removed by surface runoff, entering the soil at a rate computed from the ratio between the amount of water available for infiltration and the time step. The surface runoff is first calculated as follows:

$$Q = \frac{(P - I_a)^2}{(P - I_a) + S} \quad \text{(Eq. 5.4)}$$

where Q is the runoff (L, mm), P is the rainfall (L, mm), S is the potential maximum retention (L, mm) after runoff begins, and I_a is the initial abstraction (L, mm). Initial abstraction considers all losses before runoff begins, as water retained in surface depressions, water intercepted by vegetation, evaporation, and infiltration, and is calculated as:

$$I_a = 0.2S \quad \text{(Eq. 5.5)}$$

The S parameter is related to soil properties and land use through the curve number (CN):

$$S = \frac{25400}{CN} - 254 \quad \text{(Eq. 5.6)}$$

The CN values may range between 0 and 100 (-). Higher values of CN are related with more impermeable soils and, consequently, with higher runoff values. In MOHID-Land, the user can define average curve number values (CNII). However, because runoff is affected by soil moisture before a precipitation event, these average values are adjusted for dry (CNI) and wet (CNIII) conditions. The adjustment of the CNII values considers the comparison of the accumulated precipitation during the last five days with predefined thresholds. Under dry conditions, CN values will then decrease while under wet conditions CN values will increase. Nonetheless, it is important to note that, in MOHID-Land, the amount of water in I_a may not fully infiltrate if the soil is saturated, being transformed back to surface runoff and summed to Q in Eq. 5.4.

5.2.2.2 Surface Flow

Surface flow is computed by solving the Saint-Venant equation in its conservative form, accounting for advection, pressure, and friction forces:

$$\frac{\partial Q_u}{\partial t} + v_v \frac{\partial Q_u}{\partial x_v} = -gA\left(\frac{\partial H}{\partial x_i} + \frac{|Q|Q_i n^2}{A_v^2 R_h^{4/3}}\right) \quad \text{(Eq. 5.7)}$$

where Q is the water flow in the river (L^3T^{-1}), A is the cross-sectional flow area (L^2), g is the gravitational acceleration (LT^{-2}), v is the flow velocity (LT^{-1}), H is the hydraulic head (L), n is the Manning coefficient ($TL^{-1/3}$), R_h is the hydraulic radius (L), and subscripts u and v denote flow directions. In the drainage network, surface flow is solved for one direction (1D domain) considering the water lines obtained from the DTM. The cross-sections in the nodes of the river network are defined by the user. Outside the drainage network, surface flow results from the amount of water that does not infiltrate or ascends by capillarity and is solved on a 2D domain considering the directions of the horizontal grid. Water exchanges between the soil surface and the drainage network are computed according to a kinematic approach, neglecting bottom friction, and using an implicit algorithm to avoid instabilities.

5.2.2.3 Porous Media

The movement of infiltrated water in the porous media is computed by the Richards equation:

$$\frac{\partial \theta}{\partial t} = \frac{\partial}{\partial x_i}\left(K(\theta)\left(\frac{\partial h}{\partial x_i} + \frac{\partial}{\partial x_i}\right)\right) - S(h) \quad \text{(Eq. 5.8)}$$

where θ is the volumetric water content (L^3L^{-3}), x_i represents the xyz directions (-), K is the hydraulic conductivity (LT^{-1}), and S is the sink term representing root water uptake ($L^3L^{-3}T^{-1}$). The soil hydraulic properties are described using the Mualem-van Genuchten functional relationships (Mualem, 1976; van Genuchten, 1980):

$$S_e(h) = \frac{\theta(h) - \theta_r}{\theta_s - \theta_r} = \frac{1}{(1 + |\alpha h|^{\eta})^m} \quad \text{(Eq. 5.9)}$$

$$K(h) = K_{sat} S_e^{\ell}\left[1 - \left(1 - S_e^{1/m}\right)^m\right]^2 \quad \text{(Eq. 5.10)}$$

where S_e is the effective saturation (L^3L^{-3}), θ_r and θ_s are the residual and saturated water contents, respectively (L^3L^{-3}), K_{sat} is the saturated hydraulic conductivity (LT^{-1}), α (L^{-1}) and η (-) are empirical shape parameters, $m = 1 - 1/\eta$, and ℓ is a pore connectivity/tortuosity parameter (-). In MOHID-Land, the relation between the horizontal and vertical hydraulic conductivities is defined by a factor ($f_h = K_{hor}/K_{ver}$) that can be adjusted by the user. The model uses the Richards equation in the whole subsurface domain and simulates saturated and unsaturated

flow using the same grid. A cell is considered saturated when moisture is above a threshold value (e.g., 98%) defined by the user. When a cell reaches saturation, the model uses the saturated conductivity to compute flow and the pressure becomes hydrostatic, corrected by friction. This procedure eases the implementation of the model and simplifies its use at an annual scale. The penalty is the time step that during the wetting period must be shorter to guarantee stability. The constraint is minimized using parallel computing. The water fluxes between the porous media and the drainage network are also driven by the pressure gradient in the interface of these two mediums.

5.2.2.4 Root Water Uptake

Root water uptake considers the weather conditions and soil water contents. The reference evapotranspiration rates (ET_o, LT^{-1}) are first computed according to the FAO Penman–Monteith method (Allen et al., 1998). Crop evapotranspiration rates (ET_c, LT^{-1}) are then obtained from the product of ET_o and a single crop coefficient (Kc). The K_c is imposed, with the model either assuming a constant value representing the average characteristics of each vegetation type over the entire growing season as well as average effects of evaporation from the soil (Canuto et al., 2019) or a crop stage-dependent value as used in Allen et al., 1998. Advantages and limitations of these approaches are discussed in Canuto et al. (2019).

The ET_c values are partitioned into potential soil evaporation (E_p, LT^{-1}) and crop transpiration (T_p, LT^{-1}) as a function of the simulated leaf area index (LAI, L^2L^{-2}) (Ritchie, 1972):

$$T_p = ET_c\left(1 - e^{(-\lambda LAI)}\right) \quad \text{(Eq. 5.11)}$$

$$E_p = ET_c - T_p \quad \text{(Eq. 5.12)}$$

where λ is the extinction coefficient of radiation attenuation within the canopy (-). The LAI values are simulated using a modified version of the EPIC model (Neitsch et al., 2011; Williams et al., 1989), considering the heat units for the plant to reach maturity, the crop development stages, and crop stress. Additional details can be found in Ramos et al. (2017).

Root water uptake reductions, i.e., T_p reductions, are finally computed using the macroscopic approach proposed by Feddes et al. (1978) as follows:

$$T_a = \alpha(h)T_p(z) \quad \text{(Eq. 5.13)}$$

where T_a is the actual transpiration rate (T_a, LT^{-1}) and α is a prescribed dimensionless function of h ($0 \leq \alpha \leq 1$) limiting T_p over the root zone in the presence of depth-varying stressors, such as water stress (Šimůnek and Hopmans, 2009; Skaggs et al., 2006). According to the linear model proposed by Feddes et al. (1978), root water uptake is maximum when the pressure head

is between h_2 and h_3, has a linear reduction when $h>h_2$ or $h<h_3$, and becomes zero when $h<h_4$ and $h>h_1$ (subscripts 1−4 denote different threshold pressure heads). Finally, the actual soil evaporation (E_a, LT^{-1}) is calculated from E_p values by imposing a pressure head threshold value (ASCE, 1996).

5.2.3 Model Set-Up (Reference Simulation)

The MOHID-Land model was applied to the study area using a constant horizontally spaced grid in the eastern and northern directions (215 columns × 115 rows), with origin on 42.468498°N and 8.801326°W, and a resolution of 0.005° (≈500 m). The DTM was provided by the European Environment Agency (EU-DEM) (Copernicus Land Monitoring Service—EU-DEM, n.d.), with a resolution of approximately 30 m (0.00028°). This DTM is a hybrid product based on the Shuttle Radar Topography Mission (SRTM) and the Advanced Spaceborne Thermal Emission and Reflection Radiometer (ASTER) Global Digital Elevation Model (GDEM) data fused by a weighted averaging approach.

The drainage network was derived from the DTM. The geometry of the river cross-sections was defined according to Andreadis et al. (2013). This database relates the drained area in each node to the top width and depth of the cross-section at that node (Table 5.1). All cross-sections were considered rectangular, with bottom width equal to the top width. For the nodes with intermediate drainage areas, the dimensions of the cross-section were linearly interpolated from the upper and lower classes defined in Table 5.1. The Manning coefficient was set to a constant value of 0.035 s $m^{-1/3}$ for the entire drainage network (the model does not allow setting up different values along the river network).

Table 5.1 Cross-section drained area, width, and depth.

Area (km^2)	Reference set-up		Sensitivity analysis		Model calibration	
	Top width (m)	Depth (m)	Top width + 25% (m)	Depth + 100% (m)	Top width (m)	Depth (m)
37.85	12.71	0.42	15.89	0.84	12.71	2.0
62.65	16.45	0.51	20.56	1.02	16.45	2.0
84.49	19.16	0.58	23.95	1.16	19.16	2.0
123.35	23.24	0.67	29.05	1.34	23.24	3.0
161.90	26.71	0.75	33.39	1.50	26.71	3.0
195.10	29.38	0.81	36.72	1.62	29.38	3.0
312.45	37.36	0.98	46.70	1.96	37.36	3.0
503.12	46.95	1.17	58.69	2.34	46.95	4.0
1164.36	73.16	1.65	91.45	3.30	73.16	4.0
2246.34	102.33	2.14	127.91	4.28	102.33	4.0
2785.08	114.21	2.33	142.76	4.66	114.21	4.0

Corine Land Cover (FAO, 2009) data with a resolution of 100 m were used to identify land use. For each land use, the vegetation type and respective Manning's coefficient were defined. Vegetation type was defined according to MOHID's vegetation database, while the Manning's coefficients were defined according to Pestana et al. (2013). The K_c values were set based on vegetation type. As mentioned earlier, these coefficients represent empirical average values for the growing season and are not stage dependent as in Allen et al. (1998). The resulting interpolation to the MOHID's simulation domain (Figure 5.2) showed a variation for the Manning coefficient from 0.023 to 0.298 s $m^{-1/3}$ while the K_c values varied from 0.15 to 1.0 (Figure 5.2).

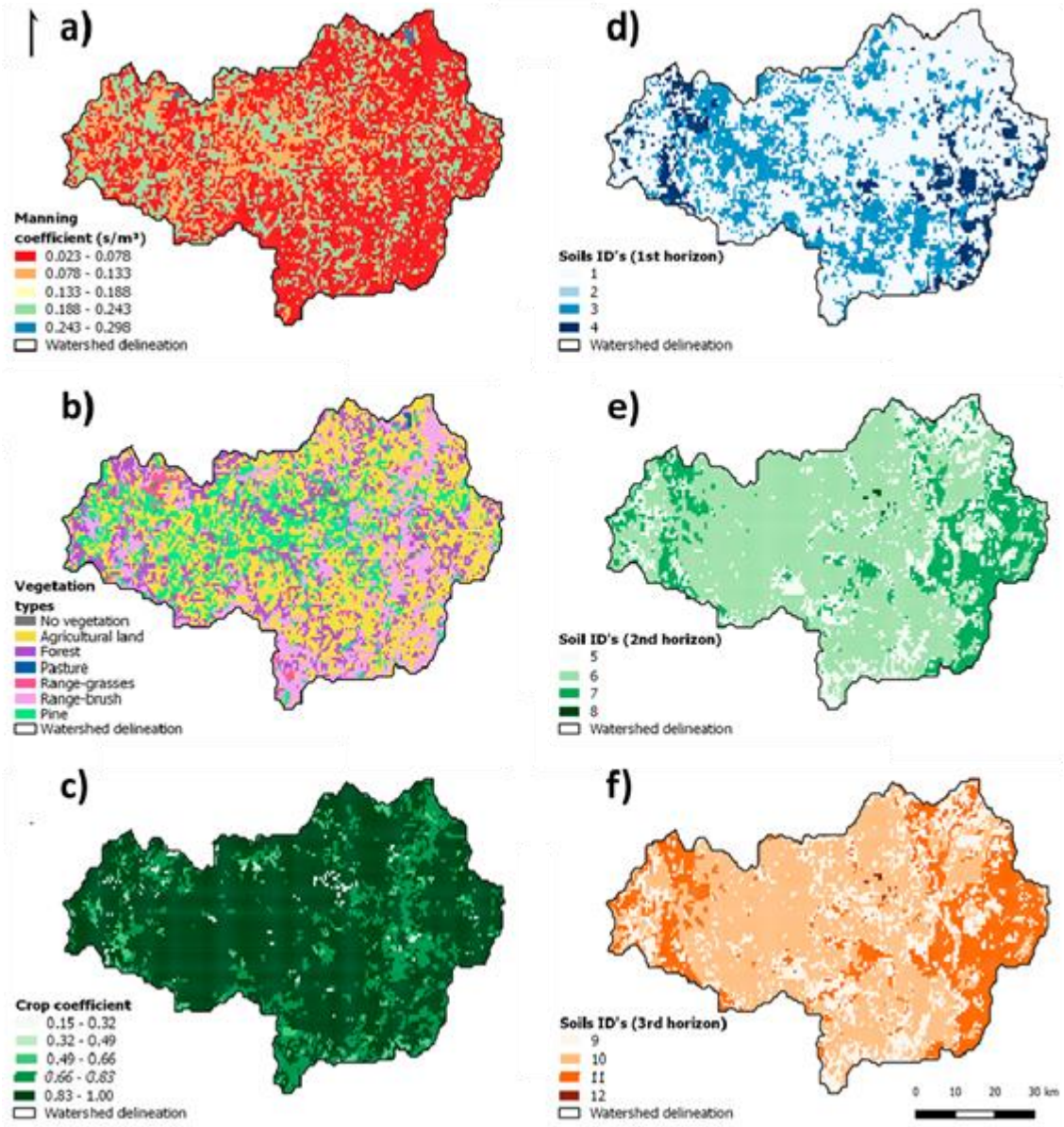

Figure 5.2 MOHID-Land input data: Manning coefficients (a); main land uses (b); crop coefficients (c); and soil data for horizons 1 (d), 2 (e), and 3 (f).

The soil domain was divided into six grid layers, with a thickness from the surface to the bottom layers of 0.3, 0.3, 0.7, 0.7, 1.5, and 1.5 m (vertical grid). On the other hand, the soil profile was characterized by three horizons: 0 to 0.6 m, 0.6 to 2.0 m, and 2.0 m to the soil bottom. Thus, the first horizon included the first two grid layers, the second horizon included the two middle grid layers, and the third horizon consisted of the two bottom layers of the vertical grid domain. The soil depth in each cell was estimated considering the cell slope, with flat areas approximating a maximum predefined value while sloped areas approached a minimum. These maximum and minimum soil depths were defined as 5.0 and 0.1 m, respectively. Soil data were extracted from the multilayered European Soil Hydraulic Database (Tóth et al., 2017). This database includes the Mualem–van Genuchten hydraulic parameters for the whole of Europe at a resolution of 250 m. Information is provided at 0, 0.05, 0.15, 0.3, 0.6, 1.0, and 2.0 m depths. For the present application, the 0.3 m layer was used to characterize the first horizon, the 1.0 m layer was used for the second horizon, and the 2.0 m layer was used for the bottom horizon. Figure 5.2 shows the spatial distribution of soil data in the Ulla watershed while Table 5.2 presents the corresponding Mualem–van Genucthen parameters. The f_h parameter, which relates the horizontal and vertical hydraulic conductivities, was set to 10. For the initial conditions, the soil was assumed as saturated for 95% of the profile (from the bottom to the surface), while the soil water content in the vadose zone was set to field capacity. Soil water infiltration was computed following the Darcian approach (Eq. 5.1).

Table 5.2 Soil hydraulic parameters.

ID	θ_s	θ_r	η	$K_{sat,ver}$	α	ℓ
1 and 2	0.4912	0	1.9131	1.64×10^{-6}	3.47	−4.3
3	0.4646	0	1.116	2.26×10^{-5}	12.84	−5.0
4	0.4086	0	1.1335	5.05×10^{-6}	7.00	−5.0
5	0.4332	0	1.1701	9.93×10^{-7}	3.36	−5.0
6	0.4133	0	1.1191	1.43×10^{-6}	2.27	−5.0
7 and 8	0.3839	0	1.1206	4.29×10^{-6}	7.17	−5.0
9	0.4322	0	1.1701	9.93×10^{-7}	3.36	−5.0
10	0.4133	0	1.1191	1.43×10^{-6}	2.27	−5.0
11 and 12	0.3839	0	1.1206	4.29×10^{-6}	7.17	−5.0

θ_r, residual water content; θ_s, saturated water content; α and μ are empirical shape parameters; ℓ, pore connectivity/tortuosity parameter; K_{sat}, saturated hydraulic conductivity.

Meteorological data were extracted from the ERA5-Reanalysis dataset (Copernicus Climate Change Service (C3S), 2017). This dataset provides several gridded meteorological parameters with an hourly timestep and with a resolution of 0.28125° (31 km). The variables used were the u and v components of wind velocity at 10 m height, dewpoint temperature and air temperature at 2 m height, surface solar radiation downwards, surface pressure, total cloud

cover, and total precipitation. The ERA5 precipitation data were first validated through comparison with measured values obtained at Melide and Santiago meteorological stations (Figure 5.1). For the Melide station, a comparison was conducted from 1 January 2008 to 31 December 2012, resulting in a coefficient of determination (R^2) of 0.74 (Figure 5.3). For the Santiago station, that period was from 1 January 2016 to 31 December 2017, with the R^2 value reaching 0.78. The ERA5 data were then interpolated to the case study grid.

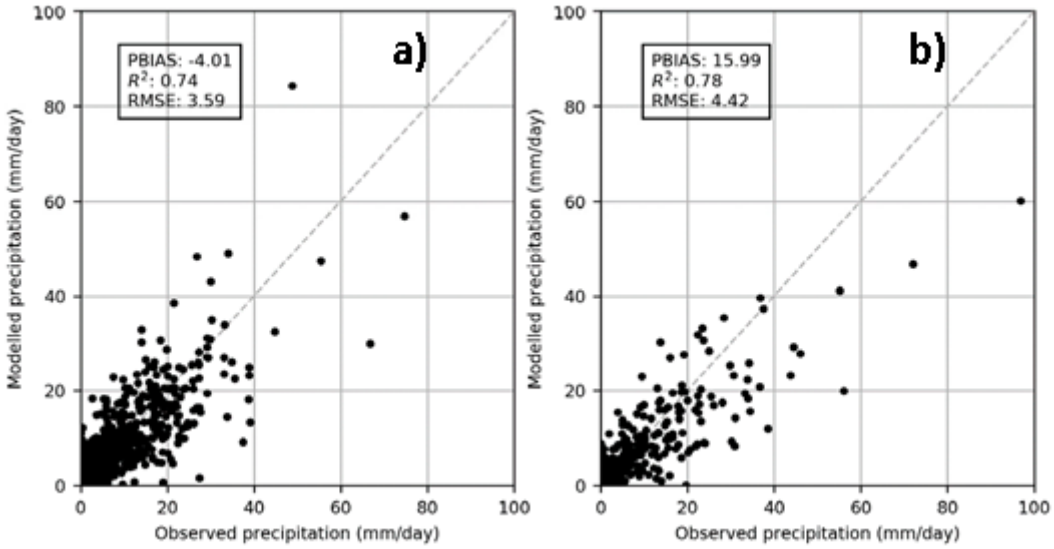

Figure 5.3 Validation of precipitation data measured at Melide (a) and Santiago (b) meteorological stations.

5.2.4 Sensitivity Analysis

The computational cost of one single run with the MOHID-Land model made it impossible to carry out thousands of runs to perform a global and detailed sensitivity analysis. Thus, a local sensitivity analysis was performed by modifying selected MOHID-Land parameters and processes one at the time and evaluating their impact on river flow. The respective flow-duration curves, which express the exceedance probability of a certain flow (Searcy, 1959), were then compared against the reference simulation. A sensitivity index was finally computed following the methodology proposed by Ranatunga et al. (2017).

The simulated river flows at a specific location were arranged in a descending order and ranked from 1 to N with the exceedance probability (frequency of occurrence) being given as follows:

$$F = 100\frac{R}{N+1} \qquad \text{(Eq. 5.14)}$$

where F is the exceedance probability (expressed as a percentage of time a flow value is equaled or exceeded), R is the rank, and N is the total number of flow values resulting from the simulation. The flow duration curve is thus the graphical representation of flow values and the corresponding F values. The flow duration curves were then divided into five zones based on

the percentage exceedance as shown in Figure 5.4. Flows with an F value from 0 to 10% were considered high flows; 10 to 40% corresponded to moist conditions; 40 to 60% corresponded to mid-range flows; 60 to 90% corresponded to dry flows; and 90 to 100% corresponded to low flows (Ranatunga et al., 2017).

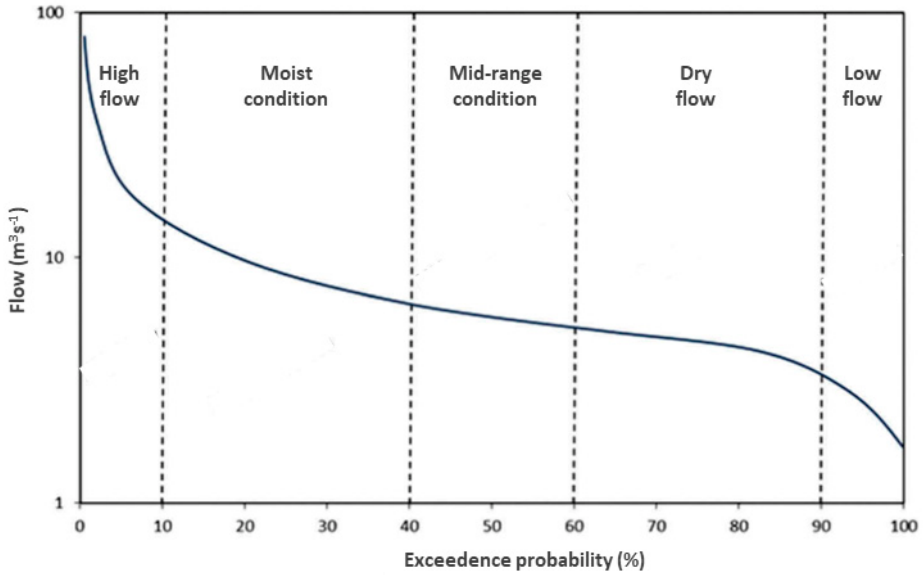

Figure 5.4 Division of the flow duration curve (adapted from Ranatunga et al., 2017).

The sensitivity index (SI) aimed at measuring the relative influence of the analyzed parameters/processes on river flow. This index results from the normalization of the root mean square error (RMSE) by dividing the error of the estimate of each simulated scenario by the range of flow values of the reference simulation:

$$RMSE = \sqrt{\frac{\sum_{i=1}^{p}(Q_i^{ref} - Q_i^{sim})^2}{p}} \quad \text{(Eq. 5.15)}$$

$$SI = \frac{RMSE}{\left(Q_{max}^{ref} - Q_{min}^{ref}\right)} \quad \text{(Eq. 5.16)}$$

where Q_i^{ref} is the flow of the reference simulation on day i, Q_i^{sim} is the flow of the analyzed simulation on day i, Q_{max}^{ref} and Q_{min}^{ref} are the maximum and minimum flow values of the reference simulation in the respective flow classes, and p is total number of flow daily values in the same flow class. A larger influence of a parameter/process on watershed hydrology is represented by higher values of SI, while lower values of SI mean a lower influence of the analyzed parameter/process.

Model simulations were performed from 1 January 2008 to 31 December 2012 (five years). The first four months of simulations were considered as the warm-up period and were not included in the analysis of the results. Flows were analyzed at a daily scale. Due to MOHID-

Land's high computational requirements and having as the ultimate goal the calibration of Ulla River watershed, the sensitivity analysis focused on a single variation of the selected parameters/processes, illustrating the impact of those variables on model performance. The analyzed parameters/processes as well as the variations imposed on model inputs were defined based on previous calibrations of the MOHID-Land model for different watersheds (Brito et al., 2017; Epelde et al., 2016; Bernard-Jannin et al., 2016; Canuto et al., 2019). Additionally, the calibration processes performed on similar physically based models were also considered (Shrestha et al., 2010, Pieri et al., 2014; Zhang et al., 2016; Moreira et al., 2018; Nazari-Sharabian et al., 2019; Sreedevi and Eldho, 2020). Thus, sixteen parameters/processes influencing water dynamics at the catchment scale were analyzed:

- The resolution of the simulation grid was modified from 0.005◦ (≈500 m) used in the reference simulation to 0.01° (≈1000 m; 140 columns × 100 rows) (simulation 1, S1).
- The DTM was changed from the EU-DEM (30 m) to the one provided by the National Geographic Institute of Spain, with a resolution of 5 m (PNOA, n.d.). The new DTM was interpolated to the simulation grid, with the model also delineating a new catchment area and drainage network based on that input (S2).
- The effect of cross-section geometry on river flow was assessed in two simulations. In one (S3), the top and bottom widths were increased by 25% (i.e., larger river) while the depth and the shape of the cross-section remained the same. In the other (S4), the river depth was increased by 100%, while the top and bottom widths and the shape of the cross-section were maintained as in the default simulation. Table 5.1 shows the variations introduced to those parameters per drainage area.
- The K_{sat} value of each cell was multiplied by a factor of 10 while f_h was maintained (S5). As a result, the horizontal hydraulic conductivity was also modified since $f_h = K_{hor}/K_{vert}$.
- The f_h value was analyzed in a separate test by changing this parameter from 10, in the reference simulation, to 20 (S6). The $K_{sat,vert}$ values were the same as in the default scenario, meaning that a change in f_h led to an increase in the K_{hor}.
- The number of layers in the vertical grid increased from 6 to 12 as defined in Table 5.3 (S7), thus decreasing the thickness of the layers when compared with the reference simulation.
- The soil depth also increased from 5 to 10 m (S8), with the number of layers in the vertical grid increasing from six to nine (Table 5.3).
- The surface Manning coefficients increased by 50% when compared with the reference simulation (S9).

- The channel Manning coefficient also increased from 0.035 s $m^{-1/3}$ to 0.0525 s $m^{-1/3}$, corresponding to a 50% increase (S10).
- The SCS curve number method was used to compute runoff and soil water infiltration as an alternative to Eq. 5.1 (S11). The CN values were defined for each grid cell according to the soil type and land cover. The hydrologic soil groups (HSGs) were extracted from the HYSOGs250 m dataset (Ross et al., 2018), which derived that information from the soil texture classes and depth to bedrock available in the SoilGrids250 m product (Hengl et al., 2017). That information was then merged with Corine Land Cover (CLC, n.d.) data following the United States Department of Agriculture (NRCS, 2004) guidelines to derive the CN values. Figure 5.5 presents the CN values adopted in this study. Additionally, changes in the CN values were also assessed by decreasing the values set in S11 by 25% (S12).
- The Green and Ampt infiltration method was now used as an alternative to Eq. 5.1 (S13). The MOHID-Land model needed the values of $K_{sat,ver}$, suction head, porosity, and wilting point in each cell as inputs (Figure 5.6). These inputs were obtained by combining the information available in the LUCAS database (Ballabio et al., 2016) with data from Rossman, 2015, who related the soil texture classes with the soil hydraulic characteristics.
- The importance of the porous media and vegetation growth processes for river flow results were investigated in three separate simulations. Firstly, vegetation growth processes were deactivated (S14), meaning that no evapotranspiration occurred in the catchment area. Secondly, both the porous media and vegetation growth processes were deactivated (S15). In the absence of porous media, the SCS CN method was used to compute the partitioning of rainfall data between surface runoff and infiltration. Infiltration water was then lost to the system since soil porous processes were not considered. The CN values presented in Figure 5 were adopted for this analysis. Lastly, both porous media and vegetation growth processes remained deactivated, but the CN values were reduced by 25% (S16) as in S12.

Table 5.3 Soil discretization for the reference simulation and simulations S7 and S8.

	Depth (m)	**Layers thickness (m)**															
		1st horizon				**2nd horizon**				**3rd horizon**							
Reference simulation	5	0.3		0.3		0.7		0.7		1.5			1.5				
S7	5	0.15	0.15	0.15	0.15	0.35	0.35	0.35	0.35	0.75	0.75	0.75	0.75				
S8	10	0.3		0.3		0.7		0.7		1.0	1.0	1.5	2.0	2.5			

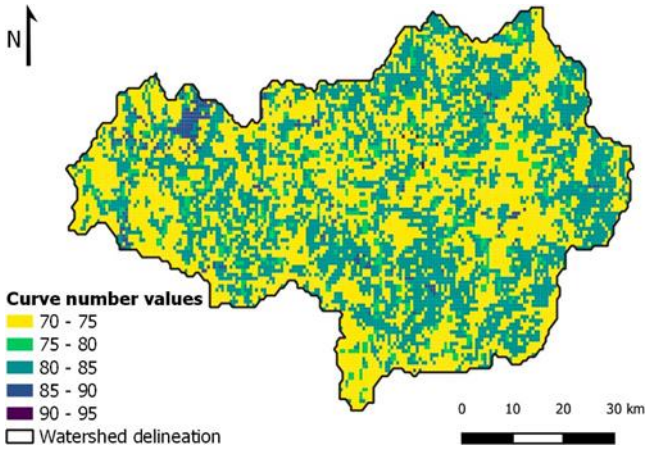

Figure 5.5 Curve number values.

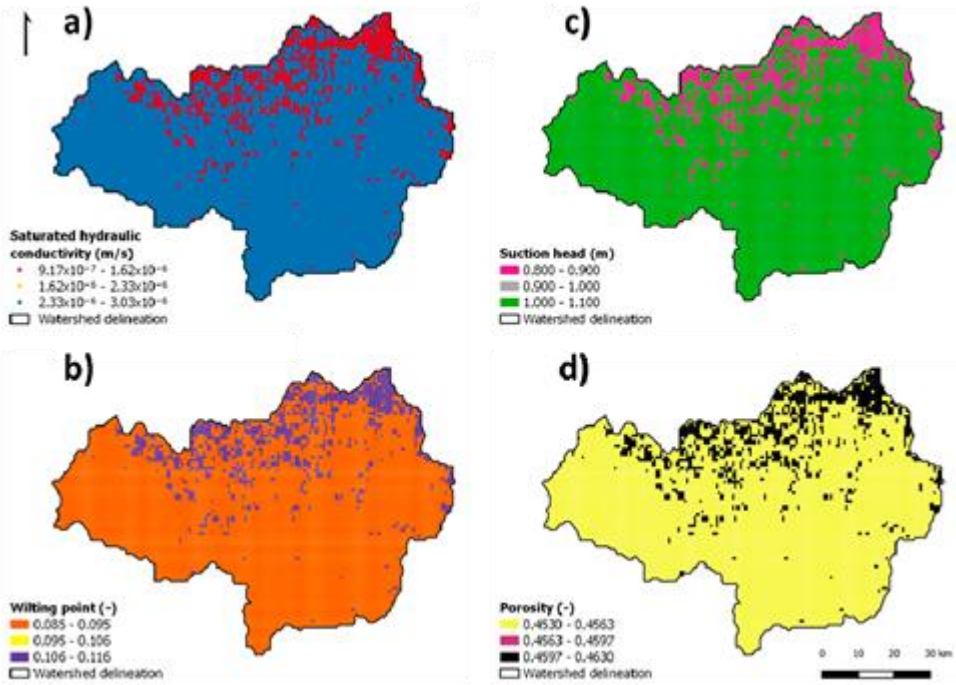

Figure 5.6 Parameters used in the Green and Ampt model: (a) saturated hydraulic conductivity; (b) wilting point; (c) suction head; (d) soil porosity.

The time required for MOHID-Land to compute each simulation was also quantified. The average, maximum, and minimum time (in seconds) required to complete each day of simulation were compared for all scenarios. This information was critical to understand which parameters/processes would improve computational speed during model calibration/validation.

5.2.5 Model Calibration/Validation

Based on results from the sensitivity analysis, the following parameters/processes were modified from those adopted in the reference simulation during model calibration/validation: the vertical hydraulic saturated conductivity ($K_{sat,ver}$); the relation factor between the horizontal and vertical hydraulic conductivities (f_h); and the dimensions of the cross-sections in the river

network. Model calibration consisted of modifying these parameters one at a time, and adjusting them by trial-and error, until deviations between model simulations and flow measurements at Sar, Ulla, Arnego-Ulla, and Deza hydrometric stations (Figure 5.1) were minimized. Validation was then performed by simply comparing model simulations using the calibrated parameters with flow measurements at the same hydrometric stations. The Sar, Ulla, Arnego-Ulla, and Deza hydrometric stations were selected because their data describe the natural flow regime of the Ulla watershed, which was obtained from Augas de Galicia (2020). The Ulla-Teo station (Figure 5.1) was under the influence of reservoir management and therefore its data were not considered for evaluating model performance. Model simulations were carried out from 1 January 2008 to 31 December 2017 (10 years). The first four months were considered as the warm-up period, while the period between 1 May 2008 and 31 December 2012 was considered for calibration. The validation period was defined between 1 January 2013 and 31 December 2017.

Different goodness-of-fit tests were considered for assessing model performance, including the Nash and Sutcliffe model efficiency (NSE), the percent bias (PBIAS), the RMSE-observation standard deviation ratio (RSR), and the coefficient of determination (R^2). The NSE (Nash and Sutcliffe, 1970) was computed as:

$$NSE = 1 - \frac{\sum_{i=1}^{p}(Q_i^{obs} - Q_i^{sim})^2}{\sum_{i=1}^{p}(Q_i^{obs} - Q_{mean}^{obs})^2} \quad \text{(Eq. 5.17)}$$

where Q_i^{obs} is the observed flow on day i, Q_i^{sim} is the simulated flow for day i, Q_{mean}^{obs} is the observed mean flow for the period under consideration, and p is the total number of days in that same period. The NSE is used to assess the relative magnitude of residual variance compared to the measured data variance and it ranges between $-\infty$ and 1.0, being 1.0 the optimal value. Values between 0.0 and 1.0 are classified as acceptable levels of performance, and values ≤ 0.0 indicate that the mean observed value is a better predictor than the simulated value.

The PBIAS is a statistical parameter that measures the average tendency of the simulated data to be larger or smaller than their observed counterparts, and was computed as follows:

$$PBIAS = \frac{\sum_{i=1}^{p}(Q_i^{obs} - Q_i^{sim})}{\sum_{i=1}^{p} Q_i^{obs}} \times 100 \quad \text{(Eq. 5.18)}$$

The optimal value of PBIAS is 0.0 and low-magnitude values indicate accurate model simulation. Positive values demonstrate model underestimation while negative values represent model overestimation.

The RSR results from the ratio between the RMSE and the standard deviation of observed values were obtained as follows:

$$RSR = \frac{RMSE}{STDEV_{obs}} = \frac{\sqrt{\sum_{i=1}^{p}(Q_i^{obs} - Q_i^{sim})^2}}{\sqrt{\sum_{i=1}^{p}(Q_i^{obs} - Q_{mean}^{sim})^2}} \quad \text{(Eq. 3.6)}$$

RSR incorporates the benefits of error index statistics and includes a scaling/normalization factor. RSR is equal to 0.0 when RMSE is 0.0, indicating that the variation is residual, and the model is perfect. Thus, low RSR values correspond to low RMSE values and a good model simulation performance.

Finally, R^2 describes the degree of collinearity between simulated and measured data and ranges from 0 to 1, with higher values indicating less error variance. This statistical parameter was computed as follows:

$$R^2 = \left[\frac{\sum_{i=1}^{p}(Q_i^{obs} - Q_{mean}^{obs})(Q_i^{sim} - Q_{mean}^{sim})}{\sqrt{\sum_{i=1}^{p}(Q_i^{obs} - Q_{mean}^{obs})^2}\sqrt{\sum_{i=1}^{p}(Q_i^{sim} - Q_{mean}^{sim})^2}}\right]^2 \quad \text{(Eq. 3.4)}$$

According to Moriasi et al. (2007), model performance for streamflow can be classified as satisfactory when NSE > 0.50, RSR ≤ 0.70, PBIAS ± 25%, and $R^2 > 0.5$.

5.3 Results and Discussion

5.3.1 Impact of Model Parameters/Processes on River Flow

Although flow-duration curves were compared for all flow stations, only results for the Ulla-Teo station (Figure 5.1) are presented graphically, to limit the number of figures and to maintain consistency. This station was not considered for evaluating model performance because of the influence of reservoir management on river flow. However, its larger drainage area produced the most contrasting differences between the simulation scenarios and the reference simulation, which helped demonstrate model behavior during the sensitivity analysis. Figure 5.7 shows the flow-duration curves for each simulation included in the sensitivity analysis, while Table 5.4 and Table 5.5 present the mean flow and respective SI values for each exceedance probability class.

Decreasing the resolution of the base grid from 500 m (reference simulation) to 1000 m (S1) had a substantial impact on river flow, with mean values decreasing between 71% and 97% in all ranges of the flow-duration curve (Table 5.4). That was also visible in the SI values, which ranged from 0.42 to 0.93 (Table 5.5). These results showed that setting up the base grid, which basically defined how detailed the study area would be represented, was an important

step for accurately simulating river flow at the catchment scale. A more detailed grid led to a more dynamic watershed than when using a coarser one. These results contrast with Sreedevi and Eldho (2020) who, after testing three grid sizes (4000, 2000, and 1000 m), found no scale dependency on streamflow generation values using the SHETRAN model. Nevertheless, the use of a coarser resolution grid in the Ulla River watershed had a contrasting result at the hydrometric stations located in the river heads above 600 m (Sar, Arnego-Ulla, and Deza). In those locations with a drainage area smaller than at Ulla-Teo, the coarser steeper slopes in the DTM ended up promoting surface runoff and higher flow peaks, which eventually disappeared by the time the flow reached the Ulla-Teo station.

On the other hand, for the same resolution grid (500 m), results with a more detailed DTM (S2) did not differ much from the reference simulation (Table 5.4 and Table 5.5). The use of high-resolution data in coarse scale applications seems thus to be irrelevant when not accompanied by a base grid also with greater resolution to be able to consider such detailed information. Yet, improvements in streamflow simulations using more detailed grids and DTMs can only go so far, as shown by Pieri et al. (2014). These authors found no statistically significant differences in the accuracy of DTMs varying between 10 and 2 m resolution when simulating streamflow and sediment yield using the WEPP model in a considerably smaller basin than the Ulla River catchment (the Centonara catchment in northern Italy, 1.92 km^2). Also, Zhang et al. (2016) and Nazari-Sharabian et al. (2019) showed the influence of the DTM resolution on the calibration of streamflow simulations using different physically based models.

Increasing the width (S3) and depth (S4) of the cross-sections (i.e., the river network) promoted higher river flow in all the exceedance intervals except for the moist conditions ($Q_{10–40}$), where it slightly decreased (Figure 5.7). The largest increase was in the higher flow class ($Q_{0–10}$), i.e., the flow peaks, with S3 and S4 leading to an increase of the mean flow by 11% and 39%, respectively (Table 5.4). This was explained by the fact that increasing the dimensions of the cross-sections meant that the boundary between the riverbed and the porous media would also increase, promoting water exchanges between these two mediums, mainly from the porous media to the riverbed. However, only S4 resulted in higher SI values in the extremes of the flow duration curve, reaching 0.29 for the $Q_{90–100}$ class and 0.26 for the $Q_{0–10}$ class.

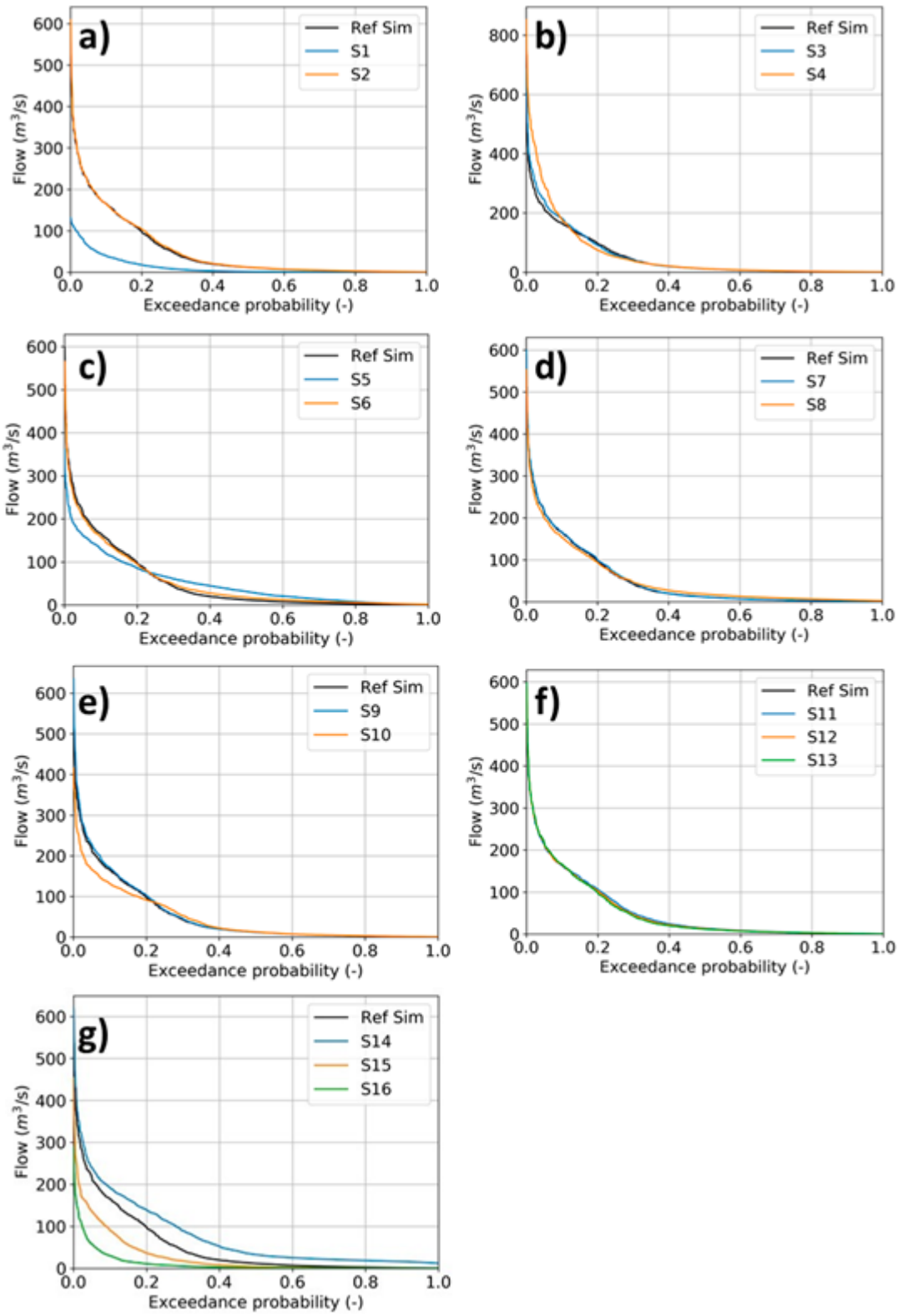

Figure 5.7 Flow-duration curves for the simulations considered during sensitivity analysis. Impact of: (a) grid resolution (S1) and elevation data (S2); (b) cross-section widths and heights (S3 and S4); (c) vertical and horizontal saturated hydraulic conductivities (S5 and S6); (d) vertical soil discretization and soil depth (S7 and S8); (e) surface and channel Manning coefficients (S9 and S10); (f) infiltration methods (S11, S12, and S13); (g) porous media and vegetation processes (S14, S15, and S16) (see Section 5.2.4 for details).

Table 5.4 Mean river flow values at the station Ulla-Teo for each exceedance probability class of the reference simulation flow-duration curve and respective variation in each class for each simulation scenario compared with the reference simulation.

Simulation (% Variation)	Class (%)				
	0-10	10-40	40-60	60-90	90-100
Reference simulation ($m^3 s^{-1}$)	241.25	75.69	12.45	3.82	0.89
1	−71	−80	−88	−92	−97
2	+1	+4	+5	+7	+9
3	+11	−1	+1	+2	+4
4	+39	−11	+5	+9	+30
5	−27	+1	+153	+188	+116
6	−4	+1	+48	+91	+161
7	+1	+3	−3	−2	−22
8	−6	0	+53	+119	+289
9	+6	+3	+1	0	0
10	−23	−3	+7	+6	+10
11	−1	+8	+19	+14	−8
12	−1	+3	+9	+6	−6
13	0	0	0	0	0
14	+12	+54	+181	+434	+1531
15	−37	−57	−63	−71	−85
16	−69	−87	−87	−90	−97

Simulations: 1—grid resolution; 2—elevation data; 3 and 4—cross-section widths and heights; 5 and 6—vertical and horizontal saturated hydraulic conductivities; 7 and 8—vertical soil discretization and soil depth; 9 and 10—surface and channel Manning coefficients; 11, 12, and 13—infiltration methods; 14, 15, and 16—porous media and vegetation processes (see Section 5.2.4 for details).

Table 5.5 Sensitivity index (-) at the station Ulla-Teo for each exceedance probability class of the flow-duration curve.

Simulation	Class (%)				
	0-10	10-40	40-60	60-90	90-100
1	0.42	0.48	0.88	0.67	0.93
2	0.01	0.03	0.05	0.05	0.09
3	0.07	0.04	0.02	0.02	0.04
4	0.26	0.09	0.05	0.06	0.29
5	0.17	0.14	1.52	1.41	1.20
6	0.17	0.14	0.48	0.64	1.52
7	0.01	0.02	0.03	0.02	0.21
8	0.04	0.04	0.52	0.82	2.71
9	0.04	0.02	0.01	0.00	0.00
10	0.14	0.10	0.08	0.04	0.10
11	0.02	0.05	0.20	0.13	0.08
12	0.01	0.02	0.09	0.05	0.06
13	0.00	0.00	0.00	0.00	0.00
14	0.07	0.28	1.79	2.94	14.32
15	0.21	0.33	0.63	0.51	0.82
16	0.39	0.20	0.88	0.66	0.94

Simulations: 1—grid resolution; 2—elevation data; 3 and 4—cross-section widths and heights; 5 and 6—vertical and horizontal saturated hydraulic conductivities; 7 and 8—vertical soil discretization and soil depth; 9 and 10—surface and channel Manning coefficients; 11, 12, and 13—infiltration methods; 14, 15, and 16—porous media and vegetation processes (see Section 5.2.4 for details).

The increase in $K_{sat,ver}$ (S5) and f_h (S6) led to a rise of river flow values in the mid-range ($Q_{40–60}$), low ($Q_{60–90}$), and dry ($Q_{90–100}$) classes of the flow duration curve, which varied from 48% to 188% when compared with the reference simulation. On the other hand, flow values in the $Q_{0–10}$ range (high flows) showed a decreasing trend while the $Q_{10–40}$ class (moist condition) remained basically unchanged. Thus, the increase in those parameters promoted the infiltration process (exchange between the surface and the porous media), the faster movement of soil water (subsurface flow), and the exchange between the porous media and river sections. Higher subsurface flows caused the water to allocate to the baseflow instead of generating flow peaks, increasing the mean values in the lower classes of the flow-duration curve. As a result, the SI values were notoriously higher in the lower classes of the flow duration curve ($Q_{40–60}$ to $Q_{90–100}$), reaching values from 1.20 to 1.52 in S5 and from 0.48 to 1.52 in S6 (Table 5.5) due to the increasing baseflow. Note that a scaling factor of 10 was considered for varying Ksat,ver, in line with previous calibrations of this parameter performed by Canuto et al. (2019) in the Guadiana catchment, Iberian Peninsula. However, this parameter is known to be one of the most variable in nature, being affected by soil physical, chemical, and biological properties. There is also the fact that Tóth et al. (2017) maps were developed from a database containing measurements of this parameter carried out in the laboratory on samples of limited size, with issues related to their representativeness being often raised when describing actual flow conditions, transport, and reaction processes occurring at the field/catchment scales due to limitations in the porous medium continuum (Ramos et al., 2013; van Looy et al., 2017). Similarly, a scaling factor of 20 was considered in this application for f_h. The literature is far less rich on variations of this parameter since it is specific to the MOHID-Land model. Yet, f_h has been found to vary between 3.0 (Canuto et al., 2019) and 25.0 (Epelde et al., 2016). The latter was used to fit simulated streamflow to measurement values in the Alegria River watershed, northern Spain. Thus, different scaling factors could have been here considered for $K_{sat,ver}$ and f_h, but results would not differ much since the main point was to identify which hydrological processes would be affected by these parameters.

The influence of vertical discretization (S7) on river flow was practically null. This explains the relatively coarse discretization of the vertical grid in existing applications of the MOHID-Land model at the watershed scale (Bernard-Jannin et al., 2016; Epelde et al., 2016; Brito et al., 2017; Canuto et al., 2019). These studies reported vertical grids varying from 7 to 12 layers when describing soil profiles reaching 8 to 30 m depth. More detailed grids would have increased the computational burden with no practical benefit for model performance. Nonetheless, those numbers contrast with the one-dimensional application presented in Ramos

et al., 2017, who used 100 grid cells with 0.02 m thickness each to describe soil water dynamics in a soil profile with 2 m depth and respective interactions between the vadose zone and a shallow groundwater table. On the other hand, a deeper soil profile (S8) led to an increase in the lower exceedance probability classes of the flow-duration curve ($Q_{40–60}$, $Q_{60–90}$ and $Q_{90–100}$) from 53% to 289% (Table 5.4), resulting in higher SI values in those classes (0.52 to 2.71). The increase in soil depth represented a larger volume of water stored below the surface, at depths (bottom profile) that were not affected by evapotranspiration. This water stored at deeper depths became thus an additional resource for exchanges between the porous media and the river network, leading to higher baseflow.

The impact of modifying the surface's Manning coefficients was small (S9). This agreed with Canuto et al. (2019,) who considered this parameter in the calibration of streamflow simulations in the Guadiana basin, but changes to the model's default values ended up being only minor. Changing the channel's Manning coefficient (S10) resulted in a decrease of the mean flow in the $Q_{0–10}$ class by 23% and an increase in the $Q_{90–100}$ class by 10% (Figure 5.7, Table 5.4). Increasing the roughness and, consequently, the friction between the water and the surface led to a decrease in flow velocity. The infiltration process was then promoted, causing an increase in baseflow and a reduction of the flow peaks. Nonetheless, the SI values were always smaller than 0.14, which show the reduced influence of this parameter in the generation of streamflow.

The use of the SCS CN method (S11) promoted the increase in mean flow values for the moist ($Q_{10–40}$), mid-range ($Q_{40–60}$), and dry flow classes ($Q_{60–90}$) by 8%, 19%, and 14%, respectively, when compared with the reference simulation (Table 5.4). Flow in the $Q_{40–60}$ class also corresponded to the highest SI value (0.20; Table 5.5). Reducing the CN values of all grid cells by 25% (S12) naturally led to less runoff, with the mean flow values for the same classes referred to above being 3%, 9%, and 6% higher than in the reference simulation while in the $Q_{90–100}$ class they were lower by 6%. The use of the Green and Ampt method as an alternative to Eq 5.1 had no real impact on river flow. Obviously, future works need to analyze the sensitivity of the MOHID-Land model to inputs used for computing soil water infiltration with this method. Notwithstanding, the MOHID-Land model offers analytical, semi-analytical, but also empirical solutions for modeling a key process in the hydrological cycle, which can be selected depending on the complexity of users' applications.

Finally, the deactivation of vegetation (S14) and porous media (S15) modules produced a strong modification of the flow-duration curve at the Ulla-Teo station (Figure 5.7), which was expected since most processes included in the reference simulation were disregarded.

Ignoring the evapotranspiration process in the catchment (S14) led to an increase in the mean flow in all intervals of the flow duration curve, particularly in the mid-range ($Q_{40–60}$), dry ($Q_{60–90}$), and low flow ($Q_{90–100}$) classes (Table 5.4). Flow in the $Q_{90–100}$ class also returned the highest SI value of 14.32 (Table 5.5). Without the main driver for soil water dynamics, soil water contents as well as exchanges between the porous media and the river network simply increased, promoting mainly baseflow. The porous media module was responsible for the occurrence of subsurface flow and baseflow. This constituted a major component in the water budget of the Ulla River catchment. Disregarding this module naturally led to a decrease in the mean river flow values in all classes of the flow-duration curve because the infiltrated water simply disappeared from the system. With the reduction of the CN values by 25% (S16), that drop was even higher (Table 5.4).

5.3.2 Impact of Model Parameters/Processes on Model Time Consumption

Figure 8 presents the boxplot of the time required for MOHID-Land to compute each day of the simulations considered in the sensitivity analysis, while Table 5.6 summarizes those results by presenting the minima, mean, and maxima values. The fastest computation time was naturally obtained by running the simplest applications, i.e., S2 with the coarser grid resolution of 1000 m, and S15 and S16 without considering the porous media processes. The former can be explained by a simulation grid four times smaller than the one in the reference simulation, substantially decreasing the calculations needed to run the simulation, and the latter by disregarding subsurface flow, with MOHID-Land distancing from its physically based nature and relying on a more empirical basis. On the other hand, the longest simulation performance was achieved with a more detailed vertical grid domain (S7). The higher number of vertical layers increased the calculations related to the porous media processes, with the model spending more time to perform the simulation. However, as showed earlier, this had no impact on river flow. All other simulations presented a similar computation time, with no real influence on the number of days (seven days) the reference simulation took to run.

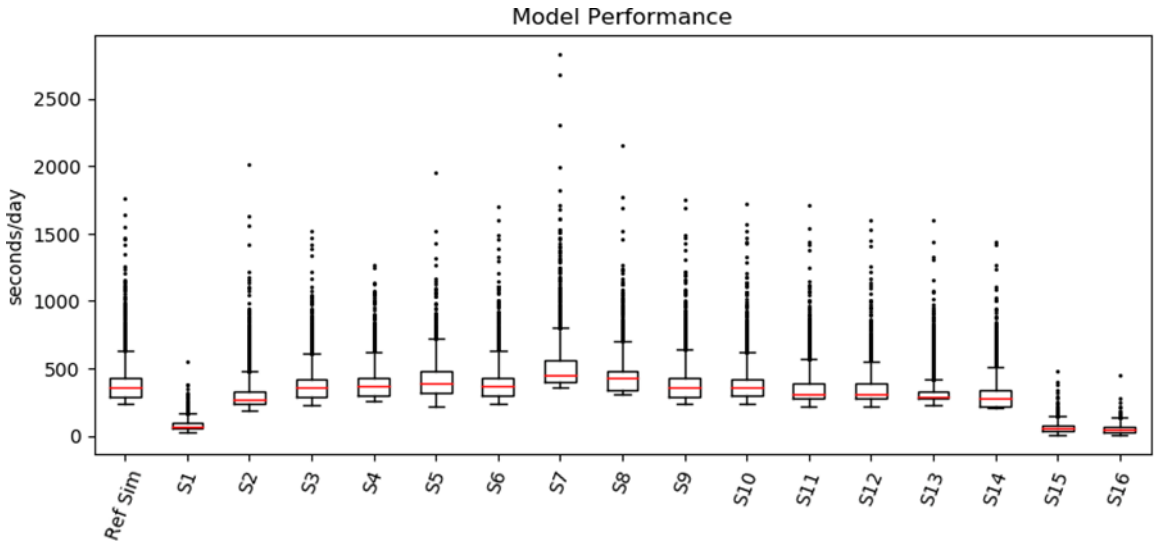

Figure 5.8 Boxplot graph with the computation time spent for each day of the simulation performed in the sensitivity analysis (Simulations: Ref Sim—reference simulation; 1—grid resolution; 2—elevation data; 3 and 4—cross-section widths and heights; 5 and 6—vertical and horizontal saturated hydraulic conductivities; 7 and 8—vertical soil discretization and soil depth; 9 and 10—surface and channel Manning coefficients; 11, 12, and 13—infiltration methods; 14, 15, and 16—porous media and vegetation processes (see Section 5.2.4 for details)).

Table 5.6 Minimum, mean, and maximum computation times for each simulation test.

Simulation	Computation time (s day^{-1})		
	Minimum	Mean	Maximum
Reference simulation	238	402	1764
S1	29	83	550
S2	190	319	2011
S3	228	389	1513
S4	255	399	1269
S5	213	422	1947
S6	237	407	1702
S7	354	528	2829
S8	303	447	2155
S9	235	404	1752
S10	234	399	1723
S11	216	360	1711
S12	221	359	1600
S13	231	334	1599
S14	209	309	1437
S15	6	65	475
S16	5	52	448

Simulations: 1—grid resolution; 2—elevation data; 3 and 4—cross-section widths and heights; 5 and 6—vertical and horizontal saturated hydraulic conductivities; 7 and 8—vertical soil discretization and soil depth; 9 and 10—surface and channel Manning coefficients; 11, 12, and 13—infiltration methods; 14, 15, and 16—porous media and vegetation processes (see Section 5.2.4 for details)

5.3.3 Prediction of River Flow in the Ulla River Watershed

Figure 5.9 visually compares the measured and modeled river flow values at the Sar, Ulla, Arnego-Ulla, and Deza hydrometric stations during the calibration (2008−2012) and validation (2013−2017) periods. The respective goodness-of-fit indicators are presented in

Table 5.7. These results were obtained after modifying $K_{sat,ver}$, f_h, and the dimensions of the cross-sections in the river network defined for the reference simulation. The $K_{sat,ver}$ values for each soil horizon in Table 5.2 were multiplied by a scaling factor of 10, similarly as performed in the sensitivity analysis. The f_h value was then automatically updated since this parameter represents the relation between horizontal and vertical conductivities in each cell. The dimensions of the cross-sections were defined as shown in Table 5.1 and consisted of increasing river depth and interactions between the porous media and the river network. Thus, by modifying these parameters, the calibration process mainly focused on increasing baseflow in the Ulla River watershed.

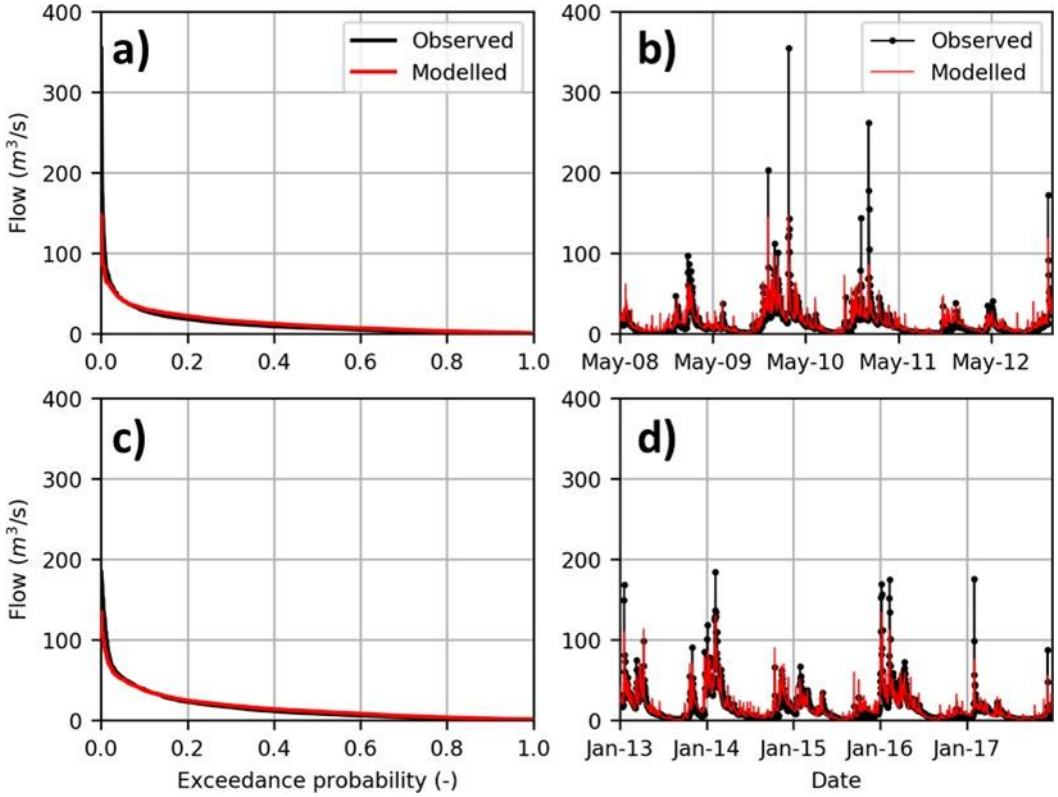

Figure 5.9 Comparison between modeled and observed flow values for calibration (a,b) and validation (c,d) periods in the Deza station.

Table 5.7 Statistical parameters obtained during model calibration/validation at the Sar, Ulla, and Arnego-Ulla, and Deza hydrometric stations.

Station	Calibration				Validation			
	R^2 (-)	RSR (-)	PBIAS (%)	NSE (-)	R^2 (-)	RSR (-)	PBIAS (%)	NSE (-)
Sar	0.75	0.53	0.18	0.72	0.83	0.44	16.09	0.81
Ulla	0.56	0.67	-11.24	0.55	0.76	0.53	-18.54	0.72
Arnego-Ulla	0.70	0.55	-12.29	0.69	0.78	0.49	-16.82	0.76
Deza	0.74	0.53	-8.93	0.72	0.85	0.40	-4.35	0.84

R^2, coefficient of determination; RSR, root mean square error-observations standard deviation ratio; PBIAS, percent bias; NSE, Nash Sutcliffe efficiency.

The R^2 values varied from 0.56 to 0.75 during the calibration period and from 0.76 to 0.85 during the validation period (Table 5.7), showing that the model could explain most of the variability of the measured data in all hydrometric stations. The errors of the estimates were relatively small as shown by the low RSR values obtained at the different stations during both simulation periods (RSR $\leq$ 0.67). On the other hand, the PBIAS values showed some underestimation of measured values at the Sar hydrometric station (PBIAS $\leq$ 16.09%), and some overestimation of measured data for the remaining stations ($-18.54\% \leq$ PBIAS $\leq -4.35\%$). Finally, the NSE values were relatively high in most locations, ranging from 0.55 to 0.84 during both periods, indicating that the residual variance was much smaller than the measured data variance. These indicators are comparable with the best flow estimates under natural regimes in Canuto et al. (2019) with model predictions for the Ulla River watershed being considered extremely satisfactory if Moriasi et al. (2007) guidelines are considered.

Despite the good statistical results, Figure 5.9 further showed the difficulty of the MOHID-Land model in predicting the highest flow peaks in the Ulla River watershed. This was attributed to the precipitation inputs provided by the ERA5 dataset, which also failed to represent higher precipitation values as shown in Figure 3 for the Santiago meteorological station. This tendency was also verified by Hénin et al. (2018), who concluded that reanalysis products such as ERA5 present an underestimation of heavy precipitation events. Hence, the amount of water entering the basin during heavy rain events in that dataset was clearly below measured rainfall and proved to be insufficient for the model to reach higher flow peaks. However, the replacement of the ERA5 data by measured values from the different weather stations was not considered as a viable solution to overcome this problem. Rainfall measurements were only available at a daily time step while the ERA5 data have an hourly time step. In the MOHID-Land model, daily measured data are distributed evenly during the day, reducing rainfall intensity rates, which would further reduce or even miss flow peaks. Besides that, one should consider that the model was calibrated for the entire period without special distinction between dry and wet seasons, which could also explain the difficulty for the model to reach peak flows in the Ulla River watershed. One way to overcome the problem from the model point of view would have been to define distinct geometries of the cross-sections per subbasin, and not per drainage area. This would increase model accuracy of river flow predictions at the watershed scale.

5.4 Conclusions

The MOHID-Land model is a complex, physically based, three-dimensional model used for catchment scale applications. The sensitivity analysis helped to identify the most relevant parameters/processes influencing river flow generation and for accurately modeling baseflow and peak flows. For the application in the Ulla River catchment, the resolution of the simulation grid, the choice of the infiltration method, and the evapotranspiration process were the main factors influencing river flow generation. The soil hydraulic properties, the depth of the soil profile, and the dimensions of the river cross-sections, which basically control the interactions between the porous media and the river, influenced baseflow. On the other hand, peak flows were mostly constrained by the channel's Manning coefficient, as well as the dimensions of the river cross-sections.

The sensitivity analysis further showed that the use of a too coarse resolution grid as well as the deactivation of the porous media and vegetation processes can compromise the quality of results, which should then be subjected to careful revision. Also, model simulations of soil infiltration considering the Darcian and the Green and Ampt approaches produced very similar outputs, both in terms of river flow values and computational time, meaning that users can choose between the two solutions depending on available data. Finally, the number of layers in the vertical simulation grid can lead to a substantial increase in the time needed to compute model simulations with no effect on river flow predictions. It is also important to note that the sensitivity analysis focused on just a few input parameters/processes used in MOHID-Land for simulating river flow at the watershed scale. Others should also be considered in future analysis, namely, the remaining soil hydraulic parameters, the crop coefficients, as well as the parameters used for water quality modeling.

Nevertheless, the MOHID-Land model is a powerful tool for simulating river flow at a daily scale in areas under natural flow regimes. This was demonstrated in simulations of the Ulla River flow at four locations, with comparisons between model predictions and measured values returning $R^2 \geq 0.56$, RSR ≤ 0.67, and NSE ≥ 0.55. These same simulations showed a clear underestimation of river flow peaks, which was attributed to the quality of the ERA5 dataset and the misrepresentation of higher rainfall events.

Author contributions

Conceptualization, A.R.O.; Formal analysis, A.R.O.; Investigation, A.R.O.; Methodology, A.R.O. and T.B.R.; Software, A.R.O.; Visualization, A.R.O.; Writing—original

draft, A.R.O. and T.B.R.; Writing—review & editing, L.S., L.P. and R.N. All authors have read and agreed to the published version of the manuscript.

Funding

This work was supported by FCT/MCTES (PIDDAC) through project LARSyS—FCT Pluriannual funding 2020−2023 (UIDB/50009/2020). The authors also acknowledge project Hazrunoff (UCPM-783208) supported by the Directorate-General for European Civil Protection and Humanitarian Aid Operations. T. B. Ramos was supported by contract CEECIND/01152/2017.

5.5 References

Abbott, M.B.; Bathurst, J.C.; Cunge, J.A.; O'Connell, P.E.; Rasmussen, J. An introduction to the European Hydrological System, Systeme Hydrologique Europeen, "SHE", 1: History and philosophy of a physically-based, distributed modelling system. J. Hydrol. 1986a, 87, 45–59. https://doi.org/10.1016/0022-1694(86)90114-9

Abbott, M.B.; Bathurst, J.C.; Cunge, J.A.; O'Connell, P.E.; Rasmussen, J. An introduction to the European Hydrological System, Systeme Hydrologique Europeen, "SHE", 2: Structure of a physically-based, distributed modelling system. J. Hydrol. 1986b, 87, 61–77. https://doi.org/10.1016/0022-1694(86)90115-0

Allen, R.G.; Pereira, L.S.; Raes, D.; Smith, M. Crop Evapotranspiration—Guidelines for Computing Crop Water Requirements; Irrigation & Drainage Paper 56; Food and Agriculture Organization (FAO): Rome, Italy, 1998.

American Society of Civil Engineers (ASCE). Hydrology Handbook Task Committee on Hydrology Handbook; II Series, GB 661.2. H93; American Society of Civil Engineers (ASCE): Reston, VA, USA, 1996; pp. 96–104.

Andreadis, K.M.; Schumann, G.J.P.; Pavelsky, T. A simple global river bankfull width and depth database. Water Resour. Res. 2013, 49, 7164–7168. https://doi.org/10.1002/wrcr.20440

Augas de Galicia. Available online: https://augasdegalicia.xunta.gal/ (accessed on 8 October 2020).

Augas de Galicia. Descrición xeral da demarcación. In Plan Hidrolóxico da Demarcación Hidrográfica de Galicia-Costa 2015–2021; Xunta de Galicia: Santiago de Compostela, Spain, 2015.

Ballabio, C.; Panagos, P.; Monatanarella, L. Mapping topsoil physical properties at European scale using the LUCAS database. Geoderma 2016, 261, 110–123. https://doi.org/10.1016/j.geoderma.2015.07.006

Bernard-Jannin, L.; Brito, D.; Sun, X.; Jauch, E.; Neves, R.; Sauvage, S.; Sánchez-Pérez, J.M. Spatially distributed modelling of surface water-groundwater exchanges during overbank flood events—A case study at the Garonne River. Adv. Water Resour. 2016, 94, 146–159. https://doi.org/10.1016/j.advwatres.2016.05.008

Brito, D.; Campuzano, F.J.; Sobrinho, J.; Fernandes, R.; Neves, R. Integrating operational watershed and coastal models for the Iberian Coast: Watershed model implementation—A first approach. Estuar. Coast. Shelf Sci. 2015, 167, 138–146. https://doi.org/10.1016/j.ecss.2015.10.022

Brito, D.; Neves, R.; Branco, M.C.; Gonçalves, M.C.; Ramos, T.B. Modeling flood dynamics in a temporary river draining to an eutrophic reservoir in southeast Portugal. Environ. Earth Sci. 2017, 76, 377. https://doi.org/10.1007/s12665-017-6713-7

Brito, D.; Ramos, T.B.; Gonçalves, M.C.; Morais, M.; Neves, R. Integrated modelling for water quality management in a eutrophic reservoir in south-eastern Portugal. Environ. Earth Sci. 2018, 77, 40. https://doi.org/10.1007/s12665-017-7221-5

Canuto, N.; Ramos, T.B.; Oliveira, A.R.; Simionesei, L.; Basso, M.; Neves, R. Influence of reservoir management on Guadiana streamflow regime. J. Hydrol. Reg. Stud. 2019, 25, 100628. https://doi.org/10.1016/j.ejrh.2019.100628

Christiaens, K.; Feyen, J. Use of sensitivity and uncertainty measures in distributed hydrological modeling with an application to the MIKE SHE model. Water Resour. Res. 2002, 38. https://doi.org/10.1029/2001WR000478

Copernicus Climate Change Service (C3S). ERA5: Fifth Generation of ECMWF Atmospheric Reanalyses of the Global Climate. Copernicus Climate Change Service Climate Data Store (CDS). 2017. Available online: https://cds.climate.copernicus.eu/cdsapp#!/home (accessed on 15 November 2019).

Copernicus Land Monitoring Service. Corine Land Cover (CLC). Available online: https://land.copernicus.eu/pan-european/corine-land-cover/clc-2012 (accessed on 3 July 2018).

Copernicus Land Monitoring Service—EU-DEM. Available online: https://www.eea.europa.eu/data-and-maps/data/copernicus-land-monitoring-service-eu-dem (accessed on 17 August 2020).

Devia, G.K.; Ganasri, B.P.; Dwarakish, G.S. A review on hydrological models. Aquat. Procedia 2015, 4, 1001–1007. https://doi.org/10.1016/j.aqpro.2015.02.126

Doherty, J.; Hunt, R.J. Two statistics for evaluating parameter identifiability and error reduction. J. Hydrol. 2009, 366, 119–127. https://doi.org/10.1016/j.jhydrol.2008.12.018

Epelde, A.M.; Antiguedad, I.; Brito, D.; Jauch, E.; Neves, R.; Garneau, C.; Sauvage, S.; Sánchez-Pérez, J.M. Different modelling approaches to evaluate nitrogen transport and turnover at the watershed scale. J. Hydrol. 2016, 539, 478–494. https://doi.org/10.1016/j.jhydrol.2016.05.066

Fatichi, S.; Vivoni, E.R.; Ogden, F.L.; Ivanov, V.Y.; Mirus, B.; Gochis, D.; Downer, C.W.; Camporese, M.; Davidson, J.H.; Ebel, B.; et al. An overview of current applications, challenges and future trends in distributed process-based models in hydrology. J. Hydrol. 2016, 537, 45–60. https://doi.org/10.1016/j.jhydrol.2016.03.026

Feddes, R.A.; Kowalik, P.J.; Zaradny, H. Simulation of Field Water Use and Crop Yield; Wiley: Hoboken, NJ, USA, 1978.

Food and Agriculture Organization (FAO). Harmonized World Soil Database, version 1.1. Rome, Italy; International Institute for Applied Systems Analysis (IIASA): Laxenburg, Austria, 2009.

Green, W.H.; Ampt, G.A. Studies on Soil Physics, Part 1, the Flow of Air and Water through Soils. J. Agric. Sci. 1911, 4, 11–24. https://doi.org/10.1017/S0021859600001441

Hamby, D.M. A review of techniques for parameter sensitivity. Environ. Monit. Assess. 1994, 32, 135–154. https://doi.org/10.1007/BF00547132

Hengl, T.; de Jesus, J.M.; Heuvelink, G.B.M.; Gonzalez, M.R.; Kilibarda, M.; Blagotic´, A.; Shangguan, W.; Wright, M.N.; Geng, X.; Bauer-Marschallinger, B.; et al. SoilGrids250 m: Global gridded soil information based on machine learning. PLoS ONE 2017, 12, e0169748. https://doi.org/10.1371/journal.pone.0169748

Hénin, R.; Liberato, M.L.R.; Ramos, A.M.; Gouveia, C.M. Assessing the use of satellite-based estimates and high-resolution precipitation datasets for the study of extreme

precipitation events over the Iberian Peninsula. Water 2018, 10, 1688. https://doi.org/10.3390/w10111688

Moreira, L.L.; Schwamback, D.; Rigo, D. Sensitivity analysis of the Soil and Water Assessment Tools (SWAT) model in streamflow modeling in a rural river basin. Rev. Ambient. Água 2018, 13, e2221. https://doi.org/10.4136/ambi-agua.2221

Moriasi, D.N.; Arnold, J.G.; van Liew, M.W.; Bingner, R.L.; Harmel, R.D.; Veith, T.L. Model evaluation guidelines for systematic quantification of accuracy in watershed simulations. Trans. Am. Soc. Agric. Biol. Eng. 2007, 50, 885–900. https://doi.org/10.13031/2013.23153

Mualem, Y. A new model for predicting the hydraulic conductivity of unsaturated porous media. Water Resour. Res. 1976, 12, 513–522. https://doi.org/10.1029/WR012i003p00513

Nash, J.E.; Sutcliffe, J.V. River flow forecasting through conceptual models part I—A discussion of principles. J. Hydrol. 1970, 10, 282–290. https://doi.org/10.1016/0022-1694(70)90255-6

National Resources Conservation Service (NRCS). Hydrologic soil-cover complexes. In National Engineering Handbook; Chapter 9; Part 630 Hydrology; United States Department of Agriculture: Washington, DC, USA, 2004.

Nazari-Sharabian, M.; Taheriyoun, M.; Karakouzian, M. Sensitivity analysis of the DEM resolution and effective parameters of runoff yield in the SWAT model: A case study. J. Water Supply Res. Technol. Aqua 2019, 69, 39–54. https://doi.org/10.2166/aqua.2019.044

Neitsch, S.L.; Arnold, J.G.; Kiniry, J.R.; Williams, J.R. Soil and Water Assessment Tool, Theoretical Documentation, Version 2009; Texas Water Resources Institute. Technical Report No. 406; Texas A&M University System: College Station, TX, USA, 2011.

Pestana, R.; Matias, M.; Canelas, R.; Araújo, A.; Roque, D.; van Zeller, E.; Trigo-Teixeira, A.; Ferreira, R.; Oliveira, R.; Heleno, S. Calibration Of 2D hydraulic inundation models in the floodplain region of the Lower Tagus River. In Proceedings of the ESA Living Planet Symposium, Edimburgh, UK, 9–13 September 2013.

Pianosi, F.; Beven, K.; Freer, J.; Hall, J.; Rougier, J.; Stephenson, D.; Wagener, T. Sensitivity analysis of environmental models: A systematic review with practical workflow.

Environ. Model. Softw. 2016, 79, 214–232. https://doi.org/10.1016/j.envsoft.2016.02.008

Pieri, L.; Poggio, M.; Vignudelli, M.; Bittelli, M. Evaluation of the WEPP model and digital elevation grid size, for simulation of streamflow and sediment yield in a heterogeneous catchment. Earth Surf. Process. Landf. 2014, 39, 1331–1344. https://doi.org/10.1002/esp.3527

Plan Nacional de Ortofotografía Aérea (PNOA). Available online: https://pnoa.ign.es/productos_lidar (accessed on 8 October 2020).

Ramos, T.B.; Gonçalves, M.C.; Brito, D.; Martins, J.C.; Pereira, L.S. Development of class pedotransfer functions for integrating water retention properties into Portuguese soil maps. Soil Res. 2013, 51, 262–277. http://dx.doi.org/10.1071/SR12347

Ramos, T.B.; Simionesei, L.; Jauch, E.; Almeida, C.; Neves, R. Modelling soil water and maize growth dynamics influenced by shallow groundwater conditions in the Sorraia Valley region, Portugal. Agric. Water Manag. 2017, 185, 27–42. https://doi.org/10.1016/j.agwat.2017.02.007

Ramos, T.B.; Simionesei, L.; Oliveira, A.R.; Darouich, H.; Neves, R. Assessing the impact of LAI data assimilation on simulations of the soil water balance and maize development using MOHID-Land. Water 2018, 10, 1367. https://doi.org/10.3390/w10101367

Ranatunga, T.; Tong, S.T.Y.; Yang, Y.J. An approach to measure parameter sensitivity in watershed hydrological modelling. Hydrol. Sci. J. 2017, 62, 76–92. https://doi.org/10.1080%2F02626667.2016.1174335

Ritchie, J.T. Model for predicting evaporation from a row crop with incomplete cover. Water Resour. Res. 1972, 8, 1204–1213. https://doi.org/10.1029/WR008i005p01204

Ross, C.W.; Prihodko, L.; Anchang, J.Y.; Kumar, S.; Ji, W.; Hanan, N.P. Global Hydrologic Soil Groups (HYSOGs250m) for Curve Number-Based Runoff Modeling; ORNL DAAC: Oak Ridge, TN, USA, 2018.

Rossman, L.A. Storm Water Management Model User's Manual Version 5.1; EPA/600/R-14/413b; United States Environmental Protection Agency: Cincinnati, OH, USA, 2015; 352p.

Searcy, J.K. Flow-duration curves. In Manual of Hydrology: Part 2, Low-Flow Techniques; Pecora, W.T., Ed.; U.S. Government Printing Office: Washington, DC, USA, 1959.

Shi, Y.; Xu, G.; Wang, Y.; Engel, B.A.; Peng, H.; Zhang, W.; Cheng, M.; Dai, M. Modelling hydrology and water quality processes in the Pengxi River basin of the Three Gorges Reservoir using the soil and water assessment tool. Agric. Water Manag. 2017, 182, 24–38. https://doi.org/10.1016/j.agwat.2016.12.007

Shrestha, N.K.; Shakti, P.C.; Gurung, P. Calibration and validation of SWAT model for low lying watersheds: A case study on the Kliene Nete Watershed, Belgium. Hydro Nepal J. Water Energy Environ. 2010, 6, 47–51. https://doi.org/10.3126/hn.v6i0.4194

Silva, M.G.; Netto, A.O.A.; Neves, R.J.J.; Vasco, A.N.; Almeida, C.; Faccioli, G.G. Sensitivity analysis and calibration of hydrological modeling of the watershed Northeast Brazil. J. Environ. Prot. 2015, 6, 837–850. http://www.scirp.org/journal/PaperInformation.aspx?PaperID=58940&#abstract

Simionesei, L.; Ramos, T.B.; Brito, D.; Jauch, E.; Leitão, P.C.; Almeida, C.; Neves, R. Numerical simulation of soil water dynamics under stationary sprinkler irrigation with MOHID-Land. Irrig. Drain. 2016, 65, 98–111. https://doi.org/10.1002/ird.1944

Simionesei, L.; Ramos, T.B.; Oliveira, A.R.; Jongen, M.; Darouich, H.; Weber, K.; Proença, V.; Domingos, T.; Neves, R. Modeling soil water dynamics and pasture growth in the montado ecosystem using MOHID-Land. Water 2018, 10, 489. https://doi.org/10.3390/w10040489

Simionesei, L.; Ramos, T.B.; Palma, J.; Oliveira, A.R.; Neves, R. IrrigaSys: A web-based irrigation decision support system based on open source data and technology. Comput. Electron. Agric. 2020, 178, 105822. https://doi.org/10.1016/j.compag.2020.105822

Šimůnek, J.; Hopmans, J.W. Modeling compensated root water and nutrient uptake. Ecol. Model. 2009, 220, 505–521. https://doi.org/10.1016/j.ecolmodel.2008.11.004

Sitterson, J.; Knightes, C.; Parmar, R.; Wolfe, K.; Muche, M.; Avant, B. An Overview of Rainfall-Runoff Model Types; U.S. Environmental Protection Agency: Washington, DC, USA, 2017.

Skaggs, T.H.; van Genuchten, M.T.; Shouse, P.J.; Poss, J.A. Macroscopic approaches to root water uptake as a function of water and salinity stress. Agric. Water Manag. 2006, 86, 140–149. https://doi.org/10.1016/j.agwat.2006.06.005

Soil Conservation Service (SCS). Design hydrographs. In National Engineering Handbook; United States Department of Agriculture: Washington, DC, USA, 1972.

Song, X.; Zhang, J.; Zhan, C.; Xuan, Y.; Ye, M.; Xu, C. Global sensitivity analysis in hydrological modeling: Review of concepts, methods, theoretical framework, and applications. J. Hydrol. 2015, 523, 739–757. https://doi.org/10.1016/j.jhydrol.2015.02.013

Sreedevi, S.; Eldho, T.I. A two-stage sensitivity analysis for parameter identification and calibration of a physically-based distributed model in a river basin. Hydrol. Sci. J. 2019, 64, 701–719. https://doi.org/10.1080/02626667.2019.1602730

Sreedevi, S.; Eldho, T.I. Effects of grid-size on effective parameters and model performance of SHETRAN for estimation of streamflow and sediment yield. Int. J. River Basin Manag. 2020, 19(4), 535-551. https://doi.org/10.1080/15715124.2020.1767637

Tóth, B.; Weynants, M.; Pásztor, L.; Hengl, T. 3D soil hydraulic database of Europe at 250 m resolution. Hydrol. Proc. 2017, 31, 2662–2666. https://doi.org/10.1002/hyp.11203

Trancoso, A.R.; Braunschweig, F.; Leitão, P.C.; Obermann, M.; Neves, R. An advanced modelling tool for simulating complex river systems. Sci. Total Environ. 2009, 407, 3004–3016. https://doi.org/10.1016/j.scitotenv.2009.01.015

Van Genuchten, M.T. A closed-form equation for predicting the hydraulic conductivity of unsaturated soils. Soil Sci. Soc. Am. J. 1980, 44, 892–898. https://doi.org/10.2136/sssaj1980.03615995004400050002x

van Looy, K.; Bouma, J.; Herbst, M.; Koestel, J.; Minasny, B.; Mishra, U.; Montzka, C.; Nemes, A.; Pachepsky, Y.A.; Padarian, J.; et al. Pedotransfer functions in Earth system science: Challenges and perspectives. Rev. Geophys. 2017, 55, 1199–1256. https://doi.org/10.1002/2017RG000581

Wheater, H.; Sorooshian, S.; Sharma, K.D. (Eds.) Hydrological Modelling in Arid and Semi-Arid Areas; International Hydrology Series; Cambridge University Press: Cambridge, UK, 2007; pp. 1–4.

Williams, J.R.; Jones, C.A.; Kiniry, J.R.; Spanel, D.A. The EPIC crop growth model. Trans. Am. Soc. Agric. Biol. Eng. 1989, 32, 497–511. https://doi.org/10.13031/2013.31032

Zhang, H.; Li, Z.; Saifullah, M.; Li, Q.; Li, X. Impact of DEM resolution and spatial scale: Analysis of influence factors and parameters on physically based distributed model. Adv. Meteorol. 2016, 8582041. https://doi.org/10.1155/2016/8582041

6 Streamflow Estimation in a Mediterranean Watershed Using Neural Network Models: A Detailed Description of the Implementation and Optimization

Authors: Ana Ramos Oliveira, Tiago Brito Ramos and Ramiro Neves

Centro de Ciência e Tecnologia do Ambiente e do Mar (MARETEC-LARSyS), Instituto Superior Técnico, Universidade de Lisboa, Av. Rovisco Pais, 1, 1049-001 Lisboa, Portugal

Published in: Water, 2023, 15: 947 (https://doi.org/10.3390/w15050947), **Impact Factor:** 3.53

Abstract

This study compares the performance of three different neural network models to estimate daily streamflow in a watershed under a natural flow regime. Based on existing and public tools, different types of NN models were developed, namely, multi-layer perceptron, long short-term memory, and convolutional neural network. Precipitation was either considered an input variable on its own or combined with air temperature as another input variable. Different periods of accumulation, average, and/or delay were considered. The models' structures were optimized and automatically showed that CNN performed best, reaching, for example, a Nash–Sutcliffe efficiency of 0.86 and a root mean square error of 4.2 $m^3 s^{-1}$. This solution considers a 1D convolutional layer and a dense layer as the input and output layers, respectively. Between those layers, two 1D convolutional layers are considered. As input variables, the best performance was reached when the accumulated precipitation values were 1 to 5, and 10 days and delayed by 1 to 7 days.

Keywords: neural networks; MLP; LSTM; CNN; streamflow estimation

6.1 Introduction

Accurate knowledge of streamflow is essential in a wide range of applications and studies, including the development of flood warning systems, hydroelectric reservoir operation, hydraulic structure design, fish production and survival, nutrient transport and water quality assessment, evaluation of long-term climate or land use change impacts, and the definition of water management policies (Bourdin et al., 2012; Ni et al., 2020). Humphrey et al. (2016) also state that an accurate and reliable streamflow forecast is crucial for the proper management and allocation of water resources, especially in areas with highly variable climate conditions and where there is not enough available data to adequately support decision-making.

According to Besaw et al. (2010), streamflow estimation in gauged and/or ungauged areas can be performed based on conceptual, metric, physics-based, and data-driven methods. Conceptual methods only consider simplified conceptualizations of hydrological processes (Chiew and McMahon, 1994). Methods classified as metric are based on the unit hydrograph theory, without considering hydrological features or processes (Jakeman et al., 1990). Physically based models, also known as process-based models, rely on physical principles and, consequently, are suitable to provide insights into physical processes. However, these models often incorporate many simplifying assumptions and have requirements for large sets of data, with their calibration and validation processes being particularly laborious (Mehr et al., 2013; Zhang et al., 2015). Finally, data-driven methods are empirical, are developed based on historical observations, and do not require information on physical processes (Liu et al., 2015). Multiple linear regression (MLR) variations of autoregressive moving average (ARMA) or artificial neural networks (ANN) are examples of data-driven models.

Artificial neural networks are special types of machine-learning methods, which have been extensively used in streamflow estimation with promising results in the last decades because of the nonlinear nature of the rainfall–runoff relationship and the availability of long historical records (ASCE, 2000). In the review written by Maier et al., 2010, of 210 published papers using ANN in the field of hydrology between 1999 and 2007, 90% were related to studies where the main goal was flow prediction (the other 10% were related to water quality variables). In the last few years, hydrologists have continued to investigate the ability of neural networks (NN) to predict river flow. For instance, Pham et al. (2020) used a multilayer perceptron (MLP) neural network combined with the intelligent water drop algorithm, an advanced optimization algorithm for searching the global optima, to predict the streamflow in two stations on Vu Gia Thu Bon watershed, Vietnam. Hussain and Khan (2020) tested a MLP,

a support vector regression model, and a random forest model in forecasting the monthly streamflow in the Hunza river watershed, Pakistan. Sahoo et al. (2019), Le et al. (2019), Hauswirth et al. (2021), and Althoff et al. (2021) presented the application of recurrent neural networks (RNN) for streamflow forecasting. Sahoo et al. (2019) assessed the applicability of RNN and the radial basis function network to forecast the daily streamflow in a hydrometric station placed in Mahanadi River watershed, India, while Le et al. (2019) used a RNN model for flood peak discharge forecasting one, two, and three days ahead at Hoa Binh station in the Da River basin, Vietnam. Hauswirth et al. (2021) tested five different data-driven models (multi-linear regression, lasso regression, decision trees, random forests, and RNN) on forecasting several hydrological variables, including observations on discharge and surface water levels, at a national scale and with consideration of a daily time step. Finally, Althoff et al. (2021) applied a single regional hydrological RNN model to 411 watersheds in the Brazilian Cerrado biome to predict daily streamflow, assessing the model's performance with consideration of different input configurations.

Differently, Shu et al. (2021) stated that convolutional neural networks (CNN) are also being gradually applied in hydrological forecasting in the past few years. For example, Wang et al. (2019) predicted water level values in the Yilan River, Taiwan. Hussain and Khan (2020) applied CNN to predict daily, weekly, and monthly values of the streamflow in the Gilgit River, Pakistan. Barino et al. (2020) used CNN to forecast river flow values several days ahead in the Madeira River, the Amazon's largest and most important tributary. With all those authors making use of one-dimensional CNN models to predict streamflow, Shu et al. (2021) presented a different approach based on a two-dimensional CNN model to forecast the inflow to the Huanren Reservoir and Xiangjiaba hydropower station, China.

There are also examples of the usage of model combinations, such as in the case of Anderson and Radić (2022) who developed a convolutional long short-term memory (a type of RNN) model to predict the daily streamflow in 226 watersheds across southwestern Canada, with the main goal being to learn both spatial and temporal patterns.

Thus, the vast number of studies that can be found in the literature allow us to infer that these types of models are being increasingly used in the hydrological sciences, and represent promising tools for to be applied under the most varied conditions. However, the vast number of studies, the existence of different solutions, the often vague descriptions of the solutions in the literature, and the dispersion of the information, make the learning curve difficult and time-consuming. Consequently, the present study aims to develop, optimize, and compare the performance of different neural network models to predict the daily streamflow values in a

natural watershed while focusing on all the essential information needed for their easy implementation.

The studied area contains a natural small watershed (665 km^2) in southern Portugal. This watershed drains to Ponte Vila Formosa hydrometric station and represents 30% of the Maranhão reservoir watershed, which is one of the two reservoirs included in the collective irrigation system of the Sorraia Valley. With its high runoff variability throughout the year (45% of the total runoff occurs in December and January and 14% of that occurs between April and September (SNIRH, n.d.), and with it being responsible for supplying 54% of the irrigation needs to the system, tools that can help to optimize the amount of water used in irrigation (Simionesei et al., 2020) or that can predict water availability are essential for improving water management and supporting decision-makers.

The procedure adopted to create, develop, optimize, and tune the neural network that best fits the observed values of the modeled watershed is explored in this work. Due to the innumerous solutions found in the bibliography, the application of three different types of neural networks was tested: (i) the multi-layer perceptron (MLP) model; (ii) long short-term memory (LSTM) network, which is a type of recurrent neural network (RNN); (iii) convolutional neural network (CNN). The methodology presented here is based on a simplified approach that makes use of the potentialities of the Keras (Keras, n.d.) package, on top of those of the TensorFlow (Abadi et al., 2016) and KerasTuner (O'Malley et al., n.d.) packages, to construct and optimize the models' structures. The optimization was performed for the three different types of NN models, independently, and focused on several parameters and characteristics of these structures (e.g., number of nodes, number of hidden layers, etc.). Additionally, the use of accumulated daily precipitation solely as an input variable or combined with the average daily temperature as another input variable was also tested, as well as the length of the period (i.e., the number of days) to accumulate or average those meteorological properties. The models' structures, parameters, and input variable combinations were optimized and tuned using training and validation datasets. However, to make a more reliable evaluation, neural networks were also tested with consideration of a test dataset, which was never presented to the models during the training and validation processes. Among the set of models developed, the one with the best performance was selected to represent the watershed dynamics.

Thus, this study compares the ability of different NN models to estimate the daily streamflow in a watershed under a natural flow regime. An easy-to-use approach using several tools that are already publicly available and require a regular level of programming skills is

presented to encourage the development and implementation of NN models in other situations. The results of this study will undoubtedly contribute to improving the estimation of inflows to a reservoir used for the storage and supply of water to a collective irrigation district in southern Portugal, where scarcity issues prevail.

6.2 Materials and Methods

6.2.1 Description of the Study Area

The study area contains the watershed (665 km^2) draining to Ponte Vila Formosa hydrometric station (39°12'57.6" N, 7°47'02.4" W), located in Raia River, Alter do Chão, southern Portugal (Figure 6.1).

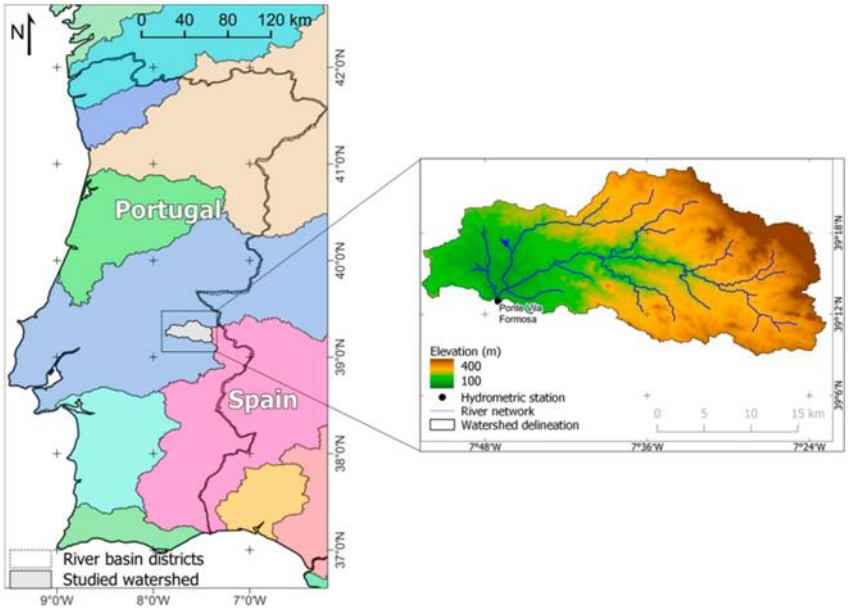

Figure 6.1 Location of the studied watershed, its delineation details, elevation, main rivers, and Ponte Vila Formosa hydrometric station.

The most representative weather stations in the study area are Aldeia da Mata (18K/01C); Alegrete (18N/02G); Alpalhão (17L/03UG); Alter do Chão (18L/01UG); Cabeço de Vide (19L/01UG); Campo Experimental Crato (Chança) (18K/01C); Castelo de Vide (17M/01G), Monforte (19M/01UG); Ribeira de Nisa (17M/04U); Vale do Peso (17L/02UG) (Figure 6.2) (SNIRH, n.d.).

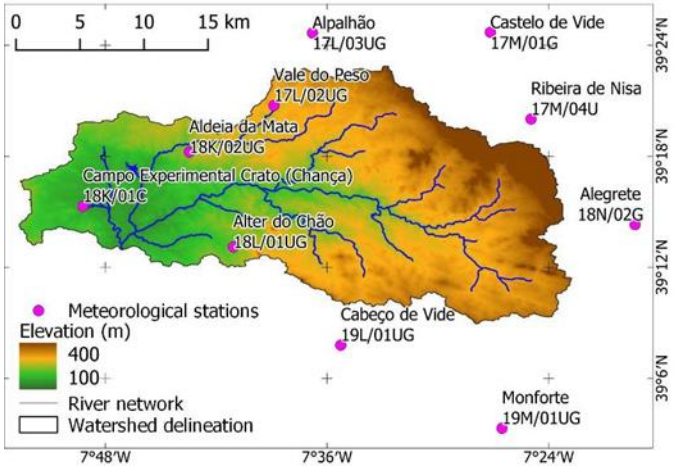

Figure 6.2 Most representative meteorological stations in the study area.

The set of stations presents an average annual precipitation of 385 mm, with Castelo de Vide and Monforte showing the maximum (824 mm) and the minimum (516 mm) average annual precipitation, respectively (Table 6.1).

Table 6.1 Average, minimum and maximum values, and number of completed years (total of daily values equals the number of days in the year) of annual precipitation registered in meteorological stations.

Station	Period	Annual precipitation			
		Average (mm)	Minimum (mm)	Maximum (mm)	Number of completed years
Aldeia da Mata	1979–2021	621	374	1056	26
Alegrete	1980–2021	794	457	1269	17
Alpalhão	1979–2021	717	365	1224	
Alter do Chão	2011–2021	614	101	1081	26
Cabeço de Vide	1931–2021	668	352	1184	90
Campo Experimental Crato (Chança)	1971–2021	662	323	973	68
Cartelo de Vide	1931–2021	824	46	1555	29
Monforte	1911–2020	516	256	1030	76
Ribeira de Nisa	1979–1985	673	452	962	88
Vale do Peso	1931–2021	757	401	1324	5

Daily average air temperature values were available from Campo Experimental Crato (Chança) station only, with a sample of 3995 values between 21 February 2001 and 14 July 2021. This dataset presents minimum and maximum air temperature values of −0.1°C and 36.1°C, respectively, and an average daily air temperature of 15.3°C. Thus, according to the Köppen–Geiger climate classification, the studied area is identified as having a Mediterranean hot summer climate (Csa) (Agencia Estatal de Meteorología (España), 2011).

Based on the delineation preformed with QGIS tools and the Digital Elevation Model provided by the European Environment Agency (EU-DEM) (European Digital Elevation Model (EU-DEM), 2019), the watershed is characterized by minimum, average, and maximum altitudes of 140 m, 235 m, and 723 m, respectively. According to European Soil Data Centre

(Panagos et al., 2012), the main soil mapping units are regosols (60%) and luvisols (40%). The main land uses are in areas of agro-forestry (30%), broad-leaved forest (25%), and non-irrigated arable land (19%) (CLC 2012, 2018).

Ponte Vila Formosa hydrometric station (18K/01H), placed on the outlet of the studied watershed, has records dating between 1 November 1979 and 30 May 2011. However, only the data in the period from 25 July 2001 until 31 December 2008 was considered because they cover the most recent period with enough continuous daily streamflow values to perform the model analysis. Table 6.2 shows the streamflow dataset characterization for both periods, including the minimum and maximum streamflow values as well as the average of those and the number of records.

Table 6.2 Characterization of the streamflow dataset (average, minimum, maximum, and standard deviation values, and number of records) of Ponte Vila Formosa hydrometric station between 1 January 1979 and 30 May 2011 (entire dataset) and 25 July 2001 and 31 December 2008 (studied period) (source: SNIRH, n.d.).

Period	Streamflow				
	Average ($m^3 s^{-1}$)	Minimum ($m^3 s^{-1}$)	Maximum ($m^3 s^{-1}$)	Std. Deviation ($m^3 s^{-1}$)	Number of records
1 November 1979−6 March 2019	3.8	0	272.8	12.7	7703
25 July 2001−31 December 2008	3.8	0	160.1	9.0	2645

The studied area is part of the watershed that drains to Maranhão reservoir, representing 30% of it. Together with Montargil reservoir, both were responsible for irrigating an area of 18,753.7 ha in Sorraia Irrigation District, in 2021 (ARBVS, n.d.). Additionally, this reservoir is one of the main recreative areas in the rural part of the Tagus River Basin District, where tourist and leisure activities have been growing in number (APA and ARH Tejo, 2012). Because of its relevance, and with some predictions pointing to an increase in the frequency and the severity of low flows in Southern Europe (Pörtner et al., 2022) and specifically in this area (Almeida et al., 2018), tools that demonstrate a good ability and capacity to estimate streamflow are essential for improving water management.

6.2.2 Neural Network Models

6.2.2.1 Artificial Neural Networks

Artificial neural networks (ANNs) were born from the attempt of scientists to mimic, in a computational environment, the capacity of the human brain to identify complex patterns and perform difficult operations, even in situations where those patterns are distorted or have a high degree of noise (ASCE, 2000). Thus, ANNs are based on simplified models of the biological neuron system, making use of the parallel distributed processing computational capacity to

store knowledge and make it available for use (Lohani et al., 2012). This capacity to identify given complex patterns makes ANNs able to solve large scale complex problems such as those of nonlinear modeling, classification, and control.

The attempt to reproduce the biological neuron system in ANNs models makes their structure composed of single elements, called nodes, units, cells, or neurons, where the information is processed. In each node, continuous linear or nonlinear transformation is applied as its net input. This transformation is called the activation function, and its result is the output signal of the node. The nodes are arranged in different layers, with each layer having the possibility to include a different number of neurons. The first layer of the ANN structure is named the input layer, while the last one is known as the output layer and consists of the model's predicted values. Between them, there can be one or more layers called hidden layers (Figure 6.3) (ASCE, 2000; Dolling and Varas, 2002).

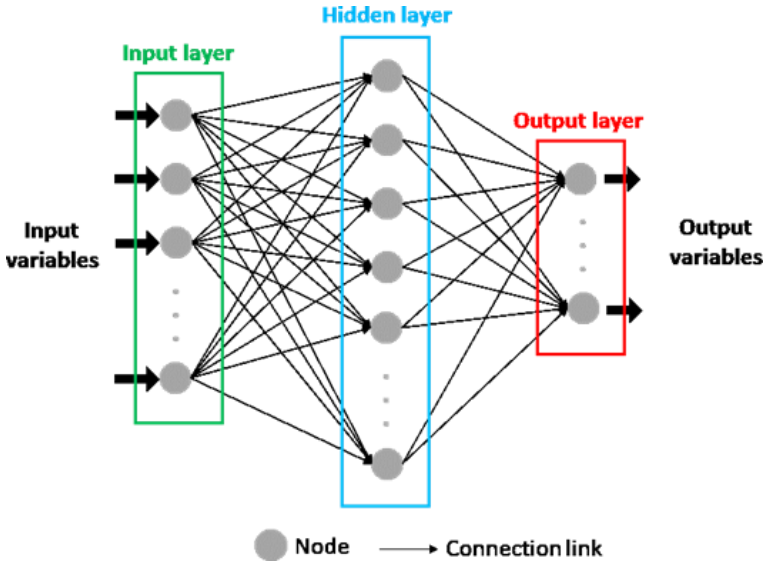

Figure 6.3 General structure of an artificial neural network.

All the nodes in a layer are connected to all the nodes in the previous and following layers through connection links which are responsible for passing signals between them, except for the input layer that receives the input variables instead of the output values of other neurons. Thus, the input layer only pretends to provide information to the network, which means that it can be considered a transparent layer. Each connection link is associated with a weight that represents its connection strength and modifies the activation function result, modifying, also, the output signal of each node that reaches the following neuron. Thus, after the ANN structure is defined, the output of the model can only be modified by changing the weights, which are adapted to correctly represent the desired output. The process of correcting or adapting the

weights, to better represent the model's output, is called the training process (ASCE, 2000; Dolling and Varas, 2002).

A detailed illustration of the general m^{th} node is presented in Figure 6.4. The scheme considers an input vector $I = (i_1, i_2, i_3, \ldots, i_n)$ where the subscript number indicates the node of the previous layer with which the connection is made. Each connection from the previous layer to the m^{th} node has an associated weight, with this set of weights being represented by vector $W_m = (w_{1m}, w_{2m}, w_{3m}, \ldots, w_{nm})$, where w_{nm} represents the connection weight from the nth node in the preceding layer to the present node.

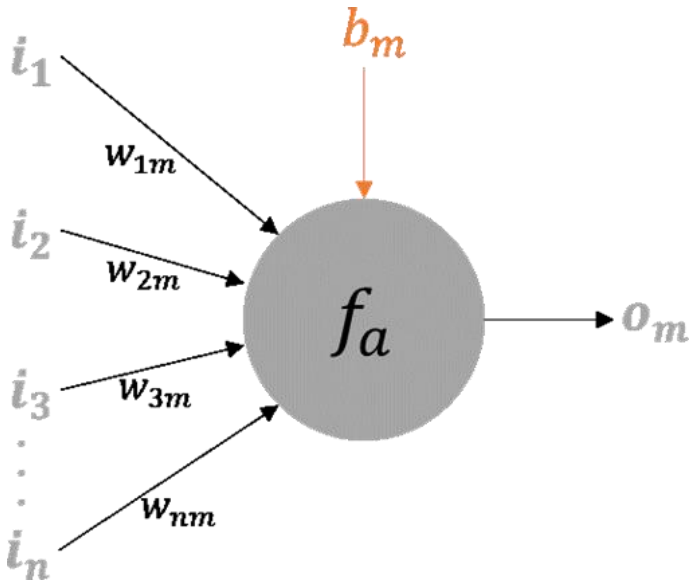

Figure 6.4 Node details (Reproduced with permission from ASCE, 2000).

In each node, an activation function is applied. This function is generically represented by Eq. 6.1:

$$o_m = f_a(I \cdot W_m - b_m) \quad \text{(Eq. 6.1)}$$

where o_m is the output value of the m^{th} node, f_a is the activation function, and bm represents the threshold value for this node, also known as bias. The activation function applied to a node determines its response to the total input signal it receives (ASCE, 2000). In the Keras package, the user can define his own activation function, however, in the present work, the activation functions to be tested were selected from those already available in the package. Thus, the linear, exponential linear unit, rectified linear unit, softsign, and hyperbolic tangent functions were considered. Table 6.3 presents a summary of the characteristics of those functions according to the Keras webpage (Keras Documentation: Layer Activation Functions, n.d.).

Table 6.3 Summary of Keras activation functions considered in the study.

Long name	Activation name	Equation
Linear	Linear	$f(x) = x$

Long name	Activation name	Equation
Exponential linear unit	Elu	$f(x) = \begin{cases} \alpha(e^x - 1), x < 0 \; and \; \alpha > 0 \\ x, \quad x \geq 0 \end{cases}$
Rectified linear unit	Relu	$f(x) = \max(x, 0)$
Softsign	Softsign	$f(x) = \frac{x}{\lvert x \rvert + 1}$
Hyperbolic tangent	tanh	$f(x) = \frac{\sin(x)}{\cosh(x)} = \frac{e^x - e^{-x}}{e^x + e^{-x}}$

An ANN can be classified as single (Hopfield nets), bilayer (Carpenter/Grossberg adaptive resonance networks), or multilayer (mostly backpropagation networks) as a function of the number of layers present in its structure (ASCE, 2000). According to Dolling and Varas (2002) a single-layer network is adequate for representing a linear model, while multiple-layer networks are more suitable for nonlinear models. On the other hand, the classification of an ANN can be based on the information and the processes' flow direction. Thus, an ANN can be classified as a feedforward or a recurrent network. In the first case, the information and the processes' flows only occur in one direction, starting from the first layer, the input layer, passing through one or more hidden layers, and ending in the final layer, the output layer. Here, the output of a node only depends on the received inputs and respective weights from previous layers. A recurrent network distinguishes itself from a feedforward network by having at least one feedback loop (Haykin, 1999), i.e., the information passes through the nodes from the input layer to the output layer and vice versa. This process, with the information flowing in both directions, consists of the usage of the previous network outputs as current inputs (ASCE, 2000). According to Haykin (1999) the feedback loops have a significative impact on the learning capacity and performance of these networks. Recurrent networks also involve the presence of unit delay elements which result in nonlinear dynamical behavior.

Multi-layer perceptron models. Multi-layer perceptron (MLP) models are a type of feedforward artificial neural network. Usually, MLP models have a back-propagation algorithm associated with the training process, which implies a feedforward phase and a backward phase (Cigizoglu, 2003). During the first phase, the input data flows forward in the network structure to estimate the output values, while in the second phase the differences between the output values estimated by the network and the respective observed values force the adaptation of the connection weights (Eberhart and Dobbins, 1990). Based on the architecture described before, MLP models are composed of three or more layers of artificial neurons, meaning that these types of models have one or more hidden layers (Maier et al., 2010).

Considering the terminology of the Keras package, MLP models are composed of dense layers, also known as fully connected layers. The implementation of one dense layer implies

the definition of the number of neurons on that layer. Besides that, the layers' activation functions are also defined by the user. However, more arguments can be set, such as bias (true by default) and its initial value (zero by default). Thus, in this study, an input layer and an output layer were considered, with the number of hidden layers being 0 (no hidden layer), 1, 2, 3, or 4. For the input layer, the number of neurons and the activation function were optimized, with the number of neurons tested varying between 1 and 6 or assuming the size of the number of input–output pairs of the set used to train the model (i.e., the training dataset, which will be elaborated further). The activation function for this layer was selected by taking into account the linear, exponential linear, and rectified linear unit functions. The option of adding a dropout layer, with a rate of 0.1 or 0.2, after the input dense layer was tested. The dropout layer is used to randomly set the input units with a frequency related to the defined rate (Keras Documentation: Dropout Layer, n.d.). This dropout layer only has an impact during the training process. For the hidden layers, the activation function was selected from a set including the softsign, linear, elu, and relu functions, and the number of neurons was defined with consideration of the same values presented for the input layer but independently of those. For these layers also, the existence (or not) of a dropout layer for each hidden layer in the structure was tested considering the same rate values. Finally, the output layer, with only one neuron, could assume a softsign or a linear function as an activation function. Table 6.4 presents a summary of the structure's characteristics which were considered to optimize the MLP model.

Table 6.4 Structure characteristics tested for MLP model.

Layers	Number of layers	Number of neurons	Activation function	Dopout after dense	Droput rate
Input dense	1	1, 2, 3, 4, 5, 6 or training set size	Linear, elu or relu	Yes/No	0.1 or 0.2
Hidden dense	0, 1, 2, 3 or 4	1, 2, 3, 4, 5, 6 or training set size	Softsign, linear, elu or relu	Yes/No (one by each hidden layer)	0.1 or 0.2
Output dense	1	1	Softsign or linear	-	-

Long short-term models. Long short-term models (LSTMs) are types of recurrent neural network (RNN) models. Although they are structurally similar to ANNs, i.e., they are composed of layers connected between them with cells representing neurons, RNNs have a recurrent hidden unit that allows the model to implicitly maintain historical information about all the past events of a sequence (Elman, 1990; LeCun et al., 2015; Lipton et al., 2015). In each instance, the recurrent hidden unit receives as input the information corresponding to that instance but also to the previous instance (Ni et al., 2020). This makes RNN very suitable for time-series data modelling (Bengio et al., 1994; Hochreiter and Schmidhuber, 1997; Saon and

Picheny, 2017), though a problem has already been identified which is related to the vanishing/exploding gradient during the learning process, which results in the loss of the ability of RNN to learn long-distance information. LSTM structure, proposed by Hochreiter and Schmidhuber (1997) emerged from the necessity to solve the vanishing/exploding gradient problem, and it has the capacity to learn long-term dependencies (Xu et al., 2020). As described by Ni et al. (2020), who cite LeCun et al. (2015) the LSTM solution makes use of a memory cell working as a gated leaky neuron, since "it has a connection to itself at the next step that has a weight of one, but this self-connection is multiplicatively gated by another unit that learns to decide when to clear the content of the memory". As referred to by Xu et al. (2020) there are several applications demonstrating the potential of LSTM in watershed hydrological modeling, namely, in river flow prediction (Shen, 2018; Kratzert et al., 2018).

Using the Keras package, the structure of LSTM models is based on LSTM layers. Thus, in this study, the LSTM solution is composed of at least one input layer of the LSTM type and one output dense layer. For the input layer, the number of neurons was optimized with 4, 8, 16, or 32 units, while in the output layer the number of neurons was set to 1 and the activation function was defined as linear. The model's structure was optimized with consideration of the existence of 0, 2, or 4 hidden LSTM layers between the input and output layers. If no hidden layer is added, the model is composed only of the input and the output layers, but when two hidden LSTM layers are considered, the number of neurons in the first hidden layer is double that in the input layer and the second hidden layer is equal to the input layer (e.g., input layer: 4 neurons; 1st hidden layer: 8 neurons; 2nd hidden layer: 4 neurons). When four hidden LSTM layers are considered, after the input layer, a LSTM layer with twice the number of neurons of the input layer is considered, followed by another LSTM layer composed by the triple of the number of neurons considered in the input layer. The third and the fourth hidden layers are composed of twice the number of neurons and the same number of neurons of the input layer, respectively (e.g., input layer: 4 neurons; 1st hidden layer: 8 neurons; 2nd hidden layer: 12 neurons; 3rd hidden layer: 8 neurons; 4th hidden layer: 4 neurons). All these LSTM layers were implemented with consideration of the activation function defined by the default for this type of layer in the Keras package, which is the hyperbolic tangent (tanh) function. Table 6.5 shows a summary of the characteristics optimized for the LSTM model.

Table 6.5 Structure characteristics tested for the LSTM model, with n_{input} representing the number of neurons in the input layer.

Layers	Number of layers	Number of neurons	Activation function
Input LSTM	1	4, 8, 16 or 32	tanh (by default)
Hidden LSTM	0, 2 or 4	If hidden layers = 2:	tanh (by default)

Layers	Number of layers	Number of neurons	Activation function
		1st layer: $2\times n_{input}$ 2nd layer: n_{input} If hidden layers = 4: 1st layer: $2\times n_{input}$ 2nd layer: $3\times n_{input}$ 3rd layer: $2\times n_{input}$ 4th layer: n_{input}	
Output dense	1	1	linear

6.2.2.2 Convolutional Neural Networks

Developed by LeCun and Bengio (1995) to automatically identify handwritten digits, convolutional neural networks (CNNs) have origins in artificial neural networks but, instead of fully connected layers, CNNs have local connections, lending more importance to high correlations with nearby data (Wang et al., 2019). This correlation with nearby data is achieved using convolutional filtering, which means that these networks work based on shared weights with filter coefficients being shared for all input positions (Wang et al., 2019; Barino et al., 2020; Chong at al., 2020). As Chong et al. (2020) state, knowing the number of filters and their values are essential for capturing the patterns present in the data. These characteristics make CNNs more suitable for identifying local patterns in images but also in time series data (Bengio, 2009; Deng, 2014), in which a certain identified pattern in a time frame can be recognized in another one independently of the time when both happened (Tao et al., 2019). On the other hand, one of the weaknesses of CNNs is the high time consumption needed for training (Huang et al., 2020).

According to Huang et al. (2020) and Shu et al. (2021) a CNN is usually composed of five layers, namely, the input, convolution, pooling, fully connected, and output layers. As the names suggest, and as in ANNs models, the input layer receives the input data, in a vector or matrix shape, while the output layer is responsible for generating the model's outputs. After the input layer, there is a convolutional layer which is responsible for the convolutional operation which considers the weights of convolutional neurons (filter) and local regions. Following the convolutional operation, a linear or nonlinear transfer can be applied. The output of the convolutional layer is, after, sent to the pooling layer. This layer will divide the data received from the convolutional layer into sub-regions where a maximizing or an averaging operation is applied, followed by a size reduction and an improvement of the translation invariance. The pooling layer's result is then passed to a fully connected layer that is the same as those described in ANNs models, and its output is sent to the output layer, which is also fully connected with the actual layer (Huang et al., 2020).

Since in the present study the predictions were made based on time series data, the CNN model was developed based on one-dimensional (1D) convolutional layers, also known as temporal convolutional layers. In this kind of layer, the user must set the number of filters and the kernel size, with filters being defined as the dimensionality of the output space, i.e., the number of output filters in the convolutional layer, and the kernel size being the value that specifies the length of the 1D convolutional window. The structure of the CNN model developed here has one input convolutional layer and one output dense layer. The output layer has just one neuron, and softsign, linear, elu, and relu functions were tested as activation functions. For the convolutional input layer, 8, 16, and 32 were the numbers of filters tested, and they were combined with a kernel size of 1, 5, or 10. The padding was defined as causal, which is usually applied in 1D convolutional layers and allows the addition of zeros at the start of the dataset. The activation function was not defined, which means that no activation function was considered. After the convolutional input layer, a pooling layer for one-dimensional data (MaxPooling1D layer) was added with a pool size of 1 or 2, according to the number of input variables. After the convolutional input layers, the model was tested to have none or 1 more convolutional layer followed by none, 1 or 2 dense layers. If the convolutional hidden layer existed, both the number of filters and the kernel size were tested as 8, 16, and 32. The padding was also set to causal, and no activation function was applied. After this layer, a MaxPooling1D layer was added with a pool size of 1 or 2, following the same criteria as in the input layer. Following the convolutional layers, a flatten layer was added. Thus, for each hidden dense layer, a dropout layer could be considered, with a rate of 0.1 or 0.2. The number of nodes in hidden dense layers was elected from the sets 3, 5, and 10, while softsign, linear, elu, and relu functions were tested as activation functions. Table 6.6 presents a summary of the optimization of the convolutional model's structure.

Table 6.6 Structure characteristics tested for the convolutional model.

Layers	**N. of layers**	**N. of filters**	**Kernel size**	**Pooling size**	**N. of neurons**	**Activation function**	**Dropout after dense**	**Dropout rate**
Input convolutional	1	8, 16 or 32	1, 5 or 10	-	-	None (by default)	-	-
MaxPooling1D	1	-	-	1 or 2	-	-	-	-
Hidden convolutional	0 or 1	8, 16 or 32	8, 16 or 32	-	-	None (by default)	-	-
MaxPooling1D	1	-	-	1 or 2	-	-	-	-
Flatten	1	-	-	-	-	-	-	-
Hidden dense	0, 1 or 2	-	-	-	3, 5 or 10	softsign, linear, elu or relu	Yes/No (one by each hidden layer)	0.1 or 0.2

Layers	N. of layers	N. of filters	Kernel size	Pooling size	N. of neurons	Activation function	Dropout after dense	Dropout rate
Output dense	1	-	-	-	1	softsign, linear, elu or relu	-	-

6.2.2.3 Training Process

The training, or learning, process of a neural network aims to find the optimal values of the weights in artificial and recurrent neural networks and of the filters in convolutional neural networks (ASCE, 2000; Chong et al., 2020). This goal is reached by changing and adapting those values to optimize the model's performance, minimizing the error function adopted in the study (ASCE, 2000). The adaptation of the weights and the filters is made with consideration of a continuous process, during which these values are changed by the stimulation of the environment in which the network is embedded. In Keras, and by default, the weights of all the types of layers used in this study were initialized with the Glorot uniform initializer (Keras Documentation: Layer Weight Initializers, n.d.), while the bias values were initialized as zero. According to Haykin (1999) and ASCE (2000) the training process can be made by following different algorithms, with most of them being classified as supervised or unsupervised training. Unsupervised training is also known as learning without a teacher and is based on adapting the connection weights of the neural network using only an input dataset in a way that ensure that the neural network will group those input patterns into classes with similar properties. However, in this study, only supervised training, also known as learning with a teacher, was employed. The learning-with-a-teacher algorithm implies the existence of a teacher that knows the environment and is responsible for the training process guidance (ASCE, 2000). To perform this process, a set of input–output examples must exist, where the inputs are the forcing variables, and the outputs are the effect variables. The basis of this method is to expose the neural network to the input variables and to adapt weights and threshold values in each node to better mimic the output variables belonging to the teacher. Thus, the main goal relies on the minimization of an error function selected by the user, which represents the difference between the values generated by the neural network and the target values, represented by the output variables of the teacher. When the training process ends, the neural network should be able to generate good-quality results given the new sets of inputs.

In the present study, training algorithms were selected from the set made available by the Keras package, and their optimizers were named. Thus, six different optimizers were considered and tested: stochastic gradient descent (SGD), AdaGrad, RMSprop, Adam,

AdaMax, and Nadam. All of them are based on the gradient descent algorithm, which has the main goals of minimizing an objective function ($J(\theta)$) dependent on the parameters of a model ($\theta \in R^d$) and adapting those parameters in the opposite direction of the gradient of the objective function ($\nabla\theta J(\theta)$) (Ruder, 2017). The changes in the parameters' values are estimated according to a learning rate which determines the size of the steps to reach the minimum value of the objective function. A detailed description of the optimizers is given below.

To perform the training process with the Keras package, the constructed model needs to be compiled. It is in the compilation function where the arguments of the optimizer are set. Besides the optimizer parameters, the user must select the loss function and the metrics for model evaluation purposes. The loss function is responsible for describing what the user wants to minimize through the learning algorithms (Ebert-Uphoff et al., 2021). Thus, the choice of the loss function is extremely important for the good performance of the model during the training process. The metrics' main goal is the follow-up of the selected criteria during and after the training process, which allows the user to prematurely detect the model's problems and weaknesses (Ebert-Uphoff et al., 2021). In the present study, the mean square error was selected to be both the loss function and the metric.

The training process of a neural network, which includes a validation of the model, is followed by the testing process. For training, validation and testing tasks, a dataset should be defined, namely the training, validation, and test datasets (Maier and Dandy, 2000). Thus, as the name indicates, the training dataset is used to train the neural network during the training process, i.e., to optimize the model parameters. According to Wu et al. (2014), the test set is also used during the training process to avoid over-fitting the model, while the validation set aims to assess the performance of the trained model independently. However, for Chong et al. (2020) and in the documentation available on the Keras webpage for "Model training APIs" (Keras Documentation: Model Training APIs, n.d.), the fit method considers an argument named "validation_data", which is the data with which the trained model will be evaluated at the end of each epoch, allowing the over-fitting analysis. Thus, in this case, the test dataset is the one with which the user can assess the model's performance after the training and validation processes are carried out. Consequently, the input dataset for the present study was divided into three different datasets following Keras website information, with the training set corresponding to 70% of the data, the validation set being 20% of the data, and the test set being the remaining 10%.

Stochastic gradient descent (SGD). The stochastic gradient descent (SGD) performs a parameter update for each training input–output example. Thus, the mathematical formulation for this method is:

$$\theta = \theta - \eta \cdot \nabla_\theta J(\theta; x^{(i)}; y^{(i)}) \quad \text{(Eq. 6.2)}$$

where η is the learning rate and the $x^{(i)}$ and $y^{(i)}$ pair represents the input–output example. The SGD can be used to learn online. However, when its frequent updates occur with a high variance, it can cause the objective function to fluctuate drastically.

This method can present some difficulties in searching the exact minimum, jumping between local minima, but when the learning rate decreases slowly, this algorithm tends to find the local and global minimum for non-convex and convex optimization, respectively (Ruder, 2017).

The mode of implementation available in the Keras package (Keras, n.d.) allows the definition of three different arguments that can influence the algorithm's behavior, namely, the learning rate and momentum values and the activation of the Nesterov momentum. As Ruder (2017) describes, the momentum method helps the convergence of the SGD algorithm in areas where the surface curves of the objective function are more steeply in one dimension than in another, giving the algorithm the capacity to predict the next step of optimization and to avoid jumps that are too big between iterations, indicating a significant improvement in the algorithm's performance. In the Keras package, the default value for momentum is 0.0, however, in this study, it was set to 0.9 (Ruder, 2017). Additionally, the Nesterov option is not used in Keras by default, but it was used in this study. Finally, the algorithm's learning rate was tested as 1×10^{-4}, 1×10^{-3}, and 1×10^{-2}.

AdaGrad. The AdaGrad algorithm (Duchi et al., 2011), i.e., the adaptive gradient algorithm, has as its main strength the capacity to adapt the learning rate to the parameters using larger updates for infrequent parameters and smaller updates for frequent parameters (Ruder, 2017). Thus, this algorithm does not require the manual tuning of the learning rate, with the most common value for this parameter being 0.01 according to Ruder, 2017. However, the main limitation of this algorithm is the fact that the learning rate can become infinitesimally small to a point where the algorithm cannot improve the results, since that value is shrunk according to the accumulation of squared gradients.

In the implementation available in the Keras package, three main arguments can be defined for the AdaGrad algorithm, namely, the learning rate, the initial accumulator value, which is the starting value for the accumulators, and the epsilon, which is used to maintain

numerical stability. Although the default values for those parameters are, respectively, 0.001, 0.1, and 1×10^{-7}, in the present study, the learning rate was set to 0.01, while the epsilon was tested as 1×10^{-7} or 1×10^{-8}.

RMSprop. The RMSprop algorithm was developed to overcome AdaGrad's problem, which is related to the extremely rapid decrease in the learning rate. Thus, this algorithm divides the learning rate by an exponentially decaying average of squared gradients (Ruder, 2017). In the Keras package, the implementation of this algorithm involves five arguments: the learning rate, with a default value of 0.001; the discounting factor for the history/coming gradient, which is by default 0.9; the momentum value, set to 0.0; the epsilon, already defined in AdaGrad and with a default value of 1×10^{-7}; the centered option, which allows the normalization of the gradients by the estimated variance of the gradient if it is activated. By default, this last option is deactivated, which makes the gradients normalized by the uncentered second moment. In the present study, the learning rate for RMSprop was set as 0.01, and the epsilon value was tested as 1×10^{-7} or 1×10^{-8}.

Adam. The Adam optimizer, the name of which comes from adaptive moment estimation, adapts the learning rate value for each parameter, like the RMSprop optimizer. However, the Adam optimizer considers an exponentially decaying average of past gradients, similarly to the momentum method described for the SGD optimizer. According to Kingma and Ba (2017) the Adam method is simple to implement, it is computationally efficient, its memory requirements are low, it is invariant to the diagonal rescaling of the gradients, and it has a good performance for noisy problems with large amounts of data. In the Keras package, the implementation of the optimizer referred to implies the definition of five arguments, namely, the learning rate, beta_1, beta_2, epsilon, and amsgrad, with default values of 0.001, 0.9, 0.999, 1×10^{-7}, and deactivated, respectively. With the learning rate and the epsilon arguments already defined, beta_1 represents the decay rate for the 1st moment estimates, beta_2 represents the decay rate for the 2nd moment estimates, and the amsgrad option allows the user to use the AMSGrad variant of the Adam algorithm (more information can be found in Reddi et al., 2019). For Ruder, 2017, the beta_1, beta_2, and epsilon values should take the values 0.9, 0.999, and 1×10^{-8}, respectively. Thus, in this study, the learning rate was optimized, taking into account the values 1×10^{-4}, 1×10^{-3}, and 1×10^{-2}, while the epsilon parameter took the value 1×10^{-7} or 1×10^{-8}.

AdaMax. The AdaMax algorithm is an extension of Adam (Kingma and Ba, 2017). Thus, AdaMax improves the stability of the Adam optimizer based on the infinity norm. In the Keras package, the implementation of AdaMax involves the same arguments as that of Adam, and

both the learning rate and epsilon were tested for the values already presented for the Adam algorithm.

Nadam. The Nesterov-accelerated adaptive moment estimation (Nadam) algorithm is the result of the combination of Adam and the Nesterov accelerate gradient (NAG) (Ruder, 2017). Nadam was developed due to the fact that Adam uses the regular momentum component, which has a lower performance than the NAG. Thus, Dozat, 2016, developed the Nadam optimizer and demonstrated that this optimizer can improve the speed of convergence and the quality of the learned models when compared to the Adam algorithm. In the Keras package, Nadam has the same arguments as the Adam optimizer. Thus, the learning rate and the epsilon were tested considering the same values presented for the Adam algorithm.

6.2.2.4 Input Variables

The dataset considered in this study is composed of the output variable and the forcing variables. As referred to before, the main goal of the neural network being developed was to estimate the daily streamflow in a cross-section of a river where the hydrometric station is located, so the output variable would be the daily streamflow at this point. On the other hand, it is necessary to define the input variables, with this task being referred to by several authors as crucial to reach in a successful model (ASCE, 2000; Dolling and Varas, 2002; Maier et al., 2010; Wu et al., 2014; Juan et al., 2017). However, Maier and Dandy (2000) indicate that most of the authors with studies in the field of prediction and forecasting water resources variables with ANN models give little attention to the former task, with input variables being determined on an ad hoc basis or by using a priori system knowledge. For predictions with a daily timestep, Cigizoglu (2003), Nacar et al. (2018), and Huang et al. (2020) only used observed streamflow values from days previous to their study while considering different time lags. Besides the streamflow, Riad et al. (2004) predicted the streamflow of a specific day considering daily precipitation values from previous. On the other hand, Besaw et al. (2010) used only meteorological data, namely, total precipitation and average temperature, to predict streamflow. Ni et al. (2020), Dolling and Varas (2002), and Yang et al. (2019) also considered runoff and/or different meteorological variables, such as precipitation, temperature, sunshine hours, snow water, relative humidity, potential evapotranspiration, and so on, as the forcing data to predict streamflow values with monthly or annual timesteps. In the present study, daily total precipitation data or the combined use of daily total precipitation and daily average temperature were considered forcing variables. The meteorological data were obtained from the ERA5-Reanalysis dataset (Hersbach et al., 2020), which is a gridded product with a resolution of 31

km and an hourly timestep. Thus, the date values belonging to the cells in which the center is within the watershed delineation were considered. The hourly total precipitation and the hourly average air temperature were collected, and both were averaged with consideration of the number of cells within the watershed. The watershed's hourly total precipitation and hourly air temperature were then accumulated and averaged, respectively, considering a daily timestep. The meteorological data collected cover the same period as the one selected for the streamflow data, which corresponds to the period between 25 July 2001 and 31 December 2008. Since a meteorological model was input, no gaps existed in the precipitation and air temperature time series, with records totalizing 2718 values for each meteorological variable. Table 6.7 presents the time series statistical characterization for both variables. In contrast to other studies, in this work, the dependence of the forecasted streamflow on previous streamflow values was avoided. This decision was related to the fact that, if the neural network produced in this study was used to estimate streamflow values in periods without observed data, such as in climate change scenarios, or implemented as an operational tool to predict the streamflow a few days in advance, the input streamflow values would have been those values already estimated by the neural network itself, which would have contained a certain level of error and uncertainty and could have led to the exacerbation of errors and uncertainty in the estimations. Additionally, the use of forcing variables derived from observed data was avoided because it would have been impracticable to feed the trained neural network with that kind of data to predict future events. However, this did not invalidate the fact that an analysis of the controlling factors of the hydrological response could be performed to investigate if there were other factors that could have had a significant impact on the streamflow estimations.

Table 6.7 Meteorological input data characterization (precipitation and air temperature, period 25 July 2001–31 December 2008).

Meteorological variable	Average	Minimum	Maximum	Std. Deviation
Daily total precipitation (mm)	1.59	0	45.50	4.24
Daily air temperature (°C)	16.09	1.77	34.74	6.46

The daily total precipitation and air temperature values were here aggregated with consideration of different periods (2, 3, 4, 5, and 10 days or 10, 30, and 60 days), with precipitation being accumulated and air temperature being averaged in those periods. The periods elected here were considered to better understand the impact of short and long-term intervals on the results. On the other hand, the delay (1, 2, 3, 4, 5, 6, and 7 days) of total precipitation and air temperature values was considered. Thus, the impact of the aggregation periods or the time lags, and the combination of both, was tested in this study, resulting in 6

different scenarios that were established for the usage of only the total precipitation or of the pair total precipitation plus air temperature. Table 6.8 presents the summary of the tested scenarios.

Table 6.8 Tested scenarios and dataset dimensions (Acc. TP—accumulated days of total precipitation; Ave. AT—averaged days of air temperature).

	Total precipitation (TP) or Total Precipitation + Air Temperature (TP&AT)					
Scenario	**Time lag (days)**	**Acc. TP (days)**	**Ave. AT (days)**	**Training set size**	**Validation set size**	**Test set size**
TP1	-	1	-	1851	529	265
TP2	-	1,2,3,4,5,10	-	1845	527	264
TP3	-	10,30,60	-	1810	517	259
TP4	1,2,3,4,5,6,7	-	-	1846	527	265
TP5	1,2,3,4,5,6,7	1,2,3,4,5,10	-	1810	517	259
TP6	1,2,3,4,5,6,7	10,30,60	-	1845	527	264
TP&AT1	-	1	1	1851	529	265
TP&AT2	-	1,2,3,4,5,10	1,2,3,4,5,10	1845	527	264
TP&AT3	-	10,30,60	10,30,60	1810	517	259
TP&AT4	1,2,3,4,5,6,7	-	-	1846	527	265
TP&AT5	1,2,3,4,5,6,7	1,2,3,4,5,10	1,2,3,4,5,10	1810	517	259
TP&AT6	1,2,3,4,5,6,7	10,30,60	10,30,60	1845	527	264

The input dataset was handled and prepared with the Pandas (McKinney, 2010) and Scikit-learn (Pedregosa et al., 2011) packages. Thus, with the Pandas package, all the accumulations, averages, and delays were performed, and days with data missing were excluded. The resulting dataset was then scaled using MinMaxScaler in the scikit-learn package to improve the learning process and avoid convergence problems. The range to scale each column of the dataset independently was set to [0,0.9] and the new values of the columns were calculated according to:

$$v_{scaled} = \frac{v - v_{min}}{v_{max} - v_{min}} * (M - m) * m \qquad \text{(Eq. 6.3)}$$

where v_{scaled} is the new value in the range [0,0.9], v is the original value in the dataset, v_{max} and v_{min} are the maximum and minimum values present in the column being scaled, respectively, M is the maximum value of the range, and m is the minimum value of the range. The range was selected considering that the maximum streamflow in this section could not be represented in the period analyzed.

Finally, because of the different time lags and aggregation periods considered, the size of the input dataset varied, with the size of the training, validation, and test datasets also being different for the different scenarios. After removing the streamflow gaps, the size of those datasets for each scenario was presented in Table 6.8.

6.2.2.5 Tunning Parameters

Besides the optimization of the weights or the filters during the model's training process, the structure of the model should also be optimized. The best structure may be considered the one that demonstrates the best performance in terms of error minimization and, at the same time, that presents its simplest form (ASCE, 2000). Usually, the definition of a neural network structure is accomplished by a trial and error procedure, which is used to define the number of hidden layers and their number of nodes and filters or their kernel size. The number of nodes in the input and output layers is problem-dependent and, consequently, they are not an optimization target (ASCE, 2000; Chong et al., 2020).

To avoid all the effort involved in manual structure optimization, the KerasTuner package was used to discern the best structure for each type of model studied in this work (MLP, LSTM, and CNN) in a more efficient way. This package allows the user to define ranges or values to test different parameters in the model's structure as well as the model's structure itself by, for example, providing the possibility to vary the number of hidden layers in the model. The parameters that can be optimized by the user, and that are set before the model's training process, are known as hyper-parameters. In this study, the hyper-parameters optimized included the number of nodes in each layer in the MLP and LSTM models and the number of filters and the kernel size in the CNN model. The model's structure was optimized with consideration of the number of hidden layers and the activation functions of the hidden, input, and output layers. The optimized hyper-parameters and the structures' composition were already discussed and are summarized in Table 6.4 for the MLP models, Table 5 for the LSTM models, and Table 6.6 for the CNN models. As referred to before, some hyper-parameters related to the training algorithms, such as the learning rate or the epsilon value, were further optimized using KerasTuner. Table 6.9 presents a summary of the hyper-parameters tuned for each training algorithm applied in this study.

Table 6.9 Summary of hyper-parameters tuned for training algorithms.

Training algorithm	**Hyper-parameters optimized**	
	Possible values tested for learning rate	**Possible values tested for ε**
SGD	1×10^{-4}, 1×10^{-3} or 1×10^{-2}	-
AdaGrad	-	1×10^{-7} or 1×10^{-8}
RMSprop	-	
Adam	1×10^{-4}, 1×10^{-3} or 1×10^{-2}	
AdaMax		
Nadam		

The batch size and the number of epochs were also optimized using a tuner customized by the user and based on the Bayesian optimization in KerasTuner. The batch size here can take

values from 10 to 50, in steps of 10, indicates the number of samples collected from the training dataset, and is used to make one update to the network parameters (Radiuk, 2017). This means that the choice of batch size has an impact on the convergence time and the fitting performance during the training process, with smaller batch sizes conducting a faster computation but forcing more samples to be passed through the model to achieve the same error because the number of updates per training iteration is lower. On the other hand, the number of epochs represents the number of times that the entire dataset flows in the model (Airola and Hager, 2017; Afaq and Rao, 2020). In this study, it was possible to assume values for this parameter between 100 and 400 in steps of 50 and with a default value of 150. Finally, Bayesian optimization (Snoek et al., 2012) is an algorithm developed to efficiently guide the search for the best combinations of hyper-parameters among the search space of a model, which is composed of different combinations of hyper-parameter values (Jin et al., 2019). The usage of the KerasTuner package implies the definition of the maximum number of model configurations (trials) that should be tested, and this value was set to 500. From the entire set of trials, the tuner elects the model with the best performance, in terms of the resulting values of the validation dataset, as the best model, i.e., the model where the predicted values best fit the output variable.

Therefore, 12 different combinations of input variables (Table 6.8) were tested in combination with each one of the three types of neural networks considered in this study, namely, MLP, LSTM, and CNN. For each pair of input variables and each type of neural network, the hyper-parameters were optimized and the performance of six different training algorithms (SGD, AdaGrad, RMSprop, Adam, AdaMax, and Nadam) was tested. In total, the hyper-parameters of 216 solutions (72 for MLP, 72 for LSTM, and 72 for CNN) were tuned with a total of 500 trials for each solution. For better understanding, Figure 6.5 presents a schematic summary of how the tests were carried out.

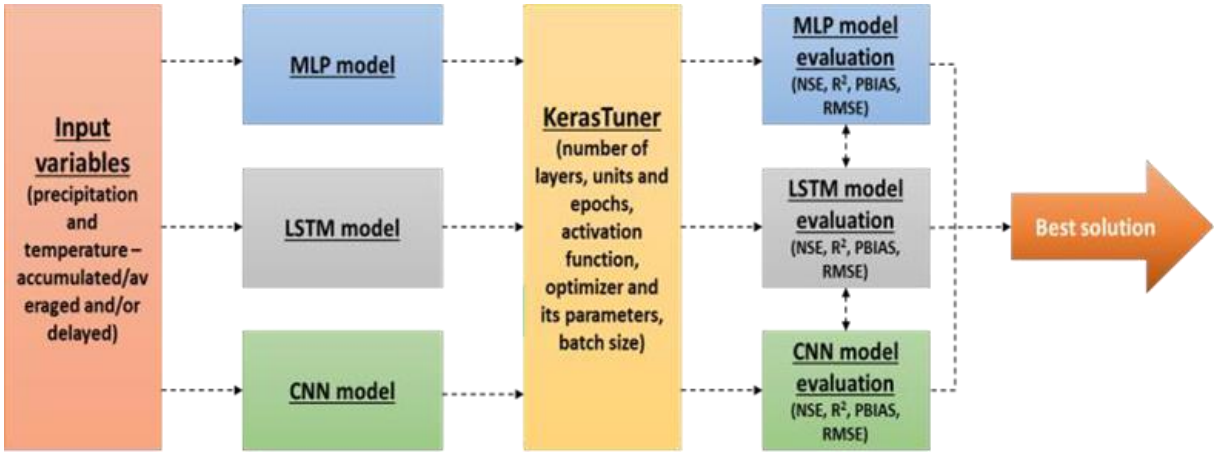

Figure 6.5 Schematic summary of the tests performed.

6.2.3 Model Evaluation

According to ASCE (2000) the performance of a neural network model can be evaluated by exposing the developed model to a new set of data containing values that had never been used during the model training process. Thus, in this study, the best solution for each combination of input variables, type of model and training algorithm was evaluated by considering the test dataset defined before. This means that each solution was run with consideration of the input variables present in the test dataset. The performance of each run was then evaluated by comparing the model results with the observed flow values. This comparison included a visual analysis and the calculation of four statistical parameters, namely, the coefficient of determination (R^2), the percent bias (PBIAS), the root mean square error (RMSE), and the Nash–Sutcliffe efficiency (NSE), which were computed, respectively as follows:

$$R^2 = \left[\frac{\sum_{i=1}^{p} \left(Q_i^{obs} - Q_{mean}^{obs}\right)\left(Q_i^{sim} - Q_{mean}^{sim}\right)}{\sqrt{\sum_{i=1}^{p} \left(Q_i^{obs} - Q_{mean}^{obs}\right)^2} \sqrt{\sum_{i=1}^{p} \left(Q_i^{sim} - Q_{mean}^{sim}\right)^2}} \right]^2 \quad \text{(Eq. 6.4)}$$

$$PBIAS = \frac{\sum_{i=1}^{p} (Q_i^{obs} - Q_i^{sim})}{\sum_{i=1}^{p} Q_i^{obs}} \times 100 \quad \text{(Eq. 6.5)}$$

$$RMSE = \sqrt{\frac{1}{p} \sum_{i=1}^{p} \left(Q_i^{obs} - Q_i^{sim}\right)^2} \quad \text{(Eq. 6.6)}$$

$$NSE = 1 - \frac{\sum_{i=1}^{p} (Q_i^{obs} - Q_i^{sim})^2}{\sum_{i=1}^{p} (Q_i^{obs} - Q_{mean}^{obs})^2} \quad \text{(Eq. 6.7)}$$

where Q_i^{obs} and Q_i^{sim} are the flow values observed and estimated by the model on day i, respectively. Q_{mean}^{obs} and Q_{mean}^{sim} are the average flow values, which consider the observed and modeled values in the period comprehended in the test dataset, and p is the total number of days/values in this period. According to Moriasi et al., 2007, the model's performance is considered satisfactory when NSE > 0.5, PBIAS ± 25%, and R^2 > 0.5. The RMSE represents the standard deviation of the residuals (the difference between the predictions and the observed values) and, consequently, lower values mean better model performance.

The model solution which combines the best statistics and the best visual fit between the modeled and observed values was elected as the one with a higher probability of better representing the watershed in the case study (Figure 6.5).

6.3 Results

The distribution of the values of the statistical parameters for the scenarios of each neural network considered (multi-layer perceptron, long sort-term model, and convolutional neural network) are presented in Figure 6.6. The dispersion of the markers presented in those graphs is a consequence of testing different optimizers, with most of the scenarios presenting a maximum of 6 markers, corresponding to the 6 optimizers tested. However, in some scenarios of optimizer–NN model combinations, the training process did not converge, and so the respective marker is not represented in the graph. In Appendix 6A, Table 6A.1, the statistical parameters are presented in detail for each scenario and each tested optimizer according to the NN model considered.

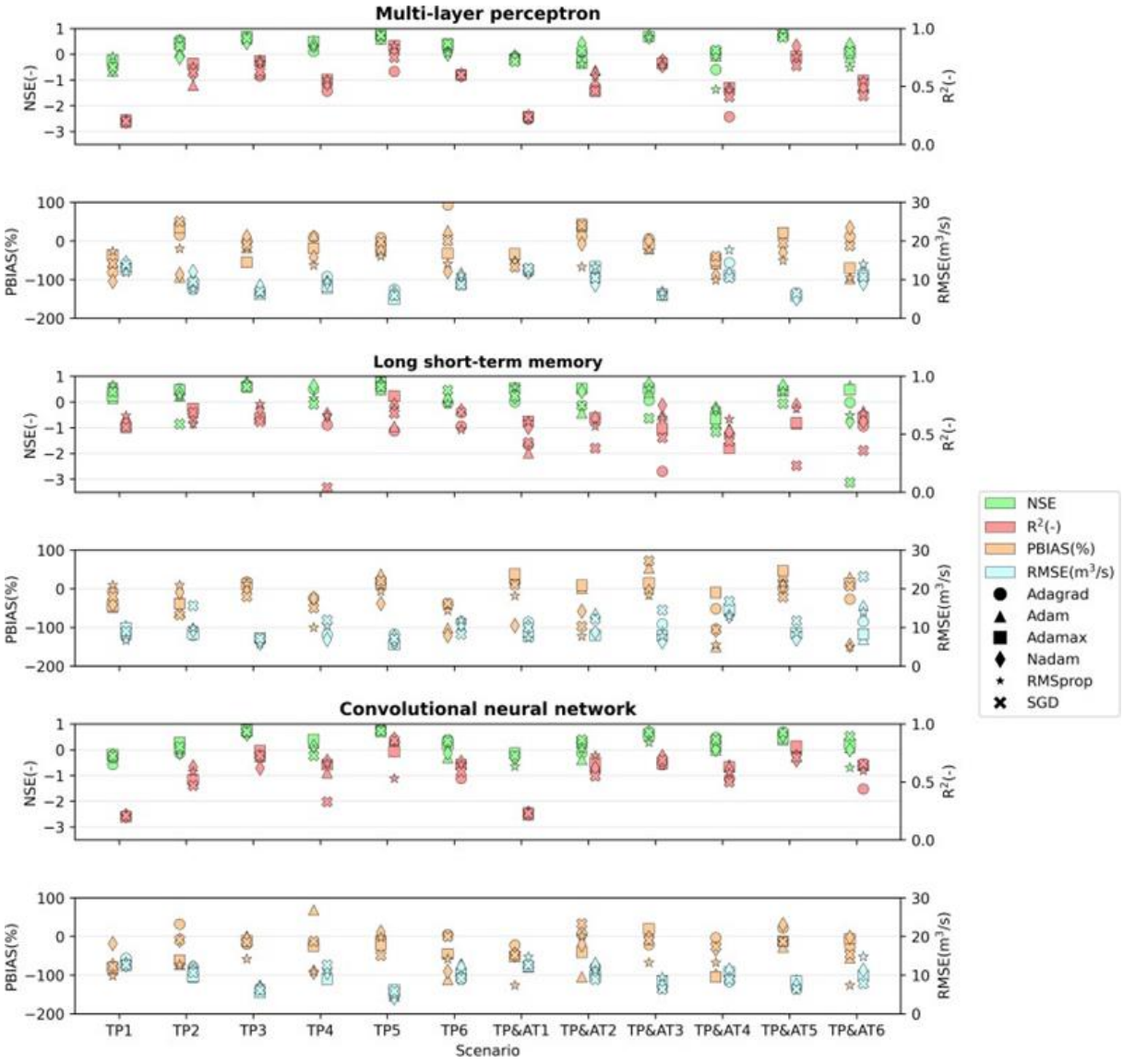

Figure 6.6 Distribution of values of statistical parameters (NSE, R^2, PBIAS, and RMSE) for each scenario in each type of neural network tested.

Considering the calculated statistical parameters and the range of values suggested by Moriasi et al. (2007), 24% (17 out of 72) of the combinations tested in the multi-layer perceptron models showed satisfactory performance in reproducing river flow. The long short-term memory models and convolutional models each presented satisfactory behavior for 18 of the combinations tested, corresponding to 25% of the tests performed.

The best solution for the multi-layer perceptron models presented a NSE of 0.8, an R^2 of 0.85, a PBIAS of −17.3%, and a RMSE of 5.0 $m^3\ s^{-1}$. This solution was obtained for the TP5 input scenario (Figure 6.7) with the Adamax optimizer.

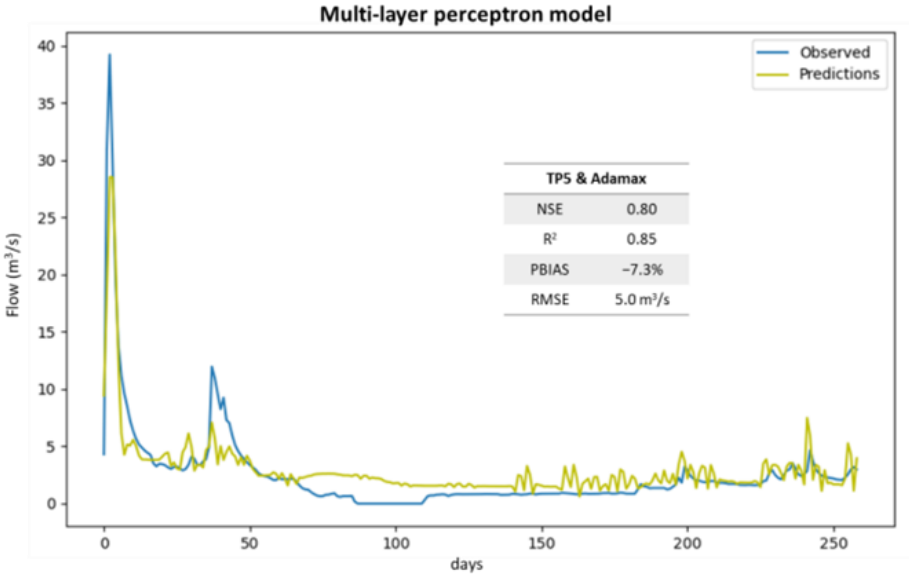

Figure 6.7 Best solution for multi-layer perceptron model (TP5 scenario with Adamax optimizer).

In the case of LSTM models, the best solution was also reached for the TP5 scenario and the Adamax optimizer (Figure 6.8a), resulting in NSE, R^2, PBIAS, and RMSE values of 0.75, 0.83, 15.8%, and 5.6 $m^3\ s^{-1}$, respectively. However, the scenario in which TP3 was combined with the RMSprop optimizer (Figure 6.8b) showed a very similar performance, presenting a NSE of 0.74, R^2 of 0.76, PBIAS of 13.6%, and RMSE of 5.8 $m^3\ s^{-1}$. As shown in Figure 6.8, both models predicted negative flow values, which was considered a non-acceptable result.

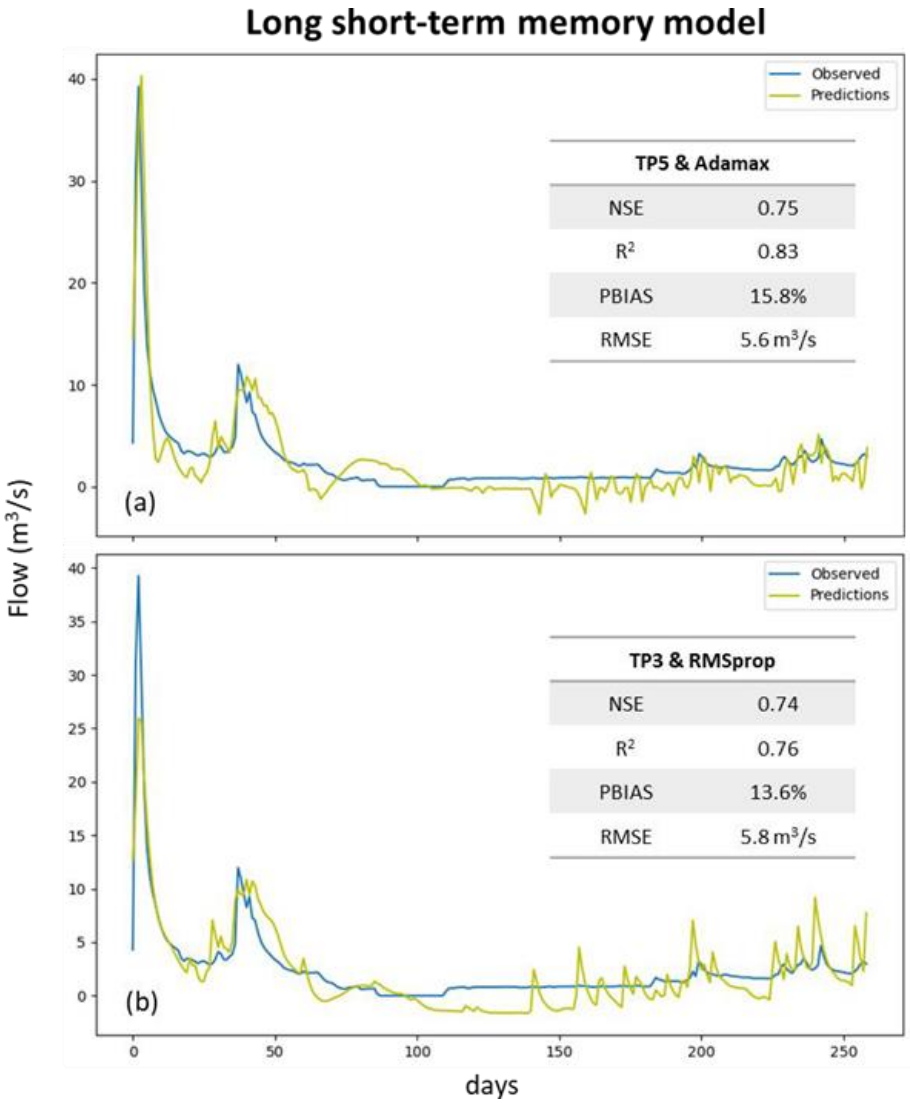

Figure 6.8 Best solutions for long short-term memory model: (a) TP5 scenario with Adamax optimizer; (b) TP3 with RMSprop optimizer.

The best LSTM solution without negative predicted values resulted from the combination of scenario TP3 and the SGD optimizer (Figure 6.9). This solution returned acceptable indicators, with a NSE of 0.59, an R^2 of 0.61, a PBIAS of −20.0%, and a RMSE of 7.2 $m^3 s^{-1}$. However, when compared with the best solution for the multi-layer perceptron model, the performance of this solution was substantially worse.

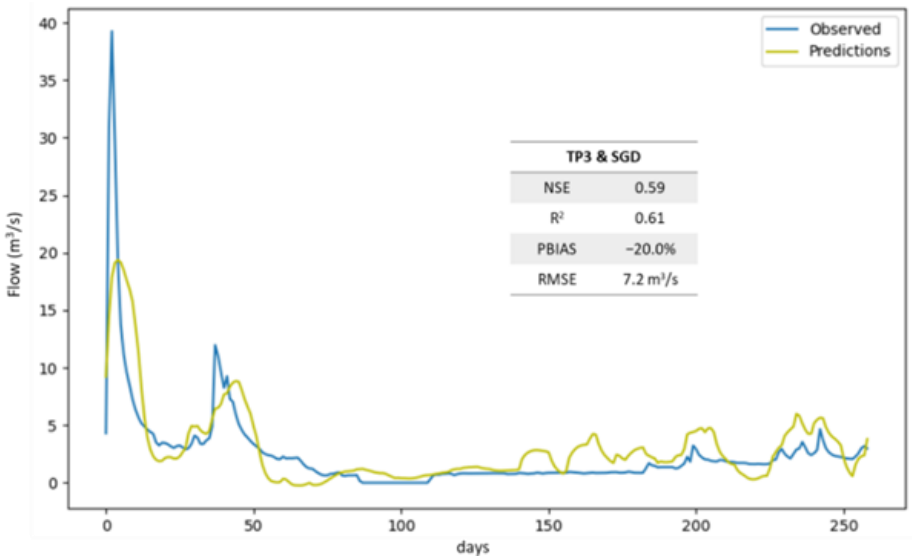

Figure 6.9 Best solution for long short-term memory model without negative predicted values.

Finally, for the convolutional models, the four best solutions were obtained for scenario TP5, and all of them have a NSE and R^2 higher than 0.82 and 0.83, respectively, with the PBIAS laying in the range of −14 to 11%, and the RMSE varying between 4.2 and 4.9 m^3 s^{-1} (Figure 10). From this set, the combination of the TP5 scenario with the Nadam optimizer is the one with the best performance, with the NSE, R^2, PBIAS, and RMSE values being 0.86, 0.87, 10.5%, and 4.2 m^3 s^{-1}, respectively.

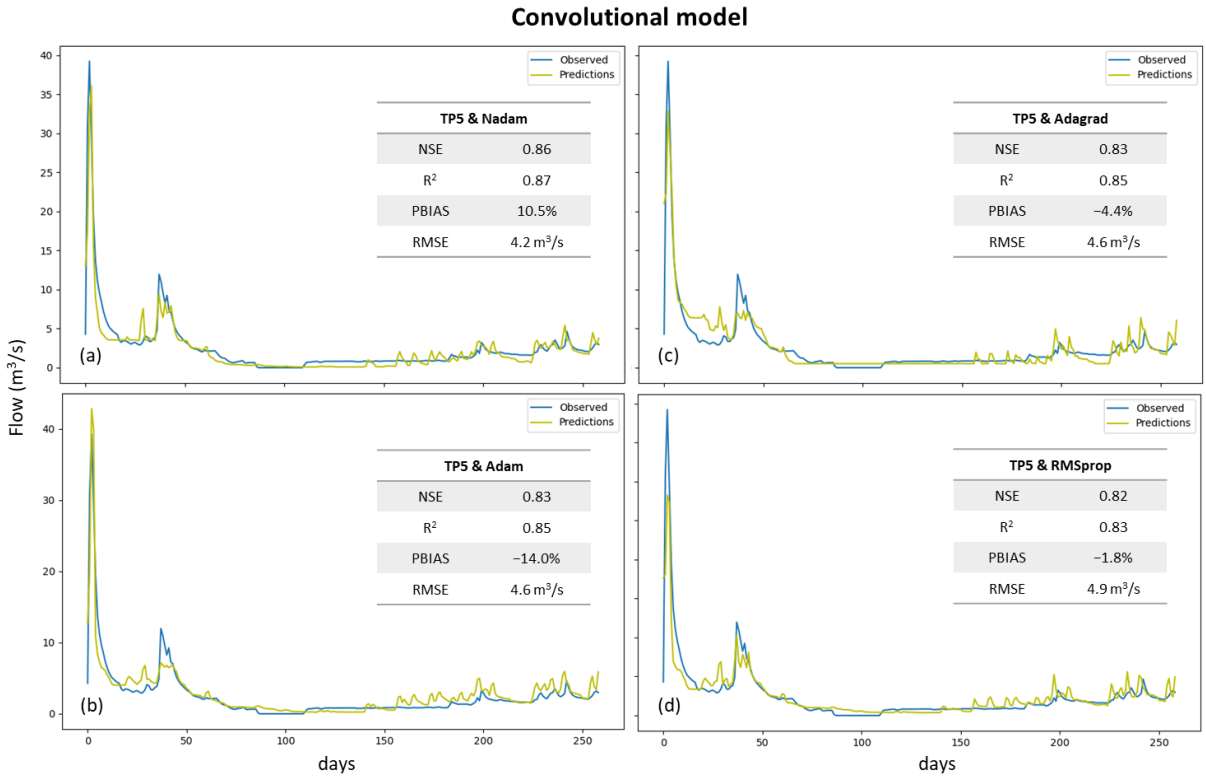

Figure 6.10 Best solutions for convolutional model: (a) TP5 scenario with Nadam optimizer; (b) TP5 with Adam optimizer; (c) TP5 with Adagrad optimizer; (d) TP5 with RMSprop scenario.

The structure of the best solution is composed of one input 1D convolutional layer with the number of filters and the kernel size being 16 and 1, respectively, and one output dense layer with a linear function as the activation function. Between them, two more convolutional 1D layers were placed, with both having 32 filters and a kernel size of 8. After each 1D convolutional layer, a MaxPooling1D layer with a pool size of 2 was set. Finally, the learning rate and the ε of the optimizer took the values 1×10^{-3} and 1×10^{-8}, respectively, with the batch size being defined as 20 while the optimum number of epochs was 200.

6.4 Discussion

In general, results show that convolutional neural networks seem better able to predict the river flow one day ahead than LSTM and MLP models. These results are in accordance with Huang et al. (2020) who compared the capability of a MLP model, a generic CNN model, and a CNN model trained with a transfer learning procedure to predict the river flow one day ahead in four different locations in the United Kingdom. For each location, the authors considered as inputs the river flow time series of neighboring sites. The results of both CNN models (average mean absolute percentage errors (MAPE): generic CNN = 27.09%; CNN with transfer learning = 22.85%) were substantially better than those presented for the MLP model (average MAPE = 31.65%). Shu et al. (2021) tested the prediction of the monthly river flow of two basins in China: the Huaren Reservoir basin, with a drained area of 10 400 km^2 and an average annual streamflow of 142 $m^3\ s^{-1}$, and the Xiangjiaba Hydropower Station basin, where the average annual streamflow is 3810 $m^3\ s^{-1}$. The authors considered 68 variables as candidate inputs, from which rainfall and streamflow were the only ones specified; all others were not given. They compared the performance of a CNN model, an ANN model of the MLP type, and an extreme learning machine (ELM) model with a different number of inputs, with the first model presenting the best performance for both watersheds and most of the number of inputs tested. They concluded that the performance of the models does not improve or worsen clearly with the inclusion of more inputs, but they also did not provide the candidate variables that reached the best performances. Barino et al. (2020) also compared the performance of four different models, including a MLP model and two CNN models, to predict the river flow in a river section of Madeira River, a tributary of the Amazon River, Brazil. The input variable of the MLP model and one of the CNN models was the river flow of the previous days, while the other CNN model had the river flow and the turbidity in previous days as input variables. The

authors concluded that CNN models were the best models for predicting the river flow, with an average NSE, R^2, and MAPE of 0.93, 0.93, and 22.44%, respectively, compared with the NSE of 0.93, R^2 of 0.91, and MAPE of 33.60% for the MLP model. Finally, Duan et al. (2020) used a CNN with past values of precipitation, temperature, and solar radiation as inputs to predict the long-term river flow, for Catchment Attributes for Large-Sample Studies watershed regions, in California, USA. The CNN model's performance was compared with that of other machine learning models, with the authors concluding that ANNs have problems capturing some important temporal features when compared with CNNs and RNNs. Additionally, the CNN model was demonstrated to be faster and more stable during the training phase, producing better results for average and high-flow regimes, while the LSTM model was better at producing results for a low-flow regime.

However, there are several studies demonstrating that MLP and LSTM models can also predict river flow in some cases with acceptable results. Cigizoglu (2003) tested the performance of a MLP model to forecast the river flow one and six days ahead, beyond the calibration range and using different time series with the model already trained in four flow stations on the rivers Göksu, Lamas, and Ermenek, Turkey. The author obtained an average R^2 of 0.94. More recently, Darbandi and Pourhosseini (2018) and Ünes et al. (2020) also used MLP algorithms to predict the river flow in the Ajichay watershed (with a drained area of 12 790 km^2), East Azerbaijan, and in a station (with a drained area of 75 km^2) of the Stilwater river, Worcester, Sterling, MA, USA, respectively. In the first case, the authors applied the MLP model to predict monthly river flow at three points of the watershed considering as input data the river flow values from the previous one, two, and three months. The average R^2 (considering all the stations and all the input data scenarios) for the training period reached 0.86, while that of the test period was 0.78. In the second case, the authors predicted daily flow values using daily average temperature, precipitation, and lagged day flow values as input variables and obtained a Pearson's correlation coefficient of 0.91. In both cases, MLP models were compared with other models, however, neither demonstrated the best performance. Ni et al. (2020) used a MLP model and three LSTM models (one simple LSTM model, a convolutional LSTM model, CLSTM, and a wavelet-LSTM model, WLSTM) to predict the monthly streamflow volume one, three and six months ahead in Cuntan and Hankou stations, Yangtze River basin, China. They demonstrated that the MLP model was the one with the worst performance (average NSE = 0.72), while the simple LSTM model reached an average NSE of 0.76, and the WLSTM and CLSTM models had average NSEs of 0.78 and 0.79, respectively. According to the authors, WLSTM and CLSTM demonstrated better performance because both

can be considered as having preprocessing methods based on the convolutional operation, both are based on filter usage, and both are responsible for extracting temporally local information from data. However, the CLSTM filters can be trained by data and, thus, they can learn, while the WLSTM model has pre-specified structured filters. Xu et al. (2020) applied several models to predict the streamflow in two watersheds in China, namely, the Hun river basin, with a drained area of 14 800 km^2, and the Yangtze river basin, with a drained area of 1 002 300 km^2. Among the applied models, the authors considered the different structures of the LSTM models for each watershed with meteorological data from different stations in both basins being used as input variables. They concluded that, during the training period, the LSTM models had the best performance among all the models used in both watersheds, while during the verification period, LSTM performance decreased, becoming the second-best solution right after the hydrological model. Additionally, Hu et al. (2020) used a LSTM model to predict stream flow 6h ahead in one hydrological station placed in Tunxi, China. Using streamflow and precipitation data to feed the model, the authors found that the LSTM model performed better than a support vector regression and the MLP models, with the LSTM solution reaching an R^2 of 0.97. On top of the good results, it is also important to note that Xu et al. (2020) and Hu et al. (2020) found some difficulties in predicting peak flow values when using LSTM models.

According to the analysis presented before, there seems to exist an agreement about CNN models having the best capacity to predict stream flow, which is frequently related to their ability to extract features and to perform a subsampling of the data gained with the usage of filters (Lee and Song, 2019; Ni et al., 2020; Shu et al., 2021; Huang et al., 2020). Additionally, Lee and Song (2019) say that CNN models have a significant advantage over MLP models that is related to the number of parameters to estimate. This comes from the fact that CNNs share filters at different local regions of the input, visiting all parts of the input sequence and performing the same identical computation on it, thus considering several input features as one instead of considering each feature as different from the others, as is the case in MLP structures. Shu et al. (2021) also says that a careful selection of the input variables for models like ANN and ELM is required, while CNN models can do this task themselves because of their capacity for feature extraction. Thus, in this study, the worse performance of the MLP and LSTM models can be partly explained by the fact that the input variables were not a target of exhaustive exploration since the authors wanted to limit them to precipitation and temperature. This imposed limitation comes from the fact that, when considering an operational system, the study of future scenarios, or even a hydrometric station with limited data availability, there are no measured river flow values available to feed the model. Thus, if the neural network is based on

river flow values from past instances, in the situations referred to before, the model needs to be fed by its own outputs, which can significantly increase the uncertainty of the predicted values.

On the other hand, in the last few years, several authors have explored different models from those presented here with promising results. This is the case of Sit et al. (2021) and Szczepanek (2022). Sit et al. (2021) used a graphical convolutional GRU model to predict the next 36 h of streamflow, obtaining a NSE very close to 1 for the first hours and decreasing to 0.85 for the last predicted hours. Szczepanek (2022) tested the prediction of daily streamflow in mountain catchments with the XGBoost, LightGBM, and CatBoost models. The authors found that, using the default model parameters, CatBoost obtained the best results (NSE = 0.78, MAE = 3.96), while for hyperparameter optimization, LightGBM obtained the best performance (NSE = 0.87, MAE = 2.70).

Finally, to improve the results of these types of data-driven models, Duan et al. (2020) proposed the use of alternative designs that can explicitly include physically based conservation laws, which also allow the physical interpretation of model results. However, even without considering these types of modifications, these models still have several advantages. Humphrey et al. (2016) suggest that the flexible model structure of neural network models allows them to capture the complex and nonlinear relationships between input and output values without taking into consideration the underlying processes. Besides the flexible structure, the advantages of ASCE (2000) include the capacity of these models to work well even when training datasets contain noise and measurement errors, the fact that they can adapt to solutions over time to compensate for changes in the modeled system, and the fact that they are easy to use once they are trained. On the other hand, there are also several disadvantages associated with the use of neural network models. These models are highly dependent on the size and quality of the input dataset, and they have many more parameters to calibrate than typical rainfall–runoff models do, which can lead to an over-parameterization of NN models (Humphrey et al., 2016; ASCE, 2000). This over-parametrization substantially increases the risk of the model's inability to make forecasts beyond the calibration process. The lack of a standardized way to select the network architecture is also a limitation of the usage of these models. The network structure, the training algorithm, and the definition of error result, most of the time, depend on the experience of the user.

6.5 Conclusions

The work presented here demonstrates that the implementation of neural network models based on tools already developed, namely, the Keras and KerasTuner packages, can constitute an easy-to-use and powerful solution to streamflow estimation with a daily time step.

Among the set of tests performed for simulating streamflow in the Ponte Vila Formosa hydrometric station, the best solution was reached with a CNN model composed of one input 1D convolutional layer with 16 filters and a kernel size equal to 1, followed by two other 1D convolutional layers, each having 32 filters and a kernel size of 8 and each being finalized with a dense layer activated by a linear function. After each 1D convolutional layer, a MaxPooling1D layer was imposed with a pool size of 2. The optimizer with the best performance was Nadam, with a learning rate of 1×10^{-3} and an ε of 1×10^{-8}. The model obtained the best solution with a batch size of 20 and with 200 as the number of epochs. The input variables of the best solution included only the average daily precipitation values in the watershed accumulated in 1, 2, 3, 4, 5, and 10 days and delayed by 1, 2, 3, 4, 5, 6, and 7 days. This solution reached a NSE of 0.86 and an R^2 of 0.87, with the PBIAS and RMSE being 10.5% and 4.2 $m^3\ s^{-1}$, respectively. However, it is important to note that the worse performances of the LSTM and MLP models, when compared with solutions found in the literature, can be closely related to the choice and treatment of the input variables.

It is also important to note that the methodology presented here focused on easy predictive data, such as meteorological conditions. However, according to different studies already presented, it seems possible that the results obtained could be improved using other parameters that are historically related as forcing variables. Additionally, the case study in this work is of a watershed characterized by a small size and natural regime flow. Thus, the transference of the methodology presented here to other watersheds should be carried out carefully and could perhaps be the target of benchmark tests (Demir et al., 2022).

Although data-driven models are easy to implement and do not require knowledge about the physical processes involved in the generation of streamflow in a watershed, it is important to note that the application of these types of models relies on the fact that they are developed under a certain combination of watershed characteristics. When those characteristics change, for example, when the land use or the construction of a dam change, an already developed and trained model can no longer be representative of that watershed. To avoid these limitations, solutions for NN models that incorporate some information about the physical processes involved can be developed, which will be the topic of a subsequent study.

6.6 Appendixes

6.6.1 Appendix 6A

Table 6A.1 Statistical parameters for each considered input variable scenario (according to Table 6.8) and for each tested optimizer for MLP, LSTM, and convolutional models.

		Scenarios											
		TP1	**TP2**	**TP3**	**TP4**	**TP5**	**TP6**	**TP&AT1**	**TP&AT2**	**TP&AT3**	**TP&AT4**	**TP&AT5**	**TP&AT6**
							MLP						
Adagrad	NSE	-0.46	0.56	0.59	0.12	0.60	0.21	-0.10	0.10	0.71	-0.59	-	0.19
	R^2	0.20	0.66	0.59	0.46	0.63	0.59	0.22	0.50	0.72	0.24	-	0.46
	PBIAS	-80.8	16.0	-0.5	11.1	8.8	93.6	-41.4	12.5	6.2	-56.3	-	12.2
	RMSE	13.9	7.5	7.2	10.8	7.5	10.1	12.0	10.9	6.1	14.4	-	10.3
Adam	NSE	-0.64	0.10	0.59	0.53	0.60	0.37	-	0.16	0.72	-0.06	-	-0.13
	R^2	0.19	0.51	0.61	0.54	0.83	0.62	-	0.64	0.74	0.47	-	0.50
	PBIAS	-54.6	-92.7	-16.4	15.3	-26.4	27.4	-	37.6	-19.3	-58.7	-	-96.7
	RMSE	14.7	10.9	7.2	7.8	7.1	9.1	-	10.5	6.0	11.8	-	12.1
Adamax	NSE	-0.23	0.41	0.69	0.49	0.80	0.40	-0.20	-0.34	0.69	0.06	0.74	0.06
	R^2	0.21	0.70	0.72	0.56	0.85	0.60	0.24	0.46	0.70	0.49	0.76	0.55
	PBIAS	-36.5	36.0	-54.9	-18.0	-17.3	-32.7	-33.4	42.5	-8.0	-49.9	21.3	-69.8
	RMSE	12.7	8.8	6.2	8.2	5.0	8.8	12.5	13.3	6.2	11.1	5.8	11.1
Nadam	NSE	-0.57	-0.12	0.46	0.34	0.66	0.01	-0.10	0.42	0.67	0.02	0.80	0.36
	R^2	0.20	0.61	0.71	0.53	0.81	0.60	0.24	0.61	0.68	0.47	0.85	0.49
	PBIAS	-104.4	-86.0	11.7	-42.5	-26.0	-79.0	-58.0	-6.9	0.7	-88.0	-29.6	34.7
	RMSE	14.4	12.1	8.3	9.3	6.6	11.3	12.0	8.7	6.5	11.4	5.1	9.1
RMSprop	NSE	-0.08	0.56	0.68	0.30	0.68	0.04	-0.08	-0.36	0.66	-1.36	0.65	-0.51
	R^2	0.20	0.67	0.71	0.56	0.85	0.59	0.22	0.59	0.68	0.47	0.76	0.55
	PBIAS	-26.5	-19.9	-17.6	-62.8	-39.2	-58.6	-51.7	-67.0	-24.2	-101.2	-50.4	-95.5
	RMSE	11.9	7.6	6.4	9.6	6.4	11.2	11.9	13.3	6.6	17.7	6.7	14.0
SGD	NSE	-0.49	0.31	0.63	-	0.73	0.42	-0.29	0.15	-	0.17	0.66	0.10
	R^2	0.20	0.62	0.63	-	0.75	0.60	0.24	0.46	-	0.41	0.68	0.42
	PBIAS	-58.0	51.0	-8.9	-	-1.5	0.3	-67.5	40.7	-	-39.4	-5.6	-12.1
	RMSE	14.0	9.5	6.9	-	5.9	8.7	13.0	10.5	-	10.5	6.6	10.8

		Scenarios											
		TP1	**TP2**	**TP3**	**TP4**	**TP5**	**TP6**	**TP&AT1**	**TP&AT2**	**TP&AT3**	**TP&AT4**	**TP&AT5**	**TP&AT6**
LSTM													
Adagrad	NSE	0.56	0.51	-	0.50	0.48	-0.03	0.01	-	0.07	-0.41	0.51	-0.02
	R^2	0.58	0.69	-	0.58	0.53	0.57	0.41	-	0.18	0.50	0.60	0.57
	PBIAS	-6.2	-35.1	-	-23.9	13.1	-39.0	17.8	-	5.6	-51.7	2.7	-26.7
	RMSE	7.6	8.0	7.0	8.1	8.2	11.5	11.4	-	10.9	13.6	7.9	11.5
Adam	NSE	0.15	0.24	0.62	-	0.49	0.22	0.30	-0.42	0.38	-0.83	0.43	0.63
	R^2	0.56	0.69	0.63	-	0.57	0.72	0.34	0.66	0.67	0.55	0.59	0.70
	PBIAS	-47.3	-58.5	17.2	-	38.3	-101.4	26.4	1.4	53.7	-149.5	33.9	30.1
	RMSE	10.5	9.9	-	-	8.1	10.1	9.6	13.7	8.9	15.5	8.5	6.9
Adamax	NSE	0.25	0.46	0.59	-	0.75	-	0.54	0.51	0.51	-0.66	0.42	0.47
	R^2	0.56	0.72	0.64	-	0.83	-	0.61	0.64	0.55	0.38	0.60	0.64
	PBIAS	-43.9	-38.5	11.7	-	15.8	-	38.4	9.4	15.5	-10.3	46.2	14.2
	RMSE	9.9	8.4	7.3	-	5.6	-	7.8	8.0	7.9	14.8	8.6	8.3
Nadam	NSE	0.53	0.33	0.72	0.63	0.69	0.10	0.21	0.41	0.69	-0.26	0.62	-0.75
	R^2	0.62	0.61	0.72	0.67	0.75	0.70	0.56	0.64	0.75	0.52	0.75	0.61
	PBIAS	-40.4	-8.5	-8.0	-24.6	-37.7	-121.1	-94.9	-58.0	-6.8	-107.4	8.1	-146.2
	RMSE	7.9	9.3	6.0	6.9	6.3	10.8	10.2	8.8	6.3	12.9	7.0	15.1
RMSprop	NSE	0.66	0.25	0.74	0.14	0.72	-0.07	0.59	-0.16	0.53	-0.26	0.42	-0.51
	R^2	0.66	0.59	0.76	0.66	0.72	0.54	0.61	0.57	0.64	0.63	0.72	0.68
	PBIAS	8.9	9.4	13.6	-100.0	-6.3	-56.6	-18.0	-122.9	-17.0	-145.1	13.4	-150.2
	RMSE	6.7	9.9	5.8	10.6	6.0	11.8	7.3	12.3	7.8	12.9	8.6	14.0
SGD	NSE	0.39	-0.85	0.59	-0.08	0.60	0.46	0.23	-0.13	-0.63	-1.15	-0.06	-3.12
	R^2	0.56	0.69	0.61	0.04	0.68	0.69	0.43	0.38	0.47	0.44	0.23	0.36
	PBIAS	-19.5	-67.4	-20.0	-49.3	20.9	-37.6	11.1	-96.6	72.6	-104.8	-21.0	6.9
	RMSE	9.0	15.6	7.2	11.9	7.1	8.3	10.0	12.2	14.5	16.8	11.7	23.2
Convolutional													
Adagrad	NSE	-0.57	-0.13	0.67	-	0.83	0.39	-0.24	-0.12	0.60	0.48	0.66	0.18
	R^2	0.21	0.50	0.71	-	0.84	0.53	0.23	0.60	0.65	0.53	0.75	0.44
	PBIAS	-89.1	31.6	-19.0	-	-4.4	4.5	-21.9	5.5	-21.4	-2.7	21.6	-26.9
	RMSE	14.4	12.2	6.4	-	4.6	8.9	12.8	12.1	7.1	8.3	6.6	10.3

		Scenarios											
		TP1	**TP2**	**TP3**	**TP4**	**TP5**	**TP6**	**TP&AT1**	**TP&AT2**	**TP&AT3**	**TP&AT4**	**TP&AT5**	**TP&AT6**
Adam	NSE	-0.21	0.29	0.72	0.28	0.83	-0.30	-0.12	-0.38	0.62	0.00	0.40	0.09
	R^2	0.21	0.57	0.72	0.58	0.85	0.67	0.22	0.63	0.68	0.65	0.72	0.66
	PBIAS	-69.0	-71.9	0.9	69.3	-14.0	-111.2	-40.0	-103.7	11.5	-95.8	-27.0	-54.9
	RMSE	12.6	9.6	6.0	9.7	4.6	13.0	12.1	13.4	6.9	11.5	8.8	10.8
Adamax	NSE	-0.19	0.28	0.76	0.39	0.71	0.20	-0.14	0.29	0.60	0.12	0.46	0.24
	R^2	0.20	0.52	0.77	0.65	0.76	0.65	0.23	0.67	0.66	0.63	0.81	0.64
	PBIAS	-79.6	-61.0	-10.5	-23.7	-21.0	-44.9	-52.3	-39.8	20.4	-103.8	-11.8	-6.2
	RMSE	12.5	9.7	5.5	9.0	6.1	10.2	12.3	9.7	8.5	10.8	8.4	9.9
Nadam	NSE	-0.23	-0.10	0.62	0.13	0.86	-0.13	-0.35	0.19	0.67	0.02	0.56	0.01
	R^2	0.21	0.63	0.62	0.68	0.87	0.67	0.23	0.62	0.72	0.61	0.69	0.64
	PBIAS	-18.3	-8.7	-6.7	-91.7	10.5	-90.2	-46.6	-20.7	-3.0	-32.0	31.1	-1.6
	RMSE	12.7	12.0	6.9	10.7	4.2	12.1	13.3	10.3	7.2	11.3	7.4	11.3
RMSprop	NSE	-0.36	-0.03	0.61	0.03	0.82	0.23	-0.64	0.03	0.29	0.29	0.71	-0.69
	R^2	0.21	0.59	0.74	0.66	0.83	0.65	0.24	0.73	0.66	0.58	0.74	0.60
	PBIAS	-102.2	-72.8	-58.1	-91.4	-1.8	-58.0	-126.1	1.7	-67.3	-67.0	-14.4	-125.9
	RMSE	13.4	11.6	7.1	11.3	4.9	10.0	14.7	11.3	9.5	9.6	6.1	14.8
SGD	NSE	-0.24	0.12	0.71	-0.23	0.73	0.34	-0.22	0.39	0.68	0.40	0.68	0.53
	R^2	0.21	0.47	0.73	0.33	0.86	0.59	0.23	0.55	0.69	0.50	0.71	0.66
	PBIAS	-76.5	-8.2	-14.7	-12.3	-48.9	-0.3	-48.4	33.0	-9.1	-26.0	-12.7	-46.1
	RMSE	12.8	10.7	6.1	12.7	5.9	9.2	12.7	8.9	6.4	8.9	6.4	7.8

Author Contributions

Conceptualization, A.R.O.; methodology, A.R.O.; validation, A.R.O.; investigation, A.R.O.; resources, A.R.O.; writing—original draft preparation, A.R.O.; writing—review and editing, T.B.R. and R.N.; supervision, T.B.R. and R.N. All authors have read and agreed to the published version of the manuscript.

Funding

This research was funded by FCT/MCTES (PIDDAC) through project LARSyS–FCT pluriannual funding 2020–2023 (UIDB/50009/2020), and by Project FEMME (PCIF/MPG/0019/2017). T. B. Ramos was supported by a CEEC-FCT contract (CEECIND/01152/2017).

Data Availability Statement

The observed streamflow and meteorological data can be downloaded from the SNIRH website (https://snirh.apambiente.pt/ (accessed on 7 February 2021)). ERA5 meteorological data is available on Climate Data Store—Copernicus website (https://cds.climate.copernicus.eu/#!/home (accessed on 10 December 2020)). The python scripts developed to implement and tune the neural networks as well as the input data time series are available on the GitHub repository: https://github.com/anaioliveira/ArtificialNeuralNetwork/tree/main/PteVilaFormosa (accessed on 23 February 2023).

6.7 References

Abadi, M.; Barham, P.; Chen, J.; Chen, Z.; Davis, A.; Dean, J.; Devin, M.; Ghemawat, S.; Irving, G.; Isard, M.; et al. Tensorflow: A system for large-scale machine learning. In Proceedings of the 12th USENIX Symposium on Operating Systems Design and Implementation (OSDI ’16), Savannah, GA, USA, 2–4 November 2016; pp. 265–283.

Afaq, S.; Rao, S. Significance of epochs on training a neural network. Int. J. Sci. Res. Sci. Eng. 2020, 9, 485–488.

Agencia Estatal de Meteorología (España). Atlas Climático Ibérico: Temperatura del Aire y Precipitación (1971–2000)=Atlas Climático Ibérico: Temperatura do ar e Precipitação (1971–2000)=Iberian Climate Atlas: Air Temperature and Precipitation (1971–2000); Instituto Nacional de Meteorología: Madrid, Spain, 2011.

Airola, R.; Hager, K. Image Classification, Deep Learning and Convolutional Neural Networks: A Comparative Study of Machine Learning Frameworks. 2017. Thesis (BSc). Available online: https://www.diva-portal.org/smash/record.jsf?pid=diva2%3A1111144&dswid=341 (accessed on 16 October 2022).

Almeida, C.; Ramos, T.; Segurado, P.; Branco, P.; Neves, R.; Proença de Oliveira, R. Water Quantity and Quality under Future Climate and Societal Scenarios: A Basin-Wide Approach Applied to the Sorraia River, Portugal. Water 2018, 10, 1186. https://doi.org/10.3390/w10091186

Althoff, D.; Rodrigues, L.N.; Silva, D.D. Addressing hydrological modeling in watersheds under land cover change with deep learning. Adv. Water Resour. 2021, 154, 103965. https://doi.org/10.1016/j.advwatres.2021.103965

Anderson, S.; Radić, V. Evaluation and interpretation of convolutional long short-term memory networks for regional hydrological modelling. Hydrol. Earth Syst. Sci. 2022, 26, 795–825. https://doi.org/10.5194/hess-26-795-2022

APA and ARH Tejo, 2012. Agência Portguesa do Ambiente and Administração da Região Hidrográfica Tejo. Plano de gestão da região hidrográfica do Tejo—Relatório técnico (Síntese). Available online: https://apambiente.pt/agua/1o-ciclo-de-planeamento-2010-2015 (accessed on 6 September 2022).

ARBVS, n.d. Área Regada. Associação de Regantes e Beneficiários do Vale do Sorraia. Available online: https://www.arbvs.pt/index.php/culturas/area-regada (accessed on 18 October 2022).

ASCE Task Committee on Application of Artificial Neural Networks in Hydrology. Artificial Neural Networks in Hydrology. I: Preliminary Concepts. J. Hydrol. Eng. 2000, 5, 115–123. https://doi.org/10.1061/(ASCE)1084-0699(2000)5:2(115)

Barino, F.O.; Silva, V.N.H.; Lopez-Barbero, A.P.; De Mello Honorio, L.; Santos, A.B.D. Correlated time-series in multi-day-ahead streamflow forecasting using convolutional networks. IEEE Access 2020, 8, 215748–215757. http://dx.doi.org/10.1109/ACCESS.2020.3040942

Bengio, Y. Learning Deep Architectures for AI. Found. Trends Mach. Learn. 2009, 2, 1–127. https://doi.org/10.1561/2200000006

Bengio, Y.; Simard, P.; Frasconi, P. Learning long-term dependencies with gradient descent is difficult. IEEE Trans. Neural. Netw. 1994, 5, 157–166. https://doi.org/10.1109/72.279181

Besaw, L.E.; Rizzo, D.M.; Bierman, P.R.; Hackett, W.R. Advances in ungauged streamflow prediction using artificial neural networks. J. Hydrol. 2010, 386, 27–37. https://doi.org/10.1016/j.jhydrol.2010.02.037

Bourdin, D.R.; Fleming, S.W.; Stull, R.B. Streamflow modelling: A primer on applications, approaches and challenges. Atmos. Ocean 2012, 50, 507–536. https://doi.org/10.1080/07055900.2012.734276

Chiew, F.; McMahon, T. Application of the daily rainfall-runoff model MODHYDROLOG to 28 Australian catchments. J. Hydrol. 1994, 153, 383–416. https://doi.org/10.1016/0022-1694%2894%2990200-3

Chong, K.L.; Lai, S.H.; Yao, Y.; Ahmed, A.N.; Jaafar, W.Z.W.; El-Shafie, A. Performance enhancement model for rainfall forecasting utilizing integrated wavelet-convolutional neural network. Water Resour. Manag. 2020, 34, 2371–2387. https://doi.org/10.1007/s11269-020-02554-z

Cigizoglu, H.K. Estimation, forecasting and extrapolation of river flows by artificial neural networks. Hydrol. Sci. J. 2003, 48, 349–361. https://doi.org/10.1623/hysj.48.3.349.45288

Corine Land Cover 2012 (CLC 2012), n.d. © European Union, Copernicus Land Monitoring Service 2018, European Environment Agency (EEA). Available online: https://land.copernicus.eu/pan-european/corine-land-cover (accessed on 22 June 2019).

Darbandi, S.; Pourhosseini, F.A. River flow simulation using a multilayer perceptron-firefly algorithm model. Appl. Water Sci. 2018, 8, 85. https://doi.org/10.1007/s13201-018-0713-y

Demir, I.; Xiang, Z.; Demiray, B.; Sit, M. WaterBench-Iowa: A large-scale benchmark dataset for data-driven streamflow forecasting. Earth Syst. Sci. Data 2022, 14, 5605–5616. https://doi.org/10.5194/essd-14-5605-2022

Deng, L. A Tutorial Survey of Architectures, Algorithms, and Applications for Deep Learning. APSIPA Trans. Signal Inf. Process. 2014, 3, E2. https://doi.org/10.1017/atsip.2013.9

Dolling, O.R.; Varas, E.A. Artificial neural networks for streamflow prediction. J. Hydraul. Res. 2002, 40, 547–554. https://doi.org/10.1016/S0022-1694(98)00242-X

Dozat, T. Incorporating Nesterov Momentum into Adam. In Proceedings of the ICLR 2016 Workshop, San Juan, Puerto Rico, India, 2–4 May 2016.

Duan, S.; Ullrich, P.; Shu, L. Using convolutional neural networks for streamflow projection in California. Front. Water 2020, 2, 28. https://doi.org/10.3389/frwa.2020.00028

Duchi, J.; Hazan, E.; Singer, Y. Adaptive subgradient methods for online learning and stochastic optimization. J. Mach. Learn. Res. 2011, 12, 2121–2159.

Eberhart, R.C.; Dobbins, R.W. Neural Network PC Tools. A Practical Guide; Academic Press: Cambridge, MA, USA, 1990. https://doi.org/10.1086/417516

Ebert-Uphoff, I.; Lagerquist, R.; Hilburn, K.; Lee, Y.; Haynes, K.; Stock, J.; Kumler, C.; Stewart, J.Q. CIRA guide to custom loss functions for neural networks in environmental sciences—Version 1. arXiv 2021. Available online: https://arxiv.org/abs/2106.09757 (accessed on 8 February 2023).

Elman, J.L. Finding structure in Time. Cogn. Sci. 1990, 14, 179–211. https://www.doi.org/10.1207/S15516709COG1402_1

European Digital Elevation Model (EU-DEM), version 1.1., n.d. © European Union, Copernicus Land Monitoring Service 2019, European Environment Agency (EEA). Available online: https://land.copernicus.eu/pan-european/satellite-derived-products/eu-dem/eu-dem-v1.1/view (accessed on 15 May 2019).

Hauswirth, S.M.; Bierkens, M.F.P.; Beijk, V.; Wanders, N. The potential of data driven approaches for quantifying hydrological extremes. Adv. Water Resour. 2021, 155, 104017. https://doi.org/10.1016/j.advwatres.2021.104017

Haykin, S. Neural Networks: A Comprehensive Foundation; Prentice Hall: Hoboken, NJ, USA, 1999.

Hersbach, H.; Bell, B.; Berrisford, P.; Hirahara, S.; Horanyi, A.; Muñoz-Sabater, J.; Nicolas, J.; Peubey, C.; Radu, R.; Schepers, D.; et al. The ERA5 global reanalysis. Q. J. R. Meteorol. Soc. 2020, 146, 1999–2049. https://doi.org/10.1002/qj.3803

Hochreiter, S.; Schmidhuber, J. Long short-term memory. Neural. Comput. 1997, 9, 1735–1780. https://doi.org/10.1162/neco.1997.9.8.1735

Hu, Y.; Yan, L.; Hang, T.; Feng, J. Stream-flow forecasting of small rivers based on LSTM. arXiv 2020. Available online: https://arxiv.org/abs/2001.05681 (accessed on 8 February 2023).

Huang, C.; Zhang, J.; Cao, L.; Wang, L.; Luo, X.; Wang, J.-H.; Bensoussan, A. Robust forecasting of river-flow based on convolutional neural network. IEEE Trans. Sustain. Comput. 2020, 5, 594–600. https://doi.org/10.1109/TSUSC.2020.2983097

Humphrey, G.B.; Gibbs, M.S.; Dandy, G.C.; Maier, H.R. A hybrid approach to monthly streamflow forecasting: Integrating hydrological model outputs into a bayesian artificial neural network. J. Hydrol. 2016, 540, 623–640. https://doi.org/10.1016/j.jhydrol.2016.06.026

Hussain, D.; Khan, A.A. Machine learning techniques for monthly river flow forecasting of Hunza River, Pakistan. Earth Sci. Inform. 2020, 13, 939–949. https://doi.org/10.1007/s12145-020-00450-z

Jakeman, A.J.; Littlewood, I.G.; Whitehead, P.G. Computation of the instantaneous unit hydrograph and identifiable component flows with application to two small upland catchments. J. Hydrol. 1990, 117, 275–300. https://doi.org/10.1016/0022-1694(90)90097-H

Jin, Y.-F.; Yin, Z.-Y.; Zhou, W.-H.; Shao, J.-F. Bayesian model selection for sand with generalization ability evaluation. Int. J. Numer. Anal. Methods Geomech. 2019, 43, 2305–2327. https://doi.org/10.1002/nag.2979

Juan, C.; Genxu, W.; Tianxu, M.; Xiangyang, S. ANN Model-based simulation of the runoff variation in response to climate change on the Qinghai-Tibet Plateau, China. Adv. Meteorol. 2017, 2017, 1–13. https://doi.org/10.1155/2017/9451802

Keras Documentation: Dropout Layer, n.d. Available online: https://keras.io/api/layers/regularization_layers/dropout/ (accessed on 14 October 2022).

Keras Documentation: Layer Activation Functions, n.d. Available online: https://keras.io/api/layers/activations/ (accessed on 14 October 2022).

Keras Documentation: Layer Weight Initializers, n.d. Available online: https://keras.io/api/layers/initializers/ (accessed on 2 December 2022).

Keras Documentation: Model Training APIs, n.d. Available online: https://keras.io/api/models/model_training_apis/ (accessed on 14 October 2022).

Keras. GitHub. Available online: https://github.com/fchollet/keras (accessed on 19 November 2020).

Kingma, D.P.; Ba, J. Adam: A method for stochastic optimization. arXiv 2017. Available online: https://arxiv.org/abs/1412.6980 (accessed on 8 February 2023).

Kratzert, F.; Klotz, D.; Brenner, C.; Schulz, K.; Herrnegger, M. Rainfall–runoff modelling using Long Short-Term Memory (LSTM) networks. Hydrol. Earth Syst. Sci. 2018, 22, 6005–6022. https://doi.org/10.5194/hess-22-6005-2018

Le, X.-H.; Ho, H.V.; Lee, G.; Jung, S. Application of Long Short-Term Memory (LSTM) neural network for flood forecasting. Water 2019, 11, 1387. https://doi.org/10.3390/w11071387

LeCun, Y.; Bengio, Y. Convolutional networks for images, speech, and time-series. In The Handbook of Brain Theory and Neural Networks; Arbib, M.A., Ed.; MIT Press: Cambridge, MA, USA, 1995.

LeCun, Y.; Bengio, Y.; Hinton, G. Deep learning. Nature 2015, 521, 436–444. https://doi.org/10.1038/nature14539

Lee, H.; Song, J. Introduction to convolutional neural network using Keras; an understanding from a statistician. Commun. Stat. Appl. Methods 2019, 26, 591–610. https://doi.org/10.29220/CSAM.2019.26.6.591

Lipton, Z.C.; Berkowitz, J.; Elkan, C. A critical review of recurrent neural networks for sequence learning. arXiv 2015. Available online: https://arxiv.org/abs/1506.00019 (accessed on 8 February 2023).

Liu, Z.; Zhou, P.; Chen, X.; Guan, Y. A multivariate conditional model for streamflow prediction and spatial precipitation refinement. J. Geophys. Res. 2015, 120, 10116–10129. https://doi.org/10.1002/2015JD023787

Lohani, A.K.; Kumar, R.; Singh, R.D. Hydrological time series modeling: A comparison between adaptive neuro-fuzzy, neural network and autoregressive techniques. J. Hydrol. 2012, 442–443, 23–35. https://doi.org/10.1016/j.jhydrol.2012.03.031

Maier, H.R.; Dandy, G.C. Neural networks for the prediction and forecasting of water resources variables: A review of modelling issues and applications. Environ. Model. Softw. 2000, 15, 101–124. https://doi.org/10.1016/S1364-8152(99)00007-9

Maier, H.R.; Jain, A.; Dandy, G.C.; Sudheer, K.P. Methods used for the development of neural networks for the prediction of water resource variables in river systems: Current status and future directions. Environ. Model. Softw. 2010, 25, 891–909. https://doi.org/10.1016/j.envsoft.2010.02.003

McKinney, W. Data structures for statistical computing in Python. In Proceedings of the 9th Python in Science Conference 2010, Austin, TX, USA, 28 June–3 July 2010; pp. 56–61. https://doi.org/10.25080/Majora-92bf1922-00a

Mehr, A.D.; Kahya, E.; Olyaie, E. Streamflow prediction using linear genetic programming in comparison with a neuro-wavelet technique. J. Hydrol. 2013, 505, 240–249. https://doi.org/10.1016/j.jhydrol.2013.10.003

Moriasi, D.N.; Arnold, J.G.; Liew, M.W.V.; Bingner, R.L.; Harmel, R.D.; Veith, T.L. Model Evaluation guidelines for systematic quantification of accuracy in watershed simulations. Trans. ASABE 2007, 50, 885–900. http://dx.doi.org/10.13031/2013.23153

Nacar, S.; Hınıs, M.A.; Kankal, M. Forecasting daily streamflow discharges using various neural network models and training algorithms. KSCE J. Civ. Eng. 2018, 22, 3676–3685. https://doi.org/10.1007/s12205-017-1933-7

Ni, L.; Wang, D.; Singh, V.P.; Wu, J.; Wang, Y.; Tao, Y.; Zhang, J. Streamflow and rainfall forecasting by two long short-term memory-based models. J. Hydrol. 2020, 583, 124296. https://doi.org/10.1016/j.jhydrol.2019.124296

O'Malley, T.; Bursztein, E.; Long, J.; Chollet, F.; Jin, H.; Invernizzi, L. Keras Tuner. Available online: https://github.com/keras-team/keras-tuner (accessed on 30 May 2021).

Panagos, P.; Van Liedekerke, M.; Jones, A.; Montanarella, L. European Soil Data Centre: Response to European policy support and public data requirements. Land Use Policy 2012, 29, 329–338. https://doi.org/10.1016/j.landusepol.2011.07.003

Pedregosa, F.; Varoquaux, G.; Gramfort, A.; Michel, V.; Thirion, B.; Grisel, O.; Blondel, M.; Prettenhofer, P.; Weiss, R.; Dubourg, V.; et al. Scikit-learn: Machine learning in Python. J. Mach. Learn. Res. 2011, 12, 2825–2830.

Pham, Q.B.; Afan, H.A.; Mohammadi, B.; Ahmed, A.N.; Linh, N.T.T.; Vo, N.D.; Moazenzadeh, R.; Yu, P.-S.; El-Shafie, A. Hybrid model to improve the river streamflow forecasting utilizing multi-layer perceptron-based intelligent water drop optimization algorithm. Soft. Comput. 2020, 24, 18039–18056. http://dx.doi.org/10.1007/s00500-020-05058-5

Pörtner, H.-O.; Roberts, D.C.; Tignor, M.; Poloczanska, E.S.; Mintenbeck, K.; Alegría, A.; Craig, M.; Langsdorf, S.; Löschke, S.; Möller, V.; et al. IPCC, 2022: Climate Change 2022: Impacts, Adaptation and Vulnerability. In Contribution of Working Group II to the Sixth Assessment Report of the Intergovernmental Panel on Climate Change; Cambridge University Press: Cambridge, UK, 2022; p. 3068. DOI: 10.1017/9781009325844

Radiuk, P.M. Impact of training set batch size on the performance of convolutional neural networks for diverse datasets. Inf. Technol. Manag. 2017, 20, 20–24. http://dx.doi.org/10.1515/itms-2017-0003

Reddi, S.J.; Kale, S.; Kumar, S. On the convergence of adam and beyond. arXiv 2019. Available online: https://arxiv.org/abs/19 04.09237 (accessed on 8 February 2023).

Riad, S.; Mania, J.; Bouchaou, L.; Najjar, Y. Rainfall-runoff model using an artificial neural network approach. Math. Comput. Model. 2004, 40, 839–846. https://doi.org/10.1016/j.mcm.2004.10.012

Ruder, S. An overview of gradient descent optimization algorithms. arXiv 2017. Available online: https://arxiv.org/abs/1609.04747 (accessed on 8 February 2023).

Sahoo, A.; Samantaray, S.; Ghose, D.K. Stream flow forecasting in Mahanadi River Basin using artificial neural networks. Procedia Comput. Sci. 2019, 157, 168–174. https://doi.org/10.1016/j.procs.2019.08.154

Saon, G.; Picheny, M. Recent advances in conversational speech recognition using convolutional and recurrent neural networks. IBM J. Res. Dev. 2017, 61, 1:1–1:10. https://doi.org/10.1147/JRD.2017.2701178

Shen, C. A transdisciplinary review of deep learning research and its relevance for water resources scientists. Water Resour. Res. 2018, 54, 8558–8593. https://doi.org/10.1029/2018WR022643

Shu, X.; Ding, W.; Peng, Y.; Wang, Z.; Wu, J.; Li, M. Monthly streamflow forecasting using convolutional neural network. Water Resour. Manag. 2021, 35, 5089–5104. https://doi.org/10.1007/s11269-021-02961-w

Simionesei, L.; Ramos, T.B.; Palma, J.; Oliveira, A.R.; Neves, R. IrrigaSys: A web-based irrigation decision support system based on open source data and technology. Comput. Electron. Agric. 2020, 178, 105822. https://doi.org/10.1016/j.compag.2020.105822

Sit, M.; Demiray, B.; Demir, I. Short-Term Hourly Streamflow Prediction with Graph Convolutional GRU Networks. arXiv 2021. Available online: https://arxiv.org/abs/2107.07039 (accessed on 8 February 2023).

SNIRH, n.d. Sistema Nacional de Informação de Recursos Hídricos. Available online: https://snirh.apambiente.pt/index.php?idMain= (accessed on 7 February 2021).

Snoek, J.; Larochelle, H.; Adams, R.P. Practical bayesian optimization of machine learning algorithms. arXiv 2012. Available online: https://arxiv.org/abs/1206.2944 (accessed on 8 February 2023).

Szczepanek, R. Daily Streamflow Forecasting in Mountainous Catchment Using XGBoost, LightGBM and CatBoost. Hydrology 2022, 9, 226. https://doi.org/10.3390/hydrology9120226

Tao, Q.; Liu, F.; Li, Y.; Sidorov, D. Air pollution forecasting using a deep learning model based on 1D convnets and bidirectional GRU. IEEE Access 2019, 7, 76690–76698. https://doi.org/10.1109/ACCESS.2019.2921578

Ünes¸, F.; Demirci, M.; Zelenakova, M.; Çalışıcı, M.; Tas¸ar, B.; Vranay, F.; Kaya, Y.Z. River flow estimation using artificial intelligence and fuzzy techniques. Water 2020, 12, 2427. https://doi.org/10.3390/w12092427

Wang, J.-H.; Lin, G.-F.; Chang, M.-J.; Huang, I.-H.; Chen, Y.-R. Real-time water-level forecasting using dilated causal convolutional neural networks. Water Resour. Manag. 2019, 33, 3759–3780. https://doi.org/10.1007/s11269-019-02342-4

Wu, W.; Dandy, G.C.; Maier, H.R. Protocol for developing ANN models and its application to the assessment of the quality of the ANN model development process in drinking water quality modelling. Environ. Model. Softw. 2014, 54, 108–127. https://doi.org/10.1016/j.envsoft.2013.12.016

Xu, W.; Jiang, Y.; Zhang, X.; Li, Y.; Zhang, R.; Fu, G. Using long short-term memory networks for river flow prediction. Hydrol. Res. 2020, 51, 1358–1376. https://doi.org/10.2166/nh.2020.026

Yang, S.; Yang, D.; Chen, J.; Zhao, B. Real-time reservoir operation using recurrent neural networks and inflow forecast from a distributed hydrological model. J. Hydrol. 2019, 579, 124229. https://doi.org/10.1016/j.jhydrol.2019.124229

Zhang, X.; Peng, Y.; Zhang, C.; Wang, B. Are hybrid models integrated with data preprocessing techniques suitable for monthly streamflow forecasting? Some experiment evidences. J. Hydrol. 2015, 530, 137–152. https://doi.org/10.1016/j.jhydrol.2015.09.047

7 Assessing the reliability of a physical based model and a convolutional neural network in an ungauged watershed for daily streamflow prediction

Authors: Ana Ramos Oliveira, Tiago Brito Ramos, Lucian Simionesei and Ramiro Neves

Centro de Ciência e Tecnologia do Ambiente e do Mar (MARETEC-LARSyS), Instituto Superior Técnico, Universidade de Lisboa, Av. Rovisco Pais, 1, 1049-001 Lisboa, Portugal

Submitted to: Environmental Earth Sciences

Abstract

The main goal of this study was to estimate inflows to the Maranhão reservoir, in southern Portugal, using two distinct modelling approaches: a one-dimensional convolutional neural network (1D-CNN) model and a physically based model. The 1D-CNN was previously trained, validated, and tested in a sub-basin of the study area where observed streamflow values were available. The trained model was here subject to an improvement and applied to the entire watershed by replacing the forcing variables (accumulated and delayed precipitation) to make them correspond to the values of the entire watershed. In the same way, the physically based MOHID-Land model was calibrated and validated for the same sub-basin, and the calibrated parameters were then applied to the entire watershed. Inflow values estimated by both models were validated considering a mass balance at the reservoir. The 1D-CNN model demonstrated a better performance in simulating daily values, peak flows, and the wet period. The MOHID-Land model showed a better performance in estimating streamflow values during dry periods and for monthly analysis. Hence, results show the adequateness of both modeling solutions for integrating a decision support system aimed at supporting decision-makers in the management of water availability in an area subjected to increasing scarcity.

Keywords: MOHID-Land; 1D-CNN; streamflow; reservoir inflow; ungauged estimation

7.1 Introduction

The IPCC 2022 report (Pörtner et al., 2022) projects an increase in the frequency and severity of low flows in Southern Europe, resulting from increasing drought and water scarcity conditions. Population exposed to moderate water scarcity will grow by 18% and 54% for a raise of 1.5°C and 2°C in air temperature, respectively. The groundwater resources will be affected by an increase in abstraction rates and a decrease in recharge rates. Agriculture, which represents the main water use in the region, may be seriously limited by water availability. Thus, there is a need to improve water management at different scales to cope with the increasing scarcity. At the regional scale, this means the construction of dams and reservoirs to increase water storage, desalination, water reuse, and the adoption of water conservation measures. At the plot scale, that means reallocation to crops more resistant to drought conditions, the improvement of water use efficiency and performance of irrigation systems, and the implementation of soil water conservation practices (Jovanovic et al., 2020; Pereira et al., 2009).

Decision-support systems (DSSs) have been developed over the last few decades to improve water resources management at different spatial and temporal scales (Teodosiu et al., 2009). These tools commonly consist of interactive software-based systems where useful information from raw data sources, documents, simulation models, and other sources, are aggregated to identify and solve problems and support decision-making. Considering the plot scale, Smart Irrigation Decision Support System (SIDSS, Navarro-Hellín et al., 2016) and IrrigaSys (Simionesei et al., 2020) are examples of DSSs for irrigation water management support. SIDSS estimates weekly irrigation needs based on data from soil sensors and/or weather stations using two machine learning techniques. IrrigaSys also estimates weekly irrigation needs using a physically based model fed by weather forecast and hindcast data. When considering larger scales, Zhang et al. (2015a) designed and developed a prototype of a DSS for watershed management by integrating open-source web-based geographical information systems, a modelling component, and a cloud computing platform. Ashrafi and Mahmoudi (2019) presented a DSS to assist decision-makers in examining the impacts of different operating policies at the basin scale. DSSs are also applied to reservoir flood control operations (Delaney et al., 2020) and early warning and detection, follow-up, and early response to flood events and hazmat pollution occurrences in inland and transitional waters (HAZRUNOFF Project - Layman's Report, 2020).

As proposed by Miser and Quade (1985), one of the steps to designing a DSS is the building of models to predict consequences. A good hydrological and/or hydraulic model with reliable results and proven forecast capacity is of paramount importance for water management DSSs. Their results can then feed other models in the DSS. For instance, modelled groundwater levels can be used to estimate irrigation needs, or the simulation of river flows can help in flood forecast. However, modelling results can also be directly used to support decision-making.

Concerning models' classification, they can be divided into three main groups according to their complexity: (i) empirical models; (ii) conceptual models; and (iii) physical models (Sitterson et al., 2017). Empirical models are based on linear and non-linear equations that relate inputs and outputs ignoring the physical processes. These types of models are considered the simplest models. Conceptual models are based on simplified equations to describe the hydrological processes and are characterized by an intermediate level of complexity. Physical-based models, also known as process-based models, are the most complex and rely on physical principles, being suitable to provide insights into physical processes. Usually, physical models use finite difference equations and state variables that can be measured and are time and space dependent (Devia et al., 2015; Fatichi et al., 2016). However, their weakness relies on the large number of parameters required to describe the physical characteristics of the watershed, which leads to high complexity levels that make their correct implementation difficult and laborious calibration and validation processes (Devia et al., 2015; Abbott et al., 1986a, 1986b; Ranatunga et al., 2016; Zhang et al., 2015b; Mehr et al., 2013).

The study presented here is included within the framework of a larger work aimed at developing a DSS for supporting water management in the Maranhão and Montargil reservoirs, in southern Portugal. These reservoirs store water that is used mainly for irrigation of the Sorraia Valley, which comprehended a cultivated area of 21,280 ha and an irrigated area of 18,754 ha (ARBVS, 2023) in 2021. With a 52% increase in the irrigated area over the last two decades (ARBVS, 2023) and facing predictions of river flow decrease between 54% and 94% due to climate change (Almeida et al., 2018), accurate forecast of streamflow is of extreme importance to improve the management of water availabilities in the region. Taking as an example the Maranhão reservoir, the work presented here makes use of two different types of models to estimate the daily inflow to the reservoir and discusses the advantages and weaknesses of both approaches. The applied models were the physically based MOHID-Land model (Trancoso et al. 2009, Canuto et al, 2019, Oliveira et al. 2020) and a convolutional neural network (CNN) (Oliveira et al., 2023), i.e., a data-driven model. In both cases, the models were calibrated/trained and validated using data from a hydrometric station that corresponds to 30%

of the Maranhão watershed. Because no stations are monitoring the entire watershed despite the importance of this information for the sustainability of the irrigation district, this study also aims to analyze the capacity of both approaches to represent streamflow generation in the entire watershed. That analysis comprehended the expansion of models' results from the referred sub-basin to the full basin scale through the extension of the calibrated parameters in MOHID-Land, or through the replacement of the forcing variables in the CNN model. The results were then validated with a monthly reservoir mass balance. Therefore, this study provides sophisticated modeling tools for streamflow predictions in the Maranhão watershed, which were developed using two distinct modelling approaches. The ultimate aim is their integration into the DSS for supporting water managers in the decision-making of water availabilities in the region.

7.2 Materials and methods

7.2.1 Description of the study area

The Maranhão dam is located at Ribeira da Seda, southern Portugal (39°0'53.846''N; 7°58'33.149''W). The corresponding reservoir has a total capacity of 205 hm^3 and drains an area close to 2300 km^2. This watershed is included in the Tagus watershed. The minimum, average, and maximum altitudes are 122, 261, and 723 m, respectively (European Digital Elevation Model (EU-DEM), Version 1.1, 2019) (Figure 7.1).

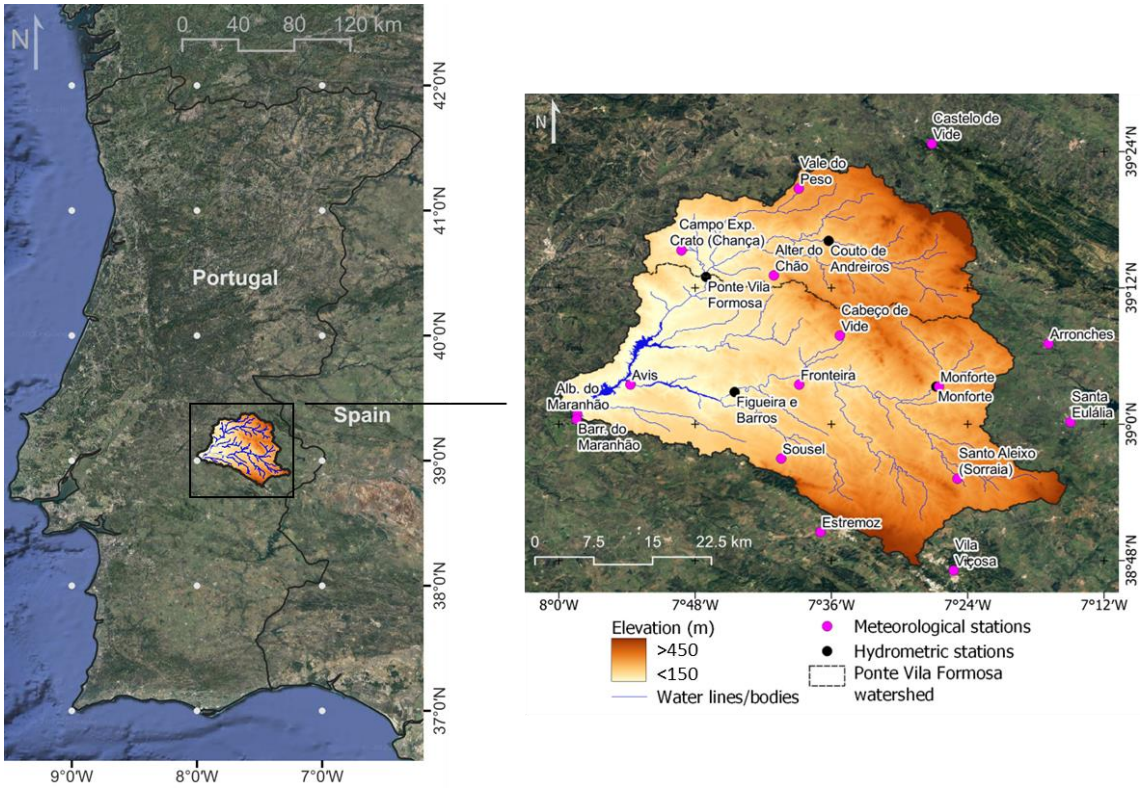

Figure 7.1 Maranhão watershed: location, delineation, elevation, main rivers, and hydrometric stations.

The climate is classified as Mediterranean hot-summer (Csa) according to the Köppen-Geiger climate classification (Agencia Estatal de Meteorología (España), 2011). The average annual precipitation is 608 mm. The minimum and maximum average monthly precipitation is 4 mm in July and August and 84 mm in December. The average monthly air temperature ranges from 24°C in July and August, and 9°C in January, while the annual average is 16°C. The main soil reference groups are Luvisols (67%), Regosols (18%), and Cambisols (11%) (Panagos et al., 2012). The main land uses are non-irrigated arable land and agro-forestry areas, both representing 28% of the watershed, broad-leaved forest, occupying 15%, and olive groves, with a representation of 11% (CLC 2012, 2019).

The Maranhão watershed has four hydrometric stations (Figure 7.1), with all measuring daily streamflow in a natural regime. Table 7.1 presents the characteristics of those stations in terms of drained area, recording period, the percentage of records within this period, and the minimum, maximum, median, and average streamflow.

Table 7.1 Characteristics of hydrometric stations: drained area, period of records, and percentage of records within this period, minimum (Min), maximum (Max), median (Med), and average (Ave) streamflow values (source: SNIRH, 2021).

Station	Drained area (km^2)	Period of records	% of records	Streamflow ($m^3 s^{-1}$)			
				Min	Max	Med	Ave
Couto de Andreiros	244.5	1 Oct 1963 – 15 Sep 2021	71	0	131.1	0.05	1.6

Station	Drained area (km^2)	Period of records	% of records	Streamflow ($m^3 s^{-1}$)			
				Min	Max	Med	Ave
Figueira e Barros	889.8	20 Dec 1985 – 30 Sep 1990	100	0	147.3	0.13	2.3
Monforte	141.5	1 Oct 1961 – 20 Oct 2020	62	0	121.7	0.03	0.9
Ponte Vila Formosa	664.8	1 Nov 1979 – 6 Mar 2019	54	0	272.8	0.63	3.8

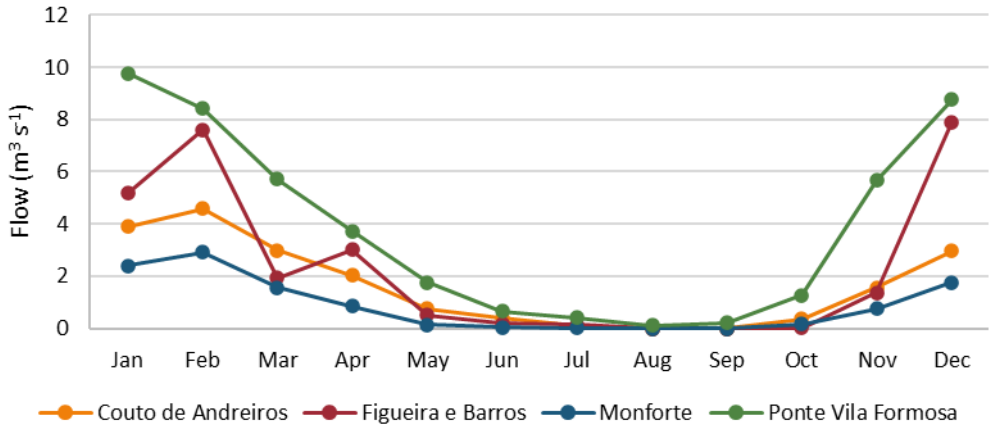

Figure 7.2 Monthly distribution of streamflow in the four hydrometric stations (source: SNIRH, 2021).

Figure 7.2 shows the monthly patterns considering the daily streamflow values at the four stations. In accordance with the meteorological characterization, streamflow patterns show higher values between November and April, while lower values occur between May and September, with August presenting the lowest value. Figueira e Barros station presents an unexpected behavior for the wet period with significative variations between months, which is not proper for natural regime flow. This is probably caused by the fact that this station only has records for 5 years, which are not enough to correctly analyze the monthly pattern. Couto de Andreiros and Monforte stations show smaller streamflow values than Ponte Vila Formosa since the drained area of the latter station is substantially higher than the former two. The specific streamflow (i.e., the average flow divided by the respective drained area) in Couto de Andreiros and Monforte is 6.0 L m^{-2}, while in Ponte Vila Formosa is 5.8 L m^{-2}. This seems to indicate that the streamflow generation is evenly distributed in the watershed.

The water stored in the Maranhão reservoir is mainly for irrigation of the Sorraia Valley (ARBVS,2023). Other uses include energy production, industrial supply, and recreation. The stored volumes normally increase during the wet period and decrease in the dry period as expected in hydroagricultural reservoirs (Figure 7.3).

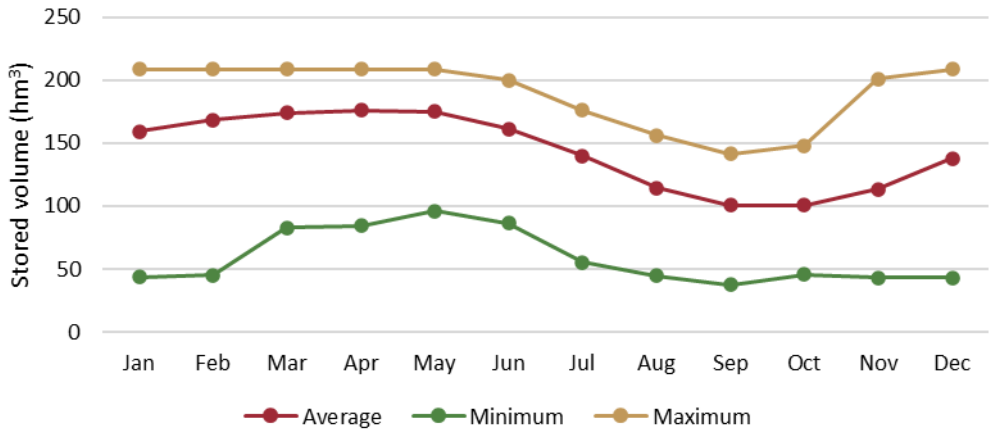

Figure 7.3 Monthly pattern of stored volume in Maranhão reservoir (source: SNIRH, 2021).

7.2.2 Convolutional neural network model description

A one-dimensional convolutional neural network (1D-CNN) was used in this study to estimate daily streamflow at Ponte Vila Formosa. This 1D-CNN model was created, developed, optimized, and tuned in Python language (version 3.8.10) using public and free tools (Keras, Chollet & others, 2015; TensorFlow, Abadi et al., 2016; KerasTuner, O'Malley et al., 2019; Pandas, McKinney, 2010; Scikit-learn, Pedregosa et al., 2011). A detailed description of the development of the 1D-CNN model used is presented in Oliveira et al. (2023). In that study, the authors carried out a set of experiments where three different neural network models were tested for streamflow estimation: a multi-layer perceptron model, a long short-term model, and a convolutional neural network model. Each type of model was presented to several combinations of precipitation and air temperature values, and their structures and hyper-parameters were optimized and tuned using six different training algorithms. Also, the batch size and the number of epochs were optimized. The best solution for streamflow estimation was then obtained with a 1D-CNN model composed of one input 1D convolutional layer with 16 filters, a kernel size equal to 1, and an output dense layer activated by a linear function. Between the input and output layers, two 1D convolutional layers, each having 32 filters and a kernel size of 8, were applied. After each 1D convolutional layer, a MaxPooling1D layer with pool_size set to 2 was placed. The Nadam optimizer was the training algorithm with the best performance combined with a learning rate of 1×10^{-3} and a ε (constant used for numerical stability) of 1×10^{-8}. A batch size of 20 and the number of epochs set to 200 were found to be the best options to optimize the model. Finally, the best performance of this model was obtained considering the input variables the daily precipitation values in the watershed accumulated in 1, 2, 3, 4, 5, and 10 days and delayed in 1, 2, 3, 4, 5, 6, and 7 days.

The CNN model was tuned, trained, and validated considering the streamflow values available in Ponte Vila Formosa hydrometric station for the period from 01/01/2001 to 01/01/2009. The model performance was considered good, reaching a Nash-Sutcliffe Efficiency (NSE) value of 0.86, a coefficient of determination (R^2) of 0.87, a percent bias (PBIAS) of 10.5%, and a root mean squared error (RMSE) of 4.2 $m^3 s^{-1}$ for the test dataset, but it only comprehended about 30% of the Maranhão watershed. Thus, in this study, the same 1D-CNN model was used by considering the precipitation of the entire Maranhão watershed instead of the sub-basin's data as in the original version.

7.2.2.1 Input variables for 1D-CNN model

The precipitation data used to train the 1D-CNN model was obtained from the ERA5 Reanalysis dataset (Hersbach et al., 2017). This is a gridded product with a resolution of 31 km and an hourly timestep. Precipitation data was extracted from the dataset considering all the cells within the limits of the watershed. Precipitation hourly values were then averaged within the watershed area and accumulated each day from 01/01/2001 to 31/12/2009. The daily precipitation values in the watershed accumulated in 1, 2, 3, 4, 5, and 10 days and delayed in 1, 2, 3, 4, 5, 6, and 7 days were considered. There were no gaps in the time series, counting a total of 78889 hourly values and 3287 daily values. The average annual precipitation for the period considered in this study was 575 mm, with July (3 mm) and August (8 mm) presenting the minimum monthly values, and October (104 mm) and November and December (both with 67 mm) the months when more precipitation was registered.

7.2.2.2 Estimation of Maranhão inflow with 1D-CNN

The Maranhão reservoir's daily inflow was estimated considering the daily precipitation in the corresponding watershed and the trained 1D-CNN model. However, because of the intrinsic random behavior verified in randomly initialized neural networks (Duan et al., 2020; Alzubaidi et al., 2021), the 1D-CNN model was trained 100 times. Those 100 runs were performed using the same dataset and division into training, validation, and test datasets presented in Oliveira et al. (2023). After each run, the trained weights were saved, and the results were compared and evaluated considering the observed streamflow in the Ponte Vila Formosa station. Based on the statistical evaluation, the model with the best performance was selected.

The selected 1D-CNN model was then exposed to Maranhão watershed daily precipitation, with results representing the daily surface flow generated in the watershed and flowing to the Maranhão reservoir. Those daily values were then aggregated by month and

transformed into volume. The estimated monthly volume that reached the Maranhão reservoir was incorporated into the reservoir mass balance to estimate the stored volume in the following month. The validation of inflow values was made through the comparison of estimated stored volumes and the corresponding observed values.

7.2.3 MOHID-Land model description

MOHID-Land is a hydrological model that is part of the MOHID (Hydrodinamic Model) Water Modelling System (Mateus and Neves, 2013). It is an open-source model, with the code available in an online repository (github.com/Mohid-Water-Modelling-System/Mohid). MOHID-Land (Trancoso et al. 2009, Canuto et al, 2019, Oliveira et al. 2020) is a fully distributed and physically based model. Considering the mass and momentum conservation equations and a finite volume approach, the model simulates the water movement between four main compartments: atmosphere, porous media, soil surface, and river network. To avoid instability problems and save computational time, the model time step is variable being higher during dry seasons and lower in wet periods when water fluxes increase.

According to his finite volume approach, the domains in MOHID-Land are discretized by a regular grid in the surface plane and by a cartesian coordinate system in the vertical direction. The land surface considers a 2D domain to simulate the water movement, while the porous media is represented by a 3D domain, which includes the same surface grid and is complemented by the vertical grid with variable thickness layers. Additionally, a 1D domain representing the river network can be derived from a digital terrain model represented in the horizontal grid. The water lines of the river network are then delineated by linking surface cell centers (nodes).

The four compartments referred to before are all explicitly simulated, except the atmosphere which is only responsible for providing the data needed for imposing surface boundary conditions. The atmospheric data can be space and/or time-variant and include precipitation, air temperature, relative humidity, wind velocity, solar radiation, and/or cloud cover.

The amount of water precipitated in each cell is divided into surface and subsurface flow considering the infiltration process and according to the soil saturation state. In this study, the infiltration rate (i, LT^{-1}) was computed according to Darcy's law:

$$i = -K_{sat}\left(\frac{\partial h}{\partial z} + 1\right) \quad \text{(Eq. 7.1)}$$

where K_{sat} is the saturated soil hydraulic conductivity (LT^{-1}), h is the soil pressure head (L), and z is the vertical space coordinate (L).

The movement of infiltrated water in porous media was simulated using Richards' equation, which is applied to the whole subsurface domain and simulates saturated and unsaturated flow using the same grid:

$$\frac{\partial \theta}{\partial t} = \frac{\partial}{\partial x_i}\left[K(\theta)\left(\frac{\partial h}{\partial x_i} + \frac{\partial}{\partial x_i}\right)\right] - S(h) \quad \text{(Eq. 7.2)}$$

where θ is the volumetric water content (L^3L^{-3}), xi represents the xyz directions (-), K is the hydraulic conductivity (LT^{-1}), and S is the sink term representing root water uptake ($L^3L^{-3}T^{-1}$). The soil hydraulic parameters were described using the van Genuchten Mualem functional relationships (Mualem, 1976, van Genuchten, 1980). When a cell reaches saturation, i.e., when soil moisture in a cell is above a threshold value defined by the user, the model considers the saturated conductivity to compute flow and pressure becomes hydrostatic, corrected by friction. The ratio between the horizontal and vertical hydraulic conductivities is defined by a factor (f_h=K_{hor}/K_{ver}) that can also be tuned by the user.

The root water uptake was estimated taking into account the weather conditions and soil water contents. The reference evapotranspiration (ET_o) rates were computed following the FAO Penman-Monteith method (Allen et al., 1998). The crop evapotranspiration (ET_c) rates were then estimated by multiplying the ET_o first with a crop coefficient (K_c). The K_c values were made to vary as a function of the plant development stage, as follows:

$$K_c = \begin{cases} K_{c,ini}, & GFr < GFr1 \\ K_{c,ini} + \dfrac{GFr - GFr1}{GFr2 - GFr1}\left(K_{c,mid} - K_{c,ini}\right), & GFr1 < GFr < GFr2 \\ K_{c,mid}, & GFr2 < PS < GFrLAI_{Sen} \\ K_{c,mid} + \dfrac{GFr - GFr2}{1.0 - GFr2}\left(K_{c,end} - K_{c,mid}\right), & GFr2 < GFr < 1.0 \\ K_{c,end}, & GFr > 1.0 \end{cases} \quad \text{(Eq. 7.3)}$$

where GFr, GFr1, GFr2, and GFrLAISen are the plant growth fractions in the simulated instant, in the initial stage, the mid-season stage, and when the LAI senescence starts, respectively, and $K_{c,\,ini}$, $K_{c,mid}$, and $K_{c,end}$ are the crop coefficients during the initial, mid-season and end-season stages, respectively. The plant growth stages are represented as a percentage of maturity heat units, and the values for GFr1, GFr2, and $GFrLAI_{Sen}$ are defined in the plant growth database of MOHID-Land. ET_c values are then partitioned into potential soil evaporation (E_s) and crop transpiration (T_c) as a function of the simulated leaf area index (LAI,) which is computed using a modified version of the EPIC model (Neitsch et al., 2011, Williams et al., 1989) and considering the heat units approach for the plant to reach maturity, the crop development stages, and crop stress (Ramos et al., 2017). Following the macroscopic approach proposed by Feddes

et al. (1978), root water uptake reductions (i.e., actual crop transpiration rates, T_a) are computed by distributing water extractions along the root zone domain and are estimated considering the presence of depth-varying stressors, such as water stress (Šimůnek and Hopmans, 2009, Skaggs et al., 2006). Finally, the actual soil evaporation is calculated from potential soil evaporation by imposing a pressure head threshold value (ASCE, 1996).

The amount of water that is not able to infiltrate is transformed into surface flow which is computed by solving the Saint-Venant equation in its conservative form, accounting for advection, pressure, and friction forces:

$$\frac{\partial Q_u}{\partial t} + \mathscr{v}_v \frac{\partial Q_u}{\partial x_u} = -gA\left(\frac{\partial H}{\partial x_u} + \frac{|Q|Q_u n^2}{A_v^2 R_h^{4/3}}\right) \quad \text{(Eq. 7.4)}$$

where Q is the water flow (L^3T^{-1}), A is the cross-sectional flow area (L^2), g is the gravitational acceleration (LT^{-2}), $\mathscr{v}$ is the flow velocity (LT^{-1}), H is the hydraulic head (L), n is the Manning coefficient ($TL^{-1/3}$), R_h is the hydraulic radius (L), and subscripts u and v denote flow directions. The Saint-Venant equation is solved on a 2D domain considering the directions of the horizontal grid except for the river network, where it is solved considering the 1D domain that comprehends the water lines. There, the cross-section for each node of the river network is defined by the user.

The water changes between the river network and the soil surface are estimated according to a kinematic approach, neglecting bottom friction, and using an implicit algorithm to avoid instabilities. The water fluxes between the river network and the porous media are driven by the pressure gradient in the interface of these two mediums.

7.2.3.1 Model set-up

The MOHID-Land model was implemented using a constant horizontal spaced grid with a resolution of 0.006º in both longitudinal and latitudinal directions (~520 m×666 m). To cover the modelled domain, the grid was composed of 140 columns and 110 rows, with its origin located at 38°45'16.5"N and 8°03'12.4"W.

Elevation data were interpolated to the MOHID-Land grid from the digital elevation model (DEM) provided by the European Environment Agency (European Digital Elevation Model (EU-DEM), Version 1.1, 2019). This DEM has a resolution of approximately 30 m (0.00028°) and results from the combination of Shuttle Radar Topography Mission (SRTM) and Advanced Spaceborne Thermal Emission and Reflection Radiometer (ASTER) Global Digital Elevation Model (GDEM) data, fused by a weighted averaging approach. The watershed's minimum and maximum elevations after the interpolation process were 107 m and

725 m, respectively (Figure 7.4a). The delineation of the watershed and the river network was performed considering the cell where the dam of Maranhão reservoir is located as the outlet. The minimum area to consider the existence of a waterline (minimum threshold area) was 10 km^2. Additionally, a rectangular geometry was chosen to represent the river cross-sections with the top (and bottom) width and the height defined according to Andreadis et al. (2013). The cross-sections' dimensions were related to the drained area and were assigned to the river network according to Table 7.2. For the nodes where the drained area relied on between the values presented in the table, the dimensions of the cross-section were linearly interpolated based on the given information.

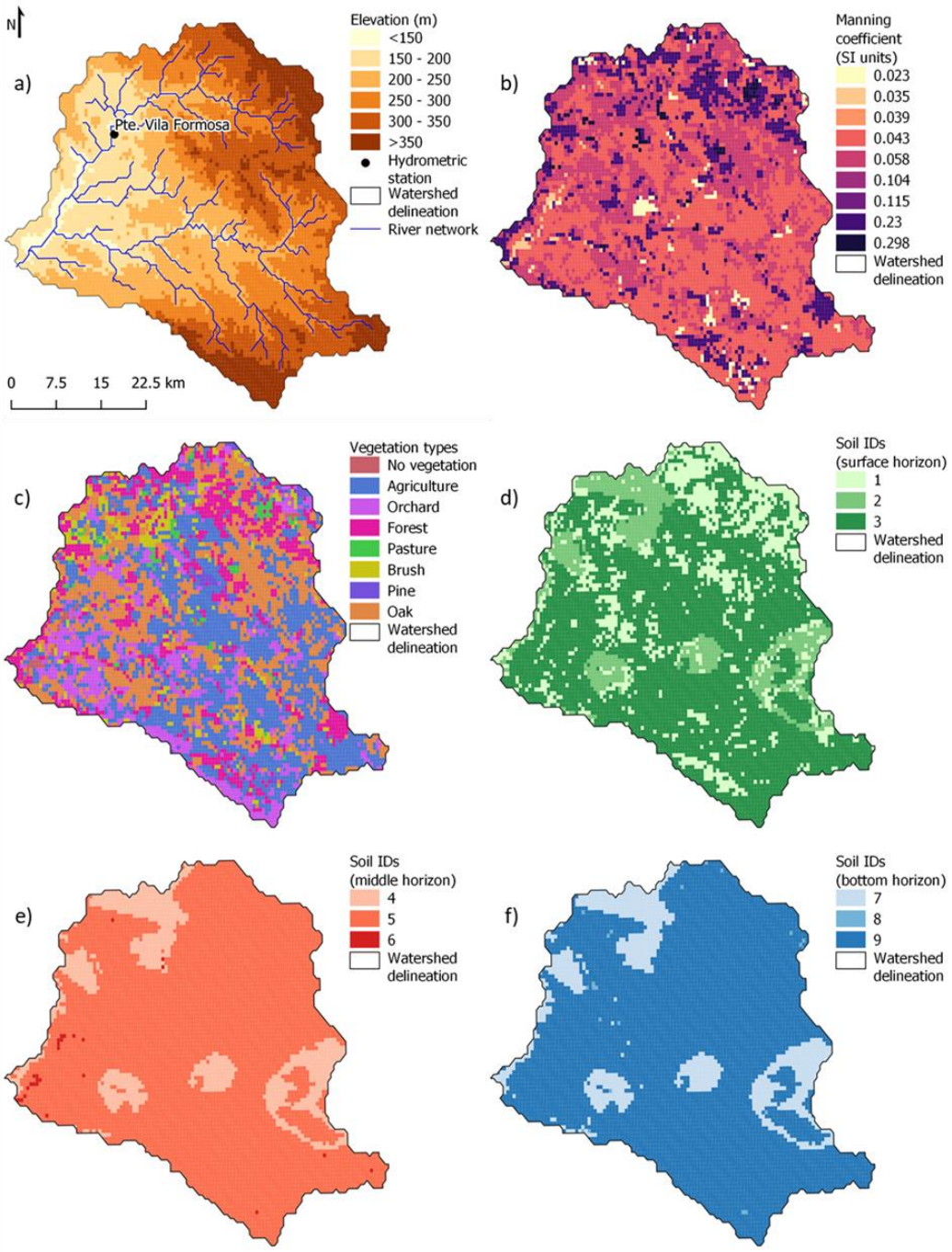

Figure 7.4 MOHID-Land inputs for Maranhão watershed: (a) digital terrain model and watershed and river network delineation; (b) Manning coefficient values; (c) types of vegetation; (d) identification number of the types of soil in the surface horizon; (e) identification number of the types of soil in the middle horizon; and (f) identification number of the types of soil in the bottom horizon.

Table 7.2 Cross sections dimensions according to the drained area.

Drained area (km^2)	Model set-up			Calibration		
	Width (m)	Height (m)	Area (m^2)	Width (m)	Height (m)	Area (m^2)
1.00	-	-	-	1.00	1.00	1.0
10.00	2	0.04	0.1	2.00	1.00	2.0

Drained area (km^2)	Model set-up			Calibration		
	Width (m)	Height (m)	Area (m^2)	Width (m)	Height (m)	Area (m^2)
49.18	4.61	0.19	0.9	4.61	1.50	6.9
86.80	6.22	0.24	1.5	6.22	1.50	9.3
143.70	8.12	0.30	2.4	8.12	2.25	18.3
395.33	13.84	0.45	6.2	13.84	3.00	41.5
748.75	19.38	0.58	11.2	19.38	3.00	58.1
2577.41	37.2	0.97	36.1	37.20	4.00	148.8

The CORINE Land Cover 2012, with a resolution of 100 m (CLC 2012, 2019), was interpolated to the MOHID-Land's grid and was used for representing land use in the watershed. Each land use class was associated with: (i) a Manning coefficient, which was defined according to Pestana et al. (2013) (Figure 7.4b), and (ii) a vegetation type class considering MOHID-Land's database (Figure 7.4c).

The K_c values were defined according to Allen et al. (1998) for agriculture (summer and winter crops), orchard, pasture, and brush, while pine, oak, and forest crop coefficients were defined based on the values proposed by Corbari et al. (2017) (Table 7.3).

Table 7.3 Crop coefficient values for initial stage ($K_{c,\ ini}$), mid- ($K_{c,\ mid}$), and late ($K_{c,\ end}$) seasons for each type of vegetation.

Type of vegetation	Crop coefficient					
	Model set-up			Calibration		
	$K_{c\ ini}$	$K_{c\ mid}$	$K_{c\ end}$	$K_{c\ ini}$	$K_{c\ mid}$	$K_{c\ end}$
Agriculture (summer crops)	0.15	1.15	0.35	0.15	0.70	0.50
Agriculture (winter crops)	0.70	1.15	0.30	0.40	0.70	0.15
Orchard	0.40	0.90	0.65	0.30	0.60	0.40
Forest	0.15	0.80	0.15	0.60	0.60	0.60
Pasture	0.30	0.75	0.75	0.30	0.60	0.60
Brush	0.40	0.40	0.40	0.30	0.30	0.30
Pine	0.15	0.80	0.15	0.60	0.60	0.60
Oak	0.15	0.80	0.15	0.60	0.60	0.60

The Mualem–van Genuchten hydraulic parameters were obtained from the multilayered European Soil Hydraulic Database (EU Soil Database, Tóth et al., 2017). Although the database provides information at 0.0, 0.05, 0.15, 0.3, 0.6, 1.0, and 2.0 m depths, with a resolution of 250 m, the present application only considered data from 0.3, 1.0, and 2.0 m depths. The porous media was divided into 6 layers, with a thickness of 0.3, 0.3, 0.7, 0.7, 1.5, and 1.5 m from surface to bottom (vertical grid), with the maximum total soil depth of 5.0 m. These layers were organized according to 3 different horizons characterized by the soil hydraulic properties acquired from the selected depths of the EU Soil Database. The 2 surface layers (0-0.6 m) were associated with the data at 0.3 m depth, the 2 middle layers (0.6-2.0 m) acquired the values at

1.0 m depth, and the information at 2.0 m depth was representative of the 2 bottom layers (2.0-5.0 m) (Table 7.4). Since MOHID-Land corrects the soil depth according to the surface slope, the thickness of the bottom layer presented a variation between 0.68 m and 1.5 m, corresponding to a minimum and maximum soil depth of 4.18 m and 5.0 m, respectively. The spatial variation of soil properties in the surface, middle and bottom horizons are shown in Figure 7.4.d, e, and f, respectively, with each ID corresponding to a different combination of soil hydraulic data.

Table 7.4 Mualem–van Genuchten hydraulic parameters by soil horizon. θ_r, residual water content; θ_s, saturated water content; α and η, empirical shape parameters; $K_{sat,vert}$, saturated hydraulic conductivity

Horizon	Layers (m)	EU Soil Database depth (m)	ID	θ_s ($m^3\ m^{-3}$)	θ_r ($m^3\ m^{-3}$)	η (-)	$K_{sat,vert}$ ($m\ s^{-1}$)	α (m^{-1})	l (-)
Surface	0 – 0.6	0.3	1	0.491	0.0	1.193	1.64×10^{-6}	3.47	-4.3
			2	0.409	0.0	1.134	5.05×10^{-6}	7.00	-5.0
			3	0.465	0.0	1.116	2.26×10^{-5}	12.84	-5.0
Middle	0.6 – 2.0	1.0	4	0.384	0.0	1.121	4.29×10^{-6}	7.17	-5.0
			5	0.413	0.0	1.119	1.43×10^{-6}	2.27	-5.0
			6	0.432	0.0	1.170	9.93×10^{-7}	3.36	-5.0
Bottom	2.0 – 5.0	2.0	7	0.384	0.0	1.121	4.29×10^{-6}	7.17	-5.0
			8	0.432	0.0	1.170	9.93×10^{-7}	3.36	-5.0
			9	0.413	0.0	1.119	1.43×10^{-6}	2.27	-5.0

The f_h parameter relating horizontal and vertical hydraulic conductivities was set to 10. Finally, the initial water table was assumed at a depth corresponding to 50% of the soil profile, with the initial soil moisture conditions above that depth set to field capacity.

As for the input variables used in the neural network model, meteorological data was obtained from the ERA5-Reanalysis dataset (Hersbach et al., 2017). For the implementation of MOHID-Land, the meteorological properties incorporated were the total precipitation, air temperature and dewpoint temperature (at 2 m height), u and v components of wind velocity (at 10 m height), surface solar radiation downwards, and total cloud cover. Wind velocity was adjusted from 10 m to 2 m height and relative humidity was estimated from air and dewpoint temperature according to Allen et al. (1998).

7.2.3.2 Estimation of Maranhão inflow with MOHID-Land

MOHID-Land was directly implemented in the entire Maranhão watershed but the lack of daily inflow data at the outlet only allowed model calibration and validation to be performed at Ponte Vila Formosa. There, the estimated daily streamflow data were compared with the observed data, and, when the performance of the model was good enough to represent the streamflow generation on that sub-basin, the calibrated parameters were assumed as

representatives of the Maranhão watershed. Hence, the daily streamflow estimated by the model in the outlet section was considered to represent the Maranhão reservoir's inflow and was transformed into monthly volume. The monthly volumes were then validated with a reservoir mass balance identical to the one presented for the validation of the 1D-CNN model's results.

7.2.4 Models' evaluation

MOHID-Land and 1D-CNN were calibrated/trained using the average daily streamflow in Ponte Vila Formosa hydrometric station. Validation was performed with daily and monthly timesteps. The dataset was also divided into wet (October to March), and dry (April to September) periods, and the results were validated, ignoring the division between calibrated/trained.

In the case of MOHID-Land, the calibration period was from 01/01/2002 to 31/01/2003 and the validation was from 01/01/2004 to 31/12/2009. For the 1D-CNN model, each of the 100 runs was evaluated considering the same test dataset presented by Oliveira et al. (2023). For both models, streamflow estimation performance was evaluated in Ponte Vila Formosa hydrometric station. The analysis was made with four different statistical parameters, namely, the coefficient of determination (R^2), the percent bias (PBIAS), the root mean square error (RMSE), and the Nash-Sutcliffe model efficiency (NSE):

$$R^2 = \left[\frac{\sum_{i=1}^{p} \left(X_i^{obs} - X_{mean}^{obs}\right)\left(X_i^{sim} - X_{mean}^{sim}\right)}{\sqrt{\sum_{i=1}^{p} \left(X_i^{obs} - X_{mean}^{obs}\right)^2} \sqrt{\sum_{i=1}^{p} \left(X_i^{sim} - X_{mean}^{sim}\right)^2}} \right]^2 \quad \text{(Eq. 7.5)}$$

$$PBIAS = \frac{\sum_{i=1}^{p} \left(X_i^{obs} - X_i^{sim}\right)}{\sum_{i=1}^{p} X_i^{obs}} \times 100 \quad \text{(Eq. 7.6)}$$

$$RMSE = \sqrt{\frac{1}{p} \sum_{i=1}^{p} \left(X_i^{obs} - X_i^{sim}\right)^2} \quad \text{(Eq. 7.7)}$$

$$NSE = 1 - \frac{\sum_{i=1}^{p} \left(X_i^{obs} - X_i^{sim}\right)^2}{\sum_{i=1}^{p} \left(X_i^{obs} - X_{mean}^{obs}\right)^2} \quad \text{(Eq. 7.8)}$$

where X_i^{obs} and X_i^{sim} are the flow values observed and estimated by the model on day i, respectively. X_{mean}^{obs} and X_{mean}^{sim} are the average flow considering the observed and the modelled values in the analyzed period, and p is the total number of days/values in this period. According to Moriasi et al. (2007), a model is considered satisfactory when NSE>0.5,

PBIAS±25%, and R^2>0.5, while the RMSE represents the standard deviation of the residuals with lower values meaning a better model's performance.

Maranhão reservoir's inflow was evaluated with a monthly timestep since this is the frequency of the data available in the reservoir. Since the models were already calibrated, the validation of the reservoir's inflow was done for the period comprehended between 01/01/2002 and 31/12/2009.

For the validation process, the monthly water volume that reaches the reservoir was incorporated into a mass balance where the observed stored volume from the previous month and the water volume that leaves the reservoir in the current month were also considered:

$$V_i^{sim} = V_{i-1}^{obs} + VI_i^{sim} - VO_i^{obs} \quad \text{(Eq. 7.9)}$$

where V_i^{sim} represents the estimated stored volume in month i, V_{i-1}^{obs} represents the observed stored volume in the previous month, VI_i^{sim} is the volume that enters the reservoir in month i resulting from the simulations, and VO_i^{obs} in the observed volume that leaves the reservoir. The stored volume estimated through the water balance was then compared to the observed stored volume of the corresponding month.

Performance assessment was made by visual comparison, and it was complemented by the estimation of the R^2, NSE, PBIAS, RMSE, and the RMSE-observation standard deviation ratio (RSR).

$$RSR = \frac{RMSE}{STDEV_{obs}} = \frac{\sqrt{\sum_{i=1}^{p}\left(X_i^{obs} - X_i^{sim}\right)^2}}{\sqrt{\sum_{i=1}^{p}\left(X_i^{obs} - X_{mean}^{obs}\right)^2}} \quad \text{(Eq. 7.10)}$$

where X_i^{obs} and X_i^{sim} are the stored volume values observed and estimated on month i, respectively, and X_{mean}^{obs} and X_{mean}^{sim} are the average stored volume in the analyzed period. It is important to note that the typical approach for inflow validation, which considers the direct calculation of inflow values from a mass balance performed in the reservoir, was also tested. However, about 30% of the inflow values estimated with that approach resulted in negative inflow values. Because of that, the referred approach was not considered in the study.

7.3 Results

7.3.1 1D-CNN at Ponte Vila Formosa

Considering the set of 100 runs performed with the 1D-CNN model and the precipitation of the Ponte Vila Formosa watershed, the four statistical parameters used to evaluate the model's performance were calculated for each run and considering the test dataset. Four sets

of 100 values were obtained. For each of those sets the minimum, maximum, average, standard deviation, median, and 1st and 3rd quartiles were estimated and are presented in Table 7.5.

Table 7.5 Goodness-of-fit indicators for the 1D-CNN model in Ponte Vila Formosa hydrometric station considering the set of 100 runs.

	NSE	**R^2**	**PBIAS (%)**	**RMSE (m^3 s^{-1})**
Minimum	0.42	0.59	-40.30	1.44
Maximum	0.88	0.90	66.76	3.13
Average	0.74	0.78	10.21	2.07
Standard deviation	0.08	0.06	19.13	0.30
Median	0.74	0.79	9.52	2.09
1st quartile	0.71	0.75	-3.51	1.90
3rd quartile	0.79	0.82	24.89	2.21
Best model	**0.88**	**0.88**	**-7.80**	**1.44**

A spread range of results was obtained for the statistical parameters, with RMSE ranging from 1.44 to 3.13 m^3 s^{-1}, PBIAS from -40 to 67%, R^2 from 0.59 to 0.90, and NSE from 0.42 to 0.88. Although some simulations did not reach the minimum requirements to be classified as satisfactory (NSE>0.5, R^2>0.5, and PBIAS>±25%), most of them got acceptable values, with the 1st quartile presenting a NSE of 0.71 and a R^2 of 0.75. This means that 75% of the simulations had higher values for NSE and R^2. However, taking into account the PBIAS results, the table shows that the value of the 3rd quartile was 25%, which means that a quarter of the simulations present higher and not satisfactory PBIAS. In turn, the 1st quartile of this statistical parameter was -3.5% and the minimum value was -40.3%, which indicates that from the 25 simulations that present lower PBIAS values, a significant part of them is still considered as having satisfactory behavior.

The simulation considered the best in fitting the observed streamflow in Ponte Vila Formosa station presented a NSE of 0.88, a R^2 of 0.88, a PBIAS of -7.8%, and a RMSE of 1.44 m^3 s^{-1} (Table 7.5). Although the R^2 of this model was not the maximum presented in the table, the combined values of the four statistical parameters represented the best solution, since the simulation with the maximum R^2 presented a PBIAS of 25%, which relies on the limit of the range for satisfactory performance.

For easier comparison with MOHID-Land, the four statistical parameters were also estimated considering the entire dataset, neglecting the first year (2001). Streamflow results show that the model outputs included negative values for 1.5% of the dataset, which means 50 of the 3229 days. Since these negative values occurred in isolated days, they were replaced by simply averaging the estimated streamflow from the previous and the next days. Table 7.6

presents those statistical parameters, while Figure 7.5 allows a visual assessment of the model's performance. In Table 7.6 are also presented the NSE, R^2, PBIAS, and RMSE values when the simulated interval was divided into wet and dry periods and considering the average monthly streamflow.

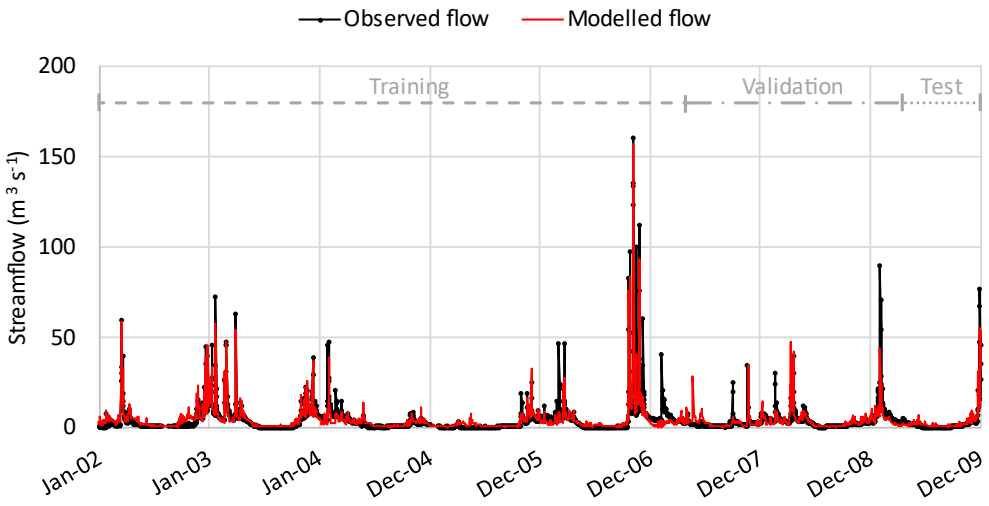

Figure 7.5 Comparison between observed and estimated streamflow values (using the 1D-CNN model) in Ponte Vila Formosa between 01/01/2002 and 31/12/2009.

Table 7.6 Goodness-of-fit indicators for the 1D-CNN model in Ponte Vila Formosa hydrometric station (best solution).

	NSE	R^2	PBIAS (%)	RMSE (m^3 s^{-1})
			Daily	
Entire dataset	0.83	0.83	-7.25	2.62
			Daily	
Wet period	0.79	0.79	8.62	5.77
Dry period	0.26	0.57	-52.74	2.16
			Monthly	
Entire dataset	0.87	0.87	2.23	2.01

When considering daily results, the 1D-CNN model demonstrated very good performance, with the NSE and R^2 reaching values of 0.65, the PBIAS being -7.21%, and the RMSE as 4.75 m^3 s^{-1}. Results were better when average monthly streamflow was considered, with NSE, R^2, PBIAS, and RMSE of 0.87, 0.87, 2.23%, and 2.01 m^3 s^{-1}, respectively. This is justified because the estimation of the average monthly values smooths out the daily errors. Considering the dry and wet periods, the 1D-CNN model shows a much better performance for the wet period. With the NSE and R^2 having both values of 0.79, and a PBIAS of 8.62% for

the wet period, the dry period obtained only a NSE value of 0.26, the R^2 decreased to 0.57, and the PBIAS presents a value of -53%.

7.3.2 MOHID-Land at Ponte Vila Formosa

MOHID-Land's calibration focused on a large number of different parameters related to the porous media, river network, and plant development processes. Among them, the f_h factor and the soil hydraulic parameters were calibration targets. In the river network, the minimum area to create a waterline, the cross-section dimensions, and the Manning coefficient were evaluated, and for the vegetation development, the K_c for different stages, and maximum root depth were also subjected to calibration.

The best solution obtained with MOHID-Land comprehended a river Manning coefficient of 0.035 s $m^{-1/3}$ and a minimum threshold area of 1 km^2. The calibrated cross-section dimensions are presented in Table 7.2, being clearly larger than those of the model set-up. In porous media, the f_h adopted the value 500 while the saturated water content of each soil type was increased by 10%. Finally, the development of the vegetation considered a triangular root profile (instead of the default exponential profile) with the maximum root depth being 25% to 60% lower than the default values of MOHID-Land's growth database.

The comparison between the streamflow values registered in the Ponte Vila Formosa station and those estimated by MOHID-Land is presented in Figure 7.6, with the corresponding statistical parameters shown in Table 7.7. Table 7.7 also shows NSE, R^2, PBIAS, and RMSE for the average monthly streamflow and the division of the analyzed period into wet and dry seasons.

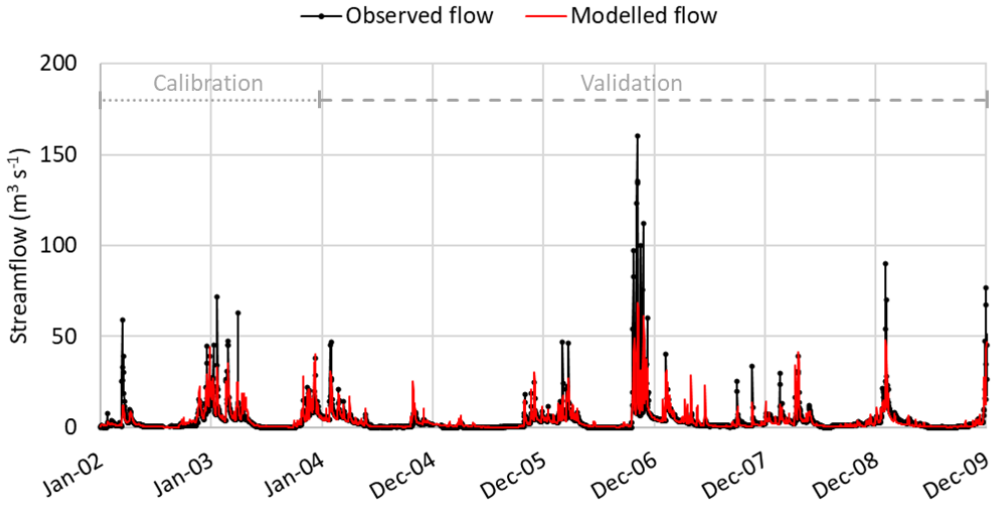

Figure 7.6 Comparison between observed and estimated streamflow values (using MOHID-Land model) in Ponte Vila Formosa between 01/01/2002 and 31/12/2009.

Table 7.7 Goodness-of-fit indicators for MOHID-Land model in Ponte Vila Formosa hydrometric station.

	NSE	R^2	PBIAS (%)	RMSE ($m^3 s^{-1}$)
			Daily	
Calibration	0.65	0.65	-7.21	4.75
Validation	0.62	0.63	4.18	6.50
			Daily	
Wet period	0.61	0.63	8.67	7.87
Dry period	0.39	0.69	-30.14	1.96
			Monthly	
Calibration	0.85	0.86	-6.59	1.97
Validation	0.92	0.95	4.15	1.57

MOHID-Land's results show the satisfactory performance obtained with this model. It reached a NSE and a R^2 of 0.65 for the calibration period with a slight decrease in the validation period (0.62 for NSE and 0.63 for R^2). PBIAS demonstrated an underestimation of streamflow in calibration and an overestimation during validation, while RMSE values were similar in both periods. When considering the monthly aggregation, the model reached a very good performance, with NSE and R^2 values above 0.85 in calibration and validation periods. The RMSE showed a decrease in both periods when compared with the daily values. Finally, PBIAS values did not suffer significant changes. During the wet period, the performance of the model was better than in the dry period. Although R^2 showed a better value for the dry period, NSE and PBIAS demonstrated an accentuated decrease in the model's performance in the dry period, with the first going from 0.61 to 0.39 and the second indicating an overestimation of about 9% in wet periods and an underestimation of about 30% in the dry period.

7.3.3 Maranhão reservoir's inflow

The characterization of the Maranhão reservoir's inflow obtained with MOHID-Land and 1D-CNN models from 01/01/2002 until 31/12/2009 are presented in Table 7.8. The respective flow duration curve is presented in Figure 7.7.

Table 7.8 Maranhão reservoir's inflow characterization for 1D-CNN and MOHID-Land models.

	Inflow ($m^3 s^{-1}$)					
	Min	**Max**	**Average**	**1st quartile**	**Median**	**3rd quartile**
1D-CNN	0	143.1	3.6	0.7	1.9	4.1
MOHID-Land	0.1	68.4	3.9	0.5	1.6	4.4

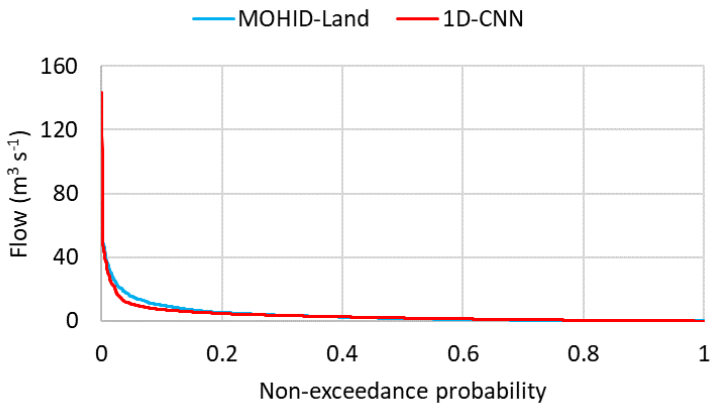

Figure 7.7 Flow duration curve for Maranhão reservoir's inflow estimated with MOHID-Land (blue line) and 1D-CNN (red line).

Results from Table 7.8 showed very similar behavior for both models apart from the maximum streamflow value. In that case, the 1D-CNN model presented a maximum streamflow of more than twice the maximum streamflow estimated by MOHID-Land. However, MOHID-Land had a slightly higher streamflow average. It indicates that for the middle streamflow values, MOHID-Land tends to overestimate 1D-CNN mode. It is also demonstrated in Figure 7.7, where it is possible to confirm that streamflow values with a non-exceedance probability between 0 and 0.3 higher values are observed for MOHID-Land.

Regarding the validation of stored volumes considering the reservoir's mass balance, NSE, R^2, PBIAS, RMSE, and RSR were estimated for the entire period, and the results are presented in Table 7.9. Figure 7.8 presents the graph with the comparison between the two models and the observed stored volumes.

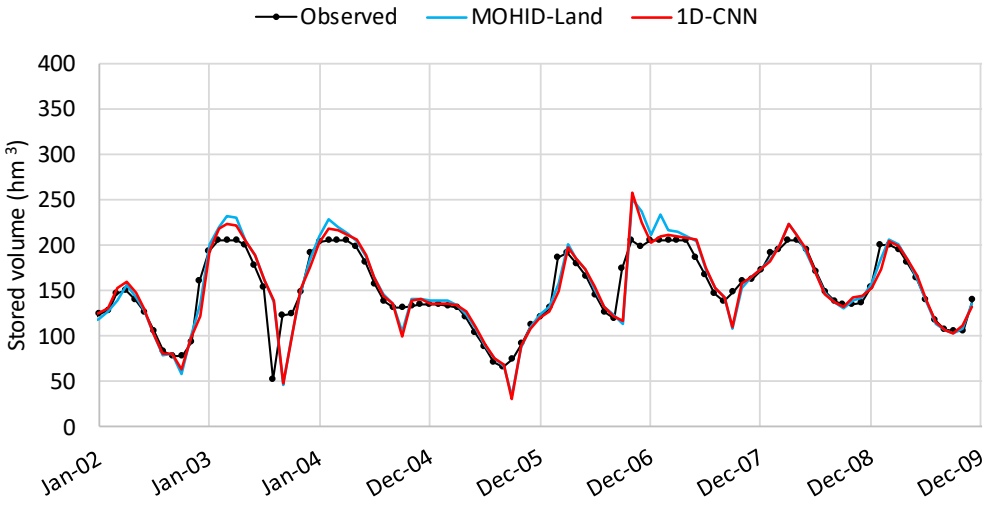

Figure 7.8 Comparison between observed stored volume (black line) and stored volumes estimated considering the streamflow simulated by MOHID-Land (blue line) and 1D-CNN model (red line).

Table 7.9 Goodness-of-fit indicators for MOHID-Land and 1D-CNN models for the reservoir's stored volume.

	NSE	R^2	PBIAS (%)	RMSE (hm^3)	RSR (-)
1D-CNN	0.79	0.84	-0.55	18.62	0.46
MOHID-Land	0.79	0.85	-1.18	18.61	0.46

Results showed good agreement between both models and observed values. In fact, 1D-CNN and MOHID-Land presented very similar R^2 (1D-CNN: 0.84; MOHID-Land: 0.85) and RMSE (1D-CNN: 18.62 hm^3; MOHID-Land: 18.61 hm^3) values. NSE and RSR values were equal in both cases, while PBIAS was the parameter in which some difference is observed. With a PBIAS of -0.55% for the 1D-CNN model and -1.18% for the MOHID-Land model, both models were slightly underestimating the reservoir's inflow. MOHID-Land showed a higher tendency for that underestimation.

7.4 Discussion

7.4.1 1D-CNN model

The 1D-CNN model had already demonstrated its adequacy to predict streamflow in the sub-basin of the Ponte Vila Formosa hydrometric station as demonstrated in Oliveira et al. (2023). The approach presented here, where 100 simulations were performed with the same 1D-CNN structure, allowed to slightly improve the results obtained in that study. From the set of 100 models, the best solution had a NSE and a R^2 of 0.88, a PBIAS of -7.80%, and a RMSE of 1.44 $m^3\ s^{-1}$, considering the test dataset. It overcame the solution presented by Oliveira et al. (2023), which obtained a NSE, a R^2, a PBIAS, and a RMSE of 0.86, 0.87, 10.5%, and 4.2 $m^3\ s^{-1}$, respectively. Results also show that half of the 100 simulations obtained a NSE higher than 0.74 and/or a R^2 above 0.79. The same number of simulations got a PBIAS lower than 9.52%. It indicates the suitability of the developed structure for streamflow estimation even with the random nature of the process involved.

The results of the 1D-CNN model are in accordance with the results of Barino et al. (2020), Huang et al. (2020), Duan et al. (2020), and Song (2020). Barino et al. (2020) used two 1D-CNN to predict multi-day ahead river flow in Madeira River, a tributary of the Amazon River, in Brazil. One of those models considered only the river flow on previous days, while the other considered that same variable combined with the turbidity on previous days. Both models obtained NSE and R^2 values higher than 0.92, while mean absolute percentage error (MAPE) and normalized RMSE were lower than 25% and 0.20, respectively. Among the models analyzed by Huang et al. (2020), two CNN models were studied to forecast daily

streamflow a day ahead. Considering the lagged streamflow values of the past 16 days in the site to be forecasted and in the neighborhood, a generic CNN model and a CNN model trained with a transfer learning procedure were tested. With four different locations in the United Kingdom being the target of the study, the generic CNN model obtained MAPE values between 14.36% and 41.95%, while the MAPE of the other CNN model laid between 12.29% and 32.17%. Duan et al. (2020) considered the watersheds within the Catchment Attributes for Large-Sample Studies (CAMELS dataset), in California, USA, to test a temporal CNN model. The model was developed for long-term streamflow projection and consisted of a one-dimensional network that used dilated causal convolutions. As input variables, authors elected precipitation, temperature, and solar radiation and tested different time window sizes to delay the values. After performing 15 runs for each watershed in the CAMELS dataset, the average NSE was 0.55, while the average NSE for the best run over all basins was 0.65. Finally, a CNN model was employed by Song (2020) to estimate daily streamflow in the Heuk River watershed, in South Korea. Using rainfall, runoff, soil map, and land use data, the authors generated a hydrological image based on the curve number method to feed the neural network and estimate streamflow in the watershed. The model evaluation resulted in a coefficient of correlation of 0.87 and a NSE of 0.60.

Usually, in machine learning methods better results are verified when antecedent streamflow is considered as a forcing variable (Barino et al., 2020; Khosravi et al., 2022). However, when the model is used in the simulation of future scenarios or periods when no observed data are available, the antecedent streamflow values to feed the model are those already calculated by the model in previous iterations. As a consequence, the propagation and exacerbation of errors in the estimates lead to a degradation of the results in the long term. There are also other types of machine learning methods for streamflow estimation emerging in the last few years. For instance, Si et al. (2021) considered a graphical convolutional GRU model to predict the streamflow in the next 36h hours, while Szczepanek (2022) used three different models, namely, XGBoost, LightGBM, and CatBoost, for daily streamflow forecast. Additionally, hybrid solutions considering different machine learning algorithms for streamflow estimation, such as Di Nunno et al. (2023) and Yu et al. (2023), are becoming widely used and with improved results.

7.4.2 MOHID-Land model

MOHID-Land daily results demonstrated to be satisfactory according to the criteria of Moriasi et al. (2007). With a NSE and a R^2 higher than 0.62 and 0.63, respectively, and a PBIAS

between -7% and 4%, and an average RMSE of 5.6 $m^3 s^{-1}$, these results were substantially better than those presented by Almeida et al. (2018) for the same study area. Using Soil Water Assessment Tool (SWAT), the authors compared the daily streamflow also in Ponte Vila Formosa hydrometric station. They obtained a NSE, a R^2, a bias and a RMSE of -3.05, 0.31, 2.93, and 12.61 $m^3 s^{-1}$, respectively, for the calibration period. For the validation, the NSE was 0.11, the R^2 was 0.24, and the bias, and RMSE were -0.46 and 15.21 $m^3 s^{-1}$, respectively. Almeida et al. (2018) also made a daily comparison in Moinho Novo hydrometric station, which is located in the Montargil watershed and is very similar to the Maranhão watershed sharing boundaries between them. For the Moinho Novo station, the authors obtained for calibration and validation periods, respectively, a NSE of 0.22 and 0.39, a R^2 of 0.41 in both cases, a bias of 0.90 and -1.07 and a RMSE of 13.1 and 16.6 $m^3 s^{-1}$. Bessa Santos et al. (2019) estimated the daily streamflow in the Sabor River watershed, placed in Northeast Portugal and with an area of 3170 km^2. Using the SWAT model, they compared the modelled and observed river flow values in a hydrometric station in which the drained area is slightly smaller than the Sabor River watershed. The results reached a NSE of 0.62 and 0.61 for calibration and validation periods, respectively, and a R^2 for those same periods of 0.63 and 0.80. The PBIAS was 2.7% for calibration and -24% for validation, while RSR for calibration and validation was 0.62 and 0.63, respectively. Considering the Pracana watershed, located in Central Portugal, Demirel et al. (2009) also used the SWAT model to predict daily streamflow. The authors classified the model as having a poor peak magnitude estimation.

Considering the monthly values, MOHID-Land's performance increased substantially when compared with the daily values. The results reached NSE values of 0.85 and 0.92 and R^2 values of 0.86 and 0.95 for calibration and validation periods, respectively. PBIAS and RMSE also demonstrated the very good behavior of the model on a monthly basis. Those parameters obtained very good results for the calibration and validation periods, with PBIAS indicating a slight underestimation during calibration (-6.59%) and an overestimation (4.15%) during validation, and the RMSE being about 2 $m^3 s^{-1}$ for both periods. In line with the work presented here, Brito et al. (2018) used SWAT for long-term forecasts of the monthly Enxoé reservoir's inflow. With this watershed located in South Portugal and draining an area of 60 km^2, the authors reached a NSE of 0.78 and a R^2 of 0.77. Almeida et al. (2018) also presented a monthly analysis for the Ponte Vila Formosa station, with SWAT obtaining a NSE of -1.26 and 0.40 for calibration and validation periods. For calibration and validation, respectively, R^2 reached values of 0.58 and 0.54, the bias was 2.97 and -0.42, and the RMSE was 6.04 and 5.93 $m^3 s^{-1}$. Ponte Vila Formosa streamflow was also modelled by van der Laan et al. (2023) with SWAT

model. They obtained a NSE, a R^2, and a PBIAS for the calibration period of 0.76, 0.77, and -7.1%, respectively. For the validation period, the NSE was 0.89, the R^2 was 0.9, and PBIAS was 15%.

The comparisons presented above allowed to conclude that MOHID-Land's performance is in line with other studies carried out in Portuguese watersheds for daily streamflow estimation. The exception was the study performed by Almeida et al. (2018) where the simulation of the same sub-basin that was being modelled here obtained a much poorer performance there. When monthly streamflow was considered, MOHID-Land's performance surpassed the results obtained with the SWAT model for the same or identical sub-basins. The difference in the performance of the models is justified by the fact that SWAT is more empirically parametrized than MOHID-Land. For instance, MOHID-Land explicitly estimates the infiltration and porous media fluxes based on Darcy's law and Richards equation, respectively, with the remaining water transformed into surface runoff where fluxes are estimated based on the Saint-Venant equation. On the other hand, in SWAT a baseflow factor, which is a direct index of groundwater flow response to changes in recharge, or a surface runoff lag coefficient to control the fraction of the total available water that will be allowed to enter the reach on one day, needs to be defined. The empirical parametrization of some processes prevents a more accurate representation of reality, leading to more errors in estimates and the degradation of the overall performance, especially beyond the period of calibration.

Nonetheless, MOHID-Land has its own limitations. On one hand, the implementation effort is significatively high, with several parameters needing to be defined, such as the six hydraulic parameters of all the soil types, the crop coefficients for each type of vegetation, the surface and the river Manning coefficients, and others. The high number of input data, parameters, and variables that the user should define conduces to an extremely high number of parameters that can be calibrated, which can be time-consuming. A consequence of this is reflected in the number of simulations performed to reach the best solution. In this study, more than 70 simulations were made to test the sensitivity of the MOHID-Land to other parameters than those studied by Oliveira et al. (2020) and to obtain the combination that allows a good fit between modelled and observed streamflow. On the other hand, the empirical representation of parts of the hydrological processes or the generalization of some parameters can make the representation of the modelled system difficult, leading to values of the calibrated parameters outside the normal ranges. That condition is here verified with the crop coefficients calibrated for the summer and winter crops, which are considered too low.

7.4.3 Models' comparison

Overall, the 1D-CNN model demonstrated a better performance than the MOHID-Land model for daily streamflow estimation in Ponte Vila Formosa hydrometric station. However, when the results are aggregated by month, MOHID-Land's performance surpassed the neural network results.

Focusing on wet and dry periods, it is interesting to verify that the results of both models complement each other. If on the one hand, the 1D-CNN model obtained a performance for the wet period better than that obtained by MOHID-Land, on the other hand, during the dry period MOHID-Land demonstrated a better performance. Thus, in the first case both models achieved satisfactory performances, but the 1D-CNN model, with a NSE and R^2 of 0.79, was better than MOHID-Land, which obtained a NSE of 0.61 and a R^2 of 0.63. In the second case, the dry period, both models experienced a decrease in their performances, but MOHID-Land, with a NSE of 0.39 and a R^2 of 0.69, performed better than the 1D-CNN model, which obtained a NSE of 0.26 and a R^2 of 0.56. These results put in evidence the difficulty of MOHID-Land in estimating the peak flow events, but also a better ability to simulate the transitions between the wet and dry periods when compared to the 1D-CNN. It can also be verified in Figure 7.5 and Figure 7.6, where the results for MOHID-Land demonstrate a more natural behavior than those obtained for the 1D-CNN model.

The more irregular behavior of the 1D-CNN model is, in part justified, by the fact that these types of models do have not a physical basis, which means that the streamflow estimation does not take into account physical laws or limitations. This characteristic of neural network models also justifies the difficulty in avoiding the existence of negative streamflow values. Although other authors did not refer to this issue, it was verified in this study and should not be ignored, since it can limit the application of the model.

7.4.4 Models' extension to Maranhão watershed

The streamflow estimated by the extension of 1D-CNN and MOHID-Land models to the entire Maranhão watershed (Maranhão reservoirs' inflow) was made by the adaptation of the trained and calibrated models to that watershed. Thus, the 1D-CNN model presents a maximum inflow value substantially higher than the maximum predicted by MOHID-Land, which is related to the fact that MOHID-Land demonstrated some difficulty in reproducing peak flow values (Table 7.8). The remaining statistics are similar between both models, with the minimum streamflow near 0 $m^3 s^{-1}$, the average between 3.6 and 3.9 $m^3 s^{-1}$, and the median is 1.9 and 1.6 $m^3 s^{-1}$ for 1D-CNN and MOHID-Land.

The evaluation of the inflow values based on the mass balance at the reservoir scale showed very good performance when using the 1D-CNN model and MOHID-Land model (Table 7.9). Both models have a NSE and RSR of 0.79 and 0.46, respectively. R^2 is 0.84 for 1D-CNN and 0.85 for MOHID-Land and the RMSE is 18.6 hm^3 for both models. The higher difference in the statistical parameters is in the PBIAS with the 1D-CNN having an underestimation of -0.55% and the MOHID-Land also presenting an underestimation but a little higher, of about -1.18%. Visually, it is also possible to verify slight differences between the stored volume estimated with inflow from the 1D-CNN model and from MOHID-Land model (Figure 7.8), with the main differences occurring in the wet season (October to March).

In a similar approach but considering the continuous simulation of the stored water in two reservoirs included in the same modelled watershed, Rocha et al. (2020) found identical results. Using the SWAT model for Monte Novo and Vigia reservoirs, in southern Portugal, the authors validated the stored volume of both reservoirs with a monthly timestep, obtaining a NSE of 0.44 and a PBIAS of 6.3% for the Monte Novo reservoir and a NSE of 0.70 and PBIAS of 10.1% for Vigia reservoirs.

In this case, models were extended to an ungauged watershed, in which physical characteristics and the rainfall regime are similar to those verified in the sub-basin where the models were trained or calibrated. In that sense, the question that arises from this study is about the behavior of this expanding approach when larger watersheds, marked by diversified characteristics and rainfall regimes, are the target of the study. In those cases, the calibrated parameters cannot be representative or even represented in the expanded area, for the typical hydrological models, or the differences in the rainfall regime when considering the expanded area cannot be correctly related to the runoff values, which was already referred to by Parisouj et al. (2020).

7.5 Conclusions

The approach proposed in this study showed the adequateness of implementing a 1D-CNN model and a physically based model for estimating daily streamflow generation at the outlet of an ungauged watershed after prior calibration/validation of those models in a subbasin of the same catchment. Considering the sub-basin modelling, the 1D-CNN model demonstrated a better performance than MOHID-Land when considering the daily values and the wet period. The MOHID-Land model showed a better performance in estimating streamflow values during dry periods and for monthly analysis. When the validation of the reservoir mass balance was taken into account, the results showed an identical behavior for both models, with only a slight

difference in the PBIAS value. That difference indicates a smaller underestimation of inflow by the 1D-CNN model than that estimated by MOHID-Land.

Although the results were considered satisfactory to very good in all the steps taken during the validation process, the generation of negative values by the 1D-CNN model is of concern. In that sense, and since there is no reference to this situation in the literature, the model presented here should be a target of improvement in future applications. In turn, the MOHID-Land model revealed a lower performance for daily streamflow estimation, but its physical basis contributes to avoiding unpredictable and incomprehensible results.

Finally, it is worth noting that neural network models are developed and trained for present and/or past conditions, and their application to study future scenarios can be limited. Also, the prediction of events that go beyond the observations can be problematic. This limitation is mainly related to its lack of capacity to absorb information about future conditions in cases where neural networks were not prepared to be forced by variables that include the impact of those future changes. Nonetheless, the changes in future conditions can be easily imposed in physically based models, with the main problems being: (i) the detail of the characterization of future conditions, which most of the time is too coarse for the detail adopted on physical models; and (ii) the high computational time needed to run long-term simulations, usually performed in the analysis of future scenarios. In that sense, hybrid solutions, combining different types of models or different models, can be used to incorporate the predicted changes in neural network models.

Author contributions

A.R.O. was responsible for the conceptualization, software, formal analysis, and writing of the original draft. The methodology was elaborated by A.R.O., L.S. and T.B.R. T.B.R., L.S. and R.N. revised the manuscript.

Funding

This research was supported by FCT/MCTES (PIDDAC) through project LARSyS–FCT pluriannual funding 2020–2023 (UIDP/50009/2020). T. B. Ramos was supported by a CEEC-FCT contract (CEECIND/01152/2017).

7.6 References

Abadi, M.; Barham, P.; Chen, J.; Chen, Z.; Davis, A.; Dean, J.; Devin, M.; Ghemawat, S.; Irving, G.; Isard, M.; et al. Tensorflow: A system for large-scale machine learning. In

Proceedings of the 12th USENIX Symposium on Operating Systems Design and Implementation (OSDI '16), Savannah, GA, USA, 2–4 November 2016; pp. 265–283.

Abbott, M.B.; Bathurst, J.C.; Cunge, J.A.; O'Connell, P.E.; Rasmussen, J. An Introduction to the European Hydrological System — Systeme Hydrologique Europeen, "SHE", 1: History and Philosophy of a Physically-Based, Distributed Modelling System. J. Hydrol. 1986a, 87, 45–59. https://doi.org/10.1016/0022-1694(86)90114-9

Abbott, M.B.; Bathurst, J.C.; Cunge, J.A.; O'Connell, P.E.; Rasmussen, J. An Introduction to the European Hydrological System — Systeme Hydrologique Europeen, "SHE", 2: Structure of a Physically-Based, Distributed Modelling System. J. Hydrol. 1986b, 87, 61–77. https://doi.org/10.1016/0022-1694(86)90115-0

Agencia Estatal de Meteorología (España) Atlas Climático Ibérico: Temperatura Del Aire y Precipitación (1971-2000)=Atlas Climático Ibérico: Temperatura Do Ar e Precipitação (1971-2000)=Iberian Climate Atlas : Air Temperature and Precipitation (1971-2000); Instituto Nacional de Meteorología: Madrid, 2011. ISBN 978-84-7837-079-5.

Allen, R.G.; Pereira, L.S.; Raes, D.; Smith, M. Crop Evapotranspiration - Guidelines for Computing Crop Water Requirements. FAO Irrigation and Drainage Paper 56. FAO 1998, 327.

Almeida, C.; Ramos, T.; Segurado, P.; Branco, P.; Neves, R.; Proença de Oliveira, R. Water Quantity and Quality under Future Climate and Societal Scenarios: A Basin-Wide Approach Applied to the Sorraia River, Portugal. Water 2018, 10, 1186. https://doi.org/10.3390/w10091186

Alzubaidi, L.; Zhang, J.; Humaidi, A.J.; Al-Dujaili, A.; Duan, Y.; Al-Shamma, O.; Santamaría, J.; Fadhel, M.A.; Al-Amidie, M.; Farhan, L. Review of Deep Learning: Concepts, CNN Architectures, Challenges, Applications, Future Directions. J Big Data 2021, 8, 53. https://doi.org/10.1186/s40537-021-00444-8

Andreadis, K.M.; Schumann, G.J.-P.; Pavelsky, T. A Simple Global River Bankfull Width and Depth Database: Data and Analysis Note. Water Resour. Res. 2013, 49, 7164–7168. https://doi.org/10.1002/wrcr.20440

ARBVS Área Regada Available online: https://www.arbvs.pt/index.php/culturas/area-regada (accessed on 18 October 2022).

ASCE, Task Committee on Hydrology Handbook of Management Group D of ASCE. Hydrology Handbook (Second Edition). American Society of Civil Engineers 1996. https://doi.org/10.1061/9780784401385

Ashrafi, S.M.; Mahmoudi, M. Developing a Semi-Distributed Decision Support System for Great Karun Water Resources System. J. Appl. Res. Water Wastewater 2019, 6(1), 16-24. https://doi.org/10.22126/arww.2019.1042

Barino, F.O.; Silva, V.N.H.; Lopez-Barbero, A.P.; De Mello Honorio, L.; Santos, A.B.D. Correlated Time-Series in Multi-Day-Ahead Streamflow Forecasting Using Convolutional Networks. IEEE Access 2020, 8, 215748–215757. https://doi.org/10.1109/ACCESS.2020.3040942

Bessa Santos, R.M.; Sanches Fernandes, L.F.; Vitor Cortes, R.M.; Leal Pacheco, F.A. Development of a Hydrologic and Water Allocation Model to Assess Water Availability in the Sabor River Basin (Portugal). Int. J. Environ. Res. Public Health 2019, 16, 2419. https://doi.org/10.3390/ijerph16132419

Brito, D.; Ramos, T.B.; Gonçalves, M.C.; Morais, M.; Neves, R. Integrated Modelling for Water Quality Management in a Eutrophic Reservoir in South-Eastern Portugal. Environ. Earth Sci. 2018, 77, 40. https://doi.org/10.1007/s12665-017-7221-5

Canuto, N.; Ramos, T.B.; Oliveira, A.R.; Simionesei, L.; Basso, M.; Neves, R. Influence of Reservoir Management on Guadiana Streamflow Regime. Journal of Hydrology: Regional Studies 2019, 25, 100628. https://doi.org/10.1016/j.ejrh.2019.100628

Chollet, F. et al. Available online: Keras, 2015. GitHub. https://github.com/fchollet/keras (accessed on: March 2021).

Corbari, C.; Ravazzani, G.; Galvagno, M.; Cremonese, E.; Mancini, M. Assessing Crop Coefficients for Natural Vegetated Areas Using Satellite Data and Eddy Covariance Stations. Sensors 2017, 17, 2664. https://doi.org/10.3390/s17112664

Corine Land Cover 2012 (CLC 2012), n.d. © European Union, Copernicus Land Monitoring Service 2018, European Environment Agency (EEA). Available online: https://land.copernicus.eu/pan-european/corine-land-cover (accessed on 22 June 2019).

Delaney, C.J.; Hartman, R.K.; Mendoza, J.; Dettinger, M.; Delle Monache, L.; Jasperse, J.; Ralph, F.M.; Talbot, C.; Brown, J.; Reynolds, D.; Evett, S. Forecast Informed Reservoir Operations Using Ensemble Streamflow Predictions for a Multipurpose Reservoir in

Northern California. Water Resour. Res. 2020, 56. https://doi.org/10.1029/2019WR026604

Demirel, M.C.; Venancio, A.; Kahya, E. Flow Forecast by SWAT Model and ANN in Pracana Basin, Portugal. Adv. Eng. Softw. 2009, 40, 467–473. https://doi.org/10.1016/j.advengsoft.2008.08.002

Devia, G.K.; Ganasri, B.P.; Dwarakish, G.S. A Review on Hydrological Models. Aquat. Procedia 2015, 4, 1001–1007. https://doi.org/10.1016/j.aqpro.2015.02.126

Di Nunno, F.; De Marinis, G.; Granata, F. Short-Term Forecasts of Streamflow in the UK Based on a Novel Hybrid Artificial Intelligence Algorithm. Sci Rep 2023, 13, 7036. https://doi.org/10.1038/s41598-023-34316-3

Duan, S.; Ullrich, P.; Shu, L. Using Convolutional Neural Networks for Streamflow Projection in California. Front. Water 2020, 2, 28. https://doi.org/10.3389/frwa.2020.00028

European Digital Elevation Model (EU-DEM), version 1.1., n.d. © European Union, Copernicus Land Monitoring Service 2019, European Environment Agency (EEA). Available online: https://land.copernicus.eu/pan-european/satellite-derived-products/eu-dem/eu-dem-v1.1/view (accessed on 15 May 2019).

Fatichi, S.; Vivoni, E.R.; Ogden, F.L.; Ivanov, V.Y.; Mirus, B.; Gochis, D.; Downer, C.W.; Camporese, M.; Davison, J.H.; Ebel, B.; Jones, N.; Kim, J.; Mascaro, G.; Niswonger, R.; Restrepo, P.; Rigon, R.; Shen, C.; Sulis, M.; Tarboton, D. An Overview of Current Applications, Challenges, and Future Trends in Distributed Process-Based Models in Hydrology. Journal of Hydrology 2016, 537, 45–60. https://doi.org/10.1016/j.jhydrol.2016.03.026

Feddes, R.A.; Kowalik, P.J.; Zaradny, H. Simulation of field water use and crop yield; Wageningen: Centre for agricultural publishing and documentation, 1978. ISBN 90-220-0676-X.

HAZRUNOFF Project - Layman’s Report. HazRunoff: Integration of sensing and modelling technologies for early detection and follow-up of hazmat and flood hazards in transitional and coastal waters, 2020. Available online: http://www.hazrunoff.eu/wp-content/uploads/2020/06/HAZRUNOFF_Layman-Report.pdf

Hersbach, H.; Bell, B.; Berrisford, P.; Hirahara, S.; Horányi, A.; Muñoz-Sabater, J.; Nicolas, J.; Peubey, C.; Radu, R.; Schepers, D.; Simmons, A.; Soci, C.; Abdalla, S.; Abellan, X.;

Balsamo, G.; Bechtold, P.; Biavati, G.; Bidlot, J.; Bonavita, M. et al. Complete ERA5 from 1979: Fifth generation of ECMWF atmospheric reanalyses of the global climate. Copernicus Climate Change Service (C3S) Data Store (CDS) 2017.

Huang, C.; Zhang, J.; Cao, L.; Wang, L.; Luo, X.; Wang, J.-H.; Bensoussan, A. Robust Forecasting of River-Flow Based on Convolutional Neural Network. IEEE Trans. Sustain. Comput. 2020, 5, 594–600. https://doi.org/10.1109/TSUSC.2020.2983097

Jovanovic, N.; Pereira, L.S.; Paredes, P.; Pôças, I.; Cantore, V.; Todorovic, M. A Review of Strategies, Methods and Technologies to Reduce Non-Beneficial Consumptive Water Use on Farms Considering the FAO56 Methods. Agricultural Water Management 2020, 239, 106267. https://doi.org/10.1016/j.agwat.2020.106267

Khosravi, K.; Golkarian, A.; Tiefenbacher, J.P. Using Optimized Deep Learning to Predict Daily Streamflow: A Comparison to Common Machine Learning Algorithms. Water Resour. Manag. 2022, 36, 699–716. https://doi.org/10.1007/s11269-021-03051-7

Mateus, M.; Neves, R. Ocean Modelling for Coastal Management - Case Studies with MOHID; 2013. ISBN 978-989-8481-24-5.

McKinney, W. Data Structures for Statistical Computing in Python. In S. van der Walt & J. Millman (Eds.), Proceedings of the 9th Python in Science Conference 2010. (pp. 56–61), https://doi.org/10.25080/Majora-92bf1922-00a

Mehr, A.D.; Kahya, E.; Olyaie, E. Streamflow Prediction Using Linear Genetic Programming in Comparison with a Neuro-Wavelet Technique. J. Hydrol. 2013, 505, 240–249. https://doi.org/10.1016/j.jhydrol.2013.10.003

Miser, H.J.; Quade, E.S. Handbook of Systems Analysis: Overview of Uses, Procedures, Applications, and Practice. Noth-Holland 1985. ISBN 978-0444009180.

Moriasi, D.N.; Arnold, J.G.; van Liew, M.W.; Bingner, R.L.; Harmel, R.D.; Veith, T.L. Model Evaluation Guidelines for Systematic Quantification of Accuracy in Watershed Simulations. Trans. Am. Soc. Agric. Biol. Eng. 2007, 50, 885–900.

Mualem, Y. A New Model for Predicting the Hydraulic Conductivity of Unsaturated Porous Media. Water Resour. Res. 1976, 12, 513–522. https://doi.org/10.1029/WR012i003p00513

Navarro-Hellín, H.; Martínez-del-Rincon, J.; Domingo-Miguel, R.; Soto-Valles, F.; Torres-Sánchez, R. A Decision Support System for Managing Irrigation in Agriculture.

Comput. Electron. Agric. 2016, 124, 121–131. https://doi.org/10.1016/j.compag.2016.04.003

Neitsch, S.L.; Arnold, J.G.; Kiniry, J.R.; Williams, J.R. Soil and Water Assessment Tool Theoretical Documentation Version 2009 2011.

O'Malley, T.; Bursztein, E.; Long, J.; Chollet, F.; Jin, H.; Invernizzi, L. Keras Tuner, 2019. Available online: https://github.com/keras-team/keras-tuner (accessed on 30 May 2021).

Oliveira, A.R.; Ramos, T.B.; Simionesei, L.; Gonçalves, M.C.; Neves, R. Modeling Streamflow at the Iberian Peninsula Scale Using MOHID-Land: Challenges from a Coarse Scale Approach. Water 2022, 14, 1013. https://doi.org/10.3390/w14071013

Oliveira, A.R.; Ramos, T.B.; Simionesei, L.; Pinto, L.; Neves, R. Sensitivity Analysis of the MOHID-Land Hydrological Model: A Case Study of the Ulla River Basin. Water 2020, 12, 3258. https://doi.org/10.3390/w12113258

Oliveira, A.R.; Ramos, T.B.; Neves, R. Streamflow Estimation in a Mediterranean Watershed Using Neural Network Models: A Detailed Description of the Implementation and Optimization. Water 2023, 15(5), 947. https://doi.org/10.3390/w15050947

Panagos, P.; Van Liedekerke, M.; Jones, A.; Montanarella, L. European Soil Data Centre: Response to European Policy Support and Public Data Requirements. Land Use Policy 2012, 29, 329–338. https://doi.org/10.1016/j.landusepol.2011.07.003

Parisouj, P.; Mohebzadeh, H.; Lee, T. Employing Machine Learning Algorithms for Streamflow Prediction: A Case Study of Four River Basins with Different Climatic Zones in the United States. Water Resour. Manag. 2020, 34, 4113–4131. https://doi.org/10.1007/s11269-020-02659-5

Pedregosa, F.; Varoquaux, G.; Gramfort, A.; Michel, V.; Thirion, B.; Grisel, O.; Blondel, M.; Prettenhofer, P.; Weiss, R.; Dubourg, V. et al. Scikit-learn: Machine learning in Python. J. Mach. Learn. Res. 2011, 12(Oct), 2825–2830.

Pereira, L.; Cordery, I.; Iacovides, I. Coping with Water Scarcity: Addressing the Challenges, 2009. ISBN 978-1-4020-9578-8.

Pestana, R.; Matias, M.; Canelas, R.; Araújo, A.; Roque, D.; Van Zeller, E.; Trigo-Teixeira, A.; Ferreira, R.; Oliveira, R.; Heleno, S. Calibration of 2D Hydraulic Inundation Models in

the Floodplain Region of the Lower Tagus River. In Proceedings of the Proc. ESA Living Planet Symposium 2013; Edinburgh, UK, 2013.

Pörtner, H.-O.; Roberts, D.C.; Tignor, M.; Poloczanska, E.S.; Mintenbeck, K.; Alegría, A.; Craig, M.; Langsdorf, S.; Löschke, S.; Möller, V.; et al. IPCC, 2022: Climate Change 2022: Impacts, Adaptation and Vulnerability. Contribution of Working Group II to the Sixth Assessment Report of the Intergovernmental Panel on Climate Change; Cambridge University Press: Cambridge University Press, Cambridge, UK and New York, NY, USA, 2022.

Ramos, T.B.; Simionesei, L.; Jauch, E.; Almeida, C.; Neves, R. Modelling Soil Water and Maize Growth Dynamics Influenced by Shallow Groundwater Conditions in the Sorraia Valley Region, Portugal. Agric. Water Manag. 2017, 185, 27–42. https://doi.org/10.1016/j.agwat.2017.02.007

Ranatunga, T.; Tong, S.T.Y.; Yang, Y.J. An Approach to Measure Parameter Sensitivity in Watershed Hydrological Modelling. Hydrol. Sci. J. 2016, 1–17. https://doi.org/10.1080/02626667.2016.1174335

Rocha, J.; Carvalho-Santos, C.; Diogo, P.; Beça, P.; Keizer, J.J.; Nunes, J.P. Impacts of Climate Change on Reservoir Water Availability, Quality and Irrigation Needs in a Water Scarce Mediterranean Region (Southern Portugal). Sci. Total Environ. 2020, 736, 139477. https://doi.org/10.1016/j.scitotenv.2020.139477

Simionesei, L.; Ramos, T.B.; Palma, J.; Oliveira, A.R.; Neves, R. IrrigaSys: A Web-Based Irrigation Decision Support System Based on Open Source Data and Technology. Comput. Electron. Agric. 2020, 178, 105822, https://doi.org/10.1016/j.compag.2020.105822

Šimůnek, J.; Hopmans, J.W. Modeling Compensated Root Water and Nutrient Uptake. Ecol. Modell. 2009, 220, 505–521. https://doi.org/10.1016/j.ecolmodel.2008.11.004

Sitterson, J.; Knightes, C.; Parmar, R.; Wolfe, K.; Muche, M.; Avant, B. An Overview of Rainfall-Runoff Model Types. U.S. Environmental Protection Agency, Washington, DC, EPA/600/R-17/482, 2017.

Skaggs, T.H.; van Genuchten, M.Th.; Shouse, P.J.; Poss, J.A. Macroscopic Approaches to Root Water Uptake as a Function of Water and Salinity Stress. Agric. Water Manag. 2006, 86, 140–149. https://doi.org/10.1016/j.agwat.2006.06.005

SNIRH, n.d. Sistema Nacional de Informação de Recursos Hídricos. Available online: https://snirh.apambiente.pt/index.php?idMain= (accessed on 7 February 2021).

Song, C.M. Hydrological Image Building Using Curve Number and Prediction and Evaluation of Runoff through Convolution Neural Network. Water 2020, 12, 2292. https://doi.org/10.3390/w12082292

Szczepanek, R. Daily Streamflow Forecasting in Mountainous Catchment Using XGBoost, LightGBM and CatBoost. Hydrology 2022, 9, 226. https://doi.org/10.3390/hydrology9120226

Teodosiu, C.; Ardeleanu, C.; Lupu, L. An overview of decision support systems for integrated water resources management. Environ. Eng. Manag. J. 2009, 8, 153–162. doi:10.30638/eemj.2009.023

Tóth, B.; Weynants, M.; Pásztor, L.; Hengl, T. 3D Soil Hydraulic Database of Europe at 250 m Resolution. Hydrol. Process. 2017, 31, 2662–2666. https://doi.org/10.1002/hyp.11203

Trancoso, A.R.; Braunschweig, F.; Chambel Leitão, P.; Obermann, M.; Neves, R. An advanced modelling tool for simulating complex river systems. Sci. Total Environ. 2009, 407, 3004–3016. https://doi.org/10.1016/j.scitotenv.2009.01.015

van der Laan, E.; Nunes, J.P.; Dias, L.F.; Carvalho, S.; Dos Santos, F.M. Climate Change Adaptability of Sustainable Land Management Practices Regarding Water Availability and Quality: A Case Study in the Sorraia Catchment, Portugal 2023 (preprint).

van Genuchten, M.Th. A Closed-Form Equation for Predicting the Hydraulic Conductivity of Unsaturated Soils. Soil Sci. Soc. Am. J. 1980, 44, 892–898. https://doi.org/10.2136/sssaj1980.03615995004400050002x

Williams; J. R.; Jones, C. A.; Kiniry, J. R.; Spanel, D. A. The EPIC Crop Growth Model. Transactions of the ASAE 1989, 32, 0497–0511. http://dx.doi.org/10.13031/2013.31032

Yu, Q.; Jiang, L.; Wang, Y.; Liu, J. Enhancing Streamflow Simulation Using Hybridized Machine Learning Models in a Semi-Arid Basin of the Chinese Loess Plateau. J. Hydrol. 2023, 617, 129115. https://doi.org/10.1016/j.jhydrol.2023.129115

Zhang, D.; Chen, X.; Yao, H. Development of a Prototype Web-Based Decision Support System for Watershed Management. Water 2015a, 7, 780–793. https://doi.org/10.3390/w7020780

Zhang, X.; Peng, Y.; Zhang, C.; Wang, B. Are Hybrid Models Integrated with Data Preprocessing Techniques Suitable for Monthly Streamflow Forecasting? Some Experiment Evidences. J. of Hydrol. 2015b, 530, 137–152, https://doi.org/10.1016/j.jhydrol.2015.09.047

8 Direct integration of reservoirs' operations in a hydrological model for streamflow estimation: coupling a CLSTM model with MOHID-land

Authors: Ana Ramos Oliveira, Tiago Brito Ramos, Lígia Pinto and Ramiro Neves

Centro de Ciência e Tecnologia do Ambiente e do Mar (MARETEC-LARSyS), Instituto Superior Técnico, Universidade de Lisboa, Av. Rovisco Pais, 1, 1049-001 Lisboa, Portugal

Submitted to: Hydrology and Earth System Sciences

Abstract

Knowledge about streamflow regimes and values is essential for different activities and situations, in which justified decisions must be made. However, streamflow behavior is commonly assumed as non-linear, being controlled by various mechanisms that act on different temporal and spatial scales, making its estimate challenging. An example is the construction and operation of infrastructures such as dams and reservoirs in rivers. The challenges faced by modelers to correctly describe the impact of dams on hydrological systems are considerable. In this study, an already implemented, calibrated, and validated solution of MOHID-Land model for natural regime flow in Ulla River basin was considered as baseline. The referred watershed comprehends three reservoirs. Outflow values were estimated considering a basic operation rule for two of them (run-of-the-river dams) and considering a data-driven model of Convolutional Long Short-Term Memory (CLSTM) type for the other (high-capacity dam). The outflow values obtained with the CLSTM model were imposed in the hydrological model, while the hydrological model fed the CLSTM model with the level and the inflow of the reservoir. This coupled system was daily evaluated in two hydrometric stations located downstream of the reservoirs, resulting in an improved performance compared with the baseline application. The analysis of the modelled values with and without reservoirs further demonstrated that considering dams' operations in the hydrological model resulted in an increase of the streamflow during the dry season and a decrease during the wet season but with no differences in the average streamflow. The coupled system is thus a promising solution for improving streamflow estimates in modified rivers.

8.1 Introduction

Knowledge about streamflow, including water quantity and quality, is fundamental for monitoring and controlling the environmental impacts of several activities and situations, including infrastructures design, support in decision-making processes, irrigation scheduling, design and implementation of water management systems, environmental management, studies of river and watershed behavior, flood warning control, optimal water resources allocation, prediction of droughts, and management of reservoir operations (Mehdizadeh et al., 2019; Mohammadi et al., 2021; Hu et al., 2021). However, the task of delivering information about streamflow can be challenging since it commonly assumes a non-linear behavior, being controlled by various mechanisms that act on different temporal and spatial scales (Wang et al., 2006). These non-linear forcing mechanisms include meteorological conditions, land use, infiltration, morphological features of the river, and catchment characteristics (Mohammadi et al., 2021). The complex and laborious process of streamflow estimation is usually exacerbated when the natural regime flow is modified by anthropogenic activities and human decisions. In this sense, reservoirs are a major concern in hydrological modelling since most models are not prepared to directly consider the existence of such infrastructures and the resulting alterations caused on the natural regime flow by their operations (Dang et al., 2020). If hydrological models are prepared to study and comprehend the behavior of natural systems, the lack of information about reservoirs' operations such as operating rules and flood contingency plans makes it impeditive for a correct representation of those infrastructures.

As pointed out by Dang et al. (2020), a postprocess methodology is often used to impose reservoirs' operations on hydrologic-hydraulic models. This way, the need for modifying models' structures is avoided. However, Bellin et al. (2016) considered the direct representation of reservoirs water storage and operation as the best approach to correctly simulate such systems. Nevertheless, the challenges faced are many, having limited the number of studies carried out (Dang et al., 2020).

Recently, Xiong et al. (2019) developed a statistical framework where an indicator combining the effects of reservoir storage capacity and the volume of the multiday antecedent rainfall input was used to assess the impact of a reservoir system on flood frequency and magnitude in downstream areas of the Han River, China. Yun et al. (2020) modified the structure of the Variable Infiltration Capacity (VIC) model to include a reservoir module for estimating the variation of streamflow and flood characteristics when impacted by climate change and reservoir operation in the Lancang-Mekong River basin, Southeast Asia. Also using

a modified VIC model, Dang et al. (2020) simulated storage dynamics of water reservoirs again in the Lancang-Mekong River basin. In both studies, a comparison between the model results with and without reservoirs was provided. It is important to denote that both Yun et al. (2020) and Dang et al. (2020) imposed operation rules on the model, with the former authors giving more importance to flood control and environmental protection while the latter focused on energy production. Also, Hughes et al. (2021) used a modified version of the SHETRAN model to simulate the streamflow considering the influence of reservoirs in Upper Cocker catchment, United Kingdom. The authors considered a weir model and two tests were performed: first the weir was simulated as static (with closed sluice) to identify the sluice operating rules by comparing results with the known outflow timeseries; second the weir model was run as non-static to implement the sluice operating rules deducted from the first approach. All studies mentioned above reproduced reservoirs' behavior considering their operation rules, which in most cases are difficult to obtain or are very laborious to reproduce.

The application of operation rules may often be adapted to specific conditions, objectives, or constraints based on the knowledge and experience of operators (Yang et al., 2019). This makes the reservoirs' operation deviate from the reference operation curves, invalidating the sole use of physical-based models and the use of pre-established rule curves to reproduce the reservoir behavior in real-time. To overcome this issue, Yang et al. (2019) referred that machine learning methods, with their capacity to understand, extract, and reproduce complex high-dimensional relationships, can be an efficient and easy-to-use solution to reproduce reservoirs' operations, contemplating the reference operation rules as well as the operators' historical experience. In this sense, the referred authors used recurrent neural network (RNN) models to extract reservoirs' operation rules from the historical operation data of three multipurpose reservoirs located in the upper Chao Phraya River basin, Thailand. Also considering the use of the Geomorphology-based hydrological model (GBHM) to forecast the reservoir's inflow, Yang et al. (2019) achieved a real-time reservoir outflow forecast. Dong et al. (2023) proposed a similar approach to improve the reconstruction of daily streamflow timeseries in the Upper Yangtze River Basin, China. These authors proposed a practical framework to quantitatively assess the cumulative impacts of reservoirs' operation on the hydrologic regime, coupling two data-driven models, namely an extreme gradient boosting (XGBoost) model and an artificial neural network (ANN) model, with a high-resolution hydrologic model, and following a calibration free conceptual reservoir operation scheme. The data-driven models were used to predict the outflow of reservoirs with historical operation data, while the calibration-free conceptual reservoir approach was used to simulate the outflow in data limited reservoirs. The

study presented by Dong et al. (2023) is a rare example of a promising solution for improving streamflow prediction in highly modified catchments, which this study aims to follow.

In the present study, the physical-based, distributed MOHID-Land model (Oliveira et al., 2020) was coupled with a Convolutional Long Short-Term Memory (CLSTM) model to estimate the daily outflow in Portodemouros reservoir, Galicia, Spain. The results obtained with the CLSTM model were estimated considering the reservoir's level and inflow simulated by MOHID-Land and then imposed in that same model for streamflow simulation downstream the reservoirs. However, the CLSTM model was first trained and tested using historical data. Thus, the main aim of this study is to verify the capacity of the coupled system to improve streamflow estimation downstream Portodemouros reservoir. This study demonstrates the ability of the proposed approach to directly simulate reservoirs' operations in a hydrological simulation and validates a solution that is accessible and easy to implement.

8.2 Materials and methods

8.2.1 Description of the study area

The Ulla River watershed is located in the Galicia region, Northwest of Spain, and drains an area of 2803 km^2 discharging on Ria de Arousa estuary (Figure 8.1). Ria de Arousa is one of the most important coastal water bodies in Galicia, having the Ulla and Umia rivers as major tributaries, and mainly used for recreative and fishery activities (da Silva et al., 2005; Outeiro et al., 2018; Blanco-Chao et al., 2020; Cloux et al., 2022). The maximum and minimum elevations of the Ulla watershed are 1160 m and -0.75 m, respectively, and the main watercourse has a bed length of 142 km with its source at an altitude of 600 m. The watershed is inserted into an area characterized by a warm-summer Mediterranean climate (Csb) according to Köppen-Geiger classification. The annual precipitation is about 1100 mm, with rainy months from October to May. The annual average temperature is 12°C, reaching a maximum of 18°C in August and a minimum of 7°C in February. According to Nachtergaele et al. (2009), the main soil units in the Ulla river watershed are Umbric Leptosols and Umbric Regosols, representing 69% and 31%, respectively. The main land uses are forest, occupying 57.2% of the area, and semi natural and agricultural areas, covering 40.3% (CLC 2012, n.d.).

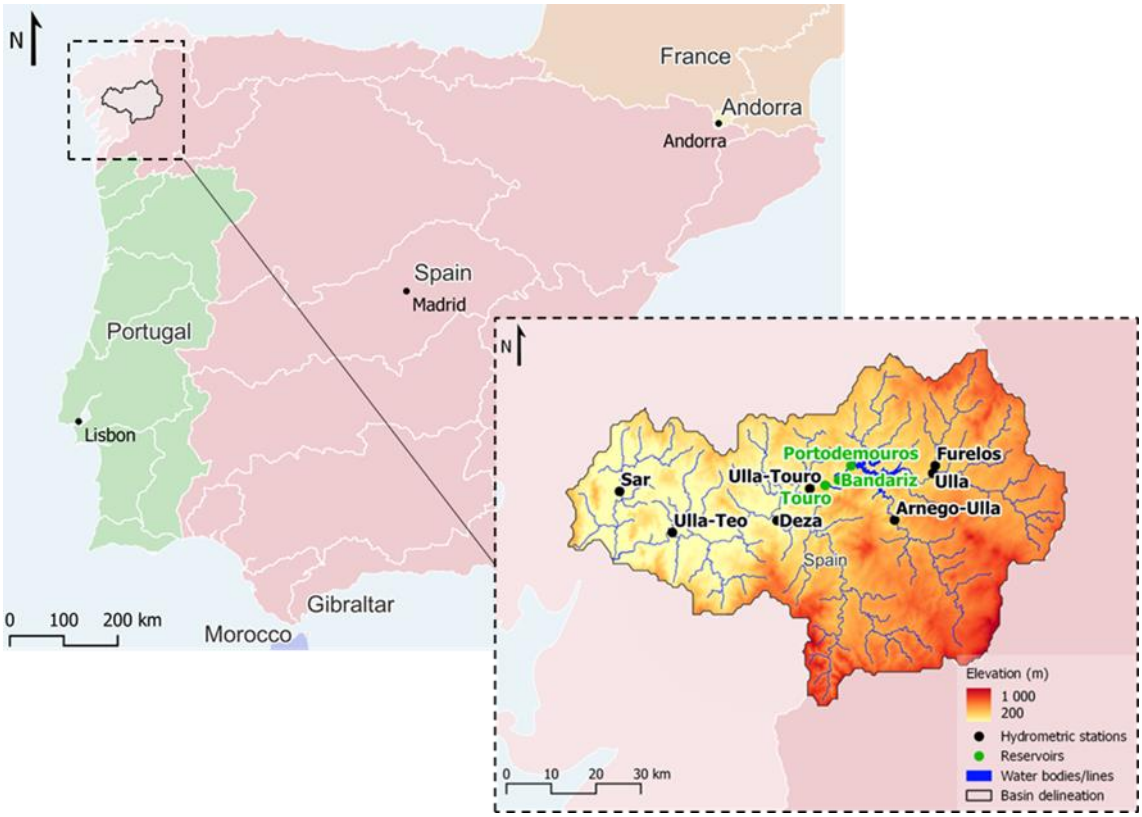

Figure 8.1 Ulla River watershed location, digital terrain model, and identification of hydrometric stations and reservoirs.

There are three reservoirs in the watershed: Portodemouros, Bandariz, and Touro (Figure 8.1). Those reservoirs were constructed in cascade and work collectively, with Portodemouros placed at the beginning of the cascade, Touro at the end, and Bandariz in between. Portodemouros has a total capacity of 297 hm^3, while Bandariz and Touro present much lower capacities, totalizing 2.7 hm^3 and 3.78 hm^3, respectively. Due to its significative storing capacity, Portodemouros reservoir can be used for flood control, however, the set of reservoirs is mainly responsible for energy production. The patterns of daily inflow and outflow of the two last reservoirs are very similar, since they are run-of-the-river dams (Figure 8.2b and c). However, Portodemouros works in a different way, presenting significative differences between the inflow and outflow patterns (Figure 8.2a and d).

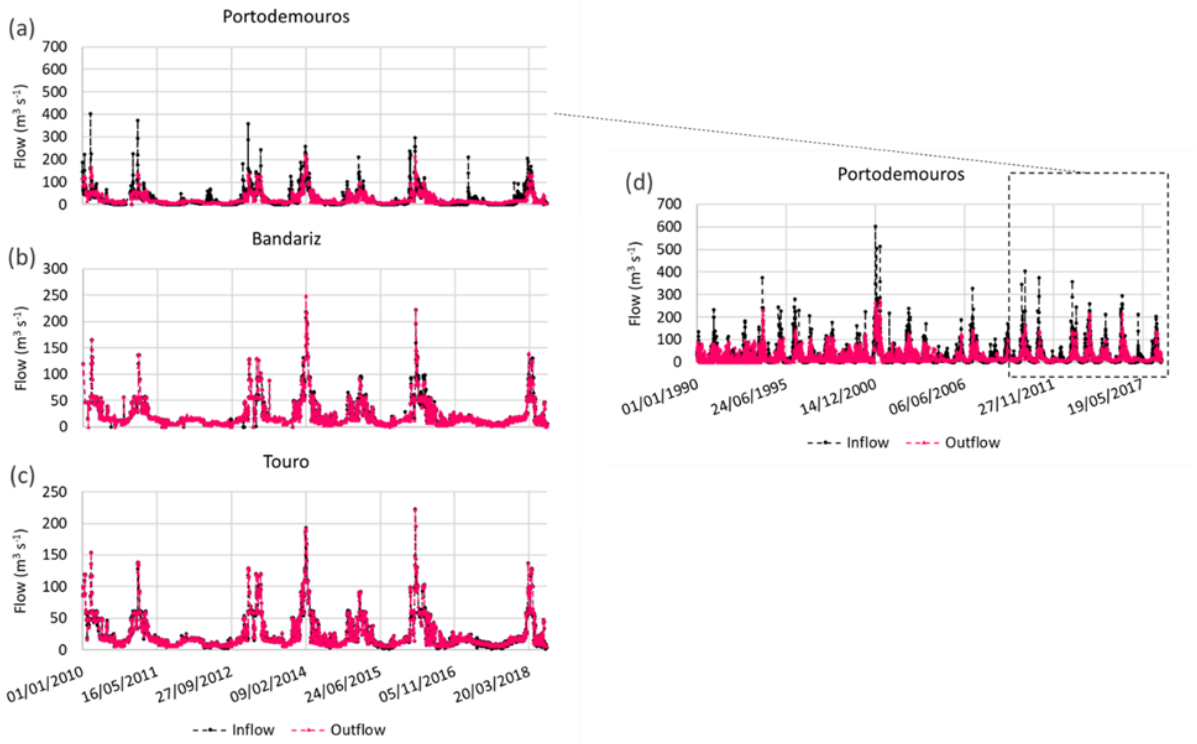

Figure 8.2 Comparison of inflow and outflow in (a) Portodemouros, (b) Touro, and (c) Bandariz reservoirs for the period 2010-2018, and in (d) Portodemouros reservoir for the period 1990-2018.

8.2.2 MOHID-Land description

MOHID-Land is an open-source model (https://github.com/Mohid-Water-Modelling-System/Mohid) and is part of the MOHID (Hydrodynamic Model) Water Modelling System. It is a fully distributed and physically based model adopting mass and momentum conservation equations considering a finite volume approach (Trancoso et al. 2009, Canuto et al., 2019, Oliveira et al., 2020). The model estimates water fluxes between four main compartments, namely, the atmosphere, the soil surface, the river network, and the porous media, which is also intimately related with the vegetation compartment. Excepting the atmosphere compartment, which is only responsible for providing the meteorological data needed to impose surface boundary conditions, the processes in all the other compartments are explicitly simulated.

In MOHID-Land, the atmosphere compartment can deal with space and/or time variable data, and the input properties include precipitation, air temperature, relative humidity, wind velocity, and solar radiation and/or cloud cover.

The simulated domain is discretized considering two grids, one in the surface plane and other in the vertical direction. While the first is defined according to the coordinate system chosen by the user, the last follows a cartesian coordinate system. The surface water movement is computed considering a 2D surface grid and solving the Saint-Venant equation in its conservative form, accounting for advection, pressure, and friction forces. The Saint-Venant

equation is also solved one-dimensionally (1D) for the river network. This network is derived from the digital terrain model represented in the 2D surface grid by connecting surface cell centers (nodes) and is characterized by a cross-section geometry defined by the user. The water fluxes between these two (2D and 1D) compartments are estimated according to a kinematic approach, neglecting bottom friction, and using an implicit algorithm to avoid instabilities.

The porous media is discretized by combining the 2D surface grid with the vertical cartesian grid, defining a 3D domain with variable thickness layers. This compartment can receive or lose water from the river network, with fluxes being computed considering a pressure gradient in the interface of these two mediums. Besides the water coming from the drainage network, the porous media also receives water from the infiltration process, which is calculated according to Darcy's law. In this 3D domain, the water movement is simulated using the Richards equation and considering the same grid for saturated and unsaturated flow. The soil hydraulic parameters are described using the van Genuchten-Mualem functional relationships (Mualem, 1976; van Genuchten, 1980). The saturation is reached when a cell exceeds the soil moisture threshold value defined by the user and, in that case, the model considers the saturated conductivity to compute flow, with pressure becoming hydrostatic and corrected by friction. To compute the lateral flow, the horizontal saturated hydraulic conductivity is given by the product of the vertical saturated hydraulic conductivity ($K_{sat,ver}$) and a factor (f_h) set by the user.

The soil water loss is mainly due to the evapotranspiration process, which is computed taking into account weather, crop, and soil conditions. The reference evapotranspiration (ET_o) is first computed according to the FAO Penman–Monteith method (Allen et al., 1998). Then, the potential crop evapotranspiration (ET_c) is obtained by multiplying the ET_o by a single crop coefficient (K_c) representing standard crop conditions. ET_c values are then partitioned into potential soil evaporation and crop transpiration rates based on the leaf area index (LAI) following Ritchie (1972). LAI is simulated using a modified version of the EPIC model (Neitsch et al., 2011, Williams et al., 1989) and considering a heat units approach for crop development, the crop development stages, and crop stress (Ramos et al., 2017). The actual transpiration is calculated based on the macroscopic approach proposed by Feddes et al. (1978), where root water uptake reductions are estimated considering the presence of depth-varying stressors (Šimůnek and Hopmans, 2009, Skaggs et al., 2006). The actual soil evaporation is estimated from the potential soil evaporation by imposing a pressure head threshold value (ASCE, 1996).

To avoid instability problems and save computational time, the model allows the use of a variable time step, which reaches higher values during dry seasons and lower values in rainy periods when water fluxes increase.

8.2.2.1 Resrevoirs module

Besides the main modules described above, MOHID-Land can also consider the existence of reservoirs in the river network domain. The operation of a reservoir needs several characteristics to be defined, namely, the minimum and maximum volumes, the minimum outflow (the definition of the maximum outflow is optional), the curve defining the relation between the level and the stored volume, the type of operation, the location in terms of coordinates, and the identification of the node in the river network where the reservoir is placed. Reservoir's operation may be defined by the relationship between the level and the outflow as absolute value or as a percentage of the inflow, the percentage of the stored volume and the outflow as absolute value or as a percentage of the inflow, and the percentage of the stored volume and the outflow as a percentage of the maximum outflow. The user can also define the existence of discharges (in and/or out) and the state of the storage capacity (full, filled with a percentage of the total capacity, or empty) at the beginning of the simulation. In that sense, the reservoirs module works with each reservoirs as a box where a mass balance is performed. This mass balance takes into account the stored volume and the amount of water that enters and leaves the reservoir. The former considers the inflow from the river network and any input discharge defined by the user. The latter considers the outflow estimated by the type of operation and any output discharge defined by the user. The new stored volume is transformed into a level according to the level/volume curve specified by the user.

8.2.2.2 Model set-up

The MOHID-Land model was already implemented, calibrated, and validated in the study area as detailed in Oliveira et al. (2020). This study was carried out from 01/01/2008 to 31/12/2017. Only the natural regime flow in the watershed was considered, with model calibration and validation using data from hydrometric stations not influenced by reservoirs' operations. Following the sensitivity analysis performed, the best solution for the Ulla River model implementation was obtained considering a constant quadrangular horizontally spaced grid with 215 columns (West-East direction) and 115 rows (North-South direction), and a resolution of 0.005° (~500 m). The calibrated parameters were the $K_{sat,ver}$, the f_h factor, and the dimensions of the cross-sections in the river network.

The elevation of the calibrated solution was interpolated based on the digital terrain model from the European Environment Agency (European Digital Elevation Model (EU-DEM), n.d.), which has a resolution of 0.00028° (~30 m). The Manning coefficient for the river network was set to 0.035 s $m^{-1/3}$, and the river cross-sections were assumed as rectangular with the dimensions varying according to the drained area of each node (Table 8.1).

Table 8.1 Cross-sections dimensions.

Drained area (km^2)	Top width (m)	Depth (m)
37.85	12.71	2.0
62.65	16.45	2.0
84.49	19.16	2.0
123.35	23.24	3.0
161.90	26.71	3.0
195.10	29.38	3.0
312.45	37.36	3.0
503.12	46.95	4.0
1164.36	73.16	4.0
2246.34	102.33	4.0
2785.08	114.21	4.0

The surface Manning coefficients were specified based on the CLC 2012 (CLC 2012, n.d.) data. For each land use, a Manning coefficient was first defined according to Pestana et al. (2013). Considering the interpolation process, those values varied from 0.023 to 0.298 s $m^{-1/3}$. CLC 2012 data was further used to identify the vegetation in the watershed, which were made to correspond to data (vegetation growth parameters) in the MOHID's vegetation database. For each type of vegetation, a single crop coefficient (K_c) was adopted based on Allen et al. (1998) tabulated values. After the interpolation process, the K_c values varied from 0.15 to 1.0.

The soil domain was vertically discretized considering three horizons that comprehended six grid layers. The layers had variable thickness increasing from surface to bottom: 0.3 (surface), 0.3, 0.7, 0.7, 1.5, and 1.5 m (bottom). The first horizon included the first two layers, while the second horizon included the two middle layers, and, finally, the bottom horizon considered the last two layers. The van Genuchten-Mualem soil hydraulic parameters were obtained from the multilayered European Soil Hydraulic Database (ESHD, Tóth et al., 2017). For the surface horizon, ESHD data at 0.3 m depth was used to represent soil hydraulic data; ESHD data at 1.0 m depth was used to characterize the middle horizon; ESHD data at 2.0 m depth described the bottom horizon. In each of these horizons, three different sets of soil hydraulic data were identified (Figure 8.3). After model's calibration, the van Genuchten-

Mualem soil hydraulic parameters assumed the values presented in Table 8.2 for each set. The horizontal saturated hydraulic conductivity was obtained assuming the f_h equal to 10.

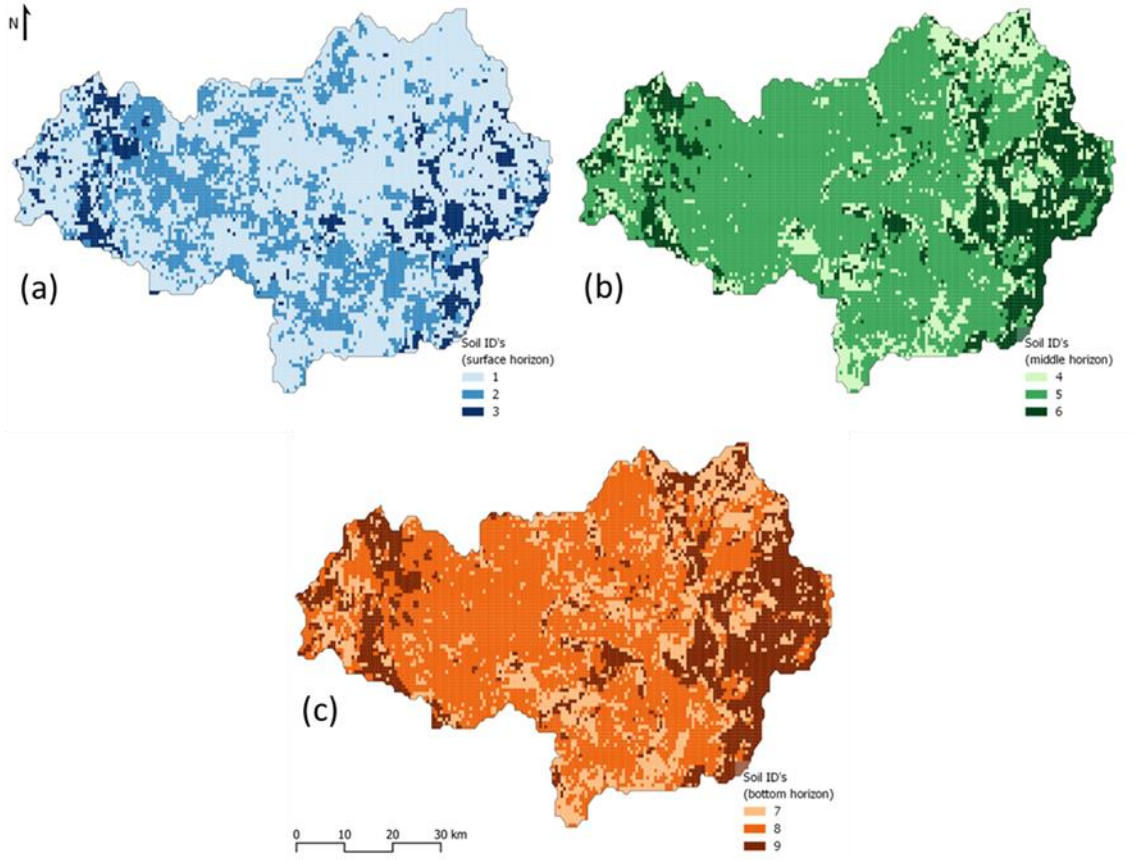

Figure 8.3 Soil IDs for each horizon: (a) surface; (b) middle; and (c) bottom horizons.

Table 8.2 Soil hydraulic properties by soil ID: θs – saturated water content; θr – residual water content; η and α – empirical shape parameters; $K_{sat,ver}$ – vertical saturated hydraulic conductivity; and l – pore connectivity/tortuosity parameter.

ID	θ_s ($m^3\ m^{-3}$)	θ_r ($m^3\ m^{-3}$)	η	$K_{sat,ver}$ ($m^3\ s^{-1}$)	α (m^{-1})	l
1	0.491	0.0	1.913	1.64×10^{-5}	3.47	-4.3
2	0.465	0.0	1.116	2.26×10^{-4}	12.84	-5.0
3	0.409	0.0	1.134	5.05×10^{-5}	7.00	-5.0
4	0.433	0.0	1.170	9.93×10^{-6}	3.36	-5.0
5	0.413	0.0	1.119	1.43×10^{-5}	2.27	-5.0
6	0.384	0.0	1.121	4.29×10^{-5}	7.17	-5.0
7	0.432	0.0	1.170	9.93×10^{-6}	3.36	-5.0
8	0.413	0.0	1.119	1.43×10^{-5}	2.27	-5.0
9	0.384	0.0	1.121	4.29×10^{-5}	7.17	-5.0

The meteorological boundary conditions were extracted from the ERA5-Reanalysis dataset (Hersbach et al., 2017), which is a gridded product with a resolution of 0.28125° (~31 km) and makes available meteorological variables with an hourly time step. The variables used and interpolated to the case study grid were the u and v components of wind velocity at 10 m

height, dewpoint and air temperatures at 2 m height, surface solar radiation downwards, surface pressure, total cloud cover, and total precipitation.

Reservoirs set-up

The three reservoirs in the studied watershed were implemented according to the characteristics presented in Table 8.3. Their curves relating the level and the stored volume are given in Figure 8.4. These data were made available by Augas de Galicia (Augas de Galicia, 2022), which is a public entity managing the Galicia-Costa basin district.

Table 8.3 Implemented characteristics for Portodemouros, Bandariz and Touro reservoirs.

	Portodemouros	Bandariz	Touro
Node location	1476	1383	1247
Coordinates	42°51'21.6"N 8°11'19.8"W	42°50'09.6"N 8°12'31.8"W	42°49'51.6"N 8°14'19.8"W
Minimum volume (hm^3)	54.5	0.33	0.015
Maximum volume (hm^3)	297	2.74	6.83
Minimum outflow ($m^3 s^{-1}$)	10	10	10

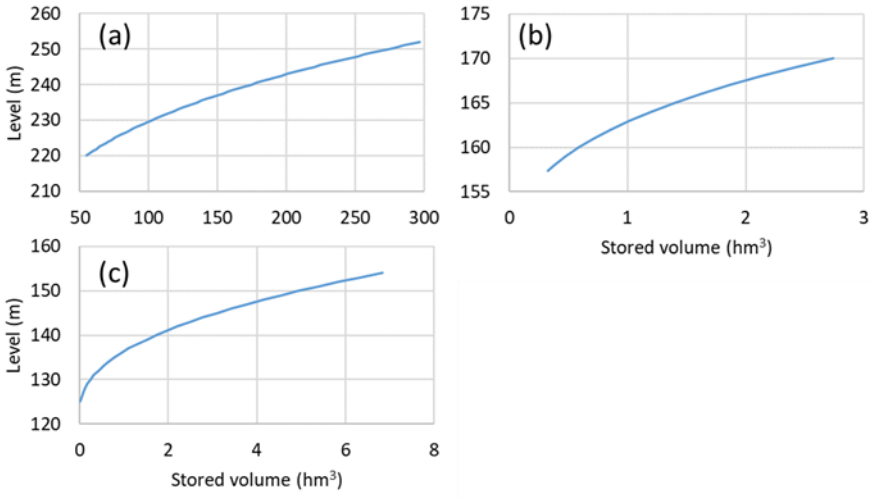

Figure 8.4 Level/stored volume curves for (a) Portodemouros, (b) Bandariz, and (c) Touro reservoirs.

The operation for Bandariz and Touro reservoirs was defined based on the relation between the percentage of the stored volume and the outflow as a percentage of the inflow. If the stored volume was between 0 and 95%, the reservoir had no outflow. If the stored volume was above 96%, the outflow equaled the inflow, i.e., all the amount of water that entered the reservoir each instant left the reservoir in the same instant. For Portodemouros, no operation rule was set since there was no clear relation between the inflow and outflow values to be used in MOHID-Land. Thus, the daily outflow of Portodemouros reservoir was estimated using a neural network model and imposed to the hydrologic model as a timeseries. Additionally, and

by default, if the stored volume of any reservoir was equal or above the total capacity, the amount of water that reached the reservoir is transformed into outflow.

8.2.3 Neural network model for reservoir outflow estimation

To estimate Portodemouros reservoir daily outflow, a neural network model was developed and tuned. It was composed by a combination of convolutional and a long short-term memory layers, hereafter defined as convolutional long short-term memory (CLSTM) model. This type of model was already applied for streamflow estimation by Ni et al. (2020) and Ghimire et al. (2021), who reported that, when compared with other neural network models (convolutional neural network, long short-term memory, multi-layer perceptron, extreme learning machine, etc.), the CLSTM represented the best solution. The demonstrated good behavior of CLSTM models is mainly related to its structure, which begins with the use of convolutional layers, responsible for the extraction of patterns in the input variables, and follows with long short-term layers, which are responsible for the prediction itself.

As referred by Wang et al. (2019), convolutional neural networks (CNN) have their origin in artificial neural networks (ANN) but instead of fully connected layers, CNN use local connections, giving more importance to high correlations with nearby data. Developed by LeCun and Bengio (1995) to identify handwritten digits, CNN uses convolutional filtering to achieve high correlation with neighboring data. This means that this type of network works based on weight sharing concept, with the filters' coefficients being shared for all input positions and their number and values being essential to capture data patterns (Wang et al., 2019, Barino et al., 2020, Chong et al., 2020). CNNs are thus recognized as more suitable solutions to identify local patterns, with a certain identified pattern being able to be recognized in another independent occurrence (Tao et al., 2019). As Ghimire et al. (2021) describes, CNN models can be used to identify patterns in one (1D), two (2D) or three (3D) dimensions. Being more adequate for time series data analysis, the 1D CNN solution was selected to be used in this study as input layer. This selection avoided the manual feature extraction process since 1D convolutional algorithms are known for their powerful capability of doing it automatically. According to Huang et al. (2020), the time needed for training CNN models is one of its main weaknesses.

As a type of recurrent neural network (RNN) model, long short-term memory (LSTM) models are known for their capacity to maintain historical information about all the past events of a sequence using a recurrent hidden unit (Elman, 1990, LeCun et al., 2015, Lipton et al., 2015). This characteristic makes RNN very suitable for time series data modelling (Bengio et

al., 1994, Hochreiter and Schmidhuber, 1997, Saon and Picheny, 2017). However, RNN models demonstrate inability in learning long-distance information because of their already known vanishing and exploding gradient problems during the training process (Ghimire et al., 2021). Trying to solve this RNN problem, Hochreiter and Schmidhuber (1997) developed the LSTM structure, which has the capacity to learn long-term dependencies (Xu et al., 2020).

8.2.3.1 Input data

The forcing variables were selected from a set that included the daily values of inflow, level, precipitation, temperature, and volume. The usage of the outflow values as a forcing variable was avoided because, when there are no observed values, the outflow data generated by the model must be used to feed the model itself, which can lead to an accumulation and propagation of errors in the estimated values. Several tests were performed considering different forcing variables and their combinations to verify which better estimate the daily outflow from Portodemouros reservoir. Also, different time lags of those forcing variables were tested. The analysis of the tests results shows that the best performance of CLSTM model was obtained with inflow and level used as forcing variables, both considering the values of 1, 2 and 3 days before the forecasted day.

The daily values of inflow, level, and volume were provided by Augas de Galicia, and original hourly values of precipitation and temperature were obtained from ERA5-Reanalysis dataset, being then accumulated or averaged considering a daily time step. The dataset made available by Augas de Galicia covered a period of about 29 years, with data from 01/01/1990 to 16/07/2018.

8.2.3.2 Structure

In this study, the model structure was developed based on Python language and using Keras package (Chollet et al., 2015), on top of TensorFlow (Abadi et al., 2016). As referred before, a CLSTM model is based on convolutional and long short-term memory layers. The types of layers made available by Keras package and used here were the Conv1D, MaxPooling, LSTM and dense. After several tests, the adopted model's structure included a Conv1D input layer followed by a MaxPooling layer. Then, two other sets of Conv1D plus MaxPooling layers were adopted. After those, an LSTM layer was introduced, and the output layer was selected to be a dense layer (Figure 8.5).

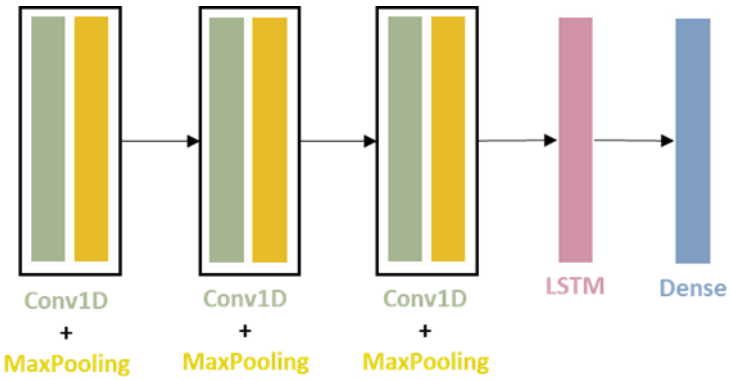

Figure 8.5 CLSTM structure.

For convolutional layers no activation function was defined, while the LSTM layer was activated with the hyperbolic tangent function. For the output dense layer, the exponential linear unit function was used as activation function.

The optimizer, i.e., the training algorithm, was selected to be the Nadam algorithm, with a learning rate of 1×10^{-3}, and an epsilon value of 1×10^{-7}. The loss was estimated using the mean absolute error. Finally, the number of epochs and the batch size were also a target for some tests, with adopted values of 300 and 20, respectively.

8.2.3.3 Model optimization

The model optimization considered two phases, namely, the manual tunning of hyperparameters, and the optimization of weights reached with the training process. In both cases, the structure presented above was exposed to a subset of the original dataset, i.e., the training dataset, where the forcing and target variables were included. The training dataset was handled and prepared with Pandas (McKinney, 2010) and Scikit-learn (Pedregosa et al., 2011) packages, with the data being delayed with the first and scaled with the latter. The scaling function was the "MinMaxScaler", which applies Eq. 8.1 to each variable in the dataset independently:

$$x_{scaled} = \frac{(x - x_{min})}{x_{max} - x_{min}}(M - m) + m \qquad \text{(Eq. 8.1)}$$

where x_{scaled} is the scaled value, x is the original value, x_{max} and x_{min} are the maximum and minimum values of the variable being scaled, and M and m are the maximum and minimum values of the desired range of the scaled data. Considering that the maximum values of the variables cannot be represented in the dataset, the desired range was defined from 0 to 0.9.

The tunning process was carried out to optimize the hyperparameters of the model. Several values for the number of filters and the kernel size for convolutional layers, and the number of units for the LSTM layer were tested. The best performance was reached with 16

filters and a kernel size of 10 for all the three convolutional layers and 10 units for the LSTM layer. The pool size was set as 2 for the first and second MaxPooling layers, and as 1 for the third layer of this type.

The training process consists of changing the weights and bias values of a model to improve its capacity to estimate the target variable. The initialization of those values followed the default definitions of Keras package for all the layers, which means that the weights were initialized according to the Glorot uniform method (Glorot and Bengio, 2010), and the bias were initialized with value 0. However, this type of initialization and the consequent training process have a random nature associated, repeatedly resulting in different estimations of the same target variable even considering the same forcing variables and the same trained structure. To overcome this problem, the CLSTM model was exposed, trained, and the final weights were saved 100 times always considering the same training dataset, with the results being evaluated individually for each experiment. Based on these results, the model with the best performance was selected to estimate the outflow values for Portodemouros reservoir.

8.2.4 Coupling MOHID-Land and CLSTM models

The operationality of the coupled system, which includes the CLSTM and MOHID-Land simulations, was divided into two phases, one that comprehended the warm-up period, and other including the calibration and validation periods defined in Oliveira et al. (2020). Since MOHID-Land is a physical model, it was necessary to consider an initial warm-up period for the stabilization of the hydrological processes and to avoid the influence of the errors related to the imposed initial conditions in the results.

In both phases, models were simulated on a daily basis, taking advantage of the possibility of doing continuous simulations in MOHID-Land. This means that in every simulation, the state of the system in the last simulated instant is saved and can be used as the initial state in the next simulation if date and time match.

In the warm-up simulation, used to stabilize the hydrological model, the reservoirs' module was deactivated. In the end of the warm-up period, the reservoirs' module was activated and the initial conditions (level and stored volume) for the three reservoirs were manually imposed considering the measured values. Then, for each simulated day, the CLSTM model was the first to be run. This model was loaded with the weights already optimized and received the information about the level and the inflow of Portodemouros reservoir estimated by MOHID-Land for the three days before the simulated day. The CLSTM used this information to estimate the outflow for the simulated day. The outflow value estimated by the CLSTM

model was then imposed in MOHID-Land. A scheme representing the described process to couple both models is presented in Figure 8.6. This scheme was coded in the Python language.

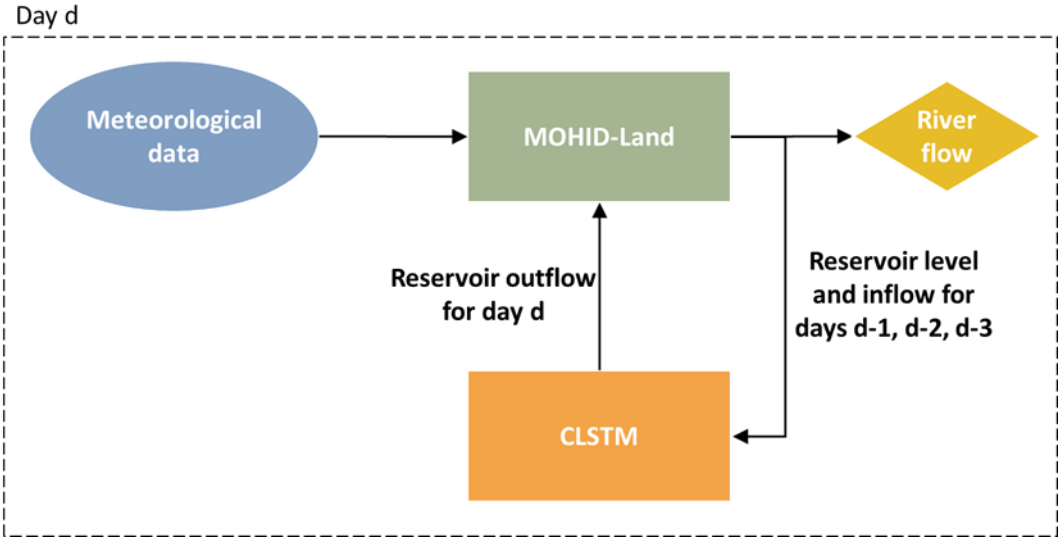

Figure 8.6 Operationality scheme for the modelling process.

8.2.5 Model's evaluation

The CLSTM model used to predict the outflow from Portodemouros reservoir was evaluated considering a subset of the original dataset from Augas de Galicia, which was not previously exposed to the trained model. That subset is known as test dataset and contained pairs of forcing (inflow and level) and target (outflow) variables. Thus, the outflow was estimated based on the forcing variables and was then compared to the corresponding measured outflow. This comparison was based on a visual analysis, and the estimation of four different statistical indicators, namely, the coefficient of determination (R^2), the percentage bias (PBIAS), the ratio of the root mean square error to the standard deviation of observation (RSR), and the Nash-Sutcliffe modeling efficiency (NSE), which were computed as follows:

$$R^2 = \left[\frac{\sum_{i=1}^{p} \left(X_i^{obs} - X_{mean}^{obs}\right)\left(X_i^{sim} - X_{mean}^{sim}\right)}{\sqrt{\sum_{i=1}^{p} \left(X_i^{obs} - X_{mean}^{obs}\right)^2} \sqrt{\sum_{i=1}^{p} \left(X_i^{sim} - X_{mean}^{sim}\right)^2}} \right]^2 \quad \text{(Eq. 8.2)}$$

$$PBIAS = \frac{\sum_{i=1}^{p} \left(X_i^{obs} - X_i^{sim}\right)}{\sum_{i=1}^{p} X_i^{obs}} \times 100 \quad \text{(Eq. 8.3)}$$

$$RSR = \frac{RMSE}{STDEV_{obs}} = \frac{\sqrt{\sum_{i=1}^{p} \left(X_i^{obs} - X_i^{sim}\right)^2}}{\sqrt{\sum_{i=1}^{p} \left(X_i^{obs} - X_{mean}^{obs}\right)^2}} \quad \text{(Eq. 8.4)}$$

$$NSE = 1 - \frac{\sum_{i=1}^{p}\left(X_i^{obs} - X_i^{sim}\right)^2}{\sum_{i=1}^{p}\left(X_i^{obs} - X_{mean}^{obs}\right)^2} \quad \text{(Eq. 8.5)}$$

where x_i^{obs} and x_i^{sim} are the outflow values observed and estimated by the model on day i, respectively, X_{mean}^{obs} and X_{mean}^{sim} are the average outflow considering the observed and the modelled values in the analyzed period, and p is the total number of days/values in this period. The test dataset corresponded to 10% of the size of the original dataset and covered the period between 19/09/2015 and 16/07/2018, totalizing 1023 daily values.

In this study the evaluation of streamflow values focused on the hydrometric stations placed downstream the set of reservoirs and intended to verify the behavior of the coupled modelling system (MOHID-Land+CLSTM). This evaluation was performed by comparing the streamflow values estimated by the coupled modelling system with those measured in Ulla-Touro and Ulla-Teo hydrometric stations. The validation of the coupled system was made from 01/01/2009 to 31/12/2017 and was based on a visual analysis and the four statistical indicators presented before, namely, the R^2, PBIAS, NSE, and RSR. According to Moriasi et al., 2007, the NSE and the R^2 values should be higher than 0.5 and the PBIAS should be ±25% for the model performance to be considered satisfactory, while RSR values closer to 0 mean a more accurate model.

8.3 Results

8.3.1 MOHID-Land model

In natural regime flow, MOHID-Land's performance reached satisfactory to good results at Sar, Ulla, Arnego-Ulla and Deza hydrometric stations (Table 8.4) as shown in Oliveira et al. (2020). The R^2 values ranged from 0.56 to 0.75 and 0.76 to 0.85 in the calibration (01/01/2009-31/12/2012) and validation (01/01/2013-31/12/2017) periods, respectively. The RSR showed values lower than 0.67 for all stations in both periods, while the NSE presented values from 0.55 to 0.72 in the calibration period and from 0.72 to 0.84 in the validation period. Finally, the PBIAS presented a slight overestimation of river flow in Sar hydrometric station (calibration: 0.18%; validation: 16.09%) while in the other three stations the model was underestimating the river flow, with PBIAS values ranging from -12.29% to -8.96% and from -18.54% to -4.35% in calibration and validation periods, respectively.

Table 8.4 Statistical indicators resulting from the comparison of the natural regime flow estimated by MOHID-Land with the observed streamflow values in 6 hydrometric stations (Cal. – calibration, Val. – validation, adapted from: Oliveira et al., 2020).

Station	R^2 (-)		NSE (-)		RSR (-)		PBIAS (%)	
	Cal.	Val.	Cal.	Val.	Cal.	Val.	Cal.	Val.
Sar	0.75	0.83	0.72	0.81	0.53	0.44	0.18	16.09

Station	R^2 (-)		NSE (-)		RSR (-)		PBIAS (%)	
	Cal.	Val.	Cal.	Val.	Cal.	Val.	Cal.	Val.
Ulla	0.56	0.76	0.55	0.72	0.67	0.53	-11.24	-18.54
Arnego-Ulla	0.70	0.78	0.69	0.76	0.55	0.49	-12.29	-16.82
Deza	0.74	0.85	0.72	0.84	0.53	0.40	-8.96	-4.35
Ulla-Touro	0.46	0.52	-0.09	0.24	1.04	0.87	-19.06	-19.12
Ulla-Teo	0.77	0.79	0.71	0.73	0.54	0.52	-16.68	-14.36

Figure 8.7 compares the observed streamflow (black line) with the respective MOHID-Land simulations without considering the influence of reservoirs (blue line) at Ulla-Touro and Ulla-Teo. Since these hydrometric stations have their natural regime flow altered by the operation of the set of reservoirs in the watershed, the performance of the hydrological model without reservoirs showed a significative decrease, as expected (Table 8.4).

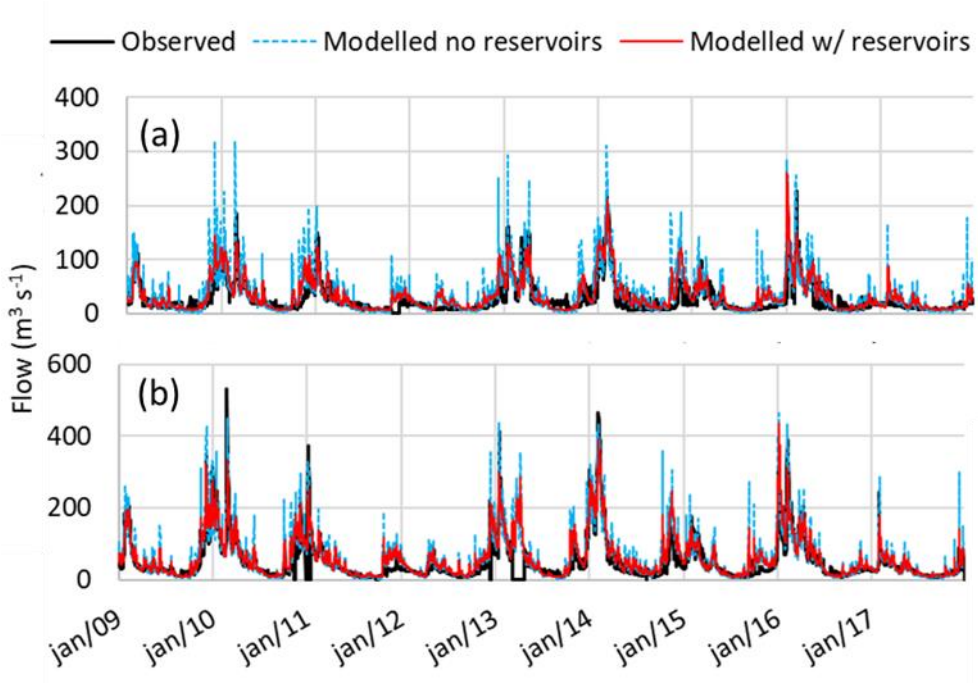

Figure 8.7 Comparison of modelled and observed streamflow in hydrometric stations (a) Ulla-Touro and (b) Ulla-Teo with and without considering the existence of reservoirs.

8.3.2 CLSTM model

To better evaluate the performance of CLSTM neural network model, the four statistical indicators were calculated for the set of 100 models trained with the same training dataset.

Table 8.5 Average, minimum, maximum and standard deviation values of the four statistical parameters estimated for the set of 100 models ran.

	R^2 (-)	NSE (-)	RSR (-)	PBIAS (%)
Average	0.90	0.89	0.33	-1.71
Minimum	0.89	0.86	0.31	-15.74
Maximum	0.91	0.90	0.37	14.07
Standard deviation	0.00	0.01	0.01	6.26

The behavior of the developed CLSTM model was extremely regular, with an R^2 always above 0.89, and the NSE higher than 0.86. The worst PBIAS was -15.74%, and the maximum value of RSR was 0.37. More specifically, the trained model elected to represent the outflow estimation of Portodemouros reservoir obtained a NSE of 0.90, a R^2 of 0.91, a PBIAS of -2.61%, and a RSR of 0.31. Figure 8.8 shows the comparison between the modelled and the observed values for Portodemouros outflow.

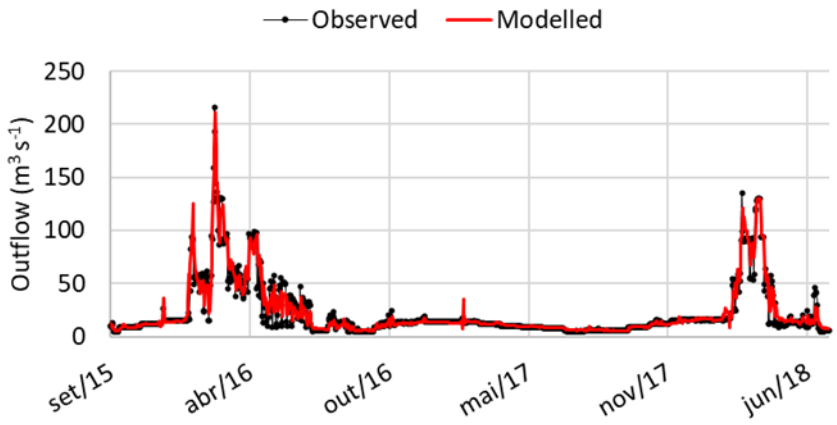

Figure 8.8 Comparison between modelled and observed Portodemouros outflow.

The CLSTM predicted the outflow of Portodemouros reservoir very accurately. However, when the observed values showed accentuated differences in a short period of time, such as two consecutive days, the model demonstrated some difficulty in reproducing that behavior, being able to reproduce the increase-decrease behavior at the right instant but unable to reach correct values. This is the case of the outflow predictions for May and June of 2016 (Figure 8.8).

8.3.3 Coupled system

In the coupled system (MOHID-Land+CLSTM), Portodemouros outflow was estimated with the CLSTM model considering the level and inflow estimated by MOHID-Land model. Then, the outflow predicted by the CLSTM model was imposed in MOHID-Land. Therefore, the inflow and outflow of the reservoir as well as the two hydrometric stations influenced by the presence of the reservoirs were the target of the validation of the coupled system.

Figure 8.9a compares the observed and modelled inflow in Portodemouros reservoir, while Figure 8.9b shows the same comparison for the outflow. The observed (black line) and modelled (red line) streamflow comparison for Ulla-Tour and Ulla-Teo stations is presented in Figure 8.7a and Figure 8.7b, respectively. The four statistical indicators used to evaluate the model's performance were also calculated for the inflow, outflow, and the streamflow in Ulla-Touro and Ulla-Teo stations and are presented in Table 8.6.

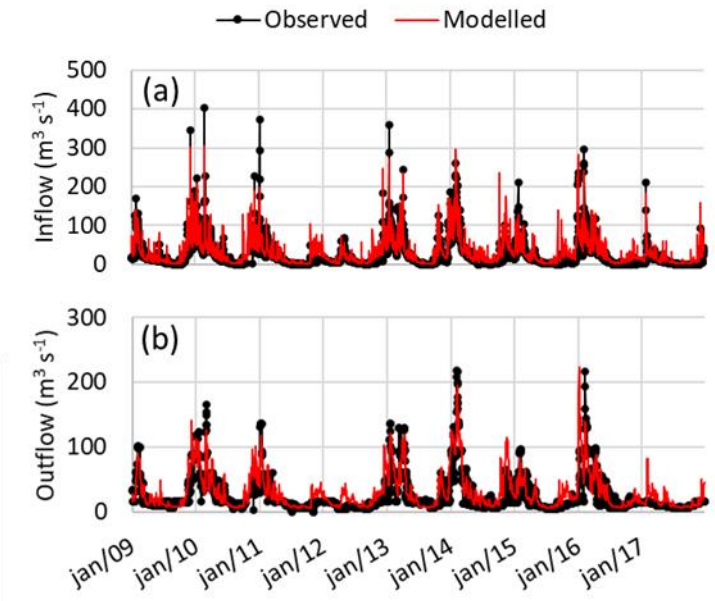

Figure 8.9 Comparison between the modelled and observed (a) inflow and (b) outflow in Portodemouros reservoir.

Table 8.6 Statistical parameters for inflow, outflow, and streamflow in Ulla-Touro and Ulla-Teo stations (Cal. – calibration, Val. – validation). The values between brackets represent the percentage of change of the statistical parameter to the corresponding value in the simulation without reservoirs.

Station	R^2 (-)		NSE (-)		RSR (-)		PBIAS (%)	
	Cal.	Val.	Cal.	Val.	Cal.	Val.	Cal.	Val.
Inflow	0.79	0.81	0.76	0.77	0.49	0.48	-23.68	-28.38
Outflow	0.71	0.66	0.64	0.55	0.60	0.67	-19.53	-25.35
Ulla-Touro	0.74 (+61%)	0.70 (+35%)	0.65 (+822%)	0.61 (+154%)	0.59 (-43%)	0.63 (-28%)	-17.20 (-10%)	-19.58 (+2%)
Ulla-Teo	0.87 (+13%)	0.86 (+9%)	0.85 (+20%)	0.83 (+14%)	0.39 (-28%)	0.41 (-21%)	-15.48 (-7%)	-14.68 (+2%)

Inflows estimates in Portodemouros reservoir were in accordance with Oliveira et al. (2020). For the outflow values estimated with the CLSTM model considering the original dataset, the performance of the coupled system slightly decreased when compared with the previous indicators, with R^2 of 0.66, NSE of 0.55, RSR of 0.67, and PBIAS of -25% for the validation period. The coupled system further showed a good performance when simulating streamflow in the two hydrometric stations (Ulla-Touro and Ulla-Teo), in which the regime flow is altered by the presence of the reservoirs. Considering both hydrometric stations, the R^2 improved about 30% compared with the results without reservoir, reaching a minimum of 0.70. The RSR indicator also demonstrated a better performance with values fitting the range from 0.39 to 0.63 and revealing an average improvement of about 30%. The higher impact was observed for the NSE indicator, which increased about 253% with the values laying in the range from 0.61 to 0.85. Finally, the PBIAS showed an average decrease of about 4%.

Despite the good results obtained for the streamflow downstream reservoirs, it is important to denote that the reservoir's level estimated by MOHID-Land model did not reach the minimum requirements to be classified as satisfactory (calibration: NSE=−2.44, R^2=0.01, PBIAS=−3.16%, RSR=1.85; validation: NSE=0.00, R^2=0.09, PBIAS=−0.67%, RSR=1.00). The coupled system overestimated Portodemouros level most of the time, with exception for the period between January 2013 and the middle of 2016, when the observed and modelled values were more similar (Figure 8.10).

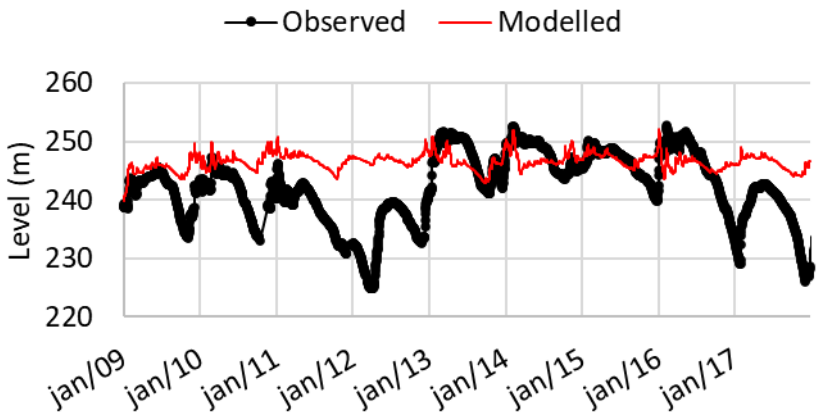

Figure 8.10 Comparison between modelled and observed level in Portoudemouros reservoir.

It could be expected that this issue would affect streamflow estimation downstream the reservoir since the outflow estimated by CLSTM model considered the level values estimated by MOHID-Land. However, as demonstrated before, this issue did not significantly impact downstream results.

8.3.4 Impact of reservoirs 'operation on streamflow

As referred to before, the reservoirs have an impact on the natural regime flow downstream those infrastructures. The impact in Ulla River watershed was here assessed by comparing the simulations under natural flow regime with the simulation of the coupled system. For this, the streamflow was evaluated in three locations along the river network, namely, at the Ulla-Touro and Ulla-Teo stations and at the outlet of the watershed. Table 8.7 shows the minimum, maximum, average, and 2nd, 3rd and 4th quartiles values of the streamflow timeseries obtained for those locations considering the scenarios with (Res.) and without (No res.) reservoirs.

Table 8.7 Alterations on streamflow downstream reservoirs considering the simulations without and with those infrastructures (No res. - without reservoirs; Res - with reservoirs).

Statistical indicator	Ulla-Touro		Ulla-Teo		Outlet	
	No res.	Res.	No res.	Res.	No res.	Res.
Minimum ($m^3 s^{-1}$)	1.4	6.2 (+356%)	3.6	8.2 (+127%)	4.2	8.7 (+105%)

Statistical indicator	Ulla-Touro		Ulla-Teo		Outlet	
	No res.	Res.	No res.	Res.	No res.	Res.
Maximum ($m^3 s^{-1}$)	319.1	260.8 (-18%)	462.2	432.8 (-6%)	569.3	511.9 (-10%)
Average ($m^3 s^{-1}$)	33.4	33.2 (-1%)	62.1	62.1 (0%)	74.1	73.9 (0%)
2nd quartile ($m^3 s^{-1}$)	8.5	10.9 (+28%)	17.2	20.1 (+17%)	20.2	23.4 (+16%)
3rd quartile ($m^3 s^{-1}$)	21.5	22.0 (+3%)	42.0	42.8 (+2%)	49.7	50.2 (+1%)
4th quartile ($m^3 s^{-1}$)	43.5	40.9 (-6%)	83.3	79.8 (-4%)	99.2	96.0 (-3%)

The most significative differences in streamflow occurred at the Ulla-Touro station, located immediately downstream the reservoirs and more influenced by reservoirs' operations. The main differences between the two scenarios were observed in the smallest values, namely, the minimum and the 2nd quartile. In both cases, the streamflow showed an increase when the reservoirs were considered in the simulation, with the minimum streamflow increasing 105% in the outlet, 127% in Ulla-Teo, and 356% in Ulla-Touro, and the 2nd quartile increasing 16%, 17% and 28% in the outlet, Ulla-Teo and Ulla-Touro, respectively. On the opposite, the main decreases were observed in the maximum and 4th quartile for all the evaluated points. However, the decreases of the highest values were not so significant as the differences observed for the smallest values, with the maximum values decreasing 10% in the outlet, 6% in Ulla-Teo and 18% in Ulla-Touro and the 4th quartile presenting differences of -3%, -4% and -6% in the outlet, Ulla-Teo and Ulla-Touro, respectively.

The distribution of streamflow along the year (Figure 8.11) showed a decrease in the average streamflow between October and December (wet season) when considering the reservoirs. Between January and March, also in the wet season, the streamflow only showed slight differences when considering or not the reservoirs. Finally, the dry season was totally characterized by an increase in the streamflow for the simulations with reservoirs, with the main differences found between July and September. For the same reasons presented before, Ulla-Touro station was the point where the main differences were observed.

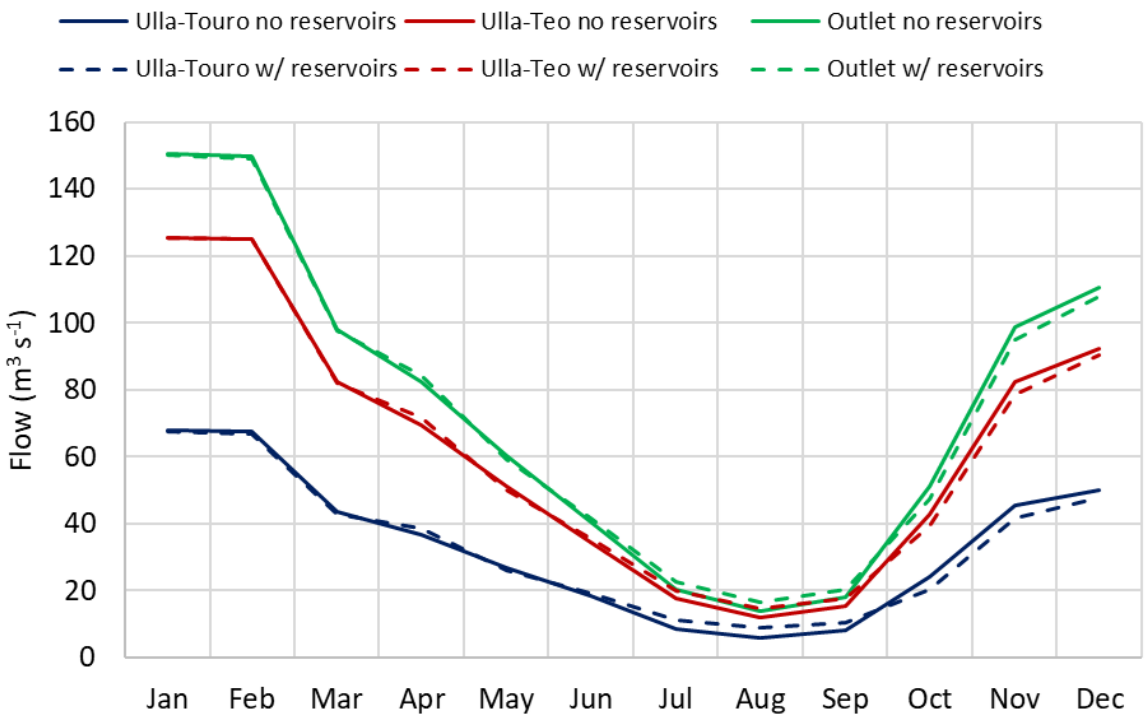

Figure 8.11 Average monthly streamflow in Ulla-Touro and Ulla-Teo stations and in the outlet for the two simulated scenarios, i.e., without and with reservoirs.

The behaviour presented in Figure 8.11 is the expected result when considering reservoirs' operations since this type of infrastructure is commonly used to store water during the wet season, causing a decrease of downstream streamflow. On the other hand, it is expected that average streamflow increases during dry seasons due to the constant necessity of energy production throughout the year and the imposition of ecological flows downstream reservoirs to maintain the health of the ecosystems.

8.4 Discussion

The results of the presented study show that the direct incorporation of reservoirs' operation in hydrologic modelling has a significative impact on the results of the modelled system, as already referred by Bellin et al. (2016). The development of the CLSTM model to predict Portodemouros outflow, which was after imposed in the hydrological model, needed to guarantee that the model estimation was good enough to avoid an error propagation. The elected CLSTM model reached a performance where the NSE was 0.90, the R^2 was 0.91, and the PBIAS and RSR were -2.61% and 0.31, respectively, considering a test dataset. Similar results were obtained by Yang et al. (2019), who estimated the daily outflow of three multipurpose reservoirs located in Thailand, considering three different types of RNN models, namely, a non-linear autoregressive model with exogenous input (NAXR), a long short-term memory (LSTM), and a genetic algorithm based on NAXR (GA-NAXR). The authors

considered as forcing variables the inflow estimated by a hydrological model in the previous two days and the following two days together with the reservoir storage volume in the previous day. They obtained an average Pearson correlation coefficient of 0.91, an average NSE of 0.81, and an average PBIAS of -0.71% with the NARX model and considering the three modelled reservoirs. The LSTM and GA-NARX models reached an average Pearson correlation coefficient of 0.88 and 0.94, respectively, an average NSE of 0.72 and 0.88 and an average PBIAS of 0.22% and -0.24%, with the GA-NARX demonstrating the best performance. Hughes et al. (2021) demonstrated the ability of a modified version of the SHETRAN model to predict the outflow of Crummock Water Lake, located in the Upper Cocker catchment, in United Kingdom. By including a dynamic weir module in the original SHETRAN model, the authors deducted the behavior of sluices by comparing the outflow values of a static and a dynamic weir models. The developed approach reached an NSE of 0.82, a value similar to the ones obtained in the present study, but its application to other case studies presents several limitations. First, it can be very laborious since it was based on a generic framework that included 12 steps. Second, the implementation of that framework implied a deep knowledge about the geometry of control structures and the details of operating procedures, with the authors referring that the broad conceptual understanding of sluice operations needed for the implementation was obtained through site visits and operator interviews.

On the other hand, the estimation of reservoirs' outflow using neural network models, such as the CLSTM model used here can also contain several limitations. With the choice of the forcing variables being pointed out by several authors as crucial for a successful model (ASCE, 1996; Maier et al., 2010; Dolling and Varas, 2002; Wu et al., 2014; Juan et al., 2017), the consideration of other forcing variables should be evaluated. Also, the structure of this type of model, that includes the number of hidden layers, the number of nodes, the kernel size, the activation functions, and other characteristics, is usually optimized by a trial-and-error procedure. However, the number of options that can be adopted for each of those structural characteristics and their combination makes the search space too wide to evaluate all the possible solutions. Thus, the manual approach adopted here to define the model's structure can be restrictive to the searching of the best solution since a small number of possible solutions were tested when considering the entire search space. It is then clear that the optimization of the structure of CLSTM model can improve the results. As suggested by Oliveira et al. (2023), this task can be done using tools that implement different algorithms to efficiently search for the best solution contained in a search space.

Considering the coupled system, the results showed a very clear and interesting improvement when compared with the implementation without reservoirs, with all the statistical indicators demonstrating a better performance in the coupled system for the two hydrometric stations influenced by reservoirs' operations. Although the coupled system has demonstrated a very good performance it is important to refer that besides the limitations already pointed to the CLSTM model, the coupled system has its own limitations. Firstly, when CLSTM is incorporated into the system it will use an estimated inflow, in opposition with the observed values used to train the model. Thus, when the inflow value is not correctly estimated by the hydrologic model it will negatively influence the estimation of the outflow by the CLSTM model, leading to an exacerbation of the error downstream this point. Also, the level used by the CLSTM model to force the outflow estimation is simulated by a mass balance performed by the hydrologic model. However, MOHID-Land does not yet incorporate the reservoir's loss by evaporation and infiltration, which can lead to an overestimation of the reservoir's level as observed in Figure 8.10. As in the case of the inflow, if the level value that feeds the CLSTM model is far from the correct value, the estimated outflow will also be inaccurate and may lead to an increased error in downstream areas.

Nevertheless, the results of this study agree with other studies. For instance, Yun et al. (2020) modified the original VIC model to contemplate the reservoirs 'operations in the Lancang-Mekong River basin, in Asia, and compared the performance of the model with observed data in five hydrometric stations. Considering the calibration and validation periods, the author obtained NSE values ranging from 0.61 and 0.75 and a model bias that varied between -3% and 4% for daily streamflow. Following a similar approach, Dang et al. (2020) modified the VIC model to integrate reservoirs' operation into hydrological simulations. 118 solutions of the model with reservoirs and 109 solutions without reservoirs were run and automatically calibrated considering the upper Mekong River basin as case study. That set of models obtained NSE values from 0.68 to 0.79, and a transformed root mean square error from 8.10 to 16.69, with the statistics of both solutions evenly distributed in those ranges. It is important to denote that the authors referred that, in the case of the implementations without reservoirs, the model reached such good performance probably because the model parameterization helped to compensate the structural error of the non-consideration of reservoirs. However, in both modified versions of the VIC model, reservoirs' operations were imposed by the authors through the definition of several operation rules that implied the knowledge of reservoirs' characteristics that sometimes are not easily available, such as the normal storage, the flood-limited storage, the environmentally friendly streamflow, the

maximum safe streamflow for the downstream area, the capacity of the turbines, the target storage, and others. This fact can limit the application of both methodologies in areas with limited information.

Dong et al. (2023) adopted a similar approach to the one presented in this study, using two data-driven models to reproduce reservoirs behavior in terms of outflow, when data was available, and coupled them with a high-resolution model. For the reservoirs with no data, a calibration-free conceptual reservoir operation scheme was designed. Considering the Upper Yangtze River Basin, China as a case study, 10 reservoirs were considered, with 4 being simulated with the data-driven models and 6 being simulated with the conceptual scheme. The authors simulated the outflow and the storage of the reservoirs using a XGBoost model and an ANN model, with the first demonstrating the best performance for both properties. Considering the test period, XGBoost obtained NSE values higher than 0.85 for the outflow simulation and higher than 0.88 for the storage simulation, while the same indicator was higher than 0.80 and 0.83 for the outflow and storage simulations, respectively, when the ANN was considered. Taking into account the set of hydrometric stations analyzed, the NSE values were higher than 0.65.

Finally, the reservoir's downstream effects on streamflow values found in this study were also in accordance with Yun et al. (2020) and Dong et al. (2023). Both authors concluded that the presence of the reservoirs decreased the average streamflow during the wet season and increased in the dry season, with a higher increase during the dry season than the decrease in the wet season. In Ulla River basin, the annual average streamflow did not verify any changes; however, the differences in wet and dry seasons were also observed (Figure 8.11). During the wet season (Oct-Mar), the streamflow suffered a decrease of about 5%, 3% and 2% in Ulla-Touro, Ulla-Teo and in the outlet of the watershed, respectively. For the dry season (Apr-Sep), increases of approximately 18%, 9% and 8% were estimated for those same points. At the same time, the maximum streamflow and the 4th quartile verified a decrease when the presence of the reservoirs was considered. The maximum streamflow decreased a maximum of 18% (from 319 $m^3 s^{-1}$ to 261 $m^3 s^{-1}$) in Ulla-Touro station and a minimum of 6% (from 462 $m^3 s^{-1}$ to 433 $m^3 s^{-1}$), while the 4th quartile presented decreases between 6% (from 44 $m^3 s^{-1}$ to 41 $m^3 s^{-1}$) and 3% (from 99 $m^3 s^{-1}$ to 96 $m^3 s^{-1}$) at Ulla-Touro and at the outlet, respectively. The capacity of decreasing and control flow peaks is of extreme importance in Ulla River basin, since the downstream area is exposed to high flood risk exacerbated by the combination of intense rainfall events and the influence of high tides (Augas de Galicia, 2019).

8.5 Conclusion

The approach presented and discussed in this work comprehended the direct integration of reservoirs operation into a hydrologic model. A CLSTM data-driven model was developed to estimate the reservoirs outflow, which values were then imposed in the MOHID-Land model. The case study focused on the Ulla River basin, which was the target of a previous work where MOHID-Land was implemented, calibrated, and validated for natural regime flow. In this watershed, a set of three reservoirs are present, with the one more upstream having the higher storing capacity while the following two work as run-of-the-river dams. The operation of run-of-the-river dams was simulated with an operation curve that relates the level, the inflow and the outflow of the reservoirs, and the outflow of the high-capacity reservoir was estimated using the CLSTM model. The target of this work was to analyze how streamflow simulations improved in the areas where the natural regime flow was modified by reservoirs' operations using the proposed coupled system. The main conclusions were:

1. The CLSTM model selected to represent Portodemouros' outflow showed a very good performance, with NSE, R^2 and RSR values of 0.90, 0.91, and 0.31, respectively. The PBIAS was -2.61% indicating a very slight underestimation of the reservoir outflow.
2. The implementation of the coupled system demonstrated a significative improvement of streamflow estimations in areas downstream reservoirs, with the NSE increasing from a minimum of -0.09 without reservoirs to a minimum of 0.61 with reservoirs. Also, the R^2 demonstrated the same improvement, increasing from a minimum of 0.46 to 0.70 without and with reservoirs, respectively.
3. The MOHID-Land model failed to reproduce the level of the high-capacity reservoir, in part because the model does not include evaporation losses. However, the lack of accuracy did not have a significative impact on the performance of the coupled system.
4. According to the validation performed downstream reservoirs, the basic operation curves selected to simulate the function of the two run-of-the-river dams in the study domain seemed adequate.
5. For the modelled 10-year period, the impacts downstream reservoirs were in line with other studies, with the maximum streamflow (wet season) values experiencing a decrease and the minimum values (dry season) suffering an increase. However, the average streamflow did not show any increase or decrease tendency.

Besides the excellent results obtained in this study, future applications of the methodology should be tested and evaluated to understand its applicability to different

scenarios. One of the doubts that remains is if the CLSTM model has the capacity to reproduce the behavior of a reservoir where water is used for irrigation, which is characterized by punctual discharges in time, instead of an almost continuous discharge as in Portodemouros. Also, the capability of the trained CLSTM model in reproducing outflow values of other reservoirs with similar purposes should be addressed.

Code availability

MOHID-Land is available on the GitHub repository https://github.com/Mohid-Water-Modelling-System/Mohid. The CLSTM model and the scripts to run the coupled system are available on https://github.com/anaioliveira/NNandMOHID.

Author contributions

A.R.O. and L.P. were responsible for the conceptualization. A.R.O. performed the formal analysis, developed and implemented the methodology and the software, and was responsible for results analysis and the visualization. T.B.R. and R.N. were responsible for the funding acquisition. The original draft was written by A.R.O. and revised by T.B.R., L.P. and R.N.

Funding

This research was supported by FCT/MCTES (PIDDAC) through project LARSyS–FCT pluriannual funding 2020–2023 (UIDP/50009/2020), and by Project FEMME (PCIF/MPG/0019/2017). T. B. Ramos was supported by a CEEC-FCT contract (CEECIND/01152/2017).

Acknowledgments

We would also like to thank Augas de Galicia for reservoirs' data availability. Without their support this work would be impossible feasible.

8.6 References

Abadi, M.; Barham, P.; Chen, J.; Chen, Z.; Davis, A.; Dean, J.; Devin, M.; Ghemawat, S.; Irving, G.; Isard, M.; et al. Tensorflow: A system for large-scale machine learning. 12th USENIX Symposium on Operating Systems Design and Implementation (OSDI '16) 2016, 265–283.

Allen, R. G.; Pereira, L. S.; Raes, D.; and Smith, M. Crop evapotranspiration – Guidelines for computing crop water requirements. FAO Irrigation and drainage paper 56. FAO 1998, 56, 327.

ASCE (American Society of Civil Engineers), Task Committee on Hydrology Handbook of Management Group D of ASCE Hydrology Handbook (Second Edition), 1996, https://doi.org/10.1061/9780784401385.

Augas de Galicia. Available online: https://augasdegalicia.xunta.gal/ (accessed on 12 December 2022).

Augas de Galicia. Revisión e actualización da avaliación preliminar do risco de inundación (EPRI 2o ciclo). Documento definitivo—Memoria. Xunta de Galicia - Consellería de Infraestruturas e Mobilidade, Ministerio para la Transición Ecológica, 2019.

Barino, F. O.; Silva, V. N. H.; Lopez-Barbero, A. P.; De Mello Honorio, L.; Santos, A. B. D. Correlated Time-Series in Multi-Day-Ahead Streamflow Forecasting Using Convolutional Networks. IEEE Access 2020, 8, 215748–215757, https://doi.org/10.1109/ACCESS.2020.3040942.

Bellin, A.; Majone, B.; Cainelli, O.; Alberici, D.; Villa, F. A continuous coupled hydrological and water resources management model, Environ. Model. Softw. 2016, 75, 176–192. https://doi.org/10.1016/j.envsoft.2015.10.013.

Bengio, Y.; Simard, P.; Frasconi, P. Learning long-term dependencies with gradient descent is difficult. IEEE Trans. Neural Netw. Learn. Syst. 1994, 5(2), 157–166, https://doi.org/10.1109/72.279181.

Blanco-Chao, R.; Cajade-Pascual, D.; Costa-Casais, M. Rotation, sedimentary deficit and erosion of a trailing spit inside ria of Arousa (NW Spain). Sci. Total Environ. 2020, 749, 141480, https://doi.org/10.1016/j.scitotenv.2020.141480.

Canuto, N.; Ramos, T. B.; Oliveira, A. R.; Simionesei, L.; Basso, M.; Neves, R. Influence of reservoir management on Guadiana streamflow regime. J. Hydrol. Reg. Stud. 2019, 25, 100628, https://doi.org/10.1016/j.ejrh.2019.100628.

Chollet, F. et al. Available online: Keras. GitHub. https://github.com/fchollet/keras (accessed on: March 2021).

Chong, K. L.; Lai, S. H.; Yao, Y.; Ahmed, A. N.; Jaafar, W. Z. W.; El-Shafie, A. Performance Enhancement Model for Rainfall Forecasting Utilizing Integrated Wavelet-Convolutional Neural Network. Water Resour. Manag. 2020, 34(8), 2371–2387, https://doi.org/10.1007/s11269-020-02554-z.

Cloux, S.; Allen-Perkins, S.; de Pablo, H.; Garaboa-Paz, D.; Montero, P.; Pérez Muñuzuri, V.: Validation of a Lagrangian model for large-scale macroplastic tracer transport using mussel-peg in NW Spain (Ría de Arousa). Sci. Total Environ. 2022, 822, 153338, https://doi.org/10.1016/j.scitotenv.2022.153338.

CLC 2012: Corine Land Cover 2012 © European Union, Copernicus Land Monitoring Service, European Environment Agency (EEA). Available online: https://land.copernicus.eu/pan-european/corine-land-cover (accessed on: July 2018)

da Silva, P. M.; Fuentes, J.; Villalba, A. Growth, mortality and disease susceptibility of oyster Ostrea edulis families obtained from brood stocks of different geographical origins, through on-growing in the Ría de Arousa (Galicia, NW Spain). Mar. Biol. 2005, 147(4), 965–977, https://doi.org/10.1007/s00227-005-1627-4.

Dang, T. D.; Chowdhury, A. F. M. K.; Galelli, S. On the representation of water reservoir storage and operations in large-scale hydrological models: Implications on model parameterization and climate change impact assessments. Hydrol Earth Syst Sci. 2020, 24(1), 397–416, https://doi.org/10.5194/hess-24-397-2020.

Dolling, O. R.; Varas, E. A. Artificial neural networks for streamflow prediction. J. Hydraul. Res. 2002, 40(5), 547–554, https://doi.org/10.1080/00221680209499899.

Dong, N.; Guan, W.; Cao, J.; Zou, Y.; Yang, M.; Wei, J.; Chen, L.; Wang, H. A hybrid hydrologic modelling framework with data-driven and conceptual reservoir operation schemes for reservoir impact assessment and predictions. J. Hydrol. 2023, 619, 129246, https://doi.org/10.1016/j.jhydrol.2023.129246.

Elman, J. L. Finding Structure in Time. Cogn. Sci. 1990, 14(2), 179–211, https://doi.org/10.1207/s15516709cog1402_1.

European Digital Elevation Model (EU-DEM), version 1.1. (n.d.). © European Union, Copernicus Land Monitoring Service 2019, European Environment Agency (EEA). Available online: http://land.copernicus.eu/pan-european/satellite-derived-products/eu-dem/eu-dem-v1.1/view.

Feddes, R. A.; Kowalik, P. J.; Zaradny, H. Simulation of field water use and crop yield. Wageningen: Centre for agricultural publishing and documentation, 1978, http://lib.ugent.be/catalog/rug01:000032129.

Ghimire, S.; Yaseen, Z. M.; Farooque, A. A.; Deo, R. C.; Zhang, J.; Tao, X. Streamflow prediction using an integrated methodology based on convolutional neural network and long short-term memory networks. Sci. Rep. 2021, 11(1), 17497, https://doi.org/10.1038/s41598-021-96751-4.

Glorot, X.; Bengio, Y. Understanding the difficulty of training deep feedforward neural networks. Proceedings of the Thirteenth International Conference on Artificial Intelligence and Statistics 2010, 9, 249–256, https://proceedings.mlr.press/v9/glorot10a.html.

Hersbach, H.; Bell, B.; Berrisford, P.; Hirahara, S.; Horányi, A.; Muñoz-Sabater, J.; Nicolas, J.; Peubey, C.; Radu, R.; Schepers, D.; Simmons, A.; Soci, C.; Abdalla, S.; Abellan, X.; Balsamo, G.; Bechtold, P.; Biavati, G.; Bidlot, J.; Bonavita, M. et al. Complete ERA5 from 1979: Fifth generation of ECMWF atmospheric reanalyses of the global climate. Copernicus Climate Change Service (C3S) Data Store (CDS) 2017.

Hochreiter, S.; Schmidhuber, J. Long Short-Term Memory. Neural Comput. 1997, 9(8), 1735–1780, https://doi.org/10.1162/neco.1997.9.8.1735.

Hu, H.; Zhang, J.; Li, T. A Novel Hybrid Decompose-Ensemble Strategy with a VMD-BPNN Approach for Daily Streamflow Estimating. Water Resour. Manag. 2021, 35(15), 5119–5138, https://doi.org/10.1007/s11269-021-02990-5.

Huang, C.; Zhang, J.; Cao, L.; Wang, L.; Luo, X.; Wang, J.-H.; Bensoussan, A. Robust Forecasting of River-Flow Based on Convolutional Neural Network. IEEE Trans. Sustain. Comput. 2020, 5(4), 594–600, https://doi.org/10.1109/TSUSC.2020.2983097.

Hughes, D.; Birkinshaw, S.; Parkin, G. A method to include reservoir operations in catchment hydrological models using SHETRAN. Environ. Model. Softw. 2021, 138, 104980, https://doi.org/10.1016/j.envsoft.2021.104980.

Juan, C.; Genxu, W.; Tianxu, M.; Xiangyang, S. ANN Model-Based Simulation of the Runoff Variation in Response to Climate Change on the Qinghai-Tibet Plateau, China. Adv. Meteorol., 2017, 1–13, https://doi.org/10.1155/2017/9451802.

LeCun, Y.; Bengio, Y. Convolutional networks for images, speech, and time-series. In M. A. Arbib (Ed.), The handbook of brain theory and neural networks. MIT Press, 1995.

LeCun, Y.; Bengio, Y.; Hinton, G. Deep learning. Nature 2015, 521(7553), 436–444, https://doi.org/10.1038/nature14539.

Lipton, Z. C.; Berkowitz, J.; Elkan, C. A Critical Review of Recurrent Neural Networks for Sequence Learning (arXiv:1506.00019), arXiv 2015, http://arxiv.org/abs/1506.00019.

Maier, H. R.; Jain, A.; Dandy, G. C.; Sudheer, K. P. Methods used for the development of neural networks for the prediction of water resource variables in river systems: Current status and future directions. Environ. Model. Softw. 2010, 25(8), 891–909, https://doi.org/10.1016/j.envsoft.2010.02.003.

McKinney, W. Data Structures for Statistical Computing in Python. In S. van der Walt & J. Millman (Eds.), Proceedings of the 9th Python in Science Conference 2010. (pp. 56–61), https://doi.org/10.25080/Majora-92bf1922-00a.

Mehdizadeh, S.; Fathian, F.; Safari, M. J. S.; Adamowski, J. F. Comparative assessment of time series and artificial intelligence models to estimate monthly streamflow: A local and external data analysis approach, J. of Hydrol. 2019, 579, 124225, https://doi.org/10.1016/j.jhydrol.2019.124225.

Mohammadi, B.; Moazenzadeh, R.; Christian, K.; Duan, Z. Improving streamflow simulation by combining hydrological process-driven and artificial intelligence-based models, Environ. Sci. Pollut. Res. 2021, 28(46), 65752–65768, https://doi.org/10.1007/s11356-021-15563-1.

Moriasi, D. N.; Arnold, J. G.; Liew, M. W. V.; Bingner, R. L.; Harmel, R. D.; Veith, T. L. Model Evaluation Guidelines for Systematic Quantification of Accuracy in Watershed Simulations. Trans. of the ASABE 2007, 50(3), 885–900, https://doi.org/10.13031/2013.23153.

Mualem, Y. A new model for predicting the hydraulic conductivity of unsaturated porous media. Water Resour. Res. 1976, 12(3), 513–522, https://doi.org/10.1029/WR012i003p00513.

Nachtergaele, F.; Van Velthuizen, H.; Verelst, L.; Batjes, N.; Dijkshoorn, K.; Van Engelen, V.; Fischer, G.; Jones, A.; Montanarella, L.; Petri, M. et al.: Harmonized World Soil Database; FAO: Rome, Italy; IIASA: Laxenburg, Austria, 2009.

Neitsch, S. L.; Arnold, J. G.; Kiniry, J. R.; Williams, J. R. Soil and Water Assessment Tool Theoretical Documentation Version 2009, 2011.

Ni, L.; Wang, D.; Singh, V. P.; Wu, J.; Wang, Y.; Tao, Y.; Zhang, J. Streamflow and rainfall forecasting by two long short-term memory-based models. J. of Hydrol. 2020, 583, 124296, https://doi.org/10.1016/j.jhydrol.2019.124296.

Oliveira, A. R.; Ramos, T. B.; Neves, R. Streamflow Estimation in a Mediterranean Watershed Using Neural Network Models: A Detailed Description of the Implementation and Optimization. Water 2023, 15(5), 947, https://doi.org/10.3390/w15050947.

Oliveira, A. R.; Ramos, T. B.; Simionesei, L.; Pinto, L.; Neves, R. Sensitivity Analysis of the MOHID-Land Hydrological Model: A Case Study of the Ulla River Basin. Water 2020, 12(11), 3258, https://doi.org/10.3390/w12113258.

Outeiro, L.; Byron, C.; Angelini, R. Ecosystem maturity as a proxy of mussel aquaculture carrying capacity in Ria de Arousa (NW Spain): A food web modeling perspective. Aquac. 2018, 496, 270–284, https://doi.org/10.1016/j.aquaculture.2018.06.043.

Pedregosa, F.; Varoquaux, G.; Gramfort, A.; Michel, V.; Thirion, B.; Grisel, O.; Blondel, M.; Prettenhofer, P.; Weiss, R.; Dubourg, V. et al. Scikit-learn: Machine learning in Python. J. Mach. Learn. Res. 2011, 12(Oct), 2825–2830.

Pestana, R.; Matias, M.; Canelas, R.; Araújo, A.; Roque, D.; Van Zeller, E.; Trigo-Teixeira, A.; Ferreira, R.; Oliveira, R.; Heleno, S. Calibration of 2D hydraulic inundation models in the floodplain region of the lower Tagus river. Proc. ESA Living Planet Symposium 2013. ESA Living Planet Symposium 2013, Edinburgh, UK, 2013.

Ramos, T. B.; Simionesei, L.; Jauch, E.; Almeida, C.; Neves, R. Modelling soil water and maize growth dynamics influenced by shallow groundwater conditions in the Sorraia Valley region, Portugal. Agric. Water Manag. 2017, 185, 27–42, https://doi.org/10.1016/j.agwat.2017.02.007.

Ritchie, J. T. Model for predicting evaporation from a row crop with incomplete cover, Water Resour. Res. 1972, 8(5), 1204– 1213, https://doi.org/10.1029/WR008i005p01204.

Saon, G.; Picheny, M. Recent advances in conversational speech recognition using convolutional and recurrent neural networks. IBM J. Res. Dev. 2017, 61(4/5), 1:1-1:10, https://doi.org/10.1147/JRD.2017.2701178.

Šimůnek, J.; Hopmans, J. W. Modeling compensated root water and nutrient uptake. Ecol. Model. 2009, 220(4), 505–521, https://doi.org/10.1016/j.ecolmodel.2008.11.004.

Skaggs, T. H.; van Genuchten, M. Th.; Shouse, P. J.; Poss, J. A. Macroscopic approaches to root water uptake as a function of water and salinity stress. Agric. Water Manag. 2006, 86(1–2), 140–149, https://doi.org/10.1016/j.agwat.2006.06.005.

Tao, Q.; Liu, F.; Li, Y.; Sidorov, D. Air Pollution Forecasting Using a Deep Learning Model Based on 1D Convnets and Bidirectional GRU. IEEE Access 2019, 7, 76690–76698, https://doi.org/10.1109/ACCESS.2019.2921578.

Tóth, B.; Weynants, M.; Pásztor, L.; Hengl, T. 3D soil hydraulic database of Europe at 250 m resolution. Hydrol. Process. 2017, 31(14), 2662–2666, https://doi.org/10.1002/hyp.11203.

Trancoso, A. R.; Braunschweig, F.; Chambel Leitão, P.; Obermann, M.; Neves, R. An advanced modelling tool for simulating complex river systems. Sci. Total Environ. 2009, 407(8), 3004–3016, https://doi.org/10.1016/j.scitotenv.2009.01.015.

van Genuchten, M. Th. A Closed-form Equation for Predicting the Hydraulic Conductivity of Unsaturated Soils. Soil Sci. Soc. Am. J. 1980, 44(5), 892–898, https://doi.org/10.2136/sssaj1980.03615995004400050002x.

Wang, J.-H.; Lin, G.-F.; Chang, M.-J.; Huang, I.-H.; Chen, Y.-R. Real-Time Water-Level Forecasting Using Dilated Causal Convolutional Neural Networks. Water Resour. Manag. 2019, 33(11), 3759–3780, https://doi.org/10.1007/s11269-019-02342-4.

Wang, W.; Vrijling, J. K.; Van Gelder, P. H. A. J. M.; Ma, J. Testing for nonlinearity of streamflow processes at different timescales. J. of Hydrol. 2006, 322(1–4), 247–268, https://doi.org/10.1016/j.jhydrol.2005.02.045.

Williams, J. R.; Jones, C. A.; Kiniry, J. R.; Spanel, D. A. The EPIC Crop Growth Model. Trans. of the ASAE 1989, 32(2), 0497–0511, https://doi.org/10.13031/2013.31032.

Wu, W.; Dandy, G. C.; Maier, H. R. Protocol for developing ANN models and its application to the assessment of the quality of the ANN model development process in drinking water quality modelling. Environ. Model. & Softw. 2014, 54, 108–127, https://doi.org/10.1016/j.envsoft.2013.12.016.

Xiong, B.; Xiong, L.; Xia, J.; Xu, C.-Y.; Jiang, C.; Du, T. Assessing the impacts of reservoirs on downstream flood frequency by coupling the effect of scheduling-related multivariate rainfall with an indicator of reservoir effects. Hydrol. Earth Syst. Sci. 2019, 23(11), 4453–4470, https://doi.org/10.5194/hess-23-4453-2019.

Xu, W.; Jiang, Y.; Zhang, X.; Li, Y.; Zhang, R.; Fu, G. Using long short-term memory networks for river flow prediction. Hydrol. Res. 2020, 51(6), 1358–1376, https://doi.org/10.2166/nh.2020.026.

Yang, S.; Yang, D.; Chen, J.; Zhao, B. Real-time reservoir operation using recurrent neural networks and inflow forecast from a distributed hydrological model. J. Hydrol. 2019, 579, 124229, https://doi.org/10.1016/j.jhydrol.2019.124229.

Yun, X.; Tang, Q.; Wang, J.; Liu, X.; Zhang, Y.; Lu, H.; Wang, Y.; Zhang, L.; Chen, D.: Impacts of climate change and reservoir operation on streamflow and flood characteristics in the Lancang-Mekong River Basin. J. Hydrol. 2020, 590, 125472, https://doi.org/10.1016/j.jhydrol.2020.125472.

9 Conclusions

The work presented here proved the ability of physically based models, in particular MOHID-Land, to simulate daily natural regime flow accurately at the watershed scale. However, implementations on large and too diversified domains containing relatively small and independent watersheds should be disregarded. This type of implementation, where the sub-domains need to be characterized in detail to correctly catch all the processes occurring there, needs high resolution grids to reach good results. However, those high-resolution solutions can raise the computational time to levels that are not acceptable, namely, to carry out the calibration and validation processes. At the same time, the generalization of some parameters considered by MOHID-Land makes the calibration process on those vast domains difficult.

The performance of a sensitivity analysis to MOHID-Land model was essential to successfully simulate Maranhão and Ulla River watersheds for natural regime flow. With the sensitivity analysis performed in the Ulla River watershed, the resolution of the simulation grid, the choice of the infiltration method, and the evapotranspiration process demonstrated to be the main factors influencing river flow generation. The soil hydraulic properties, the depth of the soil profile, and the dimensions of the river cross-sections, which basically control the interactions between the porous media and the river, influenced baseflow. Peak flows were mostly constrained by the channel's Manning coefficient, as well as the dimensions of the river cross-sections.

The monitoring network in Ulla River watershed allowed to accurately calibrate and validate the natural regime flow in most of the watershed area. However, for Maranhão, the situation was the opposite. This watershed was characterized by a significant lack of information about what concerns the streamflow. Thus, the model was calibrated and validated for a sub-basin that drains about 40% of Maranhão watershed. The calibrated parameters were then extended to the entire watershed and the results were validated with a monthly mass balance at the reservoir, which represents the outlet of the studied domain.

Considering also Maranhão watershed and trying to reach better computational times, a neural network model was also applied to estimate streamflow. After several tests at the sub-basin scale, a convolutional neural network (CNN) model considering the precipitation as forcing variable demonstrated to be the best solution for this case. With the CNN model trained and validated for the sub-basin, the extension of this model for the entire Maranhão watershed was performed replacing the values of the forcing variable by the precipitation of the larger

domain. As in the case of MOHID-Land, those results were validated at the reservoir level considering a monthly mass balance.

Results demonstrated that MOHID-Land and the CNN model can reproduce the natural regime flow in the sub-basin with satisfactory to very good performances. In turn, the extension of the calibrated and trained models to the entire Maranhão watershed showed identical performances, classified as good. Nevertheless, the study allowed to understand that the application of neural network models can be limited in what concerns the study of future scenarios or events that go beyond the observed data. This limitation is mainly related to the lack of physical comprehension to respond to events that were not verified before and with the difficulty of including all the data needed to characterize future modifications in the forcing variables. These limitations are not verified when applying a physical-based model, and the inclusion of the changes in future scenarios only finds difficulties in the uncertainty of the forecasts of those changes. However, the implementation of physical models faces other problems, such as the detail needed to characterize the modelled domain and the computational needs to run long-term simulations. Thus, hybrid solutions, combining different types of models or different models, can be used to overcome the shortcomings of both approaches.

Finally, considering that the implementation of MOHID-Land in the Guadiana watershed showed that the representation of the impact of reservoirs' operation in streamflow regime is very difficult to capture and reproduce using only purely hydrological models, a hybrid solution was developed taking advantage of the characteristics of neural network models. That hybrid solution coupled a convolutional long short-term memory (CLSTM) model for reservoir's outflow estimation with MOHID-Land implementation in Ulla River watershed. With MOHID-Land feeding the CLSTM model with inflow and level values, the outflow estimated by the CLSTM was then imposed into MOHID-Land model. Results showed a drastic improvement in streamflow estimates downstream the reservoir, proving the capacity of the proposed approach to simulate the impact of the reservoir in the alteration of streamflow regime.

In what concerns the research objectives of this thesis, it is now possible to conclude that hydrological modelling for water management purposes should be focused on the watershed scale. The modelling task can be performed using models with different levels of complexity, but it is essential to keep in mind that less complex models have limitations in the representation of scenarios in which the considered changes cannot be incorporated in the input data that feed the models. It has also been demonstrated that hydrological modelling can benefit from hybrid approaches where different types of models are considered, especially when modelled systems

have a random and not purely physical component associated with human behavior. Finally, the contribution of hydrological modelling for the systems understanding and a consequent improvement of water resources management has stayed clear.

In that sense, it is considered that the hypotheses presented in this thesis was verified with the combination of a data-driven and a physical based models demonstrating the ability to improve streamflow estimations when the human behavior takes place, as in the case of reservoirs' operation.

9.1 Future work

As referred to before, water availability is not only related to water quantity. It is also extremely important to guarantee an appropriate water quality to maintain ecosystems and to assure its availability for consumption. Thus, one of the works to be carried out in the future is to include the simulation of biogeochemical cycles with MOHID-Land to assess water quality in long-term simulations as those presented here.

Besides that, several other questions arise from the investigation described here. When only MOHID-Land simulations are considered the main question that emerges at this point is: how should irrigation be considered at watershed scale using without sacrificing the computational time? Also, future efforts should be made to include the simulation of reservoirs' surface and bottom fluxes into MOHID-Land model.

Concerning the modelling performed only with neural networks, the main questions that arise are:

- How physical processes can be incorporated into neural network solutions to give an insight of the system behavior when using this type of technique? Will it be possible to consider different conditions from those with it the neural network was trained to simulate different scenarios?
- Is the CLSTM structure developed in this work for outflow estimation capable of estimating the corresponding values for other high-capacity reservoirs just with a new training process?
- What is the suitability of neural network models to predict the outflow of supply reservoirs, which are characterized by punctual discharges to the downstream reach? And to predict the usual urban, industrial, and agricultural withdrawals?

Lastly, and taking into account the hybrid approach proposed here, the matter of whether the coupled model is adequate for more complex domains should be a target for future works.

This subject can have special impact in domains where more than one high-capacity reservoir is present or where a mix of high-capacity, supply and run-of-the river dams are identified.

Also, future developments can consider the combination of neural network models and observed data, such as satellite images, to predict the initial conditions of hydrological systems. Then, that information can be assimilated by a hydrological model, and it is expected that predictions improve, and the time needed by the model to forget initial conditions can be significantly reduced. It can be especially advantageous in warning and control systems where time is crucial.